

INFORMATION TO USERS

This manuscript has been reproduced from the microfilm master. UMI films the text directly from the original or copy submitted. Thus, some thesis and dissertation copies are in typewriter face, while others may be from any type of computer printer.

The quality of this reproduction is dependent upon the quality of the copy submitted. Broken or indistinct print, colored or poor quality illustrations and photographs, print bleedthrough, substandard margins, and improper alignment can adversely affect reproduction.

In the unlikely event that the author did not send UMI a complete manuscript and there are missing pages, these will be noted. Also, if unauthorized copyright material had to be removed, a note will indicate the deletion.

Oversize materials (e.g., maps, drawings, charts) are reproduced by sectioning the original, beginning at the upper left-hand corner and continuing from left to right in equal sections with small overlaps. Each original is also photographed in one exposure and is included in reduced form at the back of the book.

Photographs included in the original manuscript have been reproduced xerographically in this copy. Higher quality 6" x 9" black and white photographic prints are available for any photographs or illustrations appearing in this copy for an additional charge. Contact UMI directly to order.

UMI

A Bell & Howell Information Company
300 North Zeeb Road, Ann Arbor MI 48106-1346 USA
313/761-4700 800/521-0600

UNIVERSITY OF CALIFORNIA

SANTA CRUZ

**THREE-DIMENSIONAL NUMERICAL SIMULATION OF BIOSONAR SIGNAL
EMISSION AND RECEPTION IN THE COMMON DOLPHIN**

A thesis submitted in partial satisfaction
of the requirements for the degree of

DOCTOR OF PHILOSOPHY

in

PHYSICS

by

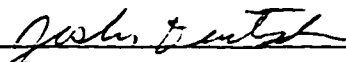
James L. Aroyan

March 1996

The dissertation of James L. Aroyan is approved:



Professor Geoffrey Vallis, Chair



Professor Joshua Deutsch



Professor William Mathews



Dean of Graduate Studies

UMI Number: 9711357

**Copyright 1996 by
Aroyan, James Lincoln**

All rights reserved.

**UMI Microform 9711357
Copyright 1997, by UMI Company. All rights reserved.**

**This microform edition is protected against unauthorized
copying under Title 17, United States Code.**

UMI
300 North Zeeb Road
Ann Arbor, MI 48103

Copyright © by

James L. Aroyan

1996

THREE-DIMENSIONAL NUMERICAL SIMULATION OF BIOSONAR SIGNAL EMISSION AND RECEPTION IN THE COMMON DOLPHIN

James L. Aroyan

ABSTRACT: This dissertation constitutes the final stage of a highly successful research project to quantitatively investigate fundamental mechanisms of dolphin biosonar. This report describes appropriate techniques for three-dimensional acoustic simulation, and demonstrates their accuracy. A novel method for mapping of acoustic tissue parameters from x-ray computed tomographic (CT) data is also introduced. These techniques, applied to models of the forehead and lower jaw tissues of the common dolphin, *Delphinus delphis*, have revealed the acoustic mechanisms involved in sonar signal emission and reception by this animal. The conclusions of this project include: 1) the acoustical parameters of soft biological tissues (including the delphinid melon) can be accurately modeled from x-ray CT data; 2) the skull plays the predominant role in beam formation; 3) the melon (in combination with other soft tissues of the forehead) plays a far more significant role in beam formation than indicated by previous simulations; 4) the melon behaves as a waveguide, a megaphone, and a lens in the biosonar signal emission process; 5) experimentally observed beam patterns are best approximated at all frequencies simulated when the sound source is placed about 1cm below the center of a region of the model known as the right MLDB (monkey lip/dorsal bursae) complex, and not elsewhere; 6) a model has been proposed for the source region which, in conjunction with the mechanisms operating in the melon, may largely explain the observed temporal and spatial characteristics of delphinid biosonar emission fields; 7) a mechanism has been proposed for the production of 'jaw pops' in dolphins; 8) the same mechanisms operating in the melon during signal emission also operate in both fat bodies of the lower jaw in the signal reception (hearing) process; 9) the lower jaw fat bodies significantly improve the forward receptivity patterns of both left and right ear complexes; 10) several mechanisms influencing the directional receptivity of the dolphin have been demonstrated.

Table of Contents

Acknowledgements	xi
Chapter 1. Introduction	
Statement of the nature and objectives of the doctoral project.	1
Chapter 2. Biological Background	
Introduction to the primary experimental characteristics of the emission and reception of dolphin biosonar signals. Description of the essential forehead and lower jaw anatomy. Statement of the questions investigated in the thesis.	6
Chapter 3. Sound Propagation in Homogeneous and Inhomogeneous Fluids	
Acoustic wave equations for homogeneous and inhomogeneous fluids. The assumption of linearity. Characteristic impedance and interface reflection coefficients. The physical behavior of resonators, waveguides, lenses, and megaphones: model of the biosonar signal source region. Derivation of the Helmholtz integral equation.	22
Chapter 4. Numerical Simulation of Sound Propagation. Part I: Finite Difference Methods	
General description of simulation process. Finite difference techniques for simulation of wave propagation; primary algorithms, grid dispersion behavior, and absorbing boundary conditions. Discussion of grid design in simulations.	39
Chapter 5. Numerical Simulation of Sound Propagation. Part II: Boundary Integral Extrapolation Methods	
Discussion of the Helmholtz integral equation and the numerical methods for solution of this equation. Description of selected method of solution. Examples of computed far-field distributions. Performance characteristics and quantization of errors.	57
Chapter 6. Acoustic Modeling of Delphinid Tissues from X-Ray CT Data	
Choice of delphinid species. The nature of x-ray CT data and model construction using this data. Acoustic characteristics of biological tissue. Soft tissue and bone density and velocity mappings from CT data. Modeling of the dolphin's air sacs.	79
Chapter 7. Results of the Simulations	
7.1. Skull-Only Simulations	95
7.2. Skull and Air Sacs Simulations	99
7.3. Skull and Soft Tissue Simulations	100
7.4. Skull, Air Sacs, and Soft Tissue Simulations	102
7.5. Inverse and Forward Hearing Simulations	104
Diagrams of tissue models, simulation grid layouts, and results	109

Chapter 8. Summary of Conclusions and Opportunities for Future Research	164
Appendix 1. A Conjecture for the 'Jaw-pop' Source Mechanism	170
Appendix 2. The Density, Velocity, and Impedance Structure of the Melon of the Common Dolphin	172
References	178

List of Figures

Figure 2.1. Signals and spectra of a biosonar click train emitted by a bottlenose dolphin (<i>Tursiops truncatus</i>) performing a target detection task.	7
Figure 2.2. The averaged waveform and spectrum for the biosonar click train shown in Figure 2.1.	7
Figure 2.3. Representative biosonar click waveform and spectrum for the common dolphin, <i>Delphinus delphis</i>	9
Figure 2.4. Broadband biosonar emission patterns of three bottlenose dolphins in the vertical and horizontal planes.	9
Figure 2.5. Receiving beam patterns in the vertical plane of a bottlenose dolphin at frequencies of 30, 60, and 120 kHz.	13
Figure 2.6. Receiving beam patterns in the horizontal plane of a bottlenose dolphin at frequencies of 30, 60, and 120 kHz.	13
Figure 3.1. Diagram of the vector geometry of the extrapolation problem.	35
Figures 4.1a-b. Normalized phase and group velocities plotted as functions of inverse wavelength.	45
Figure 4.2. Normalized phase and group velocities plotted as functions of the direction of propagation on the grid.	46
Figure 4.3. Plot of the angular divergence of the phase and group velocity vectors.	46
Figure 4.4. Diagram of angles of plane wave incidence on a grid boundary.	52
Figure 4.5. Plot of amplitude reflection coefficients as functions of the angle of incidence on a grid boundary.	52
Figure 5.1. Diagram of the geometry assumed by the Helmholtz integral equation.	58
Figure 5.2. Plot of the computed far-field emission pattern of a square transducer of side-length 2.0λ	66
Figure 5.3. Plot of the computed far-field intensity pattern emitted by four coherent point sources in a square configuration.	66
Figures 5.4. Alternate representations of the emission data in Figure 5.2.	67
Figures 5.5. Alternate representations of the emission data in Figure 5.3.	68
Figure 5.6. Diagram explaining the azimuthal equal-area global mapping of emission angles.	69
Figure 5.7. Plot of the integrated root mean square error E_{rms} and the maximum error E_{max} as functions of wavelength for a point source located at the center of a $20 \times 20 \times 20$ extrapolation surface.	74
Figure 5.8. Plot of E_{rms} and E_{max} as functions of the displacement of the source from the center of a $20 \times 20 \times 20$ extrapolation box.	74

Figure 5.9. Plot of the dependence of E_{rms} and E_{max} on the side-lengths of cubic extrapolation surfaces.	76
Figure 5.10. Emission pattern of a flat square 3.0λ transducer.	76
Figure 5.11. Tabulated angular error results for seven directions of source phasing of a 3.0λ square transducer.	78
Figure 6.1. Illustration of the spacing of the y - z planes of the original <i>Delphinus</i> CT dataset.	82
Figure 6.2. Plot of bone threshold contours in every 12th plane of the linearly interpolated dataset.	84
Figure 6.3. Visualization of the bone threshold isosurface within the interpolated volumetric CT dataset.	84
Figure 6.4. Plot of the linear mapping from CT values to tissue mass density used in the simulations.	87
Figure 6.5. Plot of approximate values and ranges of density and velocity for several types of normal terrestrial mammalian soft tissues and delphinid melon lipids at 37°C	87
Figure 6.6. Plot of the linear mapping from CT values to tissue velocity used in the simulations.	89
Figure 6.7. Visualizations of the model of the narial, vestibular, and premaxillary air sacs used in the simulations.	93
Figure 7.1. Visualization of isosurface at the bone threshold illustrating the skull surface within the CT dataset selected for all forehead simulations.	109
Figure 7.2. Visualization of skin and bone isosurfaces within the region of the CT dataset selected for all forehead simulations.	109
Figure 7.3. Grid setup for the inverse forehead tissue simulations.	110
Figure 7.4. Perspective view of a parasagittal CT data slice through the center of the right MLDB complex within the PSR region.	110
Figure 7.5. Illustration of the energy density in the PSR y -slice containing the maxima for a skull-only 5° inverse simulation at a frequency of 25 kHz.	111
Figure 7.6. Illustration of the energy density in the PSR y -slice containing the maxima for a skull-only 5° inverse simulation at a frequency of 50 kHz.	111
Figure 7.7. Illustration of the energy density in the PSR y -slice containing the maxima for a skull-only 5° inverse simulation at a frequency of 75 kHz.	112
Figure 7.8. Illustration of the energy density in the PSR y -slice containing the maxima for a skull-only 5° inverse simulation at a frequency of 100 kHz.	112
Figure 7.9. Positions of the ‘epicenters’ for the 0° inverse skull-only simulations at four frequencies.	113
Figure 7.10. Positions of the ‘epicenters’ for the 5° inverse skull-only simulations at four frequencies.	114

Figure 7.11. Positions of the 'epicenters' for the 10° inverse skull-only simulations at four frequencies.	115
Figure 7.12. Extrapolated far-field emission pattern at 25 kHz for the skull-only model.	116
Figure 7.13. Extrapolated far-field emission pattern at 50 kHz for the skull-only model.	117
Figure 7.14. Extrapolated far-field emission pattern at 75 kHz for the skull-only model.	118
Figure 7.15. Extrapolated far-field emission pattern at 100 kHz for the skull-only model.	119
Figure 7.16. Positions of the 'epicenters' for the 0° inverse skull and air sacs simulations at four frequencies.	120
Figure 7.17. Positions of the 'epicenters' for the 5° inverse skull and air sacs simulations at four frequencies.	121
Figure 7.18. Positions of the 'epicenters' for the 10° inverse skull and air sacs simulations at four frequencies.	122
Figure 7.19. Extrapolated far-field emission pattern at 25 kHz for the skull and air sacs model.	123
Figure 7.20. Extrapolated far-field emission pattern at 50 kHz for the skull and air sacs model.	124
Figure 7.21. Extrapolated far-field emission pattern at 75 kHz for the skull and air sacs model.	125
Figure 7.22. Extrapolated far-field emission pattern at 100 kHz for the skull and air sacs model.	126
Figure 7.23. Visualizations of the isosurface at 50% of the PSR acoustic energy density for a 5° inverse 50 kHz skull and soft tissue simulation.	127
Figure 7.24. Visualizations of the isosurface at 30% of the PSR acoustic energy density for a 5° inverse 50 kHz skull and soft tissue simulation.	128
Figure 7.25. Visualizations of the isosurface at 10% of the PSR acoustic energy density for a 5° inverse 50 kHz skull and soft tissue simulation.	129
Figure 7.26. Visualizations of the isosurface at 50% of the PSR acoustic energy density for a 5° inverse 75 kHz skull and soft tissue simulation.	130
Figure 7.27. Visualizations of the isosurface at 20% of the PSR acoustic energy density for a 5° inverse 75 kHz skull and soft tissue simulation.	131
Figure 7.28. Visualizations of the isosurface at 10% of the PSR acoustic energy density for a 5° inverse 75 kHz skull and soft tissue simulation.	132
Figure 7.29. Positions of the 'epicenters' from the 0° inverse skull and soft tissue simulations at four frequencies.	133
Figure 7.30. Positions of the 'epicenters' from the 5° inverse skull and soft tissue simu-	

lations at four frequencies.	134
Figure 7.31. Positions of the ‘epicenters’ from the 10° inverse skull and soft tissue simulations at four frequencies.	135
Figure 7.32. Extrapolated far-field emission pattern at 25 kHz for the skull and soft tissue model.	136
Figure 7.33. Extrapolated far-field emission pattern at 50 kHz for the skull and soft tissue model.	137
Figure 7.34. Extrapolated far-field emission pattern at 75 kHz for the skull and soft tissue model.	138
Figure 7.35. Extrapolated far-field emission pattern at 100 kHz for the skull and soft tissue model.	139
Figure 7.36. Visualizations of the isosurface at 50% of the PSR acoustic energy density for a 5° inverse 50 kHz skull, air sacs, and soft tissue simulation.	140
Figure 7.37. Visualizations of the isosurface at 30% of the PSR acoustic energy density for a 5° inverse 50 kHz skull, air sacs, and soft tissue simulation.	141
Figure 7.38. Visualizations of the isosurface at 10% of the PSR acoustic energy density for a 5° inverse 50 kHz skull, air sacs, and soft tissue simulation.	142
Figure 7.39. Visualizations of the isosurface at 50% of the PSR acoustic energy density for a 5° inverse 75 kHz skull, air sacs, and soft tissue simulation.	143
Figure 7.40. Visualizations of the isosurface at 20% of the PSR acoustic energy density for a 5° inverse 75 kHz skull, air sacs, and soft tissue simulation.	144
Figure 7.41. Visualizations of the isosurface at 10% of the PSR acoustic energy density for a 5° inverse 75 kHz skull, air sacs, and soft tissue simulation.	145
Figure 7.42. Positions of the ‘epicenters’ from the 0° inverse skull, air sacs, and soft tissue simulations at four frequencies.	146
Figure 7.43. Positions of the ‘epicenters’ from the 5° inverse skull, air sacs, and soft tissue simulations at four frequencies.	147
Figure 7.44. Positions of the ‘epicenters’ from the 10° inverse skull, air sacs, and soft tissue simulations at four frequencies.	148
Figure 7.45. Extrapolated far-field emission pattern at 25 kHz for the skull, air sacs, and soft tissue model.	149
Figure 7.46. Extrapolated far-field emission pattern at 50 kHz for the skull, air sacs, and soft tissue model.	150
Figure 7.47. Extrapolated far-field emission pattern at 75 kHz for the skull, air sacs, and soft tissue model.	151
Figure 7.48. Extrapolated far-field emission pattern at 100 kHz for the skull, air sacs, and soft tissue model.	152
Figure 7.49. Grid setup for the inverse hearing simulations.	153
Figure 7.50. Tissues within the PGR region illustrated by several slice planes.	153

Figure 7.51. Visualizations of the isosurface at 20% of the PGR acoustic energy density for a 50 kHz 5° inverse hearing simulation using a model including the skull, the nasal air sacs, and the peribullary and pterygoid sinuses.	154
Figure 7.52. Visualizations of the isosurface at 13% of the PGR acoustic energy density for a 50 kHz 5° inverse hearing simulation using a model including the skull, the nasal air sacs, and the peribullary and pterygoid sinuses.	155
Figure 7.53. Visualizations of the isosurface at 20% of the PGR acoustic energy density for a 50 kHz 5° inverse hearing simulation using the complete model including the skull, soft tissues, nasal air sacs, and the peribullary and pterygoid sinuses.	156
Figure 7.54. Visualizations of the isosurface at 13% of the PGR acoustic energy density for a 50 kHz 5° inverse hearing simulation using the complete model including the skull, soft tissues, nasal air sacs, and the peribullary and pterygoid sinuses.	157
Figure 7.55. Extrapolated far-field emission (receptivity) pattern at 50 kHz for a source placed within the LEFT inner ear for a model including only the skull and the nasal air sacs (without soft tissue and without the peribullary and pterygoid sinuses).	158
Figure 7.56. Extrapolated far-field emission (receptivity) pattern at 50 kHz for a source placed within the RIGHT inner ear for a model including only the skull and the nasal air sacs (without soft tissue and without the peribullary and pterygoid sinuses).	159
Figure 7.57. Extrapolated far-field emission (receptivity) pattern at 50 kHz for a source placed within the LEFT inner ear for a model including the skull, the nasal air sacs, and the peribullary and pterygoid sinuses (but without soft tissue).	160
Figure 7.58. Extrapolated far-field emission (receptivity) pattern at 50 kHz for a source placed within the RIGHT inner ear for a model including the skull, the nasal air sacs, and the peribullary and pterygoid sinuses (but without soft tissue).	161
Figure 7.59. Extrapolated far-field emission (receptivity) pattern at 50 kHz for a source placed within the LEFT inner ear for the full model including the skull, soft tissue, nasal air sacs, and the peribullary and pterygoid sinuses.	162
Figure 7.60. Extrapolated far-field emission (receptivity) pattern at 50 kHz for a source placed within the RIGHT inner ear for the full model including the skull, soft tissue, nasal air sacs, and the peribullary and pterygoid sinuses.	163
Figure A2.1. Density of melon tissues in a 2-D parasagittal slice through the right MLDB complex of the common dolphin.	174
Figure A2.2. Acoustic velocity of melon tissues in a 2-D parasagittal slice through the right MLDB complex of the common dolphin.	175
Figure A2.3. Acoustic impedance of melon tissues in a 2-D parasagittal slice through the right MLDB complex of the common dolphin.	176
Figure A2.4. Visualization of the 3-D configuration of the melon inside of the dolphin's forehead.	177

Acknowledgements

Advanced interdisciplinary projects of the type exemplified here are ordinarily conducted by teams of investigators through funded research initiatives. While neither collaborative assistance nor substantial funding was received during this investigation, it remains a pleasure for the author to thank the many people who have lent their encouragement and support over this long period of demanding research.

To my advisor, Geoff Vallis, who four and a half years ago took me on as a physics doctoral student working on the unusual topic of dolphin biosonar, I owe many thanks. Geoff gave me the freedom I needed to develop the numerical tools required for this project, a research group to which I could present results and from which I could obtain feedback, and complete access to a computer lab which otherwise is devoted to fluid dynamical research. In addition Geoff came up with some badly needed support over the past academic year which allowed me to make the final push to completion of this thesis.

I also wish to express thanks to several members of the UCSC physics department who over the years have come to appreciate and enjoy along with me the many interesting questions posed by delphinid biosonar systems. Discussions with Joshua Deutch, Stanley Flatté, and Michael Nauenberg on many topics have been helpful. I especially wish to thank Dave Belanger and the physics graduate committee for their partial support through fellowships over the past academic year. Amidst the many uncertainties associated with developing new techniques in applied physics, it has meant a great deal to me to have the physics faculty enthusiastically embrace my efforts and results.

I have enjoyed and benefited from all of my interactions with Professor Bill Mathews

(UCSC, Physics and Astronomy). Discussions with Bill on physical acoustics, musical acoustics, numerical simulation, and other topics have been illuminating. The fact that Bill's enthusiasm for astrophysics, for music, and for acoustics is balanced by a genuinely compassionate spirit has made him invaluable to many people including this author. Much thanks is also due to Ken Oet-sal, now at Sonic Solutions, Inc., San Rafael, CA, who as a fellow graduate student offered many remarkable insights and suggestions during our discussions of acoustics and numerical methods. Ken's previous experience at SRI with boundary extrapolation methods in acoustics was an important catalyst to my own thinking about 3-D field calculations for this project.

There are some individuals who are difficult to thank because of their many levels of input over a long period of time. Joel Kent of Elo TouchSystems, Inc., Fremont, CA, definitely falls into this category. As advisor for my M.S. thesis, as my boss and business contact in consulting arrangements at Elo and elsewhere, and as a friend and mentor, Joel has been a constant source of encouragement and inspiration. This doctoral project grew out of my Master's research which was itself an outgrowth of a speculative essay on dolphin echolocation written by Joel in response to a half-hour telephone conversation with Ken Norris (see Aroyan 1990, Appendix 2). I am also indebted to Joel for reading and commenting on drafts of the first six chapters of this dissertation.

This project also owes much to the community of marine biologists. Thanks goes to Ted Cranford of the Naval Command Control and Ocean Surveillance Center, RTD&E Division in San Diego, for providing the CT scan of a common dolphin used in this project, for answering a couple of key anatomical questions, and for obtaining two important references. In the current project, I have relied heavily on Ted's descriptions of delphinid forehead anatomy in his M.S. thesis and Ph.D. dissertation. I also wish to extend thanks to Whitlow Au of the Hawaiian Institute for Marine Biology, University of Hawaii, Kailua, for his help in locating a key reference, and for his continuing interest in this project. Whitlow's work remains an inspiration to this

author, as it does to all marine mammal researchers. Last but not least, I have been greatly enriched by my experiences and discussions with the trainers, researchers, and staff of the UCSC Long Marine Laboratory during my year-and-a-half long residence as a caretaker and graduate student researcher. Keith Skaug, Harry Prest, Steve Davenport, and especially Carl Schilt all taught me a great deal, most likely without realizing it.

A very special thanks goes to Judith Hurst and Marilyn Stevens in the physics department office. I have long since lost track of how many times their thoughtful assistance, friendship, and advice have kept me moving forward in the midst of life's ups and downs.

Finally, I wish to thank my gentle and beautiful wife Ramona who has shared with me both the frustrations and the triumphs of this research, and who has surfed with dolphins on Florida's east coast for over twenty years. Ramona's patience with financial sacrifices, an unending workload, and an absentee husband is more remarkable than anything accomplished within the covers of this thesis. Thank you my dear wife and soul mate, and may I learn the lessons you so quietly teach.

Chapter 1. Introduction

The unravelling of the physical mechanisms underlying dolphin biosonar presents fascinating challenges. Active biosonar involves the generation of acoustic waves, the scattering of these waves off of targets, and the detection and interpretation of the scattered waves (by ears and brain). It has become common knowledge that many odontocetes have excellent biosonar capabilities. However, a clear understanding of the mechanisms of odontocete biosonar has only recently begun to emerge. For example, despite the application of various experimental methodologies, the exact location of the biosonar source tissues and the physical mechanisms responsible for generation of the acoustic signals have eluded investigators for decades. Other unanswered questions include the exact mechanisms by which the signals are focused into narrow forward-directed beams and the tissue pathways for echoes returning back to the inner ears. Indeed, the literature on dolphin biosonar is rich with hypotheses that remain largely conjectural.

This dissertation constitutes the final stage of a doctoral research project to quantitatively investigate fundamental mechanisms of dolphin biosonar. This report describes appropriate techniques for three-dimensional (3-D) acoustic simulation, and demonstrates their accuracy. A novel method for mapping of acoustic tissue parameters from x-ray computed tomographic (CT) data is also introduced. These techniques, applied to models of the forehead and lower jaw tissues of the common dolphin, *Delphinus delphis*, have successfully revealed the acoustic mechanisms involved in sonar signal emission and reception by this animal. The results presented here address several key aspects of the biosonar system of the common dolphin including: the location and acoustical mechanisms of the biosonar signal source tissues; the roles of the skull, air sacs, and soft tissues (including the melon) in beam formation; the role of the lower jaw fats in the reception (hearing) process; and the mechanisms involved in the directional hearing response of

the dolphin.

Bioacoustic modeling offers an approach that is complimentary to experimental investigations of biosonar mechanisms. The author has demonstrated (Aroyan 1990, and Aroyan, *et al.*, 1992) that acoustic simulations are capable of addressing questions that have proven difficult to resolve experimentally. In his M.S. thesis, the author conducted two-dimensional (2-D) simulations of sound propagation through modeled forehead tissues of the common dolphin. The interaction of the skull with potential source locations was investigated, as well as the roles of the skull, nasal diverticula, and fatty melon on the formation of acoustic beams. Despite the limitations of 2-D modeling and sparse tissue velocity information, these simulations closely reproduced experimentally measured beam characteristics, helped confirm basic effects of tissues in beam formation, and provided substantial evidence for a recently proposed sound source location.

The current thesis presents a novel combination of techniques which removes all of these limitations, and extends the previous 2-D simulations into highly accurate 3-D modeling. The methods utilized here may be summarized as follows. First, using a new technique for the precise mapping of tissue density and acoustic velocity from x-ray attenuation data, tissue models of the dolphin's head are constructed from x-ray CT data. Second, 3-D finite difference programs are used to propagate echo waveforms back into the tissues in order to locate the 'epicenter' of the dolphin's biosonar signals (analogous to using inverse seismologic simulations to pinpoint the epicenter of an earthquake), or to simulate echo propagation back to the ear complexes. Third, given a source location from the inverse simulation, finite difference programs are again used to propagate the acoustic field of the given source and tissue model out to a surface surrounding the tissue (the forward problem). Fourth, in the forward problem, boundary extrapolation programs are used to compute the emitted acoustic far-field from the pressure and its normal derivative at

the surface. Finally, biosonar mechanisms are investigated by comparing the field emitted by specific source and tissue models to experimentally measured echolocation fields of live animals, or by studying the acoustic energy density of echoes propagating backwards into the forehead tissues or through the lower jaw tissues to the inner ear complexes.

As we shall clearly demonstrate, the combination of methods developed here permits highly realistic and accurate 3-D modeling of the acoustical roles of delphinid forehead and lower jaw tissues in biosonar signal emission and reception. Generalization to all odontocetes of the conclusions drawn in this thesis about the biosonar system of *Delphinus delphis* is limited by the large variation in odontocete forehead morphology. However, the common dolphin is a good representative of the typical forehead anatomy of members of the family Delphinidae having intermediate-to-moderate values of soft tissue asymmetry (Cranford 1992). Obviously, the techniques utilized in this thesis are directly applicable to investigation of all x-ray CT scanned odontocete species. It should also be apparent that the paired methodologies of acoustic tissue modeling from x-ray CT data and numerical simulation used in this project have applications in many other areas. The conclusions regarding biosonar mechanisms and the potential of the methodology developed for this project are discussed in the last chapter.

The scope of such an interdisciplinary thesis demands patience from an audience for its presentation. As one might guess, physicists are often impatient with anatomical and physiological details, biologists are often uncomfortable with the abstractions of mathematics, and computer specialists tend to focus on the numerical methods employed. It is hoped that the readers of this thesis will perceive some of the author's enthusiasm for the exquisite interplay of the physics, biology, and computational techniques that constitute the bases of this investigation. Chapters 2 through 6 may appear at first glance to be unrelated, since they originate from different discip-

lines and/or computational methodologies. However, the combined application of this material in Chapter 7 should demonstrate the fruitfulness of the interdisciplinary approach. Indeed, while excellence within every discipline is essential, the artificial boundaries of the scientific divisions often obscure productive avenues of interdisciplinary exploration.

The order of presentation is as follows. Chapter 2 discusses the necessary biological background, reviewing the primary experimental characteristics of biosonar signal emission and reception in odontocetes, as well as the anatomy of the dolphin forehead and lower jaw. Chapter 3 then discusses various aspects of sound propagation in homogeneous and inhomogeneous fluids, including the acoustical mechanisms underlying biosonar signal production, emission, and reception in delphinids. In Chapters 4 and 5 we shall discuss the numerical methods used to solve the acoustic wave equation; Chapter 4 emphasizes finite difference methods, while Chapter 5 discusses boundary integral extrapolation methods. A novel technique for modeling the dolphin's tissues from x-ray CT data will be discussed in Chapter 6. Finally, the results of the simulations are presented in Chapter 7, with an overall summary of conclusions and a discussion of research opportunities in Chapter 8.

Essential information not easily accommodated by the organization of the dissertation has been moved into appendices. This material includes: (1) The author's conjecture for the 'jaw-pop' source mechanism; and, (2) The detailed density, velocity, and impedance structure of the melon of the common dolphin.

Finally, I wish to share my own views on the role of a physicist studying biological organisms. A physicist's analysis often suggests functions for biological structures, but not necessarily as the 'sole purpose' of those structures. Science seeks simple answers, yet nature always has multiple purposes incorporated into her designs. However, neither does she waste anything. The

author remains awed by the fact that the simplest of living organisms functions simultaneously and successfully within multiple levels of physical, chemical, and biological interrelationships. Perhaps it is no surprise that interdisciplinary research has been and continues to be so fundamental in the life sciences.

My sincere hope is that, in the process of demonstrating the importance of interdisciplinary perspectives, I may have raised our appreciation of these unique mammals with which we share the planet as well as the remarkable beauty of their biosonar systems.

Chapter 2. Biological Background

In order to clarify the questions addressed in this dissertation, we now present a brief introduction to the primary experimental characteristics of delphinid biosonar signals and measured patterns of biosonar emission and reception. We also offer a brief description of the essential anatomy of the delphinid forehead and lower jaw pertaining to biosonar signal production, emission, and reception.

Experimental Characteristics of Delphinid Biosonar Signals

Among the many types of sounds which dolphins are capable of producing are extremely short duration, broad bandwidth, and intense acoustic pulses which are utilized during active biosonar search and investigative behavior.¹ The ability of dolphins to accurately perceive their environment and to perform difficult recognition and discrimination tasks depends to a large extent on the characteristics of these biosonar signals and how they are emitted. Signal characteristics and emission patterns have been extensively investigated for only a few species. Since data is not extensive on the sonar signals of the common dolphin, *Delphinus delphis*, we shall often refer to the signal characteristics and emission patterns of other, better studied species.

Figure 2.1 illustrates a typical echolocation click train emitted by an Atlantic bottlenose dolphin performing a target detection task. The frequency spectrum versus time is plotted on the left and the individual click waveforms are displayed on the right. Note the presence of energy in the spectra of these broadband pulses out to roughly 200kHz. Figure 2.2 displays averages of both the spectra and waveforms for the series of clicks shown in Figure 2.1. Note that the signals

¹ Another unusual sound which dolphins are capable of producing is a very loud and explosive 'jaw pop' or 'bang' which some researchers believe may be used to stun or disorient prey. The author suggests a possible mechanism for the production of jaw pops in Appendix 1 of this dissertation.

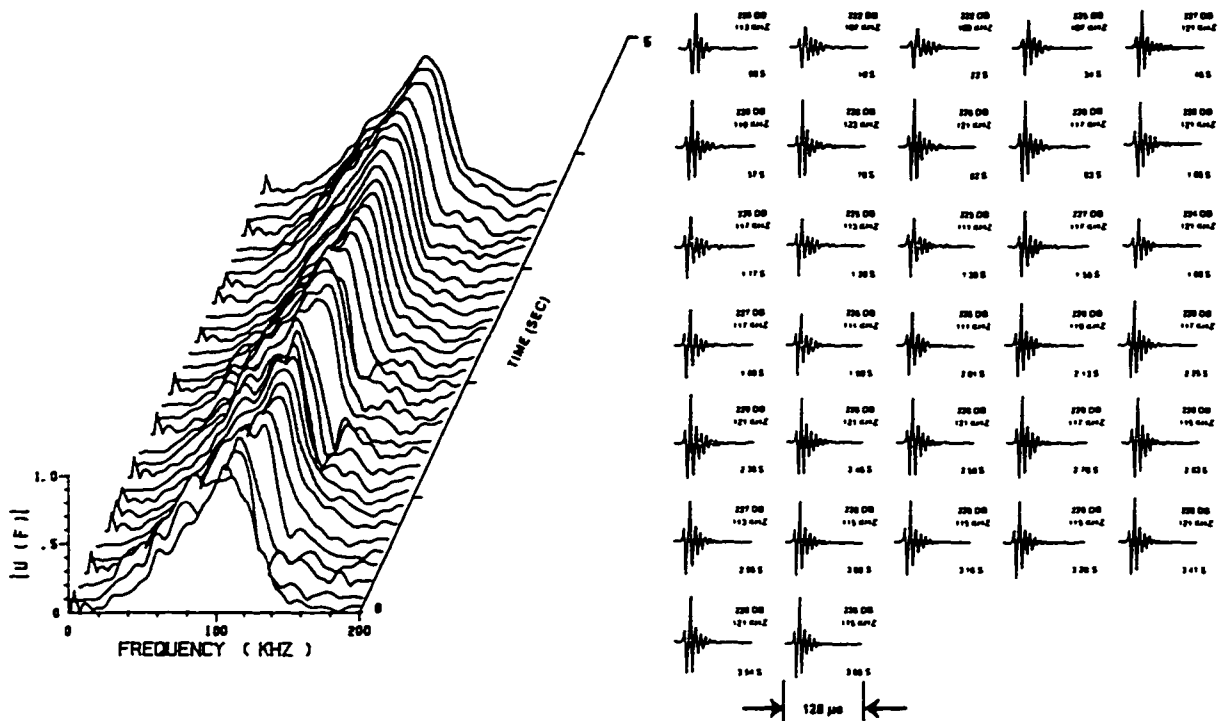


Figure 2.1. Signals and spectra of a biosonar click train emitted by a bottlenose dolphin (*Tursiops truncatus*) performing a target detection task. The frequency spectrum versus time is plotted on the left and the individual click waveforms are displayed on the right. [Reproduced from Au (1993).]

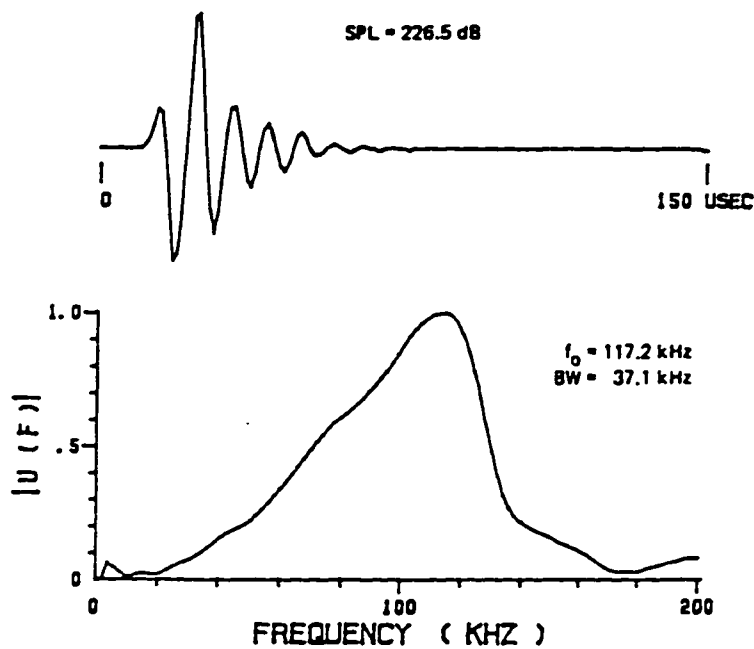


Figure 2.2. The averaged waveform and spectrum for the *Tursiops* biosonar click train shown in Figure 2.1. [Reproduced from Au (1980).]

last only about 70 μ sec on average, a remarkably short duration considering their biological origin. Traveling at 1500m/s in seawater, sound covers only about 10cm in 70 μ sec.

A representative biosonar signal waveform and spectrum for the common dolphin is reproduced from Wood and Evans (1980) in Figure 2.3. Peak frequencies for the click waveforms of *Delphinus* have been variously reported as 20-60 kHz (Titov 1972), 30-60 kHz (Evans 1973), 23-67 kHz (Dziedzic 1978), and 70 kHz (Korolev *et al.* 1973). In addition, click durations of 50-300 μ secs (Titov 1972), 50-250 μ secs (Evans 1973), 50-150 μ secs (Dziedzic 1978), and 100 μ secs (Bel'kovitch and Reznikov 1971) have been reported. In this thesis, we will conduct acoustic simulations with tissue models of the common dolphin at frequencies of 25, 50, 75, and 100 kHz. This set of frequencies spans the ranges reported for *Delphinus*, although the recording equipment used for many of these measurements apparently had a frequency bandwidth of only 100 kHz. For technical reasons discussed in Chapter 5, we have continued the use of single frequency simulations in this thesis.

Although it can be difficult to distinguish directional effects from variations in signal type, dolphins appear to emit biosonar signals that are species stereotypic even though a type of spectral adaptation to environment has been observed (see below). The higher level signals in any particular *Tursiops* click train, for example, are generally quite repetitive (Au 1980). Note the extremely high signal source levels listed for each waveform in Figure 2.1, the typical peak spectral energy at around 120kHz, and the occasional subsidiary spectral peak at around 60kHz.

Both the intensities and the peak frequencies of the signals illustrated in Figure 2.1 were considerably higher than those previously measured for tank-held animals. In fact, evidence is accumulating for a specific kind of spectral adaptation that appears to have more to do with the dolphin's mechanism of click production than with the exercise of fine control over signal spectra

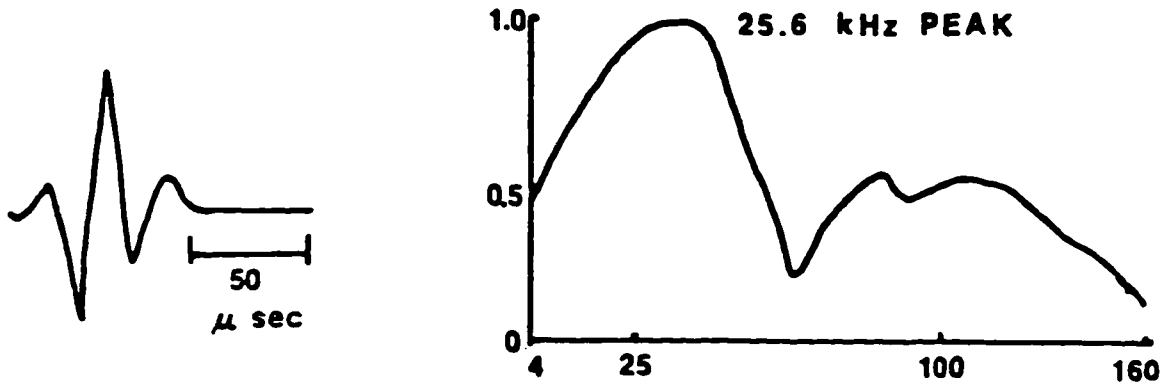


Figure 2.3. Representative biosonar click waveform and spectrum for the common dolphin, *Delphinus delphis*. [Reproduced from Wood and Evans (1980).]

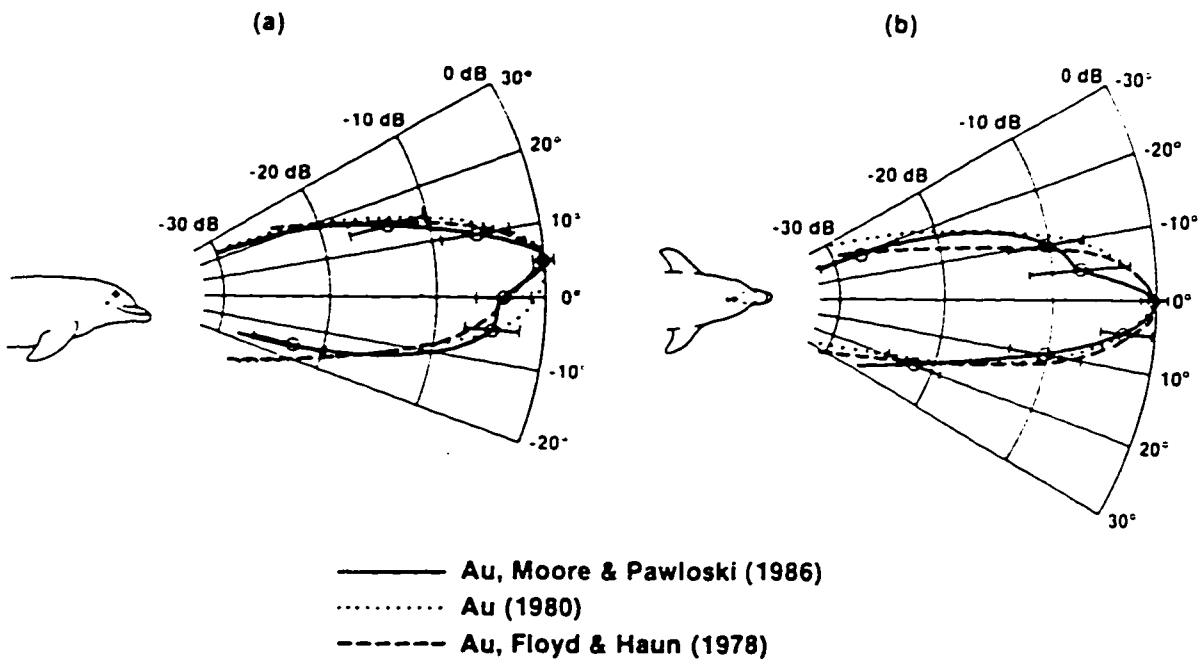


Figure 2.4. Broadband biosonar emission patterns of three bottlenose dolphins, (a) in the vertical plane, and (b) in the horizontal plane. [Reproduced from Au (1993).]

and shape. Au *et al.* (1985) postulated that shifts in the relative strengths of the (often nearly harmonic bimodal) signal components may be a by-product of shifts in the intensity level of click production. Studies with *Tursiops truncatus*, *Delphinapterus leucas*, and *Pseudorca crassidens* (Moore and Pawloski 1990, Au *et al.* 1985, 1987, 1995, Au 1980) have found that high amplitude clicks tend to be slightly bimodal in character, with a major peak frequency above 100 kHz and a secondary peak at or somewhat below half the major peak frequency. Clicks that were lower in amplitude tended to have proportionately more energy at the lower frequency peak. High amplitude emission of clicks peaked near the lower mode frequency was never observed in these studies.

All observed characteristics of the biosonar signals emitted by odontocetes (all toothed whales including dolphins) may be explicable in terms of a fairly simple set of physical mechanisms. The structure of all odontocete biosonar signals is reminiscent of the decay of a resonant but highly damped system which has been excited by an impulsive source mechanism. This analogy becomes quite compelling when we consider the acoustical impedance structure of the source region in delphinids (as established by this thesis for *Delphinus*) and the recently published bimodal variations of biosonar signal spectra. In Chapter 3, we will discuss the resonant behavior of the source region and the acoustical mechanisms operating in delphinid forehead and lower jaw tissues.

Directional Patterns of Biosonar Emission

Experimentally measured patterns of delphinid biosonar emissions are highly directional. Figure 2.4 illustrates composite 'broadband' emission patterns measured for three bottlenose dolphins in both the horizontal and vertical planes.² Note that the patterns shown have maxima at

² See Au *et al.* (1986), Au (1980), and Au *et al.* (1978). Unless one is only concerned with energy distributions, representation of a single beam pattern can be somewhat misleading. The reader is warned that em-

about 5° in the vertical plane and 0° in the horizontal plane. In addition, Au (1993) reports averaged -3dB angular widths of 10.2° and 9.7° in the vertical and horizontal planes, respectively, and an averaged 'broadband' directivity index of 25.8dB for the emission patterns presented in Figure 2.4. It is important to note that the angular resolution of even the finest reported measurements of delphinid emission patterns is quite low by standard sonar specifications. Extrapolation to a complete field from only a few samples at 5° or 10° increments in the horizontal and vertical planes of the forward beam involves several assumptions.

Comparatively little information is available on the emission patterns for *Delphinus delphis*. Korolev *et al.* (1973) measured a horizontal beam pattern at a frequency of 70 kHz having two peaks at angles of $\pm 15^\circ$. Each peak was up to 20° wide, and the overall width of the horizontal pattern about 40° . The -3dB beam width in the vertical plane was estimated to be close to 20° . Apparently Bel'kovitch and Reznikov (1971) determined the horizontal width of the common dolphin's beam to be 20° using the signal envelope (equivalent to an energy beam width). The bandwidth of the recording system in both cases only extended up to 100 kHz.

There has been a great deal of informed speculation as to how dolphins achieve these focused acoustic emission patterns. In the chapters that follow, we will present a novel combination of techniques which permits highly realistic three-dimensional modeling of the acoustical roles of delphinid tissues in both the emission and reception processes. Using these techniques, we will be able to demonstrate the focal properties of the skull, the soft tissues, and one model of the air sacs. We shall actually resolve much of the mystery that has surrounded the acoustical function of the melon and lower jaw fats in dolphins.

ission patterns always depend strongly on frequency [Ziomek (1995) and personal communication].

Directional Patterns of Biosonar Reception

The directional reception pattern of a sonar system is crucial to its capability for filtering out ambient noise in both active and passive modes. Measurement of the directional hearing sensitivity in dolphins has been carried out only for the bottlenose dolphin, *Tursiops truncatus*. Au and Moore (1984) measured masking thresholds as a function of horizontal and vertical angle to determine the dolphin's receiving beam pattern. The resulting vertical and horizontal receiving patterns at (cw) frequencies of 30, 60, and 120 kHz are reproduced in Figures 2.5 and 2.6. [Please note that the sign convention in Figure 2.6 for horizontal angles is opposite to the convention adopted in this thesis]. Au (1993) computed the directivity indexes (in dB) of these receiving patterns and reported that they increased almost linearly with the logarithm of frequency.

The techniques developed in this thesis have allowed us to compute the full 3-D receptivity patterns for each ear of the common dolphin individually, to determine the timing delay between the ears versus arrival direction at any fixed frequency, and to study the physical effects of the lower jaw fats contributing to the dolphin's directional reception. Numerical simulation offers a means for identifying the directional cues provided by the physical structure of the dolphin's skull, lower jaw fats, and ear complexes.

Dolphin Anatomy : Acoustic Role of Tissues

From the point of view of a sound wave traveling through the body of a dolphin, the tissues divide naturally into three categories: bone, for which sound has a much higher velocity than seawater; all soft tissues, which are acoustically comparable to seawater, but may contain velocity gradients affecting the path of propagation; and air cavities, with a density and sound velocity much lower than that of seawater. Chapter 6 discusses modeling of the acoustical properties of biological tissues in great detail. Here we briefly review the tissues that play major roles in the

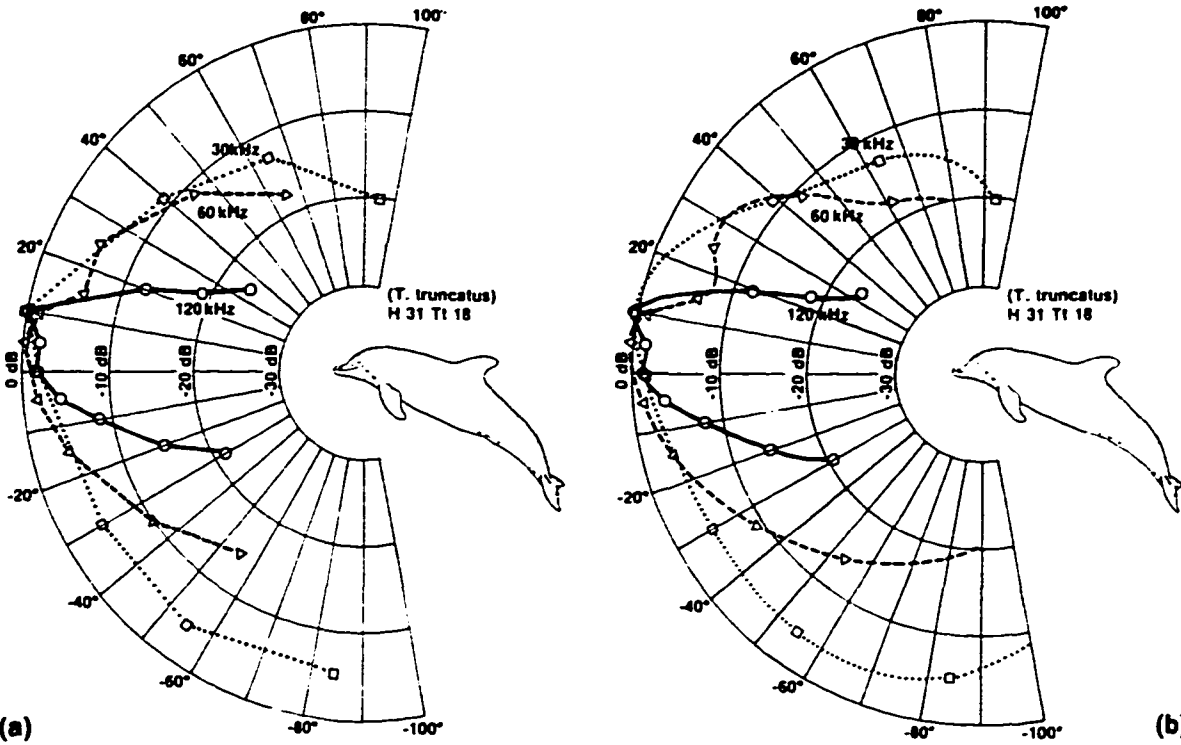


Figure 2.5. (a) Receiving beam patterns in the vertical plane of a bottlenose dolphin at frequencies of 30, 60, and 120 kHz. (b) Same data fitted by a cubic spline function. [Reproduced from Au and Moore (1984).]

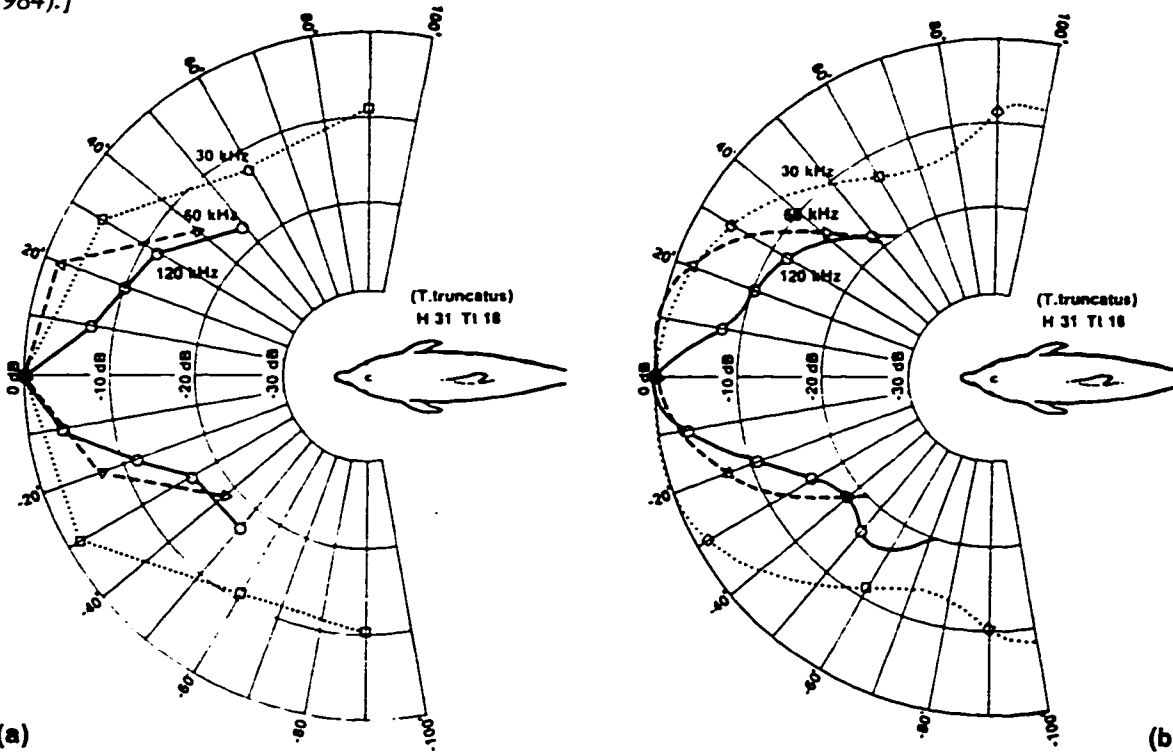


Figure 2.6. (a) Receiving beam patterns in the horizontal plane of a bottlenose dolphin at frequencies of 30, 60, and 120 kHz. (b) Same data fitted by a cubic spline function. The sign convention in this figure for horizontal angles is opposite to the convention adopted in this thesis. [Reproduced from Au and Moore (1984).]

emission and reception of biosonar signals: the skull, the nasal air sac system, and the unique fats of the melon and lower jaw. A discussion of potential source tissues will also be included as part of this review of relevant anatomy.

The Skull

The skull and its associated air sacs are the dominant features in the dolphin forehead from the point of view of acoustics. The acoustic impedance mismatch between bone and soft tissues, though not as large as the soft tissue-air mismatch (see Chapter 3), implies that bone will reflect sound effectively (especially at higher angles of incidence).³ Consequently, the shape of the skull is of greater importance than the precise acoustical properties of bone.⁴ Highly accurate data on the geometry of the skull is available. Chapter 6 explains how CT data was used to derive both the geometry and density of the dolphin's skull. A number of pertinent observations regarding skull shape are given below.

The delphinid skull is characterized by an exceptional displacement of the bones normally comprising the forehead (see Figure 6.3). In an evolutionary process called 'telescoping', the location of the nasal passages has migrated from the tip of the snout or rostrum back towards the middle of the skull and up against the brain-case. A thin cartilaginous rod (the mesorostral cartilage) divides the rostrum from the nares to the tip of the snout; the channel in the rostrum filled by this cartilage is visible in the upper rostral contours of Figure 6.2.

The role of the skull in beam formation was investigated by Evans, Sutherland and Beil (1964) using both an acoustic source and ray tracing techniques, by Dubrovskiy and Zaslavskiy

³ Note, however, that extremely thin sections of bone can transmit sound efficiently. Passage of sound through the thin bone panels of the lower jaw are important in the dolphin's reception of echoes (Norris 1968).

⁴ The acoustical properties of bone alter its surface reflectivity but not its overall focal behavior. By analogy, the geometry of a mirror is more important than small shifts in surface reflectivity.

(1975) using lightbulb-as-source techniques, and by Romanenko (1973) using an acoustic source with and without soft tissue present. In this thesis, we have utilized inverse simulations to determine the focal positions of the 3-D skull geometry (completely analogous to the use of inverse seismologic simulations to determine the epicenters of earthquakes). Placing point sources at these foci, we have then conducted forward simulation and extrapolation of the far-field patterns created by the skull. Finally we have simulated the effect of the skull on the reception of sound through the pan bone of the lower jaw both with and without soft tissue present. Thus we have determined the optimal focal behavior of the skull in 3-D, demonstrated its importance in acoustic beam formation, and studied its major effects on the process of hearing. As the simulations are based on physical acoustics as opposed to the short-wavelength geometrical acoustics approximation, we add valuable information regarding the interaction of finite wavelength sound with the skull.

The Nasal Passages and Air Sacs

The soft tissue-air interface is a very efficient reflector of sound wave energy (see Chapter 3). We can expect the geometry of the nasal passages to play an important role in biosonar beam formation.

Delphinid nasal passages differ greatly from those of terrestrial mammals.⁵ In dolphins, the single outer blowhole leads downward into at least four paired air spaces, beginning with the vestibular sacs, comparatively large air sacs capable of expanding along their upper and lateral margins, but supported by a pleated connective tissue base. The floor of the vestibular sacs opens downward into the vertically oriented spiracular cavity, which is normally flattened except during

⁵ Many excellent descriptions of the delphinid nasal sac system exist. See, for example, Schenckan (1973), Dormer (1974, 1979), or Green *et al.* (1980).

breathing or air recycling. Several chambers surround the spiracular cavity, including the anterior and posterior nasofrontal sacs and the inferior vestibules, forming a complex 3-D sac structure. Anterior to the base of the spiracular cavity, thin premaxillary sacs cover most of the shelves of the premaxillary bones. Heavily muscled nasal plugs cover the bony nares (the nasal passage through the skull). A thin but stout bony septum divides the upper nares into left and right sides.

The exact configuration of the air sacs during click production is an important issue (see discussion of mechanisms in Chapter 3), as well as the degree of the dolphin's control over this configuration. Several researchers have reported great mobility of the upper air sac region during phonation (Dormer 1979, Cranford 1992). The flexible nature of air sac geometry suggests that dolphins may achieve partial beam steering by controlling air sac shapes, yet measurements of beam patterns do not in general appear to support this idea (Au 1993). Reliable data on the exact configuration of the air sacs during click production is not available for any species. However, sufficient information is available to enable us to demonstrate that air passages play an important role in acoustic beam formation. The model of the nasal air sacs used in the current simulations is discussed and illustrated in Chapter 6.

The Source Tissues

Before leaving our discussion of the dolphin nasal passages, we shift our attention from the effect of tissues on sound propagation to their role in sound production. Several studies have implicated the general region of the nasal plugs as the source of the dolphin's echolocation pulses: cineradiographic studies (Norris *et al.* 1971, and Dormer 1974, 1979), pulsed ultrasonic imaging (Mackay 1980), ultrasonic Doppler-shift motion detection (Mackay and Liaw 1981), pressure sensing and electromyographic studies (Ridgway *et al.* 1980). However convincing

these studies may appear, some researchers⁶ have concluded from available information that the larynx is the most likely sound source. In this thesis, we will present evidence that the source of biosonar emissions is located in one particular region of the upper nasal passages.

The larynx appears to play a role in biosonar pulse generation, though probably not as the source of biosonar clicks. The larynx is located below the skull at the base of the narial passage-way.⁷ A ring of muscular tissue (the palatopharyngeal muscle) closes around the cartilaginous epiglottic spout of the larynx. During normal breathing, air passes through the upper nasal passages and enters the trachea through the epiglottic spout. However, the muscled sphincter can securely squeeze the spout shut, and the powerful set of gular muscles are capable of pulling the epiglottis up into the bony nares to create substantial air pressure within the narial chamber. A pressure increase within the nares always precedes, and the cycling of air upwards into the upper nasal sacs is always concomitant with, biosonar click production.⁸

Though most researchers have accepted the nasal passages superficial to the skull as the probable source region of echolocation pulses, information on the precise location of pulse production has remained conjectural. Recently however, x-ray computed tomography (CT) studies (Cranford 1986, 1988) and magnetic resonance imaging (MRI) (Mackay 1988) have revealed 3-D in situ tissue structure with great accuracy. From CT scans of several species, Cranford has noted similarities in the configuration of the posterior melon in the foreheads of a large number of odontocetes (and homologues in the extremely asymmetric Physeterids). At the posterior tip of the melon are two pairs of fatty bursae straddling the upper portion of the spiracular cavity (Cranford 1988, 1992) overlaid by patches of darker mucosae referred to as *museau du singe*, or 'mon-

⁶ See, for example, Purves and Pilleri (1983).

⁷ For an in-depth study of the larynx and surrounding musculature, see Green *et al.* (1980).

⁸ See Evans and Prescott (1962), Dormer (1979), and Ridgway *et al.* (1980).

key lips', which give "every appearance of being a sound generator" (Norris 1968). Cranford has emphasized the homologous relationship of the monkey lips and the bursae themselves to structures discovered in the sperm whale head (Norris 1964, Norris and Harvey 1972). It is conjectured that slapping motions of the MLDB (Monkey Lip/Dorsal Bursae) complex are responsible for the pulsed emissions of all odontocetes (Cranford *et al.* 1987). In Chapter 7, we shall see that the simulations conducted in this thesis actually implicate a region slightly (~1cm) below the center of the right MLDB complex as the most likely source location of biosonar clicks. The physical mechanisms involved in the production and projection of biosonar signals from this source region are discussed in detail in Chapter 3.

After this brief discussion of tissues involved with sound production, we return our attention to anatomical features relevant to biosonar beam formation and to signal reception.

The Melon

Much discussion has surrounded the acoustic role of the fatty lobe of tissue referred to as the 'melon' in the delphinid forehead (see Figure A2.4 of Appendix 2), as well as the related fats of the lower jaw. The melon of the dolphin rests on a concave pad of connective tissue and musculature atop the bony rostrum of the skull (Cranford 1992). The lipids of the delphinid melon and lower jaw are chemically and acoustically distinct⁹ from other body fats and the blubber (which appear to be very similar to the fats of terrestrial mammals), and exhibit a layered compositional topology. Across the family Delphinidae, the innermost melon and lower jaw lipids exhibit an approximate 60-40 percent by weight triglyceride-isovalerate wax ester composition (Litchfield *et al.* 1975). Because of the location and configuration of these unique fats, because

⁹ See Varanasi *et al.* (1982), Litchfield *et al.* (1979, 1975, 1973), Malins and Varinasi (1975), Varinasi *et al.* (1975). See Morris (1986) for an excellent discussion and synthesis of this information.

they represent a considerable metabolic investment, and because measured velocity profiles of the various lipid fractions within the delphinid melon and forehead exhibit a distinct waveguide or lensing structure, the melon has been conjectured to have an important acoustic function (Norris 1964, 1968, Norris and Harvey 1974, Morris 1986). We quote from Au (1980):

Besides the nasal sacs and the cranial bones, the melon may also play a large role in the spatial directivity of the emitted beam. In 1957, F. Wood (1964) suggested that the melon of a porpoise might be a sound transducer helping to couple internally generated sounds to sea water. He also speculated that the melon may act as an acoustic lens to focus the sound into a narrow beam. The beam patterns measured by Evans, Sutherland, and Beil (1964), using a *Tursiops* skull were considerably broader than the beam patterns of [Figures 2.3 and 2.4]. This suggests that the melon may play a role in focusing the outgoing acoustic energy, causing a narrower beam to be radiated than would otherwise exist. Romanenko (1973), studied the effects of a dolphin's skull, with and without soft tissue present, on the horizontal beam pattern. He found that for frequencies of 80kHz and higher, the beams measured with the whole head were approximately half as wide as the beams obtained with the skull alone. Norris and Harvey (1974) examined the sound velocity of the lipids in the melon and found a definite structure that could cause the focusing of the outgoing acoustic energy. By slicing the melon of a dead animal in a regular fashion and measuring the sound velocity of the various sections within each slice, they found a low-velocity core extending from just below the anterior surface towards the right nasal plug and a graded outer shell of higher velocity tissue. Such a velocity gradient would cause the signal to be focused both in the vertical and horizontal planes. The amount of refraction and the subsequent effect on the overall beam patterns have not been determined yet.¹⁰

Computer wave propagation techniques are quite appropriate for this task, and have permitted several remarkable advances here. All previous modeling attempts have lacked detailed tissue density and velocity information (Au 1993, Aroyan *et al.* 1992, Litchfield *et al.* 1979). Utilizing a novel technique for mapping of acoustical tissue parameters from x-ray CT data, the detailed density, velocity, and impedance structure of the melon of the common dolphin has been determined in this thesis (see Chapter 6 and Appendix 2). We have then applied 3-D acoustic wave propagation and extrapolation programs in order to demonstrate the acoustic behavior of

¹⁰ Au (1980), p265-67.

the melon (see Chapter 7). A brief discussion of the physical mechanisms underlying the acoustic behavior of these unique fats is presented in Chapter 3, along with suggested analogies for the entire process of biosonar click production and emission in delphinids.

The Fats of the Lower Jaw and the Hearing Process

Sound conduction into the middle and inner ear complexes of delphinids remains a topic of great interest. Some researchers have argued for the functionality of the external auditory meatus in dolphins (Fraser and Purves 1960, Purves and Pilleri 1983). However, the external meatus in cetaceans is a fibrous cord of tissue having a small (sometimes nonexistent) cross section, the outer portions of which are often filled with a waxy plug. No evidence was ever presented for how such a structure could guide sound to the middle/inner ear complexes.

As mentioned above, the lower jaw also contains two fat bodies having the same composition as the melon lipids.¹¹ These fat bodies broaden anteriorly and extend to the skin surface in front of the thin pan bones on both left and right sides of the lower jaw. The fats extend across the pan bone and fill both left and right mandibular canals. Each extends back in a narrowing channel along the inside of the mandible and ends near its respective ear complex. Norris (1968) proposed that sound enters the dolphin's head through the fatty 'acoustic window' in front of the lower jaw, passes through the thin pan bone, and is conducted to the middle/inner ears by the left and right fat bodies. The lower jaw hearing hypothesis has been confirmed by both electrophysiological techniques (Bullock *et al.* 1968, McCormick *et al.* 1970, 1980) and by behavioral investigation (Brill *et al.* 1988). However, the precise mechanisms of lower jaw hearing have remained conjectural.

¹¹ See Norris (1968) for an outstanding discussion and far-sighted analysis of the evolution and acoustics of lower jaw hearing in odontocetes.

In this thesis, we provide very detailed proof of Norris's lower jaw hearing hypothesis. Numerical simulations of sound propagation through accurate 3-D models of the lower jaw tissues have allowed us to illustrate the patterns of conduction through the fat bodies back to the ear complexes, again producing dramatically clear results (see Chapter 7). In addition, we have mapped the individual reception patterns of the left and right middle/inner ear complexes. Finally, comparing the reception patterns of various truncated models to the reception patterns with the complete model, we have been able to demonstrate several mechanisms contributing to the directional hearing of the dolphin.

Chapter 3. Sound Propagation in Homogeneous and Inhomogeneous Fluids

We are concerned with modeling the passage of sound both through seawater and through the living tissues of the dolphin forehead and lower jaw. On the scale of our simulations (less than a meter), seawater is an isotropic, homogeneous medium. Biological tissues, however, are composed of both liquids and elastic solids, mostly inhomogeneous and often intermixed. In this chapter, we first review the linearized wave equations for acoustic propagation in homogeneous and inhomogeneous fluids, and then establish the assumption of linearity. We then give some relevant details of sound transmission through fluid interfaces. Next, a brief discussion of the behavior of resonators, reduced-velocity waveguides, lenses, and megaphones is provided in order to clarify the basic mechanisms underlying the biosonar signal source tissues and the channeling properties of the 'acoustic fats' of the melon and lower jaw. Finally, we provide a brief derivation of the Helmholtz integral equation which will be applied in later chapters to compute the acoustic emission patterns of the tissue and source models.

The Wave Equations For Homogeneous and Inhomogeneous Fluids¹

The linearized equation for acoustic (compressional) wave pressure variations $p = p(\mathbf{x}, t)$ in a homogeneous fluid having sound speed c is:

$$\frac{1}{c^2} \frac{\partial^2 p}{\partial t^2} = \nabla^2 p \quad (3.1)$$

The same equation holds for the variations of density and temperature that are associated with sound waves traveling through a quiescent medium. In the case that the curl of the vector fluid velocity $\nabla \times \mathbf{v} = 0$, then each cartesian component of \mathbf{v} also satisfies the above wave equation.

¹ Derivations of the linearized homogeneous and inhomogeneous acoustic wave equations are provided in Aroyan (1990).

In inhomogeneous fluids, the background density $\rho = \rho(\mathbf{x})$ and the sound speed $c = c(\mathbf{x})$ are functions of space (not time). The linearized acoustic wave equation for inhomogeneous fluids is:

$$\frac{1}{c^2(\mathbf{x})} \frac{\partial^2 p}{\partial t^2} = \nabla^2 p - \frac{\nabla p \cdot \nabla \rho(\mathbf{x})}{\rho(\mathbf{x})} \quad (3.2)$$

This equation differs from the equation for homogeneous media only in the last term on the RHS.

From the numerical solution p of equation (3.2) we will need to obtain two quantities of special interest. Visualization of the acoustic energy density W within models of the dolphin's tissues will allow us to locate potential source positions and to demonstrate acoustic channeling within specific tissues. For inhomogeneous fluids, it can be shown that²

$$W(\mathbf{x}) = \frac{|p(\mathbf{x})|^2}{\rho(\mathbf{x}) c^2(\mathbf{x})} \quad (3.3)$$

The Assumption of Linearity

The fundamental equation describing the motion of fluids under applied forces or its evolution from initial conditions is the Navier-Stokes equation:

$$\frac{\partial \mathbf{u}}{\partial t} + \frac{\nabla p}{\rho} = -\mathbf{u} \cdot \nabla \mathbf{u} + \frac{\mu}{\rho} \nabla^2 \mathbf{u} \quad (3.4)$$

where \mathbf{u} is the vector fluid velocity and μ is the viscosity. In the derivation of the linearized acoustic equations, both the nonlinear (or advective) term $[-\mathbf{u} \cdot \nabla \mathbf{u}]$ and the viscous term $[(\mu/\rho)\nabla^2 \mathbf{u}]$ in the Navier-Stokes equation are ignored.³ The ratio of the magnitude of each of these terms to the LHS terms that were kept is characterized by a dimensionless parameter.⁴

² See, for example, Morse and Ingard (1968), or Pierce (1980). Because only the Fourier transform of $W(\mathbf{x}, t)$ is used, we have suppressed the time dependence here.

³ Static forces such as gravity are of no importance over short acoustic propagation distances, and are left out of equation (3.4).

⁴ See Morse and Ingard (1968), Medwin and Clay (1977), Tritton (1977), Pierce (1980), or Novikov *et al.* (1987).

The dimensionless ratio of the magnitude of the viscous term to the inertial terms on the LHS of equation (3.4) is $\mu\omega/\rho c^2$. Because μ is of the order of 10^{-3} kg/(m*s), $\rho = 1.03 \times 10^3$ Kg/m³ and $c = 1.5 \times 10^3$ m/s for seawater, and an upper biosonar frequency limit is approximately $\omega \approx 1 \times 10^6$ rad/s, this ratio is at maximum of order 10^{-7} . Within the frequency and spatial ranges of the present investigation, the viscous term can therefore be safely ignored.

The ratio of the magnitude of the nonlinear (advective) term to the LHS terms is the acoustic Mach number $M = u/c$. Because M is approximately equal to the magnitude of the fractional density perturbation, the criterion that $M \ll 1$ is often used as a measure of whether a fluid phenomenon can be validly treated assuming incompressibility. Values of M as large as 0.2 may permit significant predictions with linear models.⁵

Now consider the maximum value of M associated with biosonar emissions. The maximum peak-to-peak sound pressure level measured (Au 1980) at 1m from an echolocating *Tursiops* was SPL=230dB re 1 μ Pa, or a peak source level SL=224dB re 1 μ Pa. This is equivalent to $p_{peak} = 1.6 \times 10^5$ Pa. If M turns out to be quite small, then we can set the RHS of equation (3.4) equal to zero to obtain the linearized Euler equation

$$\rho \frac{\partial \mathbf{u}}{\partial t} = -\nabla p \quad (3.5)$$

For one-dimensional harmonic waves, this reduces to $u = p/\rho c$. Hence, for the peak pressure measurement at 1m from *Tursiops*, we may write

$$M_{peak} = \frac{u_{peak}}{c} \approx \frac{p_{peak}}{\rho c^2} \approx 7 \times 10^{-5} \ll 1 \quad (3.6)$$

justifying the use of equation (3.5). We conclude that the acoustic phenomena associated with delphinid biosonar emissions lie well within the linear regime. Furthermore, unless the peak

⁵ Tritton (1977), p58.

acoustic pressures inside the dolphin's source tissues during click production rise to more than 10^8 Pa (10^3 Atm, or SPL=280dB re $1\mu\text{Pa}$), it is not necessary to include nonlinear terms in the equations used to model acoustic propagation within the tissues.

The same pressure threshold for significant nonlinear effects to occur within the tissues can also be derived from consideration of the dependence of sound speed on pressure. This is usually characterized by the dimensionless ratio B/A of the quadratic to linear terms in the adiabatic Taylor expansion of the pressure in terms of the density. It can be shown that⁶

$$\frac{B}{A} = 2\rho_0 c_0 \left[\frac{\partial c}{\partial p} \right]_{\rho_0, s_0} \quad (3.7)$$

where ρ_0 , c_0 , and s_0 are the equilibrium density, sound speed, and entropy respectively. Measured values of this parameter for biological tissues⁷ are only slightly higher than for seawater, for which B/A is approximately 5. A simple estimate of the sound pressure level that would be required to cause significant nonlinear effects within the dimensions of the dolphin's forehead tissues again gives SPL \approx 280dB re $1\mu\text{Pa}$ for the highest frequencies associated with biosonar emissions. Shock wave formation does not appear to be possible unless the nonlinearity parameter B/A for the melon lipids is several hundred times its value for normal mammalian soft tissue.

The simulation procedures described in the next two chapters will allow us to demonstrate that the peak pressures inside the dolphin's modeled tissues do not rise to the nonlinear thresholds given above except within a very small radius of a (physically implausible) point source sound production mechanism.

⁶ See Beyer (1960), or Coppens *et al.* (1965).

⁷ Law *et al.* (1981, 1983), Dunn *et al.* (1981), Sehgal *et al.* (1984).

Acoustic Impedance and Transmission of Sound Through Fluid Interfaces

The specific acoustic impedance z is defined as the ratio of the complex pressure to the complex magnitude of the acoustic particle velocity. This impedance characterizes the fluid's response to pressure waves: the absolute magnitude of z equals the amplitude of the pressure oscillations required to produce a unit velocity response. The specific acoustic impedance for plane waves, or the characteristic impedance, has the value $z = \rho c$, where ρ is the density and c the speed of compressional wave propagation in the medium.

The pressure amplitude transmission coefficient $T_{1 \rightarrow 2}$ for plane waves incident on an interface between two fluids with acoustic impedances $z_1 = \rho_1 c_1$ and $z_2 = \rho_2 c_2$, incident angle θ_1 , and transmission angle θ_2 , is

$$T_{1 \rightarrow 2} = \frac{2 z_2 \sec \theta_2}{z_1 \sec \theta_1 + z_2 \sec \theta_2} \quad (3.8)$$

where θ_2 is given by

$$\cos \theta_2 = \left[1 - \left(\frac{c_2}{c_1} \right)^2 \sin^2 \theta_1 \right]^{1/2} \quad (3.9)$$

If $c_2 > c_1$, a critical angle $\theta_c = \sin^{-1}(c_1/c_2)$ exists with $T_{1 \rightarrow 2} = 0$ for all $\theta_1 \geq \theta_c$ (all energy is reflected). The power transmission coefficient is simply $(z_1/z_2)T_{1 \rightarrow 2}^2$.

Let us consider two examples of special interest. First, the transmission coefficient for sound passing from soft tissue into air. Assuming the ratios of velocities and densities to be

$$\frac{c_1}{c_2} = \frac{c_{\text{soft tissue}}}{c_{\text{air}}} \approx \frac{1500 \text{ m/s}}{350 \text{ m/s}} \approx 4.3, \quad \frac{\rho_1}{\rho_2} = \frac{\rho_{\text{soft tissue}}}{\rho_{\text{air}}} \approx 10^3 \quad (3.10)$$

we obtain the transmission coefficient for normal incidence

$$T_{1 \rightarrow 2} = \frac{2}{1 + z_1/z_2} \approx 5 \times 10^{-4} \quad (3.11)$$

Hence we obtain the power transmission coefficient $(z_1/z_2)T_{1\rightarrow 2}^2 \approx 9 \times 10^{-4}$ at normal incidence. In other words, air spaces within soft tissue constitute extremely efficient reflectors of acoustic energy.

Second, considering bone as a fluid, and taking both the density and the speed of sound in bone to be roughly twice that of soft tissue, we find a power transmission coefficient at normal incidence of $(z_1/z_2)T_{1\rightarrow 2}^2 = 0.36$ for sound passing from soft tissue into bone. We also find a critical angle of approximately 30 degrees past which all energy is reflected back into the soft tissue.

Of course, while bone may contain fluid inclusions, the bony matrix itself is an elastic solid and not a fluid. Transmission of sound from a fluid into an elastic solid depends on the elastic and absorptive properties of the solid at the frequencies of interest, and generally exhibits more complex behavior than transmission between fluids.⁸ However, in all cases of interest to this thesis, very little error is introduced by ignoring the elastic characteristics of tissues. This is because the shear wave velocity for soft tissues remains less than 1% of the compressional wave sound speed for frequencies up to 1 MHz, and soft tissue shear wave attenuation coefficients are of the order of 10^4 times the compressional wave attenuation coefficients.⁹ Air sacs normally cover much of the skull surface in the vicinity of the nasal passages (the most probable source region) in delphinids, and hence very little compressional wave energy is directly incident (at low angles) on the skull. Taken together, these considerations suggest that mode conversion at skull-soft tissue interfaces may contribute additional attenuative mechanisms, but does not argue for a significant role in biosonar emission.

⁸ See Kinsler *et al.* (1965), or Auld (1973).

⁹ See Frizzell *et al.* (1976), Carstensen (1979), and Madsen *et al.* (1983). While possible, full elastic tissue modeling was not attempted in the current project.

Fundamental Mechanisms: Acoustic Resonators, Waveguides, Lenses, Megaphones

Two of the primary goals of this thesis are to explain the physical mechanisms determining the character of delphinid biosonar signals, and to address the degree of waveguiding and/or channeling that is exhibited by the so-called 'acoustic fats' of the delphinid forehead and lower jaw. As shown below, the MLDB tissue region superior to the nares in dolphins is closely analogous to a damped acoustic resonator, while the melon exhibits properties analogous to both a reduced-velocity waveguide (and lens) and a horn (or megaphone). In order to clarify the physical meaning of these behaviors, we now offer a brief discussion of acoustic resonators, waveguides, lenses, and megaphones.

A region of soft tissue that is completely surrounded by air (pressure release surfaces) constitutes an acoustic resonator.¹⁰ The resonant frequencies depend on both the geometry of the region and the tissue velocity distribution. Let us consider the especially simple case of a uniform spherical soft tissue mass suspended in air.¹¹ The resonant modes are obtained by solving the homogeneous Helmholtz equation (3.16) in spherical coordinates and requiring the pressure to vanish at the air radius. The complete solution is usually written out as a product of spherical Bessel functions (for the radial dependence) and spherical harmonic functions (for the angular dependence). However, the frequencies of the solution are determined solely by the radial dependence. We need only examine the first few frequencies of the first two radial modes to describe the relevant resonant structure.¹² The first radial mode corresponds to purely radial oscillations of

¹⁰ The acoustic resonances of air sacs enclosed within soft tissue has been investigated as a possible source of the low frequency components of delphinid biosonar signals (Giro and Dubrovskiy 1973, 1974, Romanenko 1973, 1974) and whistles (Romanenko 1974). However, it appears that no one has considered the flip side of the coin - i.e., the resonance structure of soft tissues partially surrounded by air sacs - which, as we shall see, explains the main (high frequency) signal components.

¹¹ Rather than cataloguing resonant frequency spectra for the many possible simple (but probably incorrect) geometries, we give this one very suggestive example, and then indicate how to perform a rigorous analysis for an arbitrary 3-D soft tissue and air sac geometry (see below).

¹² If an impulsive monopole source is assumed to be located at or near the center of the sphere, then only the first radial mode is of interest because the source couples primarily into this mode. In addition, the higher

the soft tissue. For a radius of $r=1.25\text{cm}$ and a uniform tissue velocity of $c=1500\text{m/s}$, the n^{th} frequency of the first mode is given by

$$f_{1,n} = n \left[\frac{c}{2r} \right] = n f_1 = n (60 \text{ kHz}) \quad (3.12)$$

Note that the first mode contributes a set of harmonically related frequencies to the resonant spectrum.

The second mode corresponds to both radial and side-to-side (dipole) oscillations of the soft tissue, and does not contribute harmonically related frequencies. For the same radius and uniform velocity, the first three frequencies of the second mode are

$$f_{2,1} = 85.8 \text{ kHz}, \quad f_{2,2} = 148 \text{ kHz}, \quad f_{2,3} = 208 \text{ kHz} \quad (3.13)$$

The message to take home here is that any soft tissue source region completely (or partially) surrounded by air sacs has a resonant structure which can be determined (see below for general case). For an impulsive point source located at or near the center of our simple example of a spherical air-bounded mass of tissue, a predominantly harmonic response would be observed with a small degree of coupling into the non-harmonic second and higher modes. Note also that the broader the spectrum of the impulsive source, the more of the higher resonances we would expect to be excited. A resonant source region model, along with the fact that the spectrum of any impact mechanism (such as hands slapping in air, or pneumatically driven soft tissue impacts within the MLDB region) broadens with the speed of impact, offers a simple explanation for the observed bimodal variations in the sonar signals of certain odontocetes. In addition, because the resonance spectrum scales with the size of the soft tissue source region, this model also appears to explain why the smaller odontocetes can produce high frequency but low intensity signals:¹³ the

modes are expected to decay more rapidly when damping is added into the model.

¹³ See Au (1993), pp. 133-137.

frequency of the lowest mode of their soft tissue 'resonators' would be expected to scale inversely with the size of their source regions, and hence roughly inversely with body size.

Now, if the spherical region is only partially enclosed by air sacs (as is the MLBD region in dolphins), then a damped acoustic resonator results with a Q -value for spherical resonances roughly equal to¹⁴

$$Q = \frac{2\pi}{\ln(A_{total}/A_{air\ sacs})} \quad (3.14)$$

where $A_{total}/A_{air\ sacs}$ is the inverse ratio of air-covered surface to the total surface area. If we assume that an impulsive source mechanism excites the m th spectral component (with frequency f_m) to amplitude $p_{0,m}$, then we expect this component to decay according to

$$p_m(t) = p_{0,m} e^{-\beta_m t} \sin(2\pi f_m t) \quad (3.15)$$

where $\beta_m = \pi f_m / Q$ is an effective damping constant. Note that the more completely the source region is surrounded by air, the higher the expected Q -value, and hence the longer it will 'ring'. As an example, the sonar signal of the harbor porpoise, *Phocoena phocoena*, exhibits a long (~190 msec) decay with many oscillations; the harbor porpoise is also known to have a soft tissue 'capsule' that is almost entirely surrounded by air sacs (Cranford 1992). Note that, to this first order approximation, the decay rate of each component is simply linear with frequency.

Although the above quantities are only intended as rough estimates, a damped but resonant source region excited by an impulsive mechanism (such as pneumatically driven impacts of soft tissue within the MLDB complex) offers a qualitatively correct explanation for the frequency range, short duration, rapid decay, and observed modal shifts in the biosonar signals of several

¹⁴ This follows by analogy with the LRC circuit result that the ratio of successive voltage amplitude peaks V_i/V_{i+1} in the impulse decay of a lightly damped oscillator is approximately equal to $\exp(\pi/Q)$. I have simply assumed that the successive amplitude ratios in the case of the resonant sphere should vary roughly with the square root of $A_{total}/A_{air\ sacs}$.

odontocetes. A more rigorous analysis for each species might proceed as follows: first, determine the true resonant spectrum for the partially air-bounded soft tissue source region; second, multiply this spectrum by the spectrum of the assumed impulsive excitation; finally, transform the product back into the time domain to obtain the expected pressure waveform within the soft tissue region. Numerical simulations utilizing accurate air sac and soft tissue velocity information are probably the best way to determine the resonant spectra of the irregularly shaped soft tissue source regions in most species. The far-field projection of the source signal depends on the tissue structures that surround the source region, which leads us to our next consideration.

The delphinid melon exhibits an internally lowered density and velocity profile extending back to the MLDB complexes, with its posterior end surrounded by a roughly conical connective tissue theca and muscle of higher density and velocity. These structures suggest analogies to a reduced-velocity waveguide (or lens), and a horn (or megaphone), respectively. While neither the melon tissue nor the lower jaw fats constitute elementary geometries,¹⁵ and several principles may operate simultaneously, it is useful to consider the behavior of the each analogue separately.

Reduced-velocity structures can function as waveguides and/or lenses, depending on their configuration. For many simple waveguide shapes, it can be shown that certain wavefunctions (referred to as the 'modes' of the guide) propagate coherently along the direction of the guide without attenuation or change of envelope shape. The efficiency of this channeling behavior depends on several factors including the dimensions of the guide, the wavelength of the sound, and the distribution and magnitude of the velocity perturbation over the guide structure. For simple geometries, it can be shown that the percentage of the energy of a guidefunction that is trapped or channeled within the width of the guide generally increases with both frequency and

¹⁵ The detailed density, velocity, and impedance distributions within the melon of the common dolphin are illustrated in Appendix 2 of this thesis.

the magnitude of the velocity perturbation. In addition, coupling of a specific source into the modes of the guide is important in determining how much of the source energy will be coherently propagated. It will be dramatically demonstrated in Chapter 7 that the melon of *Delphinus delphis* is quite effective in channeling acoustic energy within its cone-shaped posterior throat region.

Reduced-velocity structures that do not stretch out far in any linear dimension may behave more importantly as acoustic lenses, even though waveguiding behavior may also be present. We will also demonstrate in Chapter 7 that the lens-like velocity distribution within the melon of the common dolphin does contribute significantly to biosonar beam formation.

Conical shell structures of high impedance material within a low impedance medium can act as acoustic resonators, directional emitters or collectors, and impedance matching devices. Most musical instruments with conical bores utilize all three mechanisms in the production and projection of musical tones.¹⁶ If the ratio of the wall impedance to that of the ambient fluid is very large (or very small), sound is strongly channeled within the bore and harmonically related resonant frequencies (if driven) can build up. Projection into the environment of the resonant structure within the bore depends on the impedance discontinuity at the bell of the instrument (which varies with frequency). In woodwind and brass instruments, nonlinear driving mechanisms are entrained by the harmonic structure reinforced within the bore.¹⁷ The energy spectrum within the bore eventually reaches an equilibrium with both the driving spectrum and filtering caused by the impedance of the bell of the instrument. An important efficiency aspect of the entire process is the acoustic coupling achieved between the source and the ambient fluid. Flaring horns are often used to efficiently link sources or receivers of intrinsically high impedance to

¹⁶ See any textbook on musical acoustics, for example, Backus (1977), or Benade (1976).

¹⁷ See, for example, Benade (1960, 1973).

a medium of low impedance.

Let us now consider how well these (musical) horn analogies apply to the melon. First, note that the melon 'wall' impedance rises somewhat gradually to a maximum of only about 40% above the impedance of the melon floor at the posterior melon 'throat' (see Appendix 2). This implies a relatively weak wall structure when compared to musical instrument materials in air (typically very sharp, order 10^3 impedance boundaries). Hence we expect only partial wavefunction channeling within the melon walls. Energy can therefore 'leak' out, causing the melon resonances to be weaker than those of a similarly shaped but sharp-walled instrument. Second, the lowest resonant frequency of a cone of length (apex to opening) of roughly 5cm in a medium of velocity 1500m/s is around 15kHz. The peak biosonar frequencies of delphinids therefore correspond to harmonic numbers ranging from 2-9. Third, the opening angle of the roughly conical posterior melon 'horn' in the Delphinidae¹⁸ appears to be very large (50-70 degrees) compared to typical opening angles in conical bored musical instruments (5-15 degrees). Such a wide opening angle would significantly dampen the higher horn resonances, which is equivalent to saying that higher frequencies are emitted efficiently but without much resonant interaction from the end of the horn. That is, only the megaphone effect remains important at the higher resonant frequencies.

Finally and most importantly, the impulsive nature of the biosonar signal source in all delphinids (regardless of the source mechanism) constitutes the main reason for dismissing most of the conical musical instrument analogy except for the megaphone effect. Given the brief duration

¹⁸ While the exact structure of the posterior throat of the melon differs somewhat among the delphinid specimens described by Cranford (1992), his measurements of the posterior melon throat dimensions imply opening cone angles of approximately 56 degrees in *Delphinus delphis*, 62 degrees in *Tursiops truncatus*, and 70 degrees in *Lagenorhynchus obliquidens*. The anterior opening of the soft nasal tissue capsule in *Phocoena phocoena* (similar to the posterior melon throat in delphinids) flares at about 47 degrees. On the other hand, the melon of the monodontid, *Delphinapterus leucas*, forms a longer and more even cone with a much smaller opening angle.

of delphinid biosonar signals (typically 10^{-4} s or less), there can exist no feedback between the source and the melon that could cause source entrainment at a fundamental melon resonance. Were the source duration on the order of milliseconds, feedback could initiate and begin to stabilize, making the resonant structure of the melon potentially important. However, in addition to the waveguide/lens behavior discussed above and confirmed by the current simulations, the megaphone analogy with its properties of improved directional projection and higher harmonic impedance matching appears to be appropriate for the melon tissue.

In summary, we have postulated here the analogy of a damped resonator driven by an impulsive mechanism for the source region in dolphins, with projection of the ensuing signal aided by the waveguide and megaphone effects of the throat of the melon, with mild focusing and transmission into seawater aided by the lensing and impedance matching effects of the remaining melon. The same waveguide, megaphone, and lens analogies also appear to hold for the acoustic effects of the lower jaw fats in signal reception (with the order of occurrence reversed).

Derivation of the Helmholtz Integral Equation¹⁹

The remainder of this chapter is concerned with the derivation of a result that will be central to the computational methods of Chapter 5. In order to numerically investigate biosonar signal emission from the foreheads of dolphins, it will be necessary to accurately compute the acoustic far-field for various models of tissue and source configurations. One elegant approach to solving this problem applies the mathematical relationship between the acoustic field on a surface immediately surrounding a source region and the pressure at other spatial locations. The Helmholtz integral equation, as it is commonly referred to, sums the contributions of infinitesimal

¹⁹ This brief derivation is largely excerpted from Junger and Feit (1986). For a more detailed discussion and development of boundary integral methods, see Baker and Copson (1950), Copley (1967, 1968), or Schenck (1968).

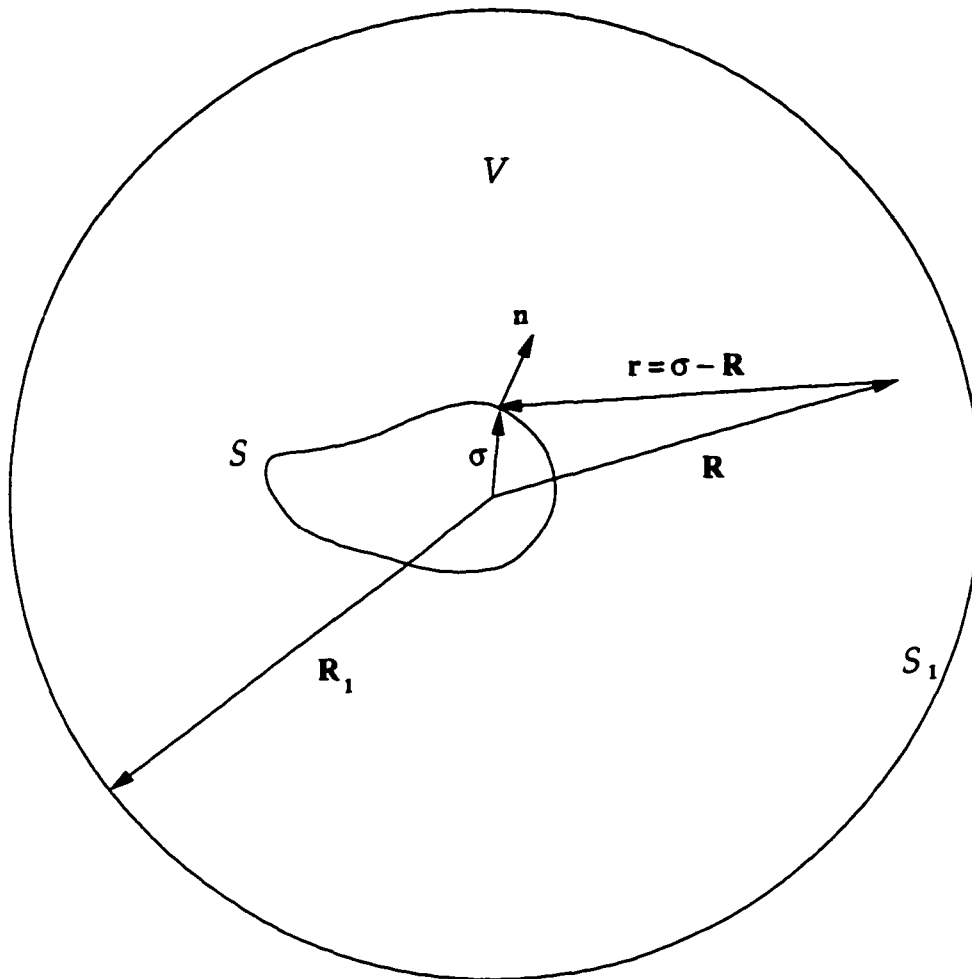


Figure 3.1. Vector geometry of the extrapolation problem. A sourceless and homogeneous volume V is bounded outwardly by spherical surface S_1 at large radius R_1 from the origin, and inwardly by surface S . The volume interior to surface S is assumed to contain an arbitrarily complex and/or inhomogeneous source medium. Note that the unit normal vector \mathbf{n} to surfaces S and S_1 is defined to point into volume V .

surface elements to the field at any location in space. It is the homogeneous nature of the surrounding (seawater) medium that allows us to perform this 'boundary extrapolation' of the field. Below we provide a brief derivation of the Helmholtz integral equation. Programs which numerically implement this equation will be performance analysed in Chapter 5 and then applied in Chapter 7 to compute the emission fields of the tissue and source models.

The geometry of the extrapolation problem is shown in Figure 3.1. Consider the volume V external to a surface S and bounded by the spherical surface S_1 at (large) radius R_1 from the

origin. We wish to obtain an expression for the pressure field $p(\mathbf{R})$ at any point \mathbf{R} within V in terms of the pressure p and the normal derivative of the pressure $\partial p/\partial n$ on S . An arbitrary distribution of field sources is assumed enclosed by surface S , while S itself and the volume external to S are assumed to be sourceless and homogeneous; i.e., the homogeneous Helmholtz equation,

$$(\nabla^2 + k^2)p = 0 \quad (3.16)$$

is satisfied everywhere in V . Here $k = \omega/c$ is the acoustic wavenumber, where ω is the angular frequency of the field, and c is the constant speed of sound in the external medium. Note that σ defines the coordinates of surface S .

The desired expression for $p(\mathbf{R})$ is obtained by using Gauss's integral theorem,

$$\int_V \nabla \cdot \mathbf{F} dV = - \int_{S+S_1} \mathbf{n} \cdot \mathbf{F} dS \quad (3.17)$$

formulated in terms of the coordinate system of the field point \mathbf{R} , with

$$\mathbf{F} = p(\mathbf{R}) \nabla_{\mathbf{R}} G(\mathbf{R}', \mathbf{R}) - G(\mathbf{R}', \mathbf{R}) \nabla_{\mathbf{R}} p(\sigma) \quad (3.18)$$

Here $G(\mathbf{R}', \mathbf{R})$ is the Green's function defined by

$$G(\mathbf{R}', \mathbf{R}) = - \frac{e^{ik|\mathbf{R}' - \mathbf{R}|}}{4\pi |\mathbf{R}' - \mathbf{R}|} \quad (3.19)$$

Note that we have assumed the unit normal vector \mathbf{n} in equation (3.17) to be oriented *into* volume V . The integrand of the volume integral thus becomes

$$\nabla_{\mathbf{R}} \cdot (p \nabla_{\mathbf{R}} G - G \nabla_{\mathbf{R}} p) = p \nabla_{\mathbf{R}}^2 G - G \nabla_{\mathbf{R}}^2 p \quad (3.20)$$

while the integrand of the surface integral becomes

$$\mathbf{n} \cdot (p \nabla_{\mathbf{R}} G - G \nabla_{\mathbf{R}} p) = p \frac{\partial G}{\partial n} - G \frac{\partial p}{\partial n} \quad (3.21)$$

where $\partial/\partial n = \mathbf{n} \cdot \nabla$ denotes the directional derivative along the unit normal vector \mathbf{n} . Substituting these results into equation (3.17), one obtains Green's identity,

$$\int_V (p \nabla_{\mathbf{R}}^2 G - G \nabla_{\mathbf{R}}^2 p) dV = - \int_{S+S_1} \left[p \frac{\partial G}{\partial n} - G \frac{\partial p}{\partial n} \right] dS \quad (3.22)$$

To evaluate the LHS volume integral we solve the homogeneous Helmholtz equation (3.16), also formulated in the coordinate system of the field point \mathbf{R} , for $\nabla_{\mathbf{R}}^2 p$,

$$\nabla_{\mathbf{R}}^2 p = -k^2 p \quad (3.23)$$

and make use of the fundamental property of the Green's function:

$$\nabla_{\mathbf{R}}^2 G = -k^2 G + \delta(\mathbf{R} - \mathbf{R}') \quad (3.24)$$

When equations (3.23) and (3.24) are substituted into the volume integral of equation (3.22), the integrand reduces to $p(\mathbf{R}') \delta(\mathbf{R} - \mathbf{R}')$. Upon integration of this product over volume V , three different results are possible depending on whether \mathbf{R} lies in V , on the boundary surfaces S or S_1 , or interior to surface S (and thus exterior to the volume of integration). These three cases yield $p(\mathbf{R})$, $p(\mathbf{R})/2$, and 0, respectively. Thus equation (3.22) becomes

$$\epsilon p(\mathbf{R}) = - \int_{S+S_1} \left[p \frac{\partial G}{\partial n} - G \frac{\partial p}{\partial n} \right] dS \quad (3.25)$$

where $\epsilon=1$ for \mathbf{R} within V , $\epsilon=1/2$ for \mathbf{R} on S or S_1 , and $\epsilon=0$ for \mathbf{R} outside V .

Now consider the integral over surface S_1 as R_1 approaches infinity. Because all sources are localized within the inner surface S , it makes sense to impose the requirement that the pressure field consists only of outgoing spherical waves as $R_1 \rightarrow \infty$. The Sommerfeld radiation condition,

$$\lim_{R_1 \rightarrow \infty} R_1 \left[ikp(\mathbf{R}_1) - \frac{\partial p(\mathbf{R}_1)}{\partial R_1} \right] = 0 \quad (3.26)$$

which implies that the pressure drops off at least as fast as R_1^{-1} over surface S_1 as $R_1 \rightarrow \infty$, holds for all sources of finite extent. In the limit that $R_1 \gg R$, it is also true that

$$G(\mathbf{R}_1, \mathbf{R}) \approx -\frac{e^{ik|\mathbf{R}_1 - \mathbf{R}|}}{4\pi R_1} \quad (3.27)$$

and that

$$\frac{\partial G}{\partial R_1} \approx ikG(\mathbf{R}_1, \mathbf{R}) \quad (3.28)$$

Finally, writing out the surface integral over S_1 and applying equations (3.26), (3.27), and (3.28), we find

$$\lim_{R_1 \rightarrow \infty} \int_{S_1} \left[p \frac{\partial G}{\partial n} - G \frac{\partial p}{\partial n} \right] dS = \lim_{R_1 \rightarrow \infty} 4\pi R_1^2 \left[p(\mathbf{R}_1) \frac{\partial G(\mathbf{R}_1, \mathbf{R})}{\partial R_1} - G(\mathbf{R}_1, \mathbf{R}) \frac{\partial p(\mathbf{R}_1)}{\partial R_1} \right] = 0 \quad (3.29)$$

The surface integral at infinity is therefore seen to vanish, and we are left with the desired expression for $p(\mathbf{R})$ in terms of the integral over S . For field points \mathbf{R} lying exterior to surface S ($\epsilon=1$), we thereby obtain the result referred to as the Helmholtz integral equation:

$$p(\mathbf{R}) = -\oint_S \left\{ p(\boldsymbol{\sigma}) \frac{\partial G(\boldsymbol{\sigma}, \mathbf{R})}{\partial n} - G(\boldsymbol{\sigma}, \mathbf{R}) \frac{\partial p(\boldsymbol{\sigma})}{\partial n} \right\} dS(\boldsymbol{\sigma}) \quad (3.30)$$

In our application we obtain both the pressure p and the normal derivative $\partial p / \partial n$ over a surface surrounding our delphinid tissue and source models from finite difference simulations (see Chapter 4). Equation (3.30) therefore can be used to compute the pressure anywhere external to the model. In Chapter 5, we will show how far-field emission patterns can be computed from equation (3.30).

Numerical Simulation of Sound Propagation -- Part I

Chapter 4. Finite Difference Methods

We are interested in solving two classes of bioacoustic problems in this thesis. The first class consists of simulations of biosonar signal echoes propagating back (returning in the reverse direction of their emission) into our models of delphinid forehead and lower jaw tissues. We are investigating two distinct questions with this first class of 'inverse' simulations. First, where in the forehead tissue model does the source have to be located in order to produce the biosonar beam that is measured experimentally for these animals?¹ Second, is sound channeled back towards the ear complexes by the fats of the lower jaw, and if so, which properties of the fats produce this waveguiding behavior? The nature of the acoustic reception process will also help answer several questions concerning delphinid mechanisms of directional hearing.

The second class of problem we wish to solve is 'forward' simulation of the acoustic far-field produced by a given model of tissues and sources. With these emission simulations we are investigating the effects of various tissues (either separately or in combination) on the formation of biosonar beams. The boundary extrapolation programs discussed in Chapter 5 constitute the second half of the forward simulation process.

Note that in both classes of problem it is necessary to propagate sound through models of biological tissue. We now turn our attention to the finite difference (FD) methods used to solve the 3-D inhomogeneous acoustic wave equation inside the models of delphinid forehead and lower jaw anatomy.²

¹ This is analogous to using an inverse seismologic simulation to pinpoint the epicenter of an earthquake from the seismic time records of the quake at the earth's surface.

² While alternative techniques exist for modeling sound propagation within inhomogeneous media, most notably (to this application) the finite element method, the FD method was chosen for the following reasons. First, the x-ray CT data from which the tissue models are constructed consists of coefficients of x-ray attenua-

This chapter presents the exact algorithms utilized in the FD programs, and provides an analysis of their dispersion behavior. Next we shall discuss the absorbing boundary algorithms applied at the edges of the grid. Finally we discuss aspects of the design of the grids in the simulations.

Primary Algorithms

Several texts offer introductions to the FD method for numerical solution of differential equations,³ which is based on the replacement of derivatives with difference quotients over small intervals. The central equation we wish to solve is the acoustic equation for fluids of inhomogeneous velocity and density [equation (3.2)], which we restate:

$$\frac{1}{c^2(\mathbf{x})} \frac{\partial^2 p}{\partial t^2} = \nabla^2 p - \frac{\nabla p \cdot \nabla \rho(\mathbf{x})}{\rho(\mathbf{x})} \quad (4.1)$$

Note that both the tissue sound speed c and mass density ρ are functions of position \mathbf{x} , while the acoustic pressure p is dependent on position and time, $p = p(\mathbf{x}, t)$.

Discretizing equation (4.1) on a cubic spatial lattice of increment size $h = 1.5\text{mm}$ (the finest CT scan increment), and discrete time increment l , we introduce the notation

$$P(x_i, y_j, z_k; t_m) = P(ih, jh, kh; ml) = P_{i,j,k}^m$$

for the value of the numerical solution of the pressure at the (i, j, k) 'th grid position and the m 'th time step.⁴ Similarly, we define grid values of velocity as $c(x_i, y_j, z_k) = c_{i,j,k}$ and density as

tion within small rectangular volume pixels (voxels). It is simpler to use a similar rectangular grid to model sound propagation through such a dataset, rather than mapping to a grid of different geometry. Second, as demonstrated below, all relevant propagation characteristics of FD grids can be calculated. Hence numerical errors can be quantified. Third, the application of boundary extrapolation techniques (see Chapter 5) means that we do not need to propagate the solution into the far-field, and hence that the uniformly dense FD grid need not extend far beyond the immediate volume of the modeled tissues. Finally, the ease with which FD algorithms can be programmed is a significant advantage.

³ See, for example, Smith (1985), or Twizell (1984). See also Alford *et al.* (1974). A brief but relevant introduction to 2-D FD methods is also provided in Aroyan (1990).

⁴ We switch notations from p to P to maintain a formal distinction between the exact solution p of equation (4.1) and the solution P of the approximating scheme (4.2). See Aroyan (1990), p26-28.

$$\rho(x_i, y_j, z_k) = \rho_{i,j,k}.$$

The following FD scheme was used to time-step the solution of equation (4.1) over the tissue region of the grid:

$$\begin{aligned}
P_{i,j,k}^{m+1} = & (2 - 7.5\kappa_{i,j,k}^2) P_{i,j,k}^m - P_{i,j,k}^{m-1} \\
& + \frac{4\kappa_{i,j,k}^2}{3} \left[P_{i+1,j,k}^m + P_{i-1,j,k}^m + P_{i,j+1,k}^m + P_{i,j-1,k}^m + P_{i,j,k+1}^m + P_{i,j,k-1}^m \right] \\
& - \frac{\kappa_{i,j,k}^2}{12} \left[P_{i+2,j,k}^m + P_{i-2,j,k}^m + P_{i,j+2,k}^m + P_{i,j-2,k}^m + P_{i,j,k+2}^m + P_{i,j,k-2}^m \right] \\
& - \frac{\kappa_{i,j,k}^2}{3\rho_{i,j,k}} \left[(P_{i+1,j,k}^m - P_{i-1,j,k}^m) - \frac{1}{8} (P_{i+2,j,k}^m + P_{i-2,j,k}^m) \right] (\rho_{i+1,j,k} - \rho_{i-1,j,k}) \\
& - \frac{\kappa_{i,j,k}^2}{3\rho_{i,j,k}} \left[(P_{i,j+1,k}^m - P_{i,j-1,k}^m) - \frac{1}{8} (P_{i,j+2,k}^m + P_{i,j-2,k}^m) \right] (\rho_{i,j+1,k} - \rho_{i,j-1,k}) \\
& - \frac{\kappa_{i,j,k}^2}{3\rho_{i,j,k}} \left[(P_{i,j,k+1}^m - P_{i,j,k-1}^m) - \frac{1}{8} (P_{i,j,k+2}^m + P_{i,j,k-2}^m) \right] (\rho_{i,j,k+1} - \rho_{i,j,k-1}) \quad (4.2)
\end{aligned}$$

Here $\kappa_{i,j,k} \equiv (l/h) c_{i,j,k}$, with $\rho_{i,j,k}$ and $c_{i,j,k}$ labeling the spatially varying density and acoustic velocity. This scheme is fourth-order in the spatial derivatives of pressure, second-order in the spatial derivatives of density, and second-order in the time derivative of pressure. Second order spatial derivatives of density were used in order to best simulate behavior at sharp tissue interfaces.

The first three lines of equation (4.2) constitute the scheme for the homogeneous wave equation. This homogeneous scheme was used outside the tissue regions of the grid and greater

than two points away from the grid faces. A second-order spatial derivative scheme was applied at the next-to-last points of the grid edges. Third-order Halpern and Trefethen absorbing boundary conditions (see below) were applied at the extreme faces of the grid. Grid corners were time-stepped using simple averaging of the forward time values of neighboring points.

Consistency and stability can be shown for the homogeneous scheme provided $\kappa_{i,j,k} \leq 0.5$. Stability for the inhomogeneous scheme further requires that density discontinuities not exceed a factor of about 2.5 per grid point.⁵ While a stability analysis for the combined grid scheme (including absorbing boundary conditions) was not attempted, instabilities never occurred over the range of simulation parameters for the scheme used here. All derivative schemes used (except at the boundaries) were symmetric and centered in both time and space. A symmetric but uncentered spatial derivative scheme is required at the extreme grid edges (see discussion of absorbing boundary conditions).

Dispersion Behavior of the Homogeneous Algorithm

All propagation characteristics of the fourth-order 3-D homogeneous algorithm may be derived from its dispersion relation, which is found by plugging the plane wave solution

$$P_{j,k,m}^n = \exp [i(k_x x_j + k_y y_k + k_z z_m - \omega t_n)] = \exp [i(k_x jh + k_y kh + k_z mh - \omega n l)] \quad (4.3)$$

into the first three lines of equation (4.2). Here, k_x, k_y, k_z are the cartesian components of the wavevector \mathbf{k} which is oriented perpendicular to the phase fronts of the wave. The following dispersion relation is thereby obtained:

$$\sin^2 \left[\frac{\omega l}{2} \right] = \frac{4\kappa^2}{3} \left\{ \sin^2 \left[\frac{hk_x}{2} \right] + \sin^2 \left[\frac{hk_y}{2} \right] + \sin^2 \left[\frac{hk_z}{2} \right] \right\}$$

⁵ As in previously reported work (Aroyan 1990, Aroyan *et al.* 1992), air sacs are therefore modeled as

$$- \frac{\kappa^2}{12} \left\{ \sin^2(hk_x) + \sin^2(hk_y) + \sin^2(hk_z) \right\} \quad (4.4)$$

The velocity with which the phase fronts of a wave packet propagate is called the phase velocity $c_{ph} = c_{ph} \hat{\mathbf{k}} = (\omega/k) \hat{\mathbf{k}}$, which we assume to be oriented along wavevector \mathbf{k} . While real fluids are acoustically isotropic, the cubic simulation lattice is nonisotropic. Hence, the phase velocity on the grid varies as a function of both wavelength and direction of phase front propagation, i.e., as a function of \mathbf{k} . From equation (4.4), we calculate c_{ph} to be

$$c_{ph}(\mathbf{k}) = \frac{2\hat{\mathbf{k}}}{lk} \sin^{-1} \kappa \left[\frac{4}{3} \left\{ \sin^2 \left[\frac{hk_x}{2} \right] + \sin^2 \left[\frac{hk_y}{2} \right] + \sin^2 \left[\frac{hk_z}{2} \right] \right\} - \frac{1}{12} \left\{ \sin^2(hk_x) + \sin^2(hk_y) + \sin^2(hk_z) \right\} \right]^{1/2} \quad (4.5)$$

In addition, the cubic grid's nonisotropy affects the velocity with which energy is transported by waves. The velocity with which the envelope of a nearly-monochromatic packet propagates is called the group (or energy) velocity c_{gr} , and is not necessarily perpendicular to the surfaces of constant phase. Hence we expect that 'quasi-longitudinal' modes⁶ exist for which c_{gr} is neither exactly parallel nor equal in magnitude to the phase velocity c_{ph} . In three dimensions, the group velocity is defined to be

$$\mathbf{c}_{gr} = \hat{\mathbf{x}} \frac{\partial \omega}{\partial k_x} + \hat{\mathbf{y}} \frac{\partial \omega}{\partial k_y} + \hat{\mathbf{z}} \frac{\partial \omega}{\partial k_z} \quad (4.6)$$

Calculating the partial derivatives from equation (4.4), we find

$$\mathbf{c}_{gr}(\mathbf{k}) = \frac{h\kappa^2}{l \sin(\omega l)} \left[\hat{\mathbf{x}} \left\{ \frac{4}{3} \sin(hk_x) - \frac{1}{6} \sin(2hk_x) \right\} + \hat{\mathbf{y}} \left\{ \frac{4}{3} \sin(hk_y) - \frac{1}{6} \sin(2hk_y) \right\} \right]$$

pressure release surfaces.

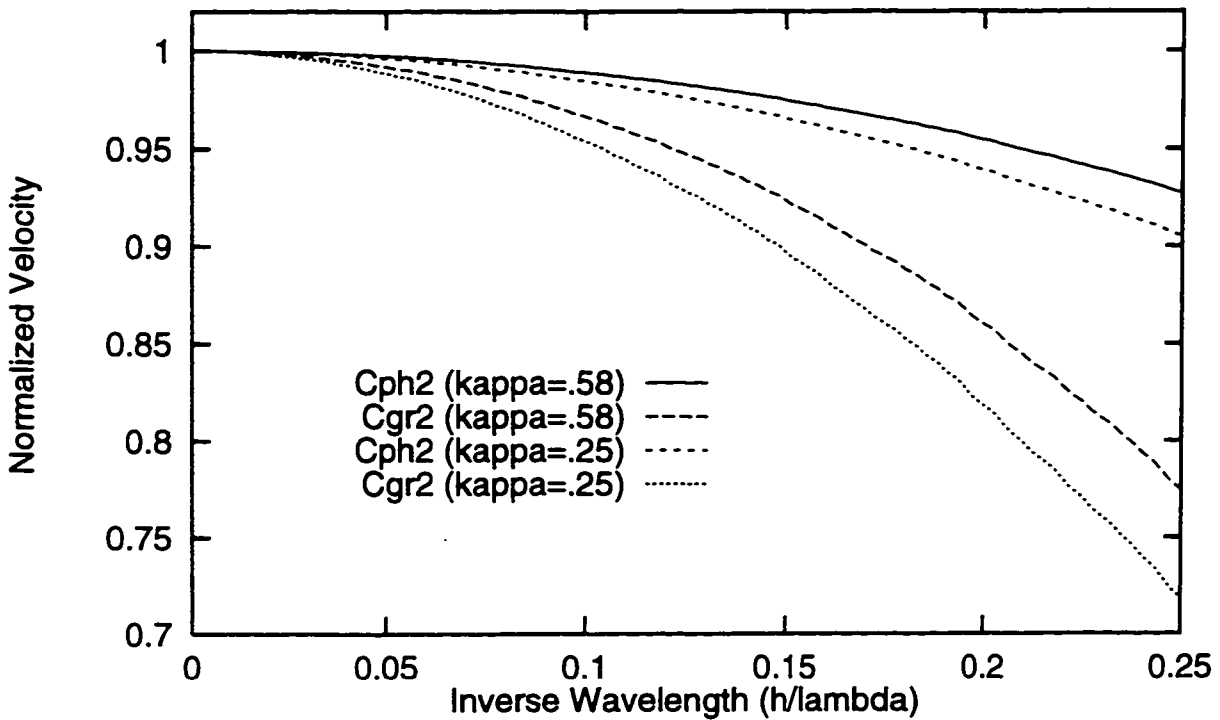
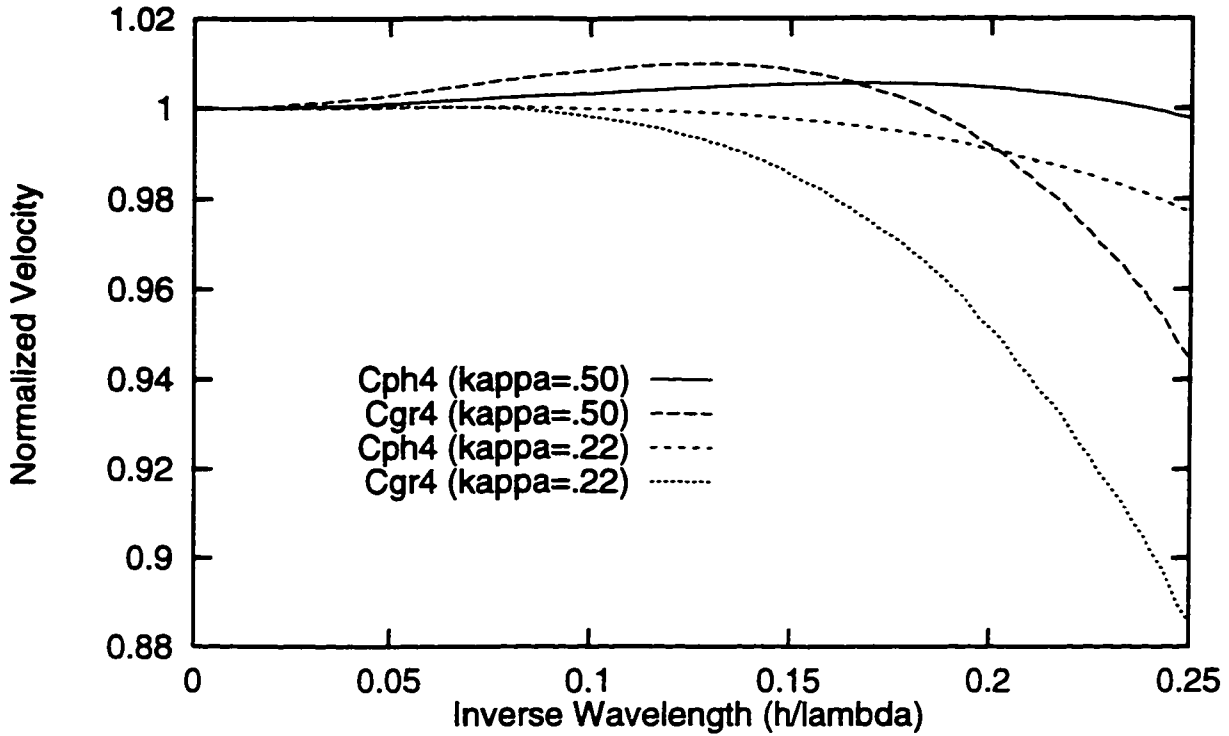
⁶ See Auld (1973), vol. 1, p227-236.

$$+ 2 \left\{ \frac{4}{3} \sin(hk_z) - \frac{1}{6} \sin(2hk_z) \right\} \quad (4.7)$$

A discretization scheme can cause propagation artifacts when either c_{ph} or c_{gr} vary substantially. Let us first examine the dependence of c_{ph} and $c_{gr} = |c_{gr}|$ on wavelength. The magnitudes of c_{ph} and c_{gr} are plotted as functions of inverse wavelength (number of wavelengths per grid increment, h/λ) for the fourth-order homogeneous algorithm in Figure 4.1a, and for the corresponding second-order algorithm⁷ in Figure 4.1b. The plots give curves for two values of the stability parameter κ , often called the numerical velocity because both c_{ph} and c_{gr} approach $\kappa h/l$ in the limit $\lambda \rightarrow \infty$ (or $h/\lambda \rightarrow 0$). In addition, the curves have been normalized to the values of $\kappa h/l$ used, and propagation along a cartesian axis direction has been assumed. Note that the fourth-order algorithm exhibits considerably less divergence of c_{ph} and c_{gr} than the second-order algorithm at all finite wavelengths.

We next examine the dependence of the magnitudes of c_{ph} and c_{gr} on the direction of (phase) propagation on the grid. Figure 4.2 plots the normalized values of c_{ph} and c_{gr} for the fourth-order homogeneous algorithm along an arc connecting the 'slow' 1,0,0 and the 'fast' 1,1,1 lattice directions for a wavelength of 10 grid increments (corresponding to a frequency of about 100kHz in the simulations). Figure 4.2 also plots normalized values of c_{ph} and c_{gr} for the related second-order algorithm. Again, the advantage of the fourth-order algorithm over the second-order is obvious. For example, the relative shift in c_{ph} between the fast and slow directions can cause phase errors to appear in the values of the pressure and its normal derivative over the surface used to extrapolate the far-field (see Chapter 5). Use of the fourth-order algorithm minimizes this problem (phase errors remain less than about 0.5% over the extrapolation surfaces used

⁷ Centered second-order spatial derivatives of pressure are used instead of the fourth-order derivatives in the first three lines of equation (4.2).



Figures 4.1a-b. Normalized phase and group velocities plotted as functions of inverse wavelength (wavelengths per grid increment, h/λ) for the fourth-order homogeneous algorithm in Figure 4.1a (above), and for the corresponding second-order algorithm in Figure 4.1b (below). Curves are also given for different values of the stability parameter κ . Velocities have been normalized to the values of $\kappa h/l$ used, and propagation along a cartesian axis direction has been assumed.

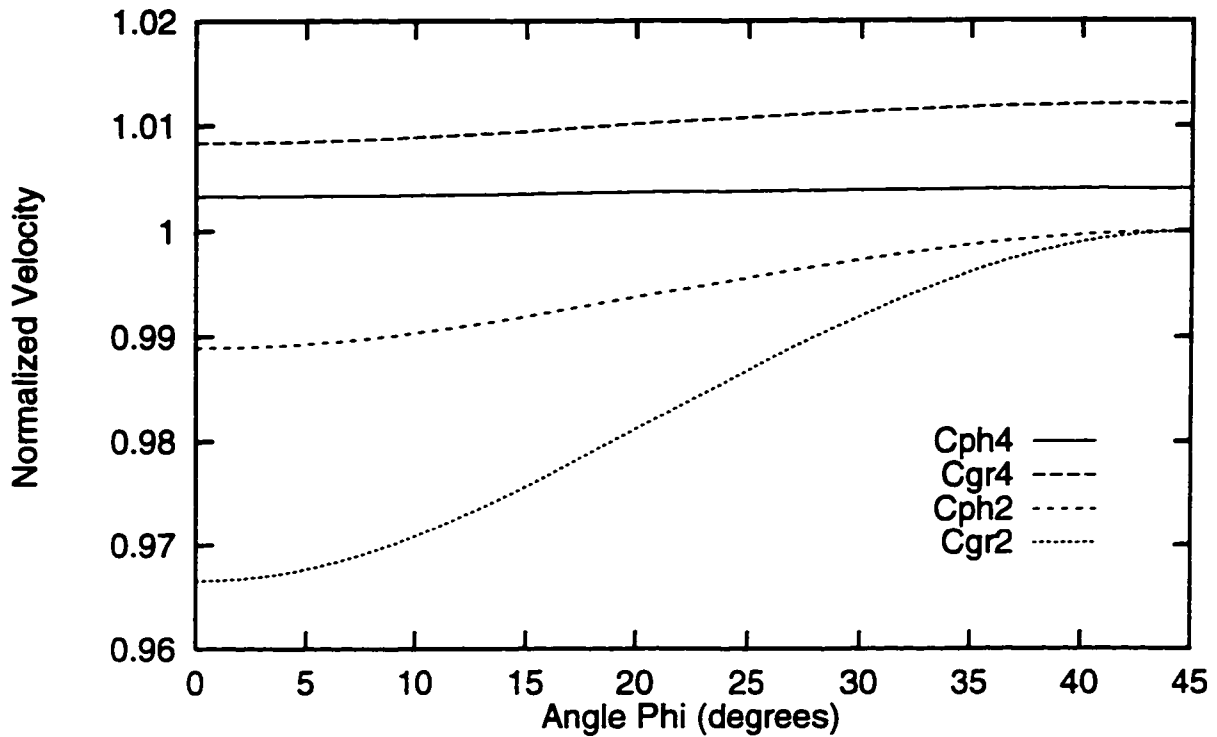


Figure 4.2. Normalized phase and group velocities plotted as functions of the direction of (phase) propagation on the grid. Phase and group velocities are plotted for both the fourth-order and second-order homogeneous algorithms along an arc connecting the 'slow' 1,0,0 and the 'fast' 1,1,1 lattice directions for a wavelength of 10 grid increments.

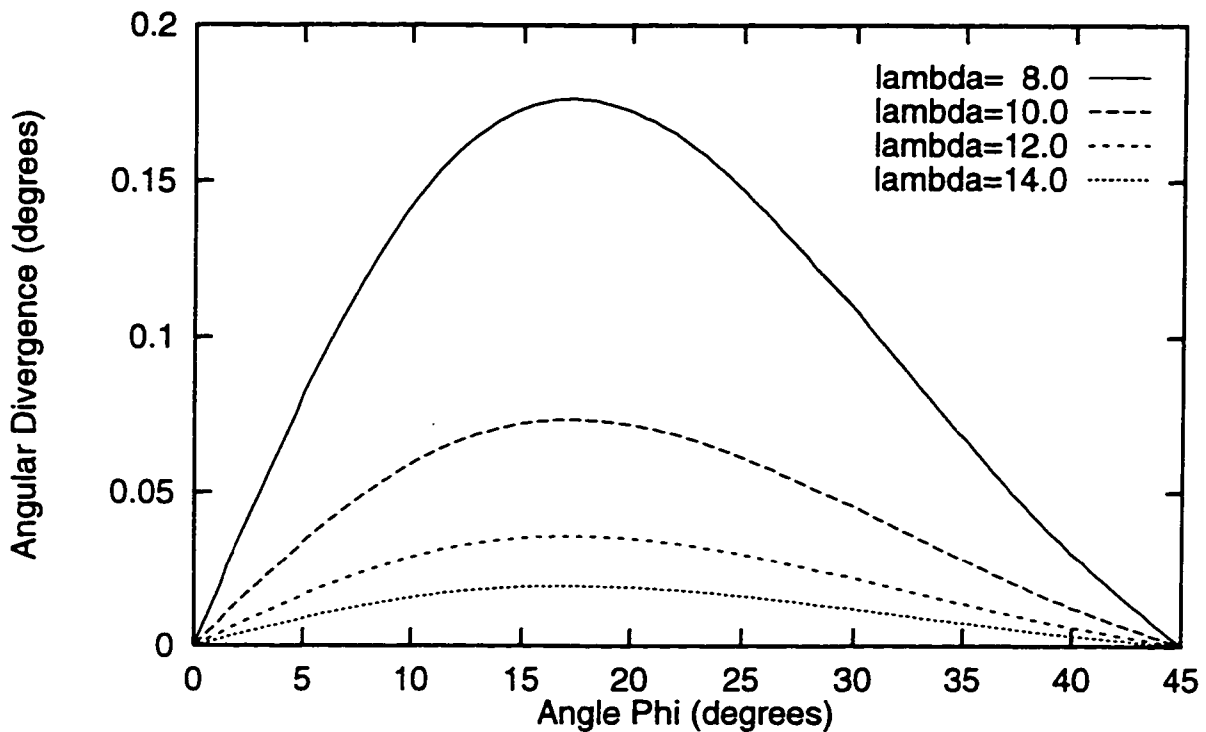


Figure 4.3. Plot of the angular divergence of the fourth-order phase and group velocity vectors plotted along the slow-to-fast directional arc for several wavelengths.

in the simulations).⁸ In addition, it can be shown that the fast-vs-slow directional shifts in c_{ph} and c_{gr} drop off with the inverse fourth power of the wavelength for the fourth-order algorithm, but only with the inverse square of the wavelength for the second-order algorithm.

Finally we examine the artifact of quasi-longitudinal wave behavior on the FD grid. The angle (in degrees) between the fourth-order vectors \mathbf{c}_{ph} and \mathbf{c}_{gr} along the slow-to-fast directional arc is plotted in Figure 4.3 for several wavelengths. For a wavelength of 10 grid increments or greater, this deviation is extremely small. This illustrates that quasi-longitudinal distortion of the wavefront cannot occur significantly on grids having dimensions of a few hundred points. This angular divergence also drops off with the inverse fourth power of the wavelength for the fourth-order algorithm.

Figures 4.1a-b also indicate that grid dispersion is minimized while efficiency is maximized for both schemes when they are run near their stability limits (maximum values of κ). All simulations in this project utilized the fourth-order algorithm over interior grid points, and were run at their stability limit for the highest velocity appearing in the simulation. Taking the fourth-order dispersion curves and the maximum required grid dimensions into account, a wavelength of 6 grid increments was determined to be the practical dispersion limit (corresponding to an upper frequency limit of about 170kHz in the simulations). However, because of an upper frequency bound of approximately 100kHz for acceptable accuracy in the extrapolation programs discussed in Chapter 5, the FD simulations were restricted to frequencies less than or equal to 100kHz in the current project. This frequency range is adequate for our study of *Delphinus* biosonar emission and reception.

⁸ From the fast-vs-slow directional shift in c_{ph} for $\lambda=10$ grid increments, it can be shown that waves propagating in these two directions will accumulate a 1 percent phase difference at a radial distance of about 200 grid increments.

Absorbing Boundary Conditions

In FD simulations of wave propagation, artificial reflections arise at the edges of the domain of computation. In order not to compromise the accuracy of results in the grid interior, one can either enlarge the domain of computation or employ conditions at the boundaries which 'absorb' incident waves. Enlarging the grid wastes computational resources since both the required storage and the number of calculations per time step increase linearly with grid length in each spatial dimension. For 3-D grids, this rapidly becomes the dominant limitation. Hence absorbing boundary conditions (ABC's) are ordinarily utilized to minimize the unwanted reflections.

Several types of ABC's have been developed.⁹ Many are based on approximations to one-way wave equations which freely allow propagation in the outgoing direction. The performance of some of the one-way wave equation formulations appears very promising. For example, Randall (1988) outlines a procedure devised by Lindman (1975) that is remarkably efficient (having a reflection coefficient less than 1 percent) for incident angles up to 89 degrees. Renaut (1992) has generalized Lindman's formulation into a computationally elegant approach to ABC's. In her reformulation, higher degree approximations to the radical in the one-way dispersion relation are achieved by simply adding more coefficients to the expansion of the radical. Surprisingly, this does not increase the order of the differential equation being applied at the boundary, yet greatly improves the boundary absorption. Unfortunately, this approach seems to be unstable when used in conjunction with the fourth-order 3-D algorithm given by equation (4.2) in the grid interior. The author implemented two different versions ($M=1$ and $M=2$) of the 3-D Lindman ABC's given in Tirkas *et al.* (1992) and found them both to be unstable. Nevertheless, because

⁹ For a tutorial on the theory and application of absorbing boundary conditions, see Moore *et al.* (1988). For excellent reviews of ABC's formulated in terms of one-way wave equations, see Renaut (1992), and Tirkas *et al.* (1992). One unusual approach (Shaw 1974) uses boundary integral equations more typically applied in radiation and scattering problems to formulate ABC's.

of the exceptional elegance and efficiency of Renault's reformulation of Lindman ABC's, the author would encourage further investigation of this approach.

For the simulations in this project, the more pedestrian variety of third-order (fourth-degree) Halpern and Trefethen (1988) ABC's was selected. This choice provides better absorption than the second-order (second-degree) ABC's utilized in the previous 2-D simulations, but still forces us to exercise some caution in the design of simulation grids. Interference effects from reflected boundary waves are greatly reduced but not absent.

We now briefly discuss the construction of the selected ABC for the rear boundary of the grid.¹⁰ Plugging a plane wave solution into the 3-D homogeneous wave equation (3.1), we obtain the full wave dispersion relation

$$\left(\frac{\omega}{c}\right)^2 = k^2 = k_x^2 + k_y^2 + k_z^2 \quad (4.8)$$

Solving this for k_x , we find

$$k_x = \pm \left(\frac{\omega}{c}\right) \left[1 - \frac{c^2 k_y^2}{\omega^2} - \frac{c^2 k_z^2}{\omega^2}\right]^{1/2} = \pm \left(\frac{\omega}{c}\right) [1 - s^2]^{1/2} \quad (4.9)$$

where the plus and minus signs respectively indicate the forward- and backward-traveling wavevector k_x component with respect to the positive x direction, and s^2 has been introduced as a shorthand for the last two terms inside the square root bracket.

Next we construct a fourth-degree rational fraction approximation of the square root function in terms of the Padé coefficients a_0, a_2, b_2 :¹¹

¹⁰ For a full discussion see Halpern and Trefethen (1988), Renault (1992), and Tirkas *et al.* (1992).

¹¹ Halpern and Trefethen (1988) analyzed seven classes of approximants to Engquist and Majda's (1977) rational function expansion of the radical. The selection of Padé coefficients from among many alternative classes is suggested by the results of Renault (1992) and Tirkas *et al.* (1992), and was confirmed by tests of the full grid scheme utilized here. The coefficients a_0, a_2, b_2 are normally labelled p_0, p_2, q_2 in the literature.

$$k_x = \pm \left[\frac{\omega}{c} \right] \left[1 - s^2 \right]^{1/2} = \pm \left[\frac{\omega}{c} \right] \frac{a_0 + a_2 s^2}{1 + b_2 s^2} \quad (4.10)$$

which we rewrite as the equality

$$c \omega^2 k_x + c^3 b_2 [k_x k_y^2 + k_x k_z^2] = \pm a_0 \omega^3 \pm c^2 a_2 [\omega k_y^2 + \omega k_z^2] \quad (4.11)$$

Selecting out waves traveling backwards into the $x=1$ grid plane (negative k_x component), and identifying the quantities k_x, k_y, k_z , and ω with the appropriate plane wave derivative operators, we associate equation 4.11 with the third-order partial differential equation

$$c p_{txx} + c^3 b_2 [p_{yyx} + p_{zzx}] = a_0 p_{ttt} + c^2 a_2 [p_{tyy} + p_{tzz}] \quad (4.12)$$

Finally, we approximate this equation with a discrete derivative scheme and apply it at the rear ($x=1$) boundary of the grid.

At the very edge of the grid, it is wisest to average grid values in both space and time to maintain a truncation error of $O(h^2) + O(l^2) + O(hl)$ (Renaut 1992). In terms of the the standard forward and backward q -derivative operators (D_+^q, D_-^q), one such discretization of equation (4.12) is:

$$\begin{aligned} & \left\{ c D_+^t D_-^t D_+^x + c^2 b_2 [D_+^y D_-^y D_+^x + D_+^z D_-^z D_+^x] \right\} (P_{1,j,k}^m + P_{1,j,k}^{m+1}) \\ & = \left\{ a_0 D_+^t D_-^t D_+^t + c^2 a_2 [D_+^y D_-^y D_+^t + D_+^z D_-^z D_+^t] \right\} (P_{1,j,k}^m + P_{2,j,k}^m) \end{aligned} \quad (4.13)$$

This discretization is carried out and solved for the forward time step. Equivalent conditions are applied at the left, right, top, bottom, and front boundaries of the grid. In effect, these ABC's simulate 'one-way' windows at each of the boundaries; that is, waves are allowed to travel outward through, but not backwards into, each boundary.

Accurate reflection coefficients for any ABC scheme can be calculated, though the author has found the subject to be incompletely treated in the literature. The standard procedure is to

insert the sum

$$P_i + P_r = \exp[i(k_x x + k_y y + k_z z - \omega t)] + R \exp[i(-k_x x + k_y y + k_z z - \omega t)] \quad (4.14)$$

of incident and reflected plane wave amplitudes into the one-way wave equation (4.12), and then solve for R .¹² This calculation is normally carried out assuming that $c_{ph} = \omega/k$ is equal to the speed c appearing in the wave equation, which is incorrect for discrete schemes. This approach therefore describes absorption by equation (4.12) in the absence of discretization error.

A more realistic procedure is the following. First derive the dispersion relation for the discrete scheme by plugging a plane wave solution [equation (4.3)] into the discretization equation (4.13), and solve for the phase velocity c_{ph} .¹³ Next, insert the usual sum of incident and reflected amplitudes [equation (4.14)] into wave equation (4.12), and solve for $R(\mathbf{k})$ by substituting the discrete scheme's c_{ph} into the expression for R wherever ω/k occurs. The amplitude reflection coefficient for our third-order ABC that results from this procedure is:

$$R(\mathbf{k}) = \frac{n_{ph} \cos\theta + b_2 n_{ph}^3 \cos\theta \sin^2\theta - a_0 - a_2 n_{ph}^2 \sin^2\theta}{n_{ph} \cos\theta + b_2 n_{ph}^3 \cos\theta \sin^2\theta + a_0 + a_2 n_{ph}^2 \sin^2\theta} \quad (4.15)$$

where θ is the (polar) angle of plane wave incidence on the boundary ($\theta=0$ at normal incidence; see Figure 4.4), and $n_{ph} = n_{ph}(\mathbf{k}) \equiv c/c_{ph}(\mathbf{k})$ is an effective index of refraction for the discretization scheme. A weak dependence on the azimuthal angle ϕ enters through n_{ph} .

Figure 4.5 plots $R(\theta)$ [equation (4.15) with $\phi=0$] using Padé coefficients for $\lambda=10$ grid increments as well as $R(\theta)$ assuming $n_{ph}=1$ (zero discretization error) as ordinarily presented in the literature.¹⁴ Several aspects of this plot deserve notice. First, the curve for R which includes discretization error actually increases beyond $R=1$ for angles of incidence between about 88 and

¹² See, for example, Moore *et al.* (1988).

¹³ This may involve numerical solution of an implicit equation for c_{ph} with high order boundary schemes.

¹⁴ Cf. Moore *et al.* (1988), equation (39) and Figure 3, p1802-1803, and Renaut (1992), Figure 1b, p239.

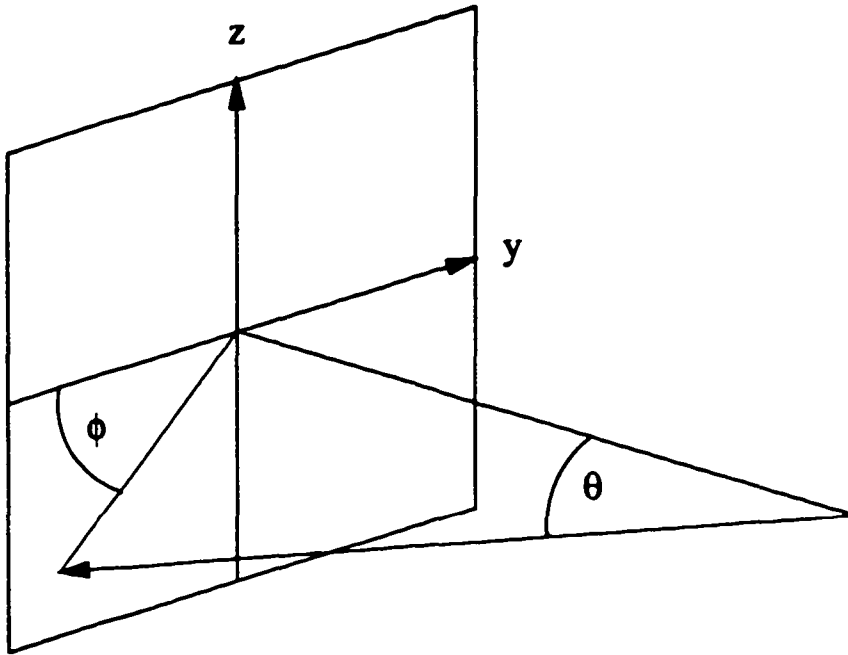


Figure 4.4. Angles of plane wave incidence on a grid boundary.

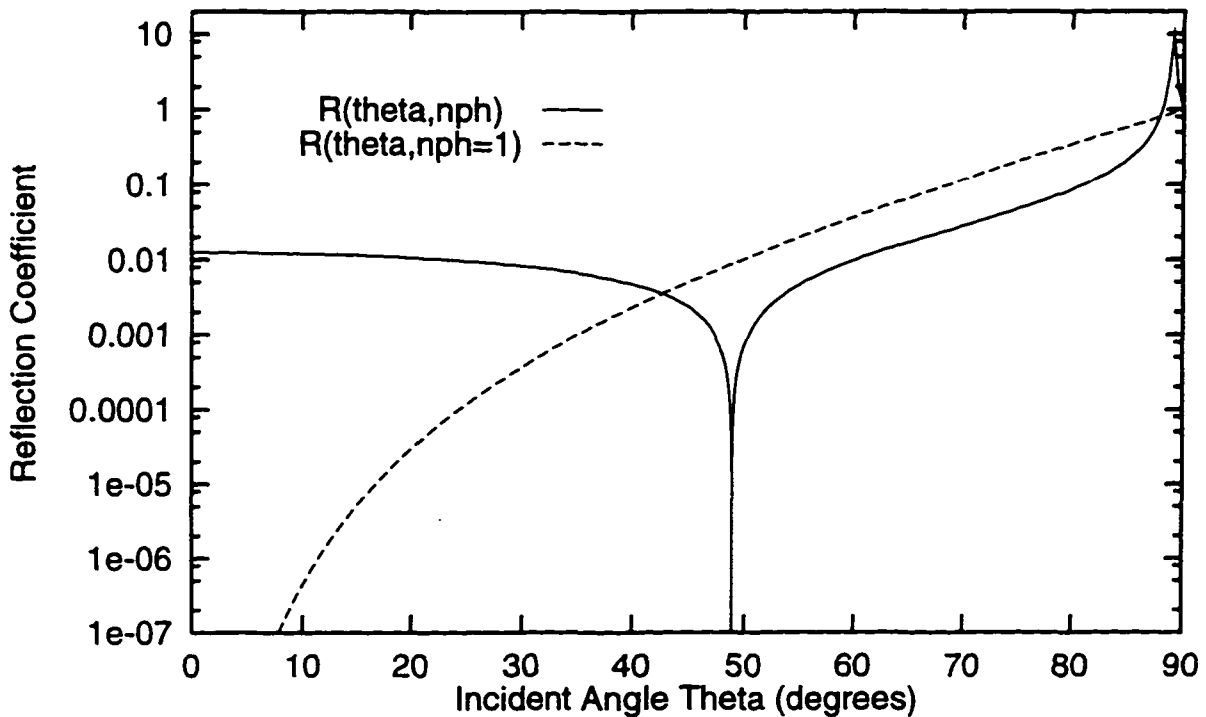


Figure 4.5. Amplitude reflection coefficients as functions of the incident angle θ . Solid curve is $R(\theta)$ for the third-order Halpern and Trefethen ABC scheme using Padé coefficients for $\lambda=10$ grid increments and $\phi=0$. Dashed curve is $R(\theta)$ assuming $n_{ph}=1$ (zero discretization error).

90 degrees. This indicates an instability in the performance of the ABC at high angles not apparent from the standard analysis. Although this instability does not ordinarily appear to cause difficulties, and there is an easy way to circumvent the problem (see next paragraph), it should not be dismissed as trivial. Second, we note that R appears to have a root (total absorption) at an angle of approximately 48.9 degrees. Finally, we note the importance of taking the discretization scheme into account in order to obtain realistic practical estimates for R . The real ABC performance is well described by the solid curve in Figure 4.5. For example, at $\lambda=10$ grid increments, the selected ABC scheme does cause less than 5 percent reflection out to ± 75 degrees. This is confirmed by examining the amplitude of the spatial interference patterns caused by boundary reflections. As a function of wavelength, R varies with the inverse square of λ .

It is worth mentioning two more tricks that help cut unwanted reflections from grid boundaries. First, slightly lowering the numerical velocity input to the ABC algorithms causes a refractive decrease in the angles of incidence on the boundary. This lowers the maximum angle of incidence below the unstable region, and, because ABC's generally perform better at lower incidence angles, slightly improves ABC performance. Another means of reducing boundary reflections is to apply mild attenuation along the grid boundaries.¹⁵ Although rarely necessary, attenuation was occasionally applied in combination with the above ABC scheme to improve overall boundary absorption.

Parenthetically, boundary reflections are not always detrimental to the purposes of our simulations. The nearly perfect reflectance of the ABC's at high angles of incidence implies that

¹⁵ Attenuation applied directly over the ABC scheme described here actually creates an instability. This problem is easily avoided by applying the attenuation near but not directly over the grid edges. Reflection from attenuating boundaries can be minimized by keeping it mild and graduating the effect into the boundary. Adding noise to the attenuation coefficients can also help reduce coherent (Bragg) diffraction from regions of layered attenuation.

the grid can function as a waveguide. This means that certain wavefunctions can propagate almost without diffraction across the grid when properly oriented. Although a tradeoff with equal illumination occurs, we will use this behavior to eliminate the near-field interference of the source of the returning echoes in the inverse simulations.

Design of Simulation Grids

For readers interested in applying the same methodology elsewhere, we briefly discuss grid design in the simulations undertaken here. Most (but not all) of this information is well known to seismologists and other specialists is FD wave propagation techniques. Although additional constraints exist, the setup of the grid in any particular simulation is closely analogous to the way that one might arrange an anechoic chamber for real acoustical measurements. Elementary principles are applied in both cases to optimize the measurement of interest.

In single frequency simulations, we usually generate a steady-state response to the source wave. The time required to build up a steady-state response depends on the performance of the ABC's -- the better the boundary absorption, the shorter the required run-time. A general rule-of-thumb for estimating the required steady-state run-time is to allow the wave energy to propagate three times across the longest (diagonal) distance of the grid. With the selected ABC's, it is the author's experience that a steady-state response is usually achieved within two crossings of the longest diagonal.

Where possible, one can attempt to time-gate the pressure records at receiver points so that reflections from the walls do not have time to occur (a common practice in real reverberant environments). However, with the limited size of 3-D grids, time-gating is often impossible. The effects of boundary reflections on the far-field extrapolation errors discussed in the next chapter is an important issue. Tests of the extrapolation results as the surface data evolves from time-gated

to initial boundary interaction to the steady state show that the lowest errors are always achieved by time-gating the data records at the extrapolation surface. Errors rise with the initial boundary interactions, but then decrease again to nearly the time-gated levels as the steady-state is approached.

The accurate simulation of sources is a topic of some importance here. Discrete modeling of an extended source generally breaks down in the immediate vicinity of the source. Instead of trying to model propagation at small scales with the standard algorithms, it is often better to substitute a small analytic source region immediately surrounding the source. Assuming the simulated field is real-valued, this can be done as follows. First, calculate the complex spatial amplitudes of grid points surrounding the source structure; next, multiply the complex amplitudes by $e^{i\omega t}$; finally, use the real part of this product to time-step the nearby points. This technique prevents difficulties associated with the simulation of small and/or phased source structures on the discrete grid.

The extrapolation procedure (see next chapter) is sensitive to errors in both amplitude and phase of the pressure and its normal derivative. Note that two separate sources of error enter from the FD simulation programs:¹⁶ the propagation algorithm causes dispersion errors; and the algorithm used to compute the normal derivative at the extrapolation surface introduces errors. In this chapter we have already discussed the mild dispersion characteristics of the fourth-order propagation algorithm. Maximum phase errors caused by dispersion in a given simulation can be estimated from the angular dependence of the phase velocity (as in Figure 4.2a) and the maximum distances from the simulated source to the grid points at which data is to be extracted.

¹⁶ All FD simulation errors combined, however, contribute a maximum of only about 20 percent to the errors in the extrapolated results of the mathematical patterns tested in Chapter 5.

The accuracy of the normal derivative algorithm in the FD simulation programs is quite crucial. It is difficult to design a normal derivative scheme that is accurate for nearby sources of all types: plane, cylindrical, and spherical. The author found that a superior procedure for computing the derivative is to keep a (complex) three-deep array over each face of the extrapolation surface, and to compute in-place Fourier transforms of the records at these points. The normal derivative may then be accurately computed in terms of centered second-order normal derivatives of the complex magnitude and phase using the transformed values at the surface and adjacent points. Tests of the extrapolation procedure presented in Chapter 5 demonstrate that this derivative scheme is sufficiently accurate to permit placement of the extrapolation surface 3 grid points away from the inhomogeneous tissue/source modeling region of the grid -- which significantly reduces the required dimensions of the extrapolation surface and the FD grid.

Numerical Simulation of Sound Propagation -- Part II

Chapter 5. Boundary Integral Extrapolation Methods

In order to investigate biosonar signal emission from the foreheads of dolphins, it is necessary to simulate the acoustic far-field for various models of tissue and source configurations. However, as discussed in the last chapter, the dimensions of finite difference (FD) spatial lattices are severely restricted by computer memory limitations. In three dimensions (3-D), this restriction limits the spatial extent of the (1.5mm cubic) grids utilized here to the acoustic near-field over the range of wavelengths of interest. One of the most elegant and accurate solutions to this problem utilizes the mathematical relationship between the acoustic field on a surface immediately surrounding a source region and the pressure at other spatial locations. In one sense, this is analogous to reconstructing a 3-D holographic image from the interference field on a 2-D photographic plane. To be precise, we can sum the contributions of infinitesimal surface elements to the field at any particular point in space. It is the homogeneous nature of the surrounding (seawater) medium that allows us to perform this 'boundary extrapolation' of the field, thus reducing the dimensionality of our problem from 3-D to 2-D. The equation describing this relationship, the Helmholtz integral equation, was derived in Chapter 3. In this chapter, we shall discuss relevant aspects of the application of the Helmholtz integral equation to our bioacoustic problem, provide some examples of extrapolated far-field patterns, and then demonstrate the accuracy of the selected numerical method of solution.

The Helmholtz Integral Equation

The Helmholtz integral equation relates the pressure p and the normal derivative of the pressure $\partial p / \partial n$ over a surface S surrounding an arbitrary distribution of sources to the pressure

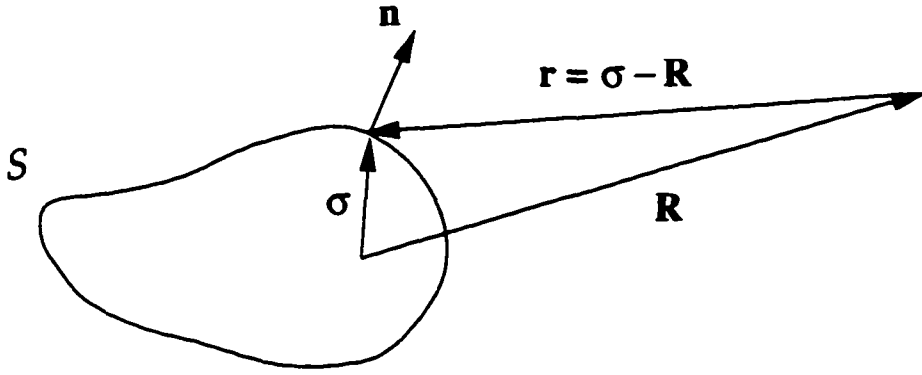


Figure 5.1. Diagram of the geometry assumed by the Helmholtz integral equation (5.1). For our application, field points \mathbf{R} are assumed to lie in the sourceless homogeneous region exterior to the extrapolation surface S which encloses an arbitrarily complex and/or inhomogeneous source volume. Note we have defined the vector connecting the field and surface points to be $\mathbf{r} = \boldsymbol{\sigma} - \mathbf{R}$, and the unit normal vector to surface S to be \mathbf{n} .

$p(\mathbf{R})$ at any field point \mathbf{R} . For points \mathbf{R} lying exterior to the source volume enclosed by surface S (see Figure 5.1), the Helmholtz integral equation has the form:¹

$$p(\mathbf{R}) = - \oint_S \left\{ p(\boldsymbol{\sigma}) \frac{\partial G(\boldsymbol{\sigma}, \mathbf{R})}{\partial n} - G(\boldsymbol{\sigma}, \mathbf{R}) \frac{\partial p(\boldsymbol{\sigma})}{\partial n} \right\} dS(\boldsymbol{\sigma}) \quad (5.1)$$

Here $\boldsymbol{\sigma}$ defines the vector coordinates of surface S , while $\partial/\partial n = \mathbf{n} \cdot \nabla$ denotes the directional derivative along the outward pointing unit vector \mathbf{n} normal to surface S . We have also used the notation $G(\boldsymbol{\sigma}, \mathbf{R})$ for the 3-D free-space Green's function,

$$G(\boldsymbol{\sigma}, \mathbf{R}) = - \frac{e^{ik|\boldsymbol{\sigma} - \mathbf{R}|}}{4\pi |\boldsymbol{\sigma} - \mathbf{R}|} = - \frac{e^{ikr}}{4\pi r}, \quad \mathbf{r} = \boldsymbol{\sigma} - \mathbf{R}. \quad (5.2)$$

Here $k = \omega/c$ is the acoustic wavenumber, where ω is the angular frequency of the field, and c is the (constant) speed of sound propagation at surface S and in the medium external to S .²

¹ This equation has a slightly different form for points lying on, or interior to, surface S . See the derivation provided in Chapter 3.

² No assumptions are made about the distribution of sound sources, speeds, or other properties of materials inside surface S . This source region may be arbitrarily complex. The medium external to S , however, is assumed to be infinite, homogeneous, and sourceless.

The Helmholtz integral equation can be applied to a wide range of 2-D and 3-D wave phenomena including diffraction by arbitrarily complex apertures, calculation of the field scattered from complex objects, and calculation of the field emitted by a complex source. Indeed, an extensive literature has developed on methods for numerical solution of equation (5.1) with applications to acoustical problems.³ In this chapter, we shall only discuss the application of the Helmholtz integral equation to the last of the aforementioned phenomena, namely to calculate the patterns of sound emitted by various 3-D models of delphinid forehead tissues and biosonar signal source locations.

One property of equation (5.1) that is highly propitious for our application is that waves incident on surface S from all sources *exterior* to S contribute nothing to the far-field integral for the internal sources. That is, the Helmholtz integral equation integrates to zero for all exterior source fields.⁴ This means that imperfect absorption at the grid boundaries generally does not cause problems as long as a steady-state solution has been reached over the extrapolation surface.⁵

It is worth emphasizing that we need both the pressure and the normal derivative of the pressure over the surface of extrapolation in order to evaluate equation (5.1). These two fields are

³ See, for example, Baker and Copson (1950), Copley (1967, 1968), Schenck (1968), Tobocman (1984), Seybert *et al.* (1985), Junger and Feit (1986), Seybert and Rengarajan (1987), Cunefare *et al.* (1989), and Hwang and Chang (1991). As a theoretical aside, note equation (5.1) may also be used to compute the time domain solution given time varying surface data by incorporating the retarded time into the Green's function. Indeed, this suggests using a delta function source signal in order to obtain the response over all frequencies simultaneously. Although this theoretically attractive approach was utilized in a 2-D scattering study (Shaw 1974), computer memory limitations in large scale 3-D simulations prohibit storage of time domain surface data (or its full Fourier transform).

⁴ The integrand of equation (5.1) is clearly zero if we insert a spherical wave solution originating from the field point R for the pressure since the pressure $p(\sigma)$ is then proportional to the Green's function $G(\sigma, R)$ everywhere.

⁵ Note, however, that program run-times required to build up the steady-state solution depend on the performance of the absorbing boundary conditions (ABC's). In addition, scattering by our tissue models of the energy from the 'virtual' sources behind the slightly reflective boundaries of the grid can affect our results. Hence ABC efficiency remains important.

not independent, and much of the literature on surface extrapolation methods has focused on the difficulties encountered when only one of these fields is known (a common predicament). However, in our application we obtain both fields from FD simulation of the tissue and source models, as discussed in the previous chapter. We therefore do not encounter the difficulties associated with non-unique surface solutions at eigenfrequencies of the interior problem which have plagued many previous formulations.⁶

Far-Field Formulation of the Helmholtz Integral Equation

Because we are concerned only with calculation of the far-field pressure (to be compared with far-field measurements with live animals), we now develop a form of equation (5.1) valid for $R \gg \sigma$. Writing equation (5.1) out explicitly, we have:

$$p(\mathbf{R}) = \oint_S \left\{ p(\boldsymbol{\sigma}) \frac{\partial}{\partial n} \left[\frac{e^{ikr}}{4\pi r} \right] - \frac{e^{ikr}}{4\pi r} \frac{\partial p(\boldsymbol{\sigma})}{\partial n} \right\} dS(\boldsymbol{\sigma}) \quad (5.3)$$

Performing the usual expansion of $r = \sigma - \mathbf{R}$ in terms of σ and \mathbf{R} , we find:

$$r^2 = \sigma^2 + R^2 - 2\mathbf{R} \cdot \boldsymbol{\sigma} \approx R^2 \left[1 - \frac{2\mathbf{R} \cdot \boldsymbol{\sigma}}{R^2} \right]$$

Hence, for $R \gg \sigma$, we have the approximation

$$r \approx R \left[1 - \frac{\mathbf{R} \cdot \boldsymbol{\sigma}}{R^2} \right] = R - \hat{\mathbf{R}} \cdot \boldsymbol{\sigma} \quad (5.4)$$

where $\hat{\mathbf{R}} = \mathbf{R}/R$ defines the unit vector in the direction of the far-field point. We now apply this result to obtain the following set of approximations:

⁶ See, for example, the discussions on uniqueness in Schenck (1967), Seybert and Rengarajan (1987), Cunefare *et al.* (1989), Hwang and Chang (1991), and Jia *et al.* (1993).

$$\frac{e^{ikr}}{r} \approx \frac{e^{ikR}}{R} e^{-ik\hat{\mathbf{R}}\cdot\boldsymbol{\sigma}} \quad (5.5)$$

and

$$\frac{\partial}{\partial n} \left[\frac{e^{ikr}}{r} \right] = \frac{\partial r}{\partial n} \frac{\partial}{\partial r} \left[\frac{e^{ikr}}{r} \right] = \hat{\mathbf{r}} \cdot \mathbf{n} \left[ik - \frac{1}{r} \right] \frac{e^{ikr}}{r} \approx -ik \hat{\mathbf{R}} \cdot \mathbf{n} \frac{e^{ikR}}{R} e^{-ik\hat{\mathbf{R}}\cdot\boldsymbol{\sigma}} \quad (5.6)$$

We have also used the approximation $\partial r/\partial n = \hat{\mathbf{r}} \cdot \mathbf{n} \approx -\hat{\mathbf{R}} \cdot \mathbf{n}$ here. Substituting equations (5.5)&(5.6) into equation (5.3), we thereby obtain:

$$p(\mathbf{R}) \approx \left[\frac{-e^{ikR}}{4\pi R} \right] \oint_S \left\{ ik \hat{\mathbf{R}} \cdot \mathbf{n} p(\boldsymbol{\sigma}) + \frac{\partial p(\boldsymbol{\sigma})}{\partial n} \right\} e^{-ik\hat{\mathbf{R}}\cdot\boldsymbol{\sigma}} dS(\boldsymbol{\sigma}) \quad (5.7)$$

The factor in parentheses multiplying the integral is merely an overall phase and/or amplitude factor. Because we are only concerned with relative phase and amplitude, we shall drop this factor and consider the result proportional to the far-field pressure:

$$p_{ff}(\hat{\mathbf{R}}) = \frac{p(\mathbf{R})}{\left[\frac{-e^{ikR}}{4\pi R} \right]} = \oint_S \left\{ ik \hat{\mathbf{R}} \cdot \mathbf{n} p(\boldsymbol{\sigma}) + \frac{\partial p(\boldsymbol{\sigma})}{\partial n} \right\} e^{-ik\hat{\mathbf{R}}\cdot\boldsymbol{\sigma}} dS(\boldsymbol{\sigma}) \quad (5.8)$$

Equation (5.8) serves as the starting point for many formulations of far-field diffraction and scattering. It also helps us resolve some puzzling theoretical aspects of wave propagation.⁷

⁷ For example, it can easily be demonstrated from equation (5.8) that Huygens wavelets do not contribute to field points in a direction opposite to their propagation vector. Consider the effect of the 'Huygens wavelet' of form $p(\mathbf{r}) = p_0 \exp(i\mathbf{k} \cdot \mathbf{r})$ incident on infinitesimal area dS of the extrapolation surface from the interior volume. Let dS have outward normal \mathbf{n} . Then $\partial p/\partial n = \mathbf{n} \cdot \nabla p(\mathbf{r}) = i\mathbf{k} \cdot \mathbf{n} p(\mathbf{r})$, and equation (5.8) (retaining the negative sign) tells us that the contribution from the 'wavelet' at dS to the far-field pressure $p_{ff}(\hat{\mathbf{R}})$ is:

$$d[p_{ff}(\hat{\mathbf{R}})] = -(ik \hat{\mathbf{R}} \cdot \mathbf{n} + i\mathbf{k} \cdot \mathbf{n}) p(\boldsymbol{\sigma}) e^{-ik\hat{\mathbf{R}}\cdot\boldsymbol{\sigma}} dS = -ik(\hat{\mathbf{R}} + \hat{\mathbf{k}}) \cdot \mathbf{n} p(\boldsymbol{\sigma}) e^{-ik\hat{\mathbf{R}}\cdot\boldsymbol{\sigma}} dS$$

The directional (or 'obliquity') factor $(\hat{\mathbf{R}} + \hat{\mathbf{k}}) \cdot \mathbf{n}$ varies from a value of 2 when the far-field direction $\hat{\mathbf{R}}$ and the propagation direction $\hat{\mathbf{k}}$ are aligned with \mathbf{n} , to a value of 0 when $\hat{\mathbf{R}}$ points opposite to $\hat{\mathbf{k}}$. That is, the wavefront at surface element dS contributes nothing to field points lying in a direction opposite to $\hat{\mathbf{k}}$. Huygens wavelets therefore do not sum in the direction opposite their propagation. Additionally, the factor $-i$ indicates that Huygens wavelets are re-radiated with a phase advance of 90 degrees.

Details of the Far-Field Integral Calculation

In order to clarify our application of equation (5.8), we now specialize this integral to the +z-face of the rectangular boxes used as extrapolation surfaces in this project. On this face, the outward unit normal vector is simply $\mathbf{n} = \hat{\mathbf{z}}$. The orthogonal coordinates are x and y , so we may take $\boldsymbol{\sigma} = (x, y, z_+)$, where z_+ is the z -coordinate of the +z-face. In terms of the spherical angles θ and ϕ , the components of the far-field unit direction vector $\hat{\mathbf{R}}$ are:

$$\hat{\mathbf{R}} = (\sin \theta \cos \phi, \sin \theta \sin \phi, \cos \theta)$$

Therefore, on this face, we also have:

$$k \hat{\mathbf{R}} \cdot \mathbf{n} = k \cos \theta = k_z \quad \text{and} \quad k \hat{\mathbf{R}} \cdot \boldsymbol{\sigma} = k_x x + k_y y + k_z z_+$$

where the wave vector $\mathbf{k} = (k_x, k_y, k_z)$ is assumed to be oriented in the direction $\hat{\mathbf{R}}$.

Using the above information, the +z-face portion of the surface integral [equation (5.8)] becomes a 2-D Fourier transform (multiplied by a phase factor) of the bracketed quantity inside the following integral:

$$p_{ff}(\mathbf{k})_{+z\text{-face}} = e^{-ik_z z_+} \iint_{xy} \left\{ ik_z p(x, y) + \left[\frac{\partial p}{\partial n} \right] (x, y) \right\} e^{-i(k_x x + k_y y)} dx dy \quad (5.9)$$

This 2-D transform is the standard far-field diffraction result for an aperture lying in the $z = z_+$ plane.⁸ The integral is to be computed over all elements of the +z-face. Similar integrals must be computed over the other faces of the extrapolation surface, and the results summed together. In effect, each face of the rectangular extrapolation surface constitutes an aperture radiating its own

⁸ For the case of an infinitely baffled aperture lying in the $z = z_+$ plane, equation (5.9) can be simplified further by choosing a different Green's function [not equation (5.2)] that satisfies either Dirichlet or Neumann boundary conditions in the aperture plane. Either the pressure or the normal derivative then drops out of the integral in equation (5.9). This approach, however, cannot be used for multiple non-coplanar (and unbaffled) apertures.

far-field diffraction pattern.

Now consider ways of numerically computing equation (5.9). The values of both the pressure p and the normal derivative of pressure $\partial p/\partial n$ at the square mesh of points defining each face of the extrapolation 'box' surface are calculated by the first-stage FD simulation programs. At first glance, it would seem that equation (5.9) can be most efficiently computed by using fast Fourier transform (FFT) methods. However, this 2-D Fourier transform remains a function of k_z . Hence we would need to compute multiple FFT's to span the range of possible values of k_z , or essentially a 3-D FFT. Likewise, the FFT's for the other faces would also be 3-D transforms.⁹ The efficiency of 2-D FFT's is therefore not attainable in this application. Also, FFT's computed for functions on a discrete spatial lattice generate exact results only at the wavevector components of the reciprocal lattice. However, it is necessary to be able to compute the integral for arbitrary orientations of the wavevector. For these reasons, it was decided not to utilize FFT's.

Another way of computing equation (5.9) is to simply pull p and $\partial p/\partial n$ outside of the integral. The integration then becomes a simple sum over the surface elements of the values of p and $\partial p/\partial n$ (assumed constant over each element) multiplying the remaining integrals (which are easily computable in closed form for the flat, square elements used here). The assumption of constant pressure and derivative values for each element was commonly made up until quite recently,¹⁰ although it merely constitutes the zeroth order approximation. Unfortunately, this approach produces unacceptably large error magnitudes within the range of wavelengths required for our application.

⁹ One could sum the resulting 3-D FFT's together, and then search the transform space over the spherical (or ellipsoidal) surface of appropriate wavevectors. However, different surface edge-lengths (transform lengths) and wavevector magnitudes would make this search procedure difficult to generalize.

¹⁰ See, for example, the CHIEF and CHIEF88 extrapolation and scattering packages first developed for sonar applications discussed in Schenck (1967).

A more accurate way of performing the integration is to model the values of p and $\partial p/\partial n$ over the entire surface with continuous polynomials.¹¹ This approach allows one to compute a high-order approximation to the integral over each surface element. The method selected for the present simulations was to model the pressure and pressure derivative data with bicubic polynomials over each face of the extrapolation surface. By construction, the bicubic interpolating polynomials have continuous zeroth, first, and second derivatives, but no cross terms.

For example, say we are modeling the pressure over each element of the $+z$ -face of the extrapolation surface. Since the orthogonal coordinates over this face are x and y , the pressure p is modeled over the m th element using the bicubic form¹²

$$p_m(x,y) = a_0 + a_1x + a_2x^2 + a_3x^3 + a_4y + a_5y^2 + a_6y^3 \quad (5.10)$$

Likewise, the normal pressure derivative $\partial p/\partial n$ is modeled as

$$\left[\frac{\partial p}{\partial n} \right]_m(x,y) = b_0 + b_1x + b_2x^2 + b_3x^3 + b_4y + b_5y^2 + b_6y^3 \quad (5.11)$$

The pressure and the normal derivative are actually complex quantities, so the real and imaginary parts of each are modeled separately. The coefficients a_i , b_i for each element can be computed using standard bicubic interpolation routines. Plugging these bicubic expressions for the pressure and the normal derivative into equation (5.9), the integral over each element of the surface can now be computed to third order in closed form. While computationally intensive, this technique produces consistent and accurate results within a broad range of simulation parameters, as we

¹¹ This approach is equivalent to what is commonly referred to as the technique of 'isoparametric elements'. See, for example, Lachat and Watson (1976), Rizzo and Shippy (1977), or Seybert *et al.* (1985).

¹² Bicubic natural splines were selected simply for convenience and computational efficiency. As the error analysis will demonstrate, the absence of cross terms does not cause problems. The cubic terms may compensate somewhat for the lack of rotational symmetry of the bicubic form. A generalized quadratic form with one $(x \cdot y)$ cross term may perform as well if not better, and would reduce the number of coefficients by one.

shall demonstrate.

Before presenting some examples of computed far-field patterns, it is worth discussing certain computational details. First, most interpolation techniques perform better inside the data domain -- that is, away from the edge-data where derivative information is least accurate. The use of 'natural' bicubic splines causes interpolation errors to increase around the perimeters of the faces of the extrapolation surface. This problem is easily remedied, however, by storing an extra row of data around the faces in the FD simulation programs. It can be shown that natural bicubic splining of the slightly enlarged dataset gives excellent results within the original domain of the face data.

Second, depending on the geometrical shape of the extrapolation surface and how the integral summations are structured, various symmetries can be exploited to reduce the amount of required computation. In the programs written for the present application, a factor of two speedup was obtained by simultaneously computing the integral for the component of the wavevector reflected about the face of the surface being extrapolated.

Finally, evaluation of the extrapolation integral requires double precision (64 bit) arithmetic because of the division by the fourth power of the wave vector components that results from inserting the bicubic forms of the interpolated data [equations (5.10) and (5.11)] into equation (5.9). This also means that far-field directions having vanishing wave vector components cannot be computed. This problem is easily avoided, however, by introducing small offsets whenever \mathbf{k} lies in an axis plane.

Examples of Extrapolated Far-field Emission Patterns

In order to familiarize readers with the results of the extrapolation process, Figures 5.2 and 5.3 illustrate far-field emission patterns computed for two simple source configurations. Figure

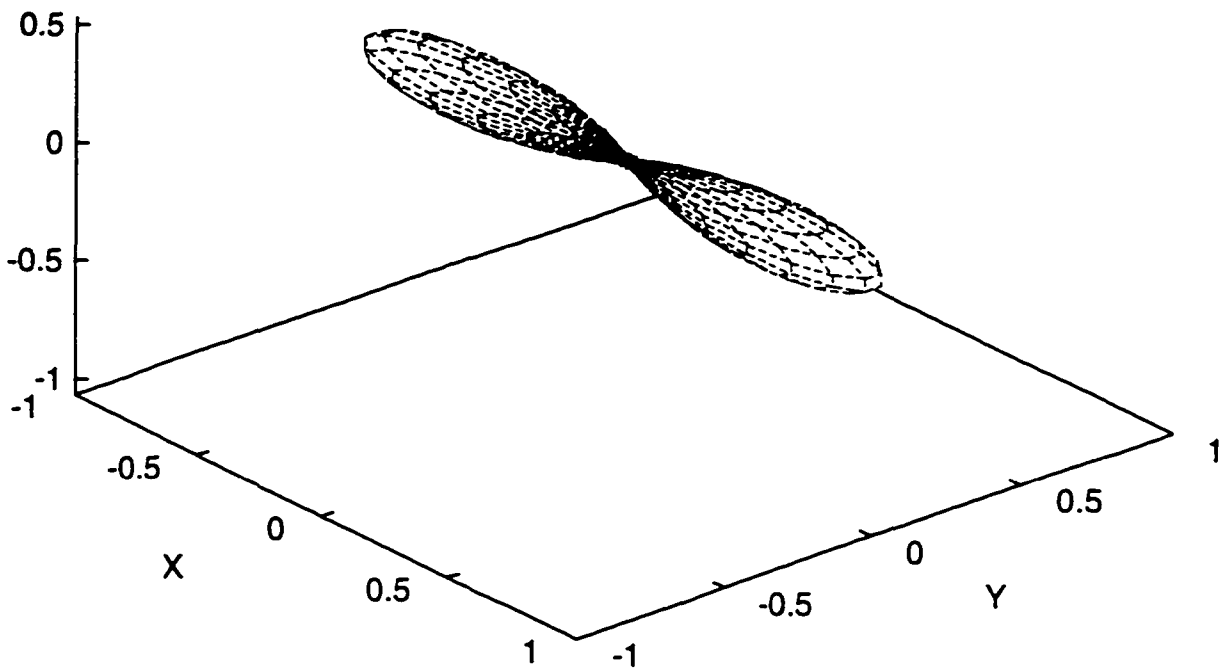


Figure 5.2. Plot of the computed far-field emission pattern of a square (unphased) transducer of side-length 2.0λ . The normalized far-field intensity is plotted for 7200 directions in spherical polar projection.

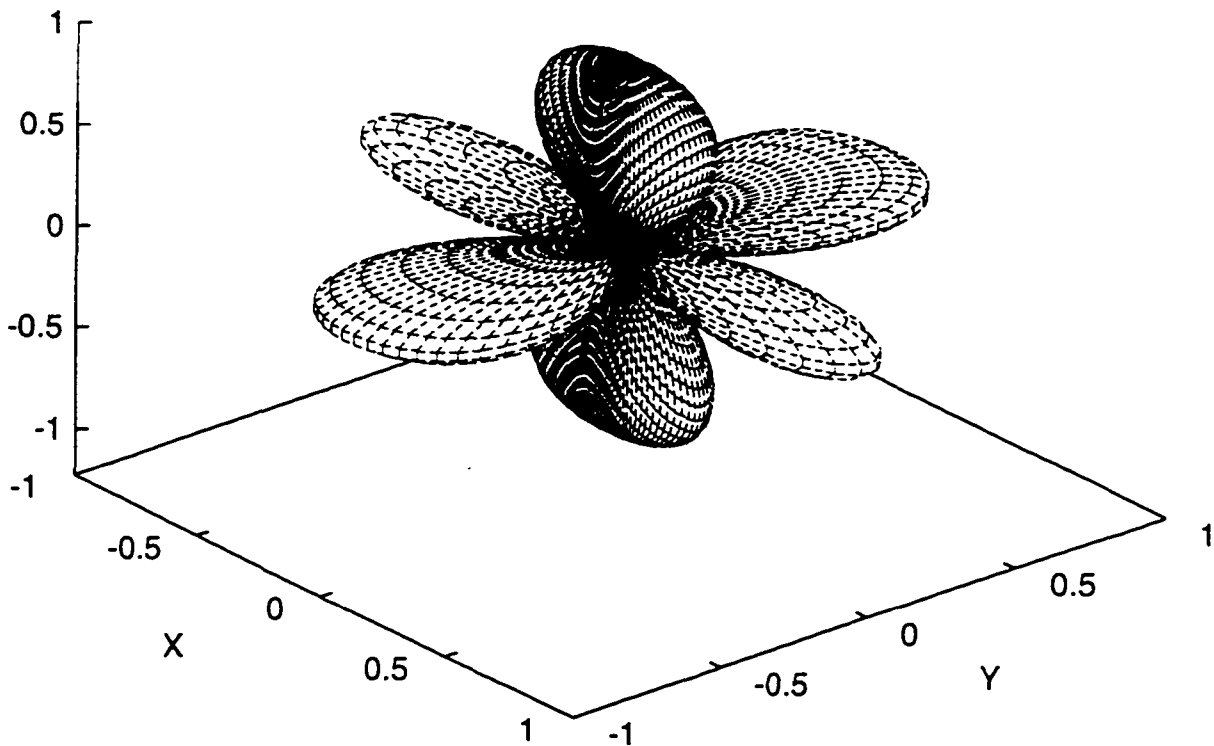
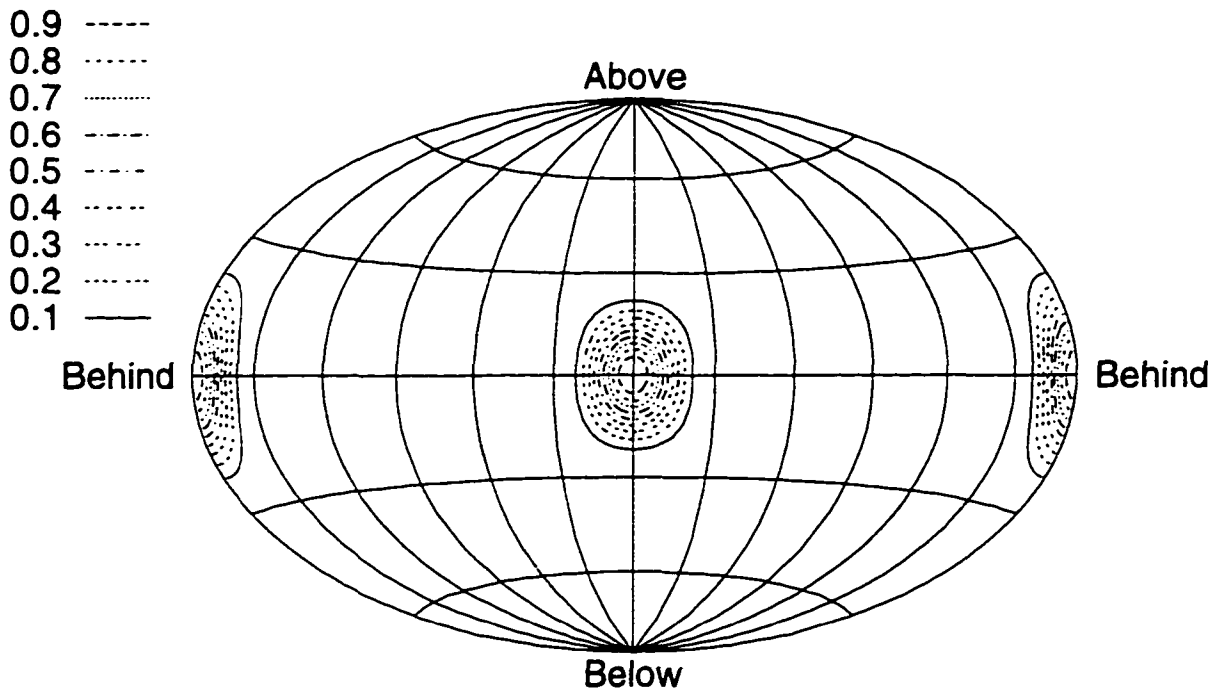
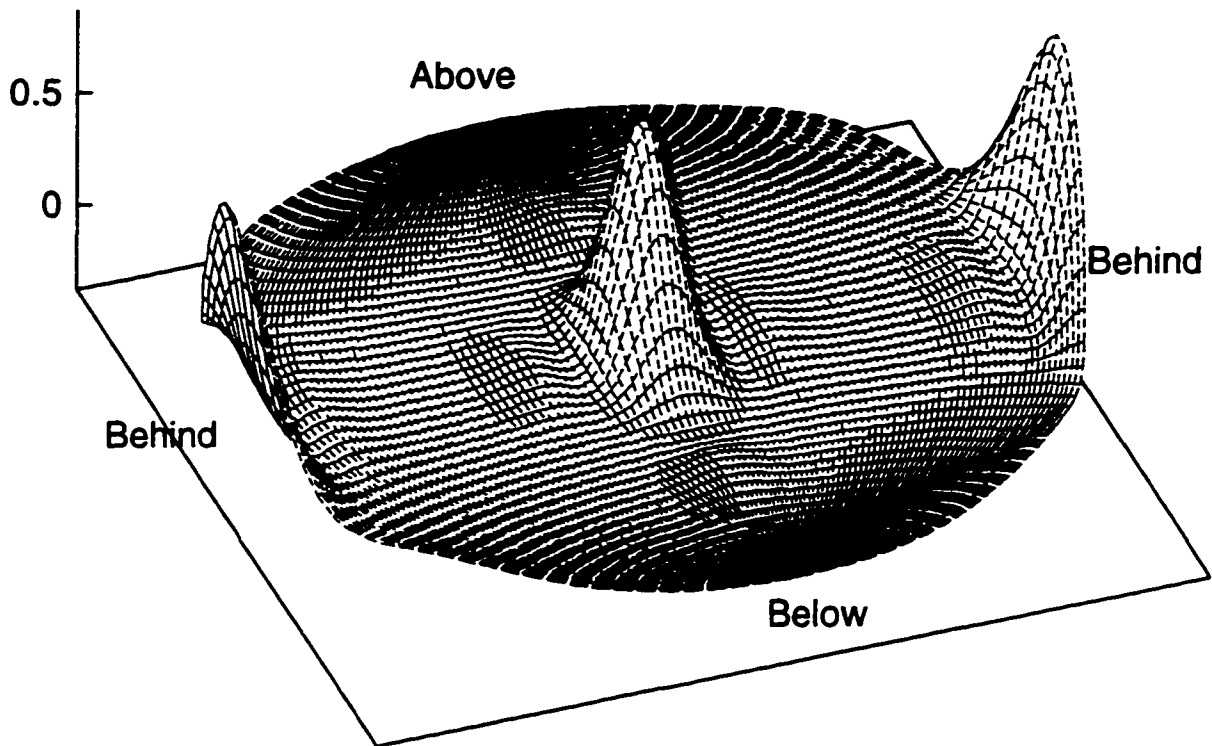
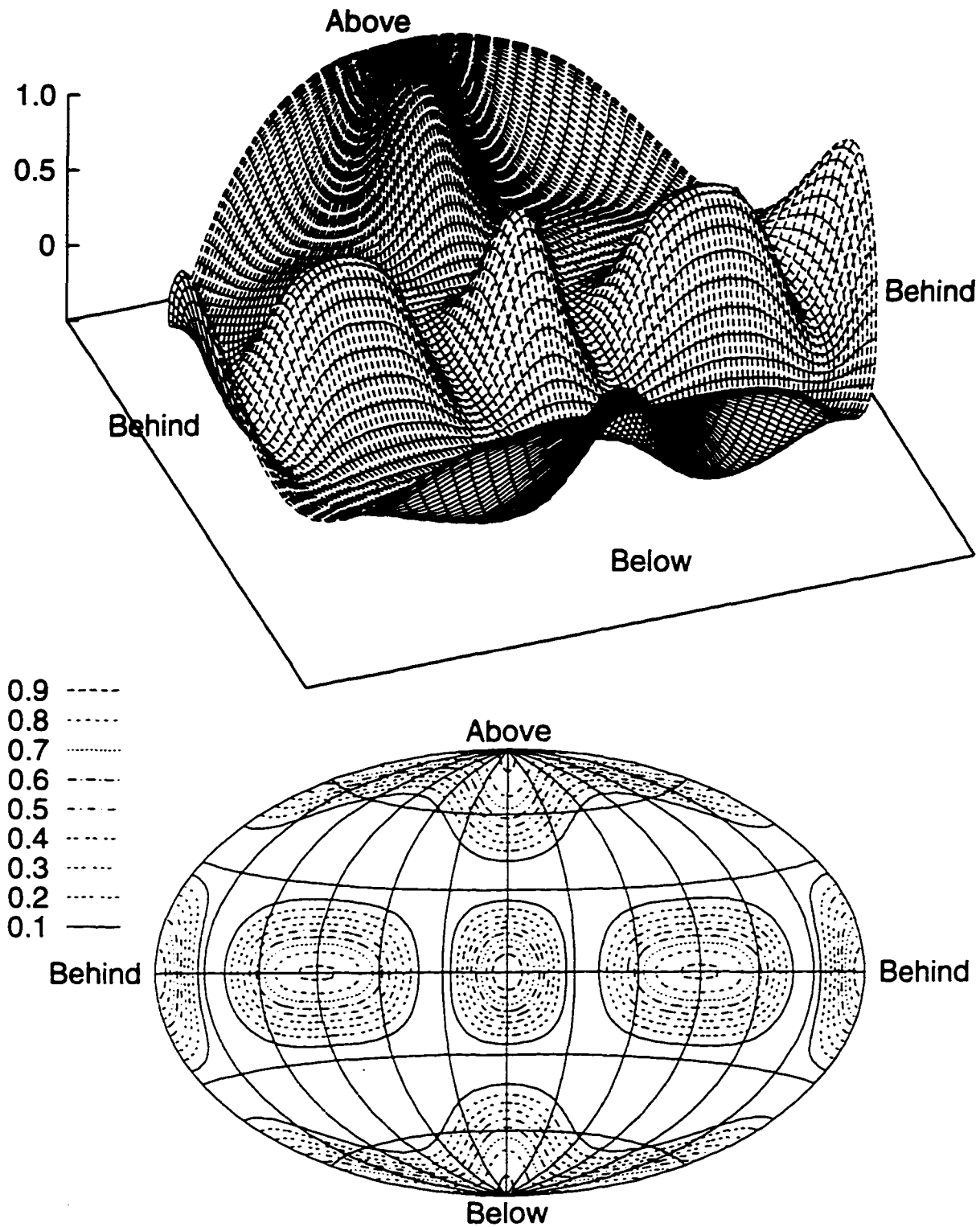


Figure 5.3. Plot of the computed far-field intensity pattern emitted by four coherent point sources in a square configuration. The normalized far-field intensity is plotted for 7200 directions in spherical polar projection.



Figures 5.4a-b. Alternate representations of the transducer emission data in Figure 5.2. Figure 5.4a (upper) is a perspective view of a global mapping of the data with height indicating intensity, while Figure 5.4b (lower) is a contour plot of the same data projected down into the plane of the global map. (See Figure 5.6 for explanation of the global equal-area mapping of emission directions used here).



Figures 5.5a-b. Alternate representations of the square configuration point source emission data in Figure 5.3. Figure 5.5a (upper) is a perspective view of a global mapping of the data with height indicating intensity, while Figure 5.5b (lower) is a contour plot of the same data projected down into the plane of the global map. (See Figure 5.6 for explanation of the global equal-area mapping of emission directions used here).

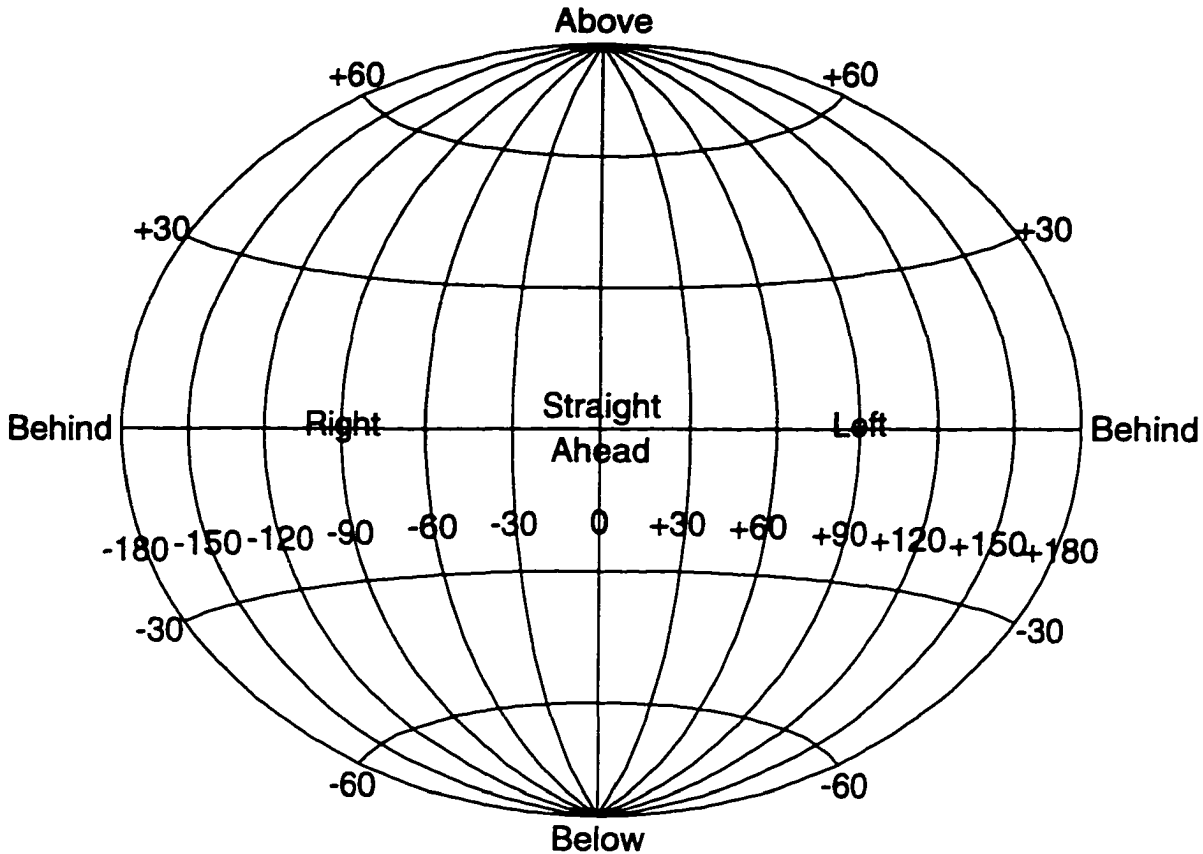


Figure 5.6. Diagram explaining the azimuthal equal-area global mapping of emission angles used in Figures 5.4a-b and 5.5a-b, and in the biosonar emission pattern results of Chapter 7. Note that the viewer orientation here is looking back at the emitter (center map) from a position forward of the emitter. Note also that vertical angle θ and horizontal angle ϕ are both defined to be zero in the forward (center map) emission direction.

5.2 plots the far-field intensity pattern produced by a square (unphased) transducer of side-length 2.0λ (transducer lying in the $x=0$ plane, $\lambda=10$ grid increments). The $20 \times 40 \times 40$ surface pressure and normal derivative data was generated by FD simulation and then input to the extrapolation program. The (normalized) squared magnitude of the far-field pressure computed for 7200 directions was plotted in spherical polar projection to create the diagram. Similarly, Figure 5.3 plots the far-field intensity pattern emitted by four coherent point sources in a square configuration (sources in the $x=0$ plane, separations $S_y=S_z=.9\lambda$, $\lambda=10$ grid increments). The basic idea is that far-field patterns can be computed for virtually any configuration of sources and/or materials that

can be accurately modeled on the FD simulation grid. We shall see below that the errors for these computed patterns are quite small.

Although 3-D polar plots of emission data are dramatic, they do not permit rapid examination of the pattern over all spherical angles. For this reason, we now illustrate two additional ways of visualizing the emission data that will be utilized in Chapter 7. Both of these alternate representations make use of an azimuthal equal-area global mapping of the emission directions (please see explanation in Figure 5.6). Figure 5.4a is a perspective view of a global mapping of the same data in Figure 5.2 with height indicating intensity, while Figure 5.4b is a contour plot of this same data projected down into the plane of the global map. Similarly, Figure 5.5a plots intensity as height in a global mapping of the data in Figure 5.3, while Figure 5.5b contours the same data projected onto the global map. Once understood, these alternate representations provide an excellent means for rapid examination of the far-field data over all angles of emission.

Analysis of the Extrapolation Procedure Errors

Errors can enter the extrapolation results at four different levels. First, the tissue and source model may be inaccurate or incomplete (see discussion of models in Chapter 6). Second, the first-stage FD simulations contribute errors, either from grid dispersion or incomplete boundary absorption (see discussion in Chapter 4 and below). Third, the discrete scheme used to calculate the normal derivative at the extrapolation surface in the FD simulation programs contributes errors (discussed in Chapter 4 and below). Finally, the numerical extrapolation procedure generates errors. We now quantify this final source of errors as well as the errors introduced by FD simulation and the discrete normal derivative.

The accuracy of the selected method of extrapolation can be demonstrated by examining the difference between mathematically calculated patterns for simple source configurations and the

numerically extrapolated versions. In order to define performance measures here, let us assume that the mathematical far-field distribution (normalized to unity maximum amplitude) has the spherical angular form $p_0(\theta, \phi)$ while the computed version is $p_{ff}(\theta_i, \phi_i)$ calculated for the $i = 1, N$ far-field directions (θ_i, ϕ_i) .

An important 'global' measure of the accuracy of the computed pressure is the integrated root mean square error in pressure magnitude E_{rms} , given by

$$E_{rms} = \left[\frac{1}{4\pi} \int_{\theta=0}^{\pi} \int_{\phi=0}^{2\pi} \left[|A_{ff} p_{ff}(\theta, \phi)| - |p_0(\theta, \phi)| \right]^2 \sin\theta \, d\theta \, d\phi \right]^{1/2}$$

$$\approx \left[\frac{\sum_{i=1}^N \left[|A_{ff} p_{ff}(\theta_i, \phi_i)| - |p_0(\theta_i, \phi_i)| \right]^2 \sin\theta_i \, \delta\theta_i \, \delta\phi_i}{\sum_{i=1}^N \sin\theta_i \, \delta\theta_i \, \delta\phi_i} \right]^{1/2} \quad (5.12)$$

The discrete sum form of E_{rms} is a very good estimate of the average error per unit solid angle provided that the density of computed far-field directions samples the mathematical distribution well. An arbitrary (real) constant A_{ff} has been included in front of the computed pressure $p_{ff}(\theta, \phi)$ in equation (5.12) because $p_{ff}(\hat{\mathbf{R}})$ in equation (5.8) is merely proportional to the desired pressure. To construct the best match between the mathematical and computed distributions, we determine A_{ff} using least-squares error minimization. E_{rms} is minimized by choosing

$$A_{ff} = \frac{\int_{\theta=0}^{\pi} \int_{\phi=0}^{2\pi} |p_{ff}(\theta, \phi) p_0(\theta, \phi)|^2 \sin\theta \, d\theta \, d\phi}{\int_{\theta=0}^{\pi} \int_{\phi=0}^{2\pi} |p_{ff}(\theta, \phi)|^2 \sin\theta \, d\theta \, d\phi}$$

$$= \frac{\sum_{i=1}^N |p_{ff}(\theta_i, \phi_i) p_o(\theta_i, \phi_i)| \sin\theta_i \delta\theta_i \delta\phi_i}{\sum_{i=1}^N |p_{ff}(\theta_i, \phi_i)|^2 \sin\theta_i \delta\theta_i \delta\phi_i} \quad (5.13)$$

A second measure of the accuracy of the computed pressure is simply the maximum error E_{max} in magnitude between the calculated and computed distributions, or

$$E_{max} = \text{Max}_{i=1,N} \left[|A_{ff} p_{ff}(\theta_i, \phi_i)|^2 - |p_o(\theta_i, \phi_i)|^2 \right]^{1/2} \quad (5.14)$$

For computed patterns that are directional (peaked in some direction), another performance measure is the error in the angular positioning of the maxima. This error is important in assessing the significance of the angular beam peak data in the forward simulations. We shall label this error E_{angle} , and define it to be the angular deviation (in degrees) between the directions of the maxima of the computed and the mathematical distributions.

As a final measure of the accuracy of the computed directional distributions, we will include both the computed and the theoretical directivity indexes. The directivity index DI characterizes the intensity of any particular maximum in the pattern relative to the total emitted power. Let the maximum of an emitted far-field pressure distribution $p(\theta, \phi)$ be p_{max} . Then DI is defined to be

$$DI = -10 \text{Log}_{10} \left[\frac{1}{4\pi} \int_{\theta=0}^{\pi} \int_{\phi=0}^{2\pi} \left| \frac{p(\theta, \phi)}{p_{max}} \right|^2 \sin\theta d\theta d\phi \right] \quad (5.15)$$

As with the definition of E_{rms} , we may substitute a discrete summation for the integral provided our computed distribution samples the emitted field 'well'. Our results will demonstrate, however, that it is not necessary to sample the emitted distributions extremely finely to obtain accurate data here. As long as the peak emitted pressure is accurately determined, the discrete version

of equation (5.15) gives remarkably close estimates of DI even for rather sparsely sampled distributions.

Errors in Point Source Patterns

First consider the computed patterns of point sources. In this case, errors represent deviations from the expected isotropic distribution. The behavior of these errors as a function of wavelength, of the location of the source point within the volume enclosed by the extrapolation surface, and of the dimensions of the extrapolation surfaces is critical to this investigation. Figure 5.7 plots both E_{rms} and E_{max} as a function of wavelength for a point source located at the center of a $20 \times 20 \times 20$ extrapolation surface. The surface data was generated by FD simulation and then extrapolated for $N=1800$ far-field directions. Note that both E_{rms} and E_{max} decrease with approximately the inverse square of the wavelength. Note also that the average or 'global' error E_{rms} rises to only about 1 percent at a wavelength of 10 grid increments. The maximum local error E_{max} appears to remain larger than E_{rms} by roughly the same ratio for all wavelengths. This maximum error usually lies along one of the 'fast' (1,1,1 or equivalent) lattice directions, and we therefore expect better accuracy for forward biosonar beam results. Although one can reasonably argue that the errors for wavelengths smaller than 10 grid increments would still permit significant quantitative investigation, it was decided to limit the use of the extrapolation procedure to wavelengths equal to or greater than 10 grid increments. A secondary reason for imposing this lower wavelength limit was that the single-frequency emission patterns generated here become sharply peaked with multiple interference lobes at higher frequencies, making the patterns more difficult to characterize.

Next consider the dependence of the point source errors on the location of the source within the volume enclosed by the extrapolation surface. Figure 5.8 plots E_{max} and E_{rms} as functions of

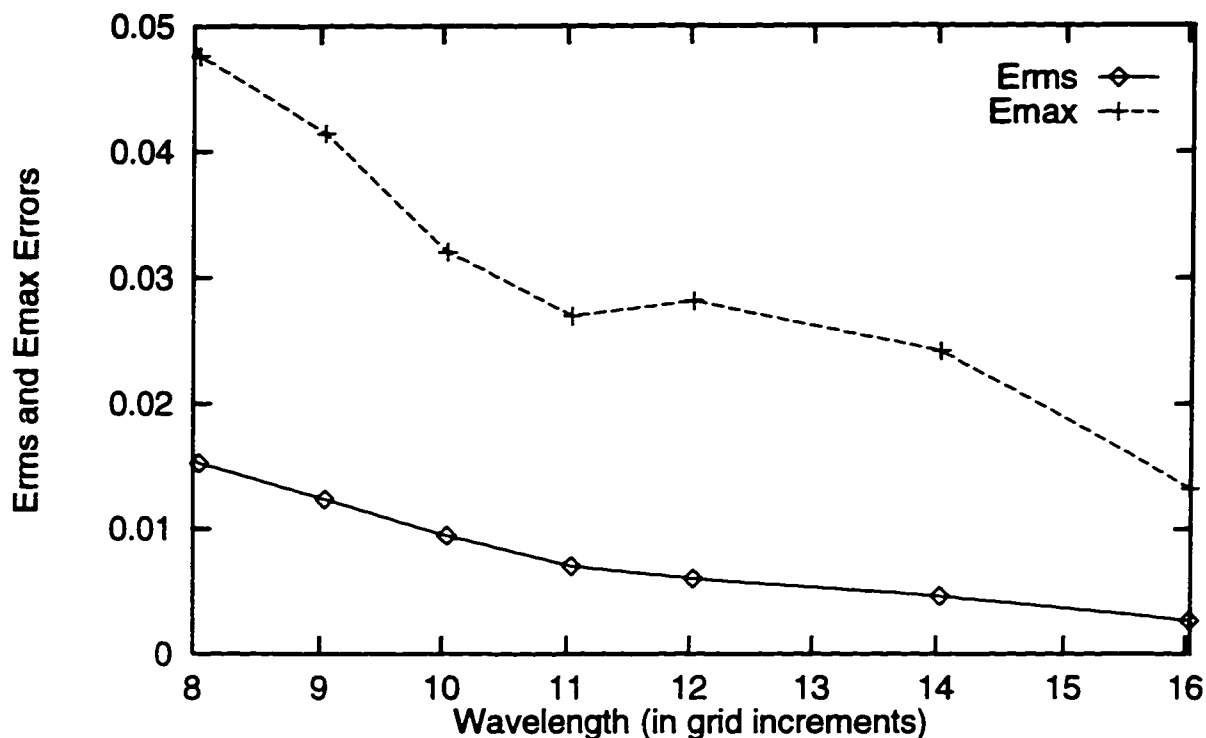


Figure 5.7. Plot of the integrated root mean square error E_{rms} and the maximum error E_{max} as functions of wavelength for a point source located at the center of a $20 \times 20 \times 20$ extrapolation surface.

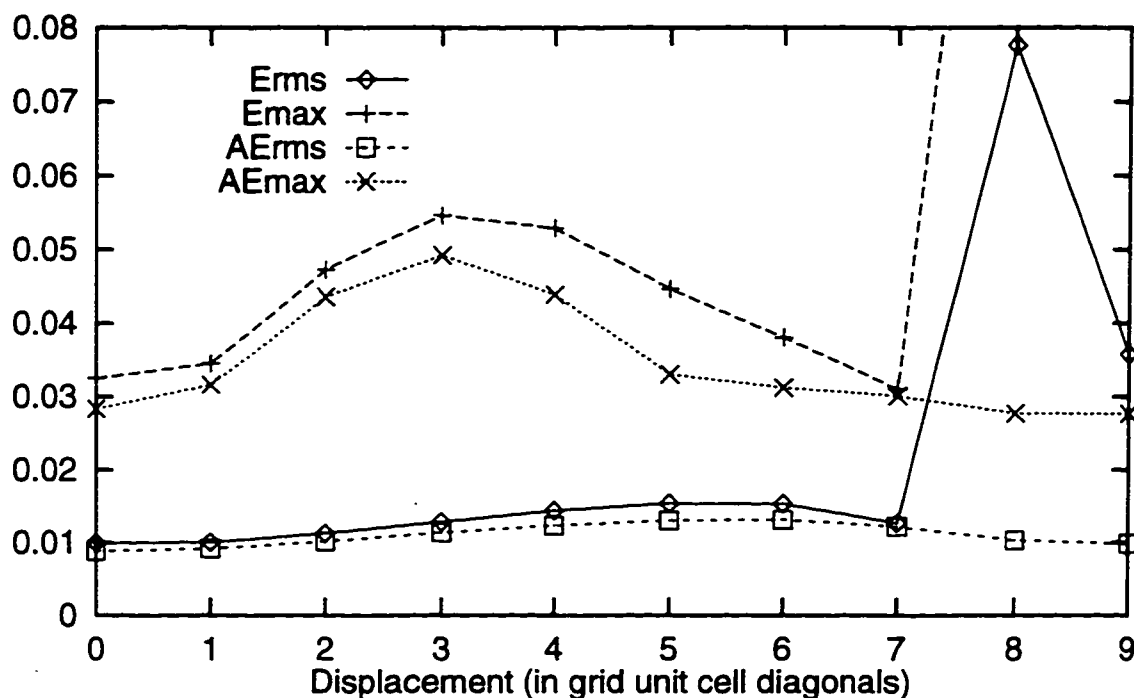


Figure 5.8. Plot of E_{rms} and E_{max} as functions of the displacement (in unit grid cell diagonals) of the point source from the center of a $20 \times 20 \times 20$ extrapolation box along the box diagonal for $\lambda = 10$ grid increments. (The last data point is one grid increment from the corner of the extrapolation box). Also plotted are E_{rms} and E_{max} (curves labelled AE_{rms} and AE_{max}) for the same source displacements and extrapolation box size, but inputting analytic data to the extrapolation program instead of simulated data.

the displacement of the source from the center of a $20 \times 20 \times 20$ extrapolation box along the box diagonal for $\lambda=10$ grid increments. It is significant that neither E_{rms} nor E_{max} increases sharply until the source is within 3 grid increments of the extrapolation surface (the surface is at a displacement of 10 grid unit cell diagonals from the box center along any box diagonal). These errors also decrease with approximately the inverse square of the wavelength, as in the previous figure. Also plotted in Figure 5.8 are E_{rms} and E_{max} (curves labelled AE_{rms} and AE_{max}) for the same source displacements and extrapolation box size, but inputting analytic point source surface data to the extrapolation program instead of simulated data. Note that, up until the source is within 3 grid increments of the extrapolation surface, all simulation errors combined (which include both FD propagation and the discrete normal derivative errors) increase E_{rms} and E_{max} by a maximum of only about 20 percent over the analytic errors. This means that both the FD simulation and the normal derivative schemes are quite adequate, and justifies locating the extrapolation surface only 3 points outside of the inhomogeneous modeling region of the grid.

Next we plot the dependence of E_{max} and E_{rms} on the side-lengths of cubic extrapolation surfaces in Figure 5.9 for centered point sources and $\lambda=10$ grid increments. Note that E_{rms} increases very slowly with extrapolation box size while E_{max} quickly reaches a maximum and appears to become independent of (or even decrease with) box size. The same behavior occurs with non-cubic boxes. Again, by inputting analytic point source surface data into the extrapolation program instead of FD simulation data, it can be shown that all FD simulation errors contribute only about 10 percent of these centered-source E_{rms} and E_{max} errors at all box sizes. In addition, as long as double precision (64 bit) arithmetic is used in evaluating the surface integral, numerical error does not appear to alter the results within the range of extrapolation surface dimensions used in this study.

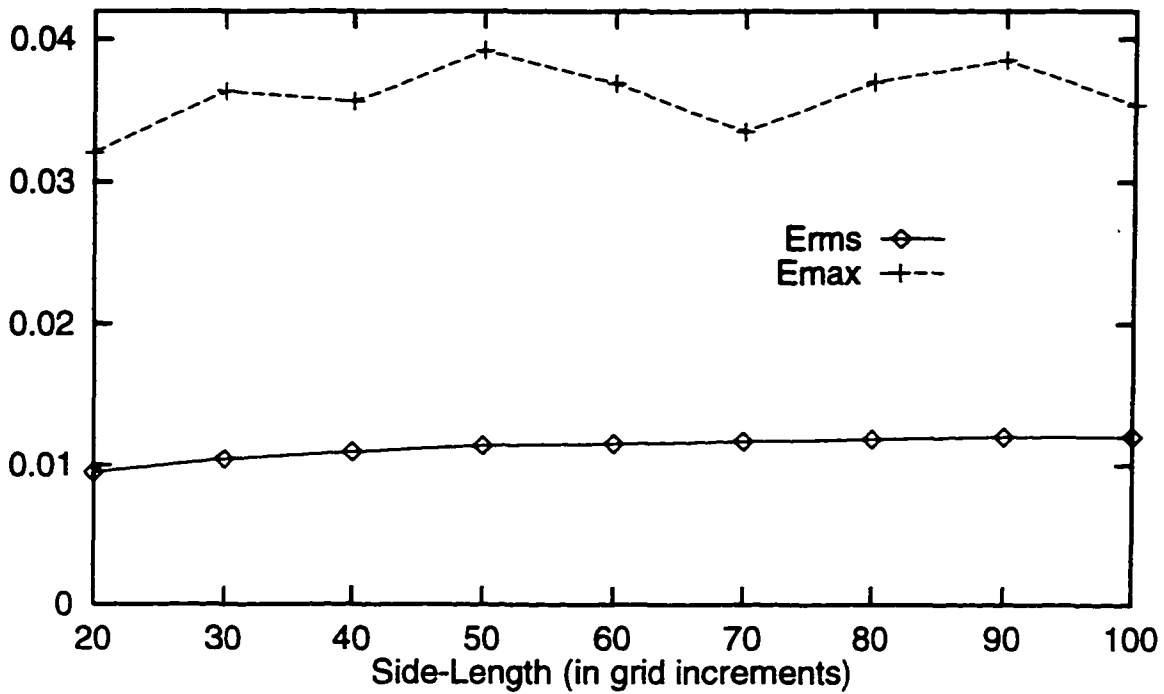


Figure 5.9. Plot of the dependence of E_{rms} and E_{max} on the side-lengths of cubic extrapolation surfaces for centered point sources and $\lambda=10$ grid increments.

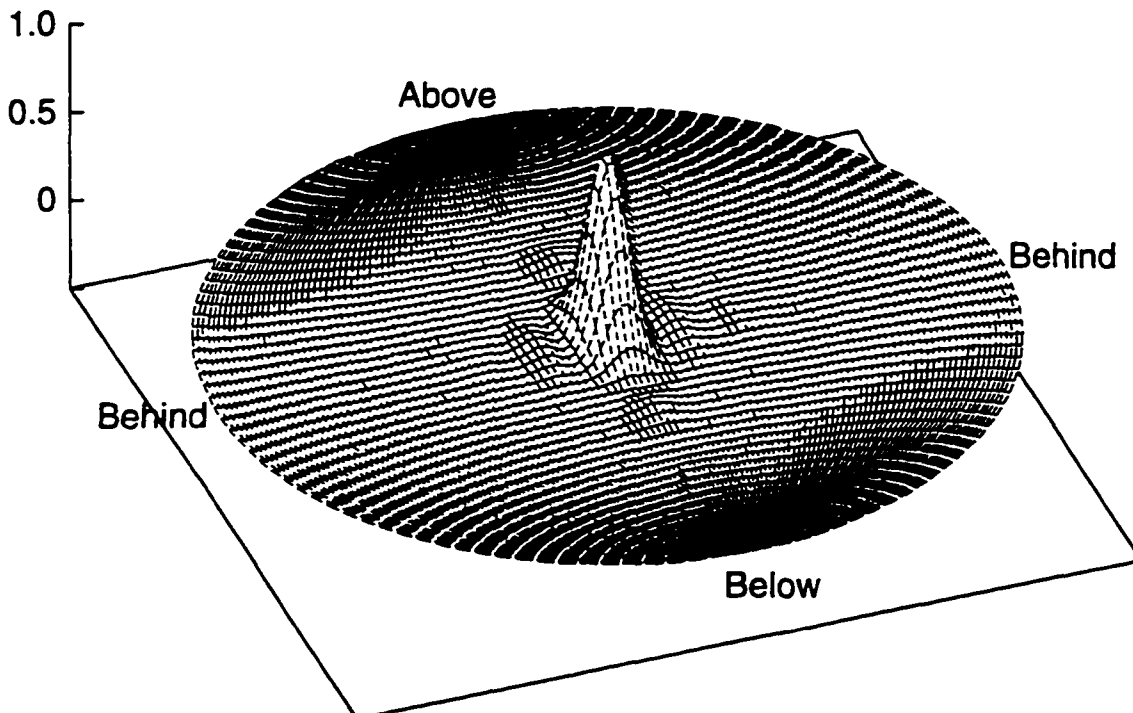


Figure 5.10. Emission pattern (height indicates intensity) of the flat square transducer of side-length 3.0λ used to study angular extrapolation errors. In this case, the source was unphased (main beam steered into the forward direction).

Errors in Directional Source Patterns

Let us now consider errors for directional source patterns. For the far-field pattern of the 2-lambda square transducer shown in Figure 5.2, the global and local errors were $E_{rms}=.00090$ and $E_{max}=.00296$. For the pattern of four point sources in a square configuration shown in Figure 5.4, the global and local errors were $E_{rms}=.00953$ and $E_{max}=.02119$. Figure 5.11 tabulates E_{rms} and E_{max} for the computed patterns of a phased 3-lambda square transducer (used below for angular tests). Like the single point source pattern errors discussed above, these small error magnitudes depend mildly on box size and on source positioning within the extrapolation surfaces, while decreasing sharply with wavelength.

Finally, we inspect the angular errors for highly directional source patterns. For these tests we shall utilize a 3-lambda square transducer at $\lambda=10$ grid increments emitting into a half-space (transducer mounted on a semi-infinite rear baffle). Phasing the source allows us to steer the main lobe in any direction we choose. We then study angular pattern errors by comparing the direction of the extrapolated pattern maximum to the mathematically expected direction. Figure 5.10 illustrates the sharply peaked far-field pattern for this source when unphased (main lobe in the forward direction). The density of far-field points computed here corresponds to 3 degree separations in latitude and longitude between sample points (7200 points total).

Figure 5.11 tabulates the results of the angular tests for seven directions of source phasing. Listed in the table are the vertical and horizontal angles (θ_0, ϕ_0) into which the beam was steered (angle definitions in Figure 5.6), the error E_{angle} (in degrees) in the direction of the computed maximum, the global and local errors (E_{rms} and E_{max}) for the distributions, and the computed and theoretical directivity indexes DI_{comp} and DI_{theory} for the main lobes of the patterns. As these results demonstrate, the accuracy of the extrapolation program's peak localization routine is quite

Directional Pattern Errors : 3-Lambda Square Transducer					
θ_0, ϕ_0 (degrees)	E_{angle} (degrees)	E_{rms}	E_{max}	DI_{comp}	DI_{theory}
0, 0	.0059	.00046	.00176	17.57	17.565
0, 27	.1201	.00106	.00586	16.96	16.956
27, 0	.1158	.00107	.00605	16.96	16.956
27, 27	.0868	.00147	.00689	16.59	16.554
0, 45	.1420	.00142	.00771	16.02	16.010
45, 0	.1382	.00142	.00787	16.02	16.010
45, 45	.3471	.00199	.01266	14.91	14.800

Figure 5.11. Tabulated angular error results for seven directions of source phasing of a 3-lambda square transducer. Listed are the vertical and horizontal angles (θ_0, ϕ_0) into which the beam was steered, the error E_{angle} in the direction of the computed maximum of the distribution, the global and local errors (E_{rms} and E_{max}) for the patterns, and the computed and theoretical directivity indexes DI_{comp} and DI_{theory} for the main lobes of the patterns.

good.¹³ The maximum angular positional error varies approximately linearly with the density of far-field sampling, and increases somewhat as the beam moves away from the global equator. However, even in the polar directions (upwards and downwards), E_{angle} only increases to a magnitude of approximately 1 degree. In addition, these results demonstrate excellent characterization of main lobe directivity. Finally, we note that both global and local errors (E_{rms} and E_{max}) remain small even for such sharply peaked distributions.

The magnitude of the errors exhibited in these tests demonstrate a level of accuracy for the extrapolation process that is quite sufficient for the purposes of this investigation. The combined accuracy and efficiency of FD simulation used in conjunction with the boundary extrapolation techniques discussed in this chapter permit us to conduct highly realistic 3-D modeling of the acoustical roles of the dolphin's forehead and lower jaw tissues in the chapters ahead.

¹³ Peaks are localized by computing a finer grid of far-field directions around the maximum direction of the primary sampling grid. Bicubic splining of the data on this finer grid permits application of a simple zero-gradient search routine.

Chapter 6. Acoustic Modeling of Delphinid Tissues from X-Ray CT Data

In the last two chapters we have demonstrated the small error magnitudes of the numerical techniques for simulation of sound propagation utilized in this study. The validity of the results of these simulations therefore depends mainly on the accuracy and appropriateness of the tissue models employed. In this chapter, it will be demonstrated that remarkably accurate acoustical models of the density and velocity of mammalian (including delphinid) tissues can be constructed from x-ray computed tomographic (CT) data. Much of this information is new and will be of quite general interest to researchers in bioacoustic or ultrasonic tissue modeling. We now discuss several aspects of the models utilized in this study including: choice of delphinid species; the nature of x-ray CT data and model construction using this data; acoustic characteristics of biological tissue; soft tissue and bone density and velocity mappings from CT data; and modeling of the dolphin's air sacs.

Choice of Delphinid Species

While the techniques presented here are directly applicable to all x-ray CT scanned species of odontocetes, available funding and time restricted the current investigation to a single species. The common dolphin is, however, a good representative of the typical forehead anatomy of members of the family Delphinidae having an intermediate-to-moderate value of soft-tissue asymmetry (Cranford 1992). The topology of the skull, the upper nasal sacs, the lower jaw fats, and the posterior melon terminus (MLDB) complex in the common dolphin is quite similar to the topology found in the spotted dolphin (*Stenella attenuata*) and the bottlenose dolphin (*Tursiops truncatus*). For the purpose of confirming the results of the earlier 2-D simulations conducted with *Delphinus* (Aroyan 1990, Aroyan *et al.* 1992), and as a means of demonstrating the effec-

tiveness of the techniques presented in this thesis for 3-D bioacoustic modeling, it is sufficient to examine a single species. The potential for novel insights to be gained from the application of these techniques to other species shall be firmly established.

X-ray CT Source Data

Complete 3-D data on delphinid forehead anatomy has only recently become available through the application of noninvasive medical scanning technologies in studies of cetacean morphology and physiology.¹ Both magnetic resonance imaging (MRI) and x-ray CT imaging techniques provide excellent volumetric data on tissue configuration. MRI is slightly better for discriminating soft tissue types, while x-ray CT is generally superior for clear demarcation of interfaces between tissues of differing densities (such as between bone and soft tissue). However, because of information about tissue mass density contained in x-ray attenuation coefficients (discussed below), CT scans constitute more appropriate data for bioacoustic simulation. Little information can be extracted directly from either type of scan regarding tissue sound velocity, but density information in the CT source data will allow us to indirectly generate surprisingly accurate velocity information.

X-ray CT scanners measure the attenuation of x-rays within small volume elements (voxels) of the scanned material. This attenuation results mostly (95 percent) from Compton scattering by atomic electrons, and measured attenuation coefficients are therefore closely related to the density of electrons in the scanned material. Because the density of electrons and protons is always the same, and the nuclei of the low-Z atoms of interest to biochemistry (except for Hydrogen) contain approximately the same number of neutrons and protons, the electron density is approximately half the nucleon density and is therefore very nearly proportional to mass density. For a broad

¹ See, for example, Cranford (1992, 1988), Ketten and Wartzok (1990), and Mackay (1988).

range of tissue types, single-energy x-ray CT attenuation coefficients can be mapped linearly to mass density with errors of ± 5 percent or less (Henson *et al.* 1987).

X-ray CT data contains several potential sources of error (see Cann 1988). The primary error in the attenuation data is caused by variation of effective beam energy with sample thickness, normally referred to as 'beam hardening'. This is a consequence of the fact that the Compton scattering cross section decreases with increasing x-ray energy for typical scan voltages (80-140 kV). Because the lower energy components of the beam are attenuated more strongly, the effective beam energy increases with sample thickness. The CT scan used in this project was performed on a GE 9800 scanner which apparently incorporates beam hardening correction software.² Further processing of the CT data to correct for beam hardening did not appear necessary since internal 'cupping' of the data over approximately 6 centimeters of plexiglass (specimen registration frame) was only of order 0.6 percent. Secondary errors are caused by 'partial-volume' sampling. This occurs, for example, when the scanned volume elements straddle a sharp tissue interface, effectively blurring the interface. We will therefore utilize interface sharpening corrections in the mapping process. Neither machine calibration nor fluctuations in x-ray tube irradiance appeared problematic in this dataset.

For this project, an x-ray CT scan of the head of a male (body length=1.92m) common dolphin, *Delphinus delphis*, was provided by Dr. Ted Cranford of the Naval Command Control and Ocean Surveillance Center, RTD&E Division in San Diego.³ After interpolation, CT numbers were mapped to a 1.5mm cubic propagation grid as a density field (see below). A novel CT-to-velocity mapping was then generated indirectly based on measured acoustic parameters of mammalian and unique odontocete tissues (see below).

² T.W. Cranford, personal communication.

³ The animal scanned was identified as specimen D4 in Cranford (1992).

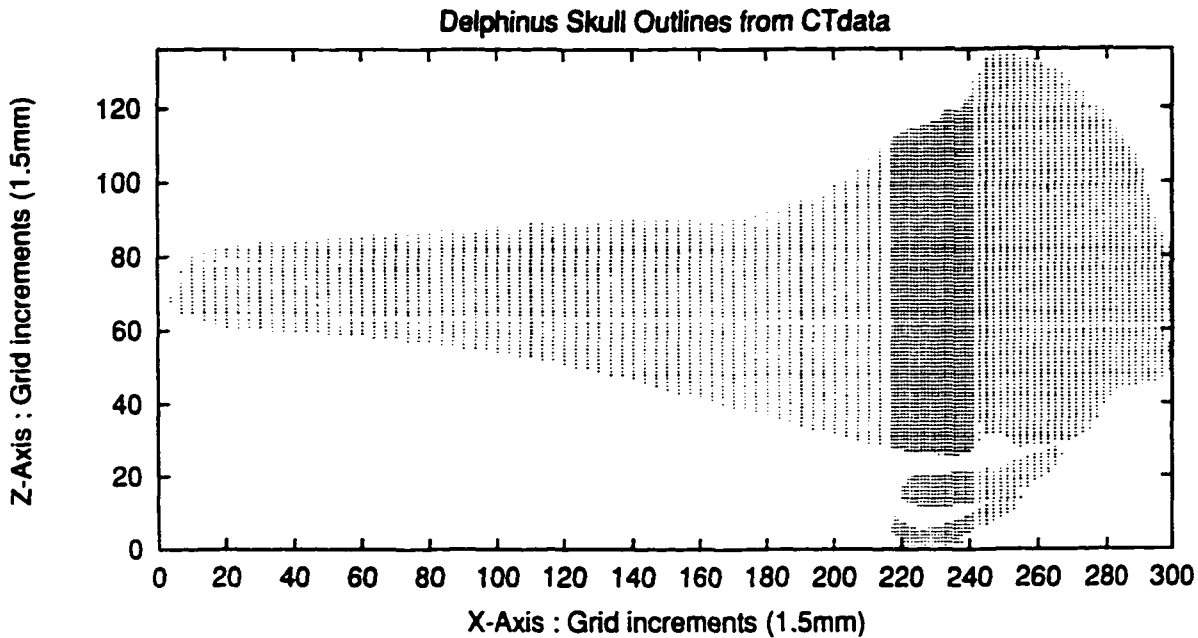


Figure 6.1. A projection into the x - z plane of all CT datapoints with values above the threshold for bone (300 HU) illustrating the spacing of the y - z planes of the original *Delphinus* dataset. The spacing of the original planes varies from 5.0mm over the rostrum, to 1.5mm over the narial/MLDB region, to 3.0mm over the posterior cranium.

The spacing of the scan planes varied in the original CT dataset from 5.0mm over the rostrum, to 1.5mm over the narial/MLDB region, to 3.0mm over the posterior cranium. Each scan plane consists of a 320x320 voxel transverse sectional image on a 1.5mm square grid. Thus scanned voxel volumes vary from 11.25mm^3 , to 3.375mm^3 , to 6.75mm^3 . An x - z projection of all datapoints with CT values above the threshold for bone (300 HU) is shown in Figure 6.1 to illustrate the y - z planes of the original *Delphinus* dataset.⁴ For the purposes of FD simulation, the original data was linearly interpolated (only) in the x -direction to planes spaced 1.5mm apart (hence to a 1.5mm cubic grid).⁵ A higher order interpolation did not appear necessary because of the smooth surfaces of the *Delphinus* rostrum. A plot of bone threshold contours in every 12th plane

⁴ Please note that a right-handed coordinate axis system is assumed in the present analysis of this CT dataset which differs from Cranford (1992).

⁵ Use of the original dataset without interpolation would have produced artifacts at all but the lowest frequencies simulated.

(1.8cm apart) of the interpolated dataset is shown in Figure 6.2. Note that the data has been rotated 180 degrees about the z-axis to make the positive x-axis point in the direction of forward emission. Note also that the y-axis is directed to the left of the animal while the z-axis points upward in all representations used in this thesis.

The information contained in the CT data may be visualized in many different ways. For example, Figure 6.3 illustrates an isosurface within the volumetric data at the CT value threshold between soft tissue and bone. The figure is thus a 3-D visualization of the surface of the dolphin's skull. Modern visualization packages permit extraordinary flexibility in viewing such volumetric data.

Acoustic Characteristics of Biological Tissues

Broadly speaking, soft biological tissues are acoustically quite similar to seawater, with densities and velocities varying roughly 10 and 15 percent, respectively, from those of seawater. They exhibit little (order 3 percent) anisotropy of velocity, and small longitudinal wave attenuation coefficients (roughly order 0.1 dB/cm at 100kHz) which, unlike water, increase linearly with frequency (Johnston *et al.* 1979). As with water, the acoustic velocity in soft tissues varies with temperature. For soft tissues other than fat, the rate of change dc/dT is of order +1 m/s/°C at 37°C. For mammalian fats (including odontocete melon and lower jaw lipids), however, dc/dT is of order -3 m/s/°C at 37°C (Bowen *et al.* 1979, Litchfield *et al.* 1979).

Bony tissues, again speaking broadly, have densities and velocities roughly twice those of seawater, with specific values grading from porous cancellous bone to compact cortical bone. The speed of longitudinal waves in cortical bone ranges from about 3200-3700 m/s. Bone matrix can also exhibit significant anisotropy of velocity, with variations as large as 20 percent about the matrix axes. In addition, longitudinal wave attenuation coefficients in bone are roughly an order

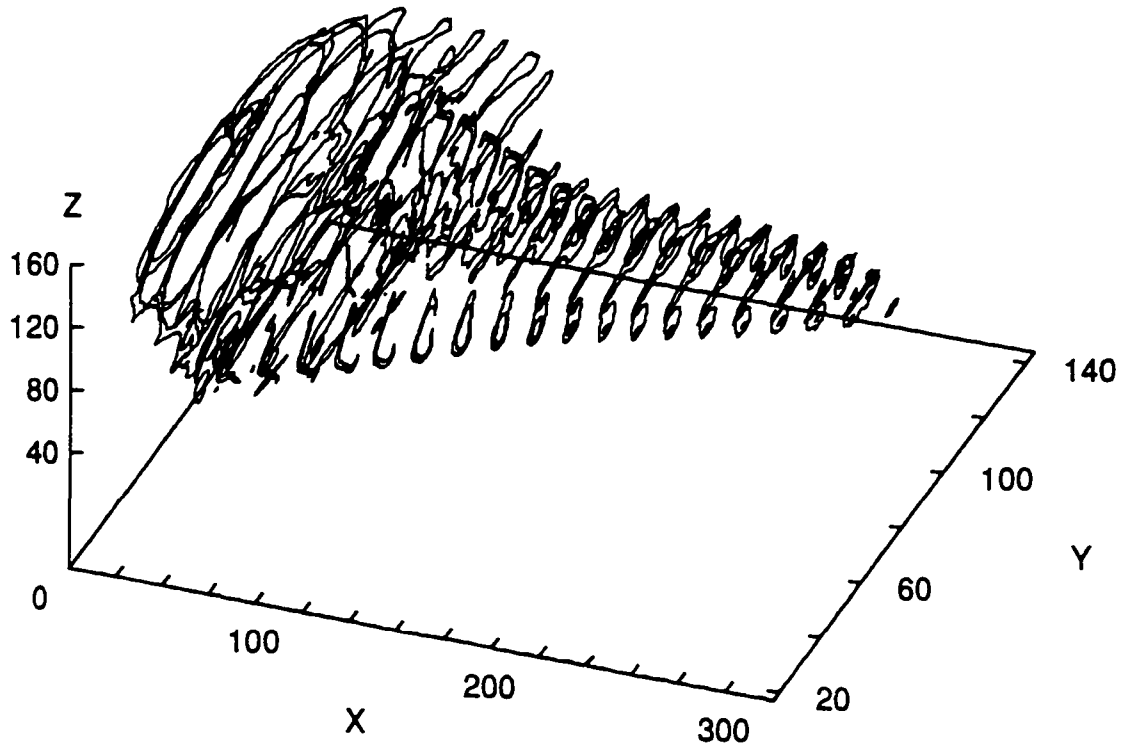


Figure 6.2. A plot of bone threshold contours in every 12th plane (1.8cm apart) of the linearly x-interpolated dataset. Note that the original data has been rotated by 180 degrees about the z-axis to make the positive x-axis point into the direction of forward emission.



Figure 6.3. Visualization of an isosurface at the CT threshold between soft tissue and bone within the interpolated volumetric data. The figure is thus a visualization of the surface of the dolphin's skull.

of magnitude larger than for soft tissue (of order 1.0 dB/cm at 100kHz) (Johnston *et al.* 1979, Goss *et al.* 1980b).⁶

With the exception of fatty tissues, soft biological tissues may be considered as composite materials whose acoustic characteristics are governed by the individual properties of both structural and globular proteins. Soft tissue velocity can be modeled quite accurately as a linear combination of the compositional percentages of structural protein (collagen) and globular protein (Goss *et al.* 1980a). While not quite as precise as this two-component model, it is also true that soft tissue velocity correlates well with density. This is of great importance to the current application because excellent volumetric tissue density information is available from x-ray CT data. As shown below, soft tissue (including fat) velocity can be modeled as an elementary function of density. A slight modification of the near-linear mapping appropriate for all typical terrestrial mammalian soft tissues will then permit us to take account of the unique velocity structure known to exist within the delphinid melon and lower jaw fat bodies.

Model Mappings of Density and Velocity for Soft Tissues and Bone

Numerical implementation of equation (3.2) for acoustic waves in inhomogeneous media requires that we specify both the velocity and density throughout the tissue model. We now describe the mappings utilized in the current simulations, and demonstrate that a mapping from tissue density yields surprisingly accurate tissue velocity data.

Measurement of bone mineral density utilizing single-photon quantitative CT is an esta-

⁶ We mention that the density and velocity of tooth dentine are roughly 10 percent above bone, while values for tooth enamel can rise as high as 75 percent beyond those of bone. Remarkably, the density of the periotic bone of the inner ear in some cetaceans can rise as high as 4-5 g/cc. In the common dolphin, the maximum density of the ear bones is about 2.6 g/cc (Cranford, personal communication). However, the acoustic properties of teeth and cetacean periotic bone do not impact upon the present modeling since only the ear bones and very small portions of the rostrum exceed cortical bone densities in the *Delphinus* dataset.

blished discipline.⁷ Henson *et al.* (1987) demonstrated that a simple linear mapping between CT attenuation values and tissue density was accurate to within ± 5 percent for densities ranging from soft tissue to cortical bone.⁸ In the present study, tissue densities were mapped from CT values using the linear model shown in Figure 6.4.⁹ The CT attenuation scale ranges from -1024 to +2519 Hounsfield Units (HU). The low end of the CT scale (below -138 HU), is below all soft-tissue structures (except air sacs which are handled separately). Since we wish to map the air surrounding the scanned specimen to seawater, we have mapped this lower range to the density of seawater (1.03 g/cc). We will see that this CT-to-density mapping can be shifted by large percentages without appreciable effects on the emitted patterns.

Tissue velocity can in turn be deduced from tissue density as follows. Figure 6.5 plots approximate density and velocity values and ranges for several types of normal terrestrial mammalian soft tissues and delphinid melon lipids measured at 37°C.¹⁰ Note that the velocities for the

⁷ See, for example, Cann (1988), Hunter (1988), or Erlichman (1986).

⁸ Note that the slope of this linear correspondence varies with the effective beam energy of the CT scanner. The GE 9800 scanner used to collect the *Delphinus* data has an effective beam energy of 80 keV (Cranford 1992, Cann 1988). It is possible to reduce tissue density errors to well below 1 percent by using dual-energy CT with phantoms and taking the slightly different electron densities of various tissues into account. The use of phantoms alone with standard CT would establish density mappings of sufficient precision for the purposes of acoustic simulation. The author strongly urges the use of phantoms in future x-ray CT studies of cetaceans.

⁹ Because a phantom was not used in Cranford's *Delphinus* CT scan, the author has made the best use of all available data in establishing this linear map. At least three calibration points are determined by the known density of the inner melon (Varanasi *et al.* 1975), the known density of the plexiglass specimen registration frame, and the maximum density of the dolphin's inner ear bones. Because these points are not exactly colinear, some uncertainty remains in this mapping. However, the primary importance of the CT-to-density mapping actually lies in its use in determining the CT-to-velocity mapping (see below). If the velocity mapping is not altered, the simulations are only weakly affected by large shifts in the tissue density mapping.

¹⁰ Terrestrial mammalian tissue data mainly from Goss *et al.* (1980b), Parry and Chivers (1979), and Lele and Sleefe (1985). Bottlenose dolphin melon lipid velocity data taken primarily from Norris and Harvey (1974) and secondarily from Litchfield *et al.* (1979), since Litchfield *et al.* apparently measured the velocities of their samples after the lipids were extracted from melon and blubber tissues. Extraction of the lipids from connective tissue components probably lowered the values reported for the velocities of the 'outer' and 'under' melon. Both papers agree approximately on the velocity range for the inner melon tissues. Melon and lower jaw lipid densities (down to by weight triglyceride-isovalerate wax ester melon lipid composition, which is similar across the family Delphinidae (Litchfield *et al.* 1975). Although very few measurements of intact tissue velocity, density, and tissue temperature are available, an attempt was made to define the ranges for normal mammalian tissues in Figure 6.5 as 1-sigma variations in the tabulated values.

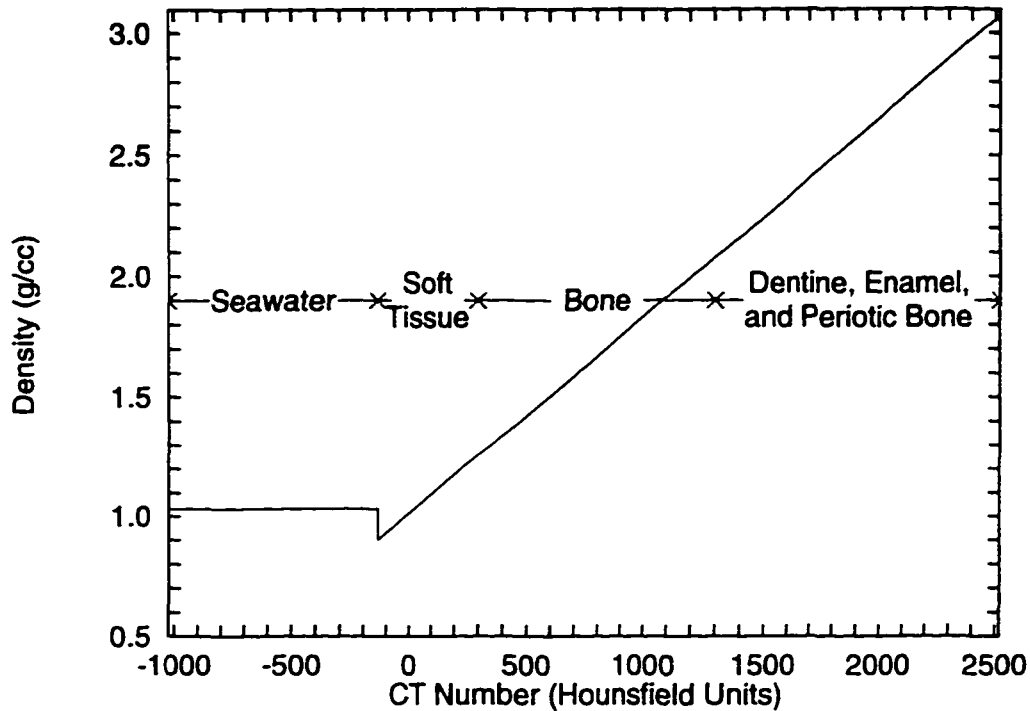


Figure 6.4. Plot of the linear mapping from CT values (in Hounsfield Units) to tissue mass density used in the simulations (based on Henson et al. 1987). Tissue types corresponding to mapped CT ranges have been indicated.

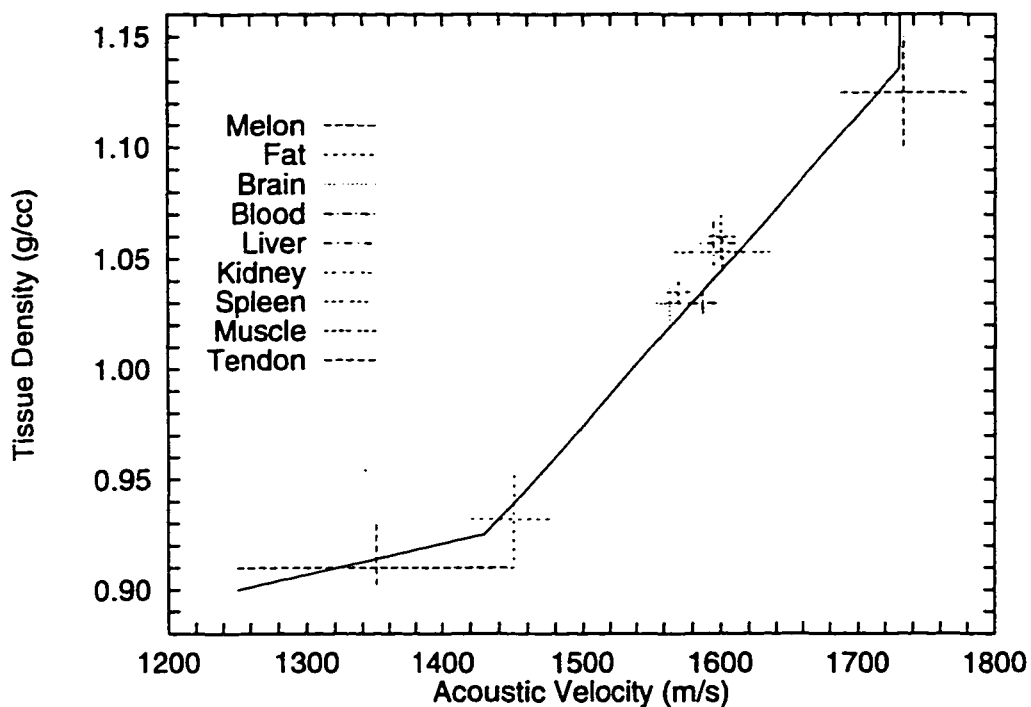


Figure 6.5. Plot of approximate values and ranges of density and velocity for several types of normal terrestrial mammalian soft tissues and delphinid melon lipids measured at 37°C. The solid line indicates the piecewise continuous linear mapping of density to velocity used in the simulations over the range of soft tissues.

normal mammalian soft tissue types can be quite well represented by mapping their density coordinate to a single line drawn from mammalian fat to tendon. However, as discussed in Chapter 2, the lipids of the delphinid melon and lower jaw are chemically and acoustically distinct¹¹ from other body fats and the blubber (which appear to be very similar to the fats of terrestrial mammals). It therefore makes sense to model the velocities of all tissues *except* the melon and lower jaw fats using a single linear mapping from mammalian fat to tendon for the characteristic mammalian tissue range.¹² The unique 'acoustic fats' can then be incorporated by adding a linear extension from typical fat down to the lower melon lipid density and velocity threshold. This piecewise linear mapping of density versus velocity for the soft tissue range is also shown in Figure 6.5, demonstrating that a good correspondence can be achieved between soft tissue velocity and density. The full range of velocities and densities from those of the inner melon lipids to those of the connective tissue theca surrounding the posterior end of the melon are correctly taken into account by this mapping. The current study is the first to correctly model the impedance structure of all tissues including the melon and lower jaw fats (Au 1993, Aroyan *et al.* 1992, Aroyan 1990, Litchfield *et al.* 1979).¹³ Appendix 2 illustrates the detailed density, velocity, and impedance structure of the melon tissue of the common dolphin.

Because the CT-to-density map has already been specified (Figure 6.4), the density-to-velocity map (Figure 6.5) determines the soft tissue CT-to-velocity mapping. The CT-to-velocity mapping across all CT values is pictured in Figure 6.6. The soft tissue range of this mapping

¹¹ See Varanasi *et al.* (1982), Litchfield *et al.* (1979, 1975, 1973), Malins and Varinasi (1975), Varinasi *et al.* (1975). See also discussion in Morris (1986).

¹² Given the magnitude of the variations in mammalian soft tissue densities and velocities, a simple linear model was deemed satisfactory for this initial series of simulations. The acoustic phenomena of interest here result mainly from the velocity shifts between fat, muscle, cartilage, and bone. The magnitude of the soft tissue shifts appears to be adequately represented by a linear model. Higher order mappings are certainly possible, and may permit application of these techniques to areas where greater precision is required.

¹³ The simplicity and accuracy of this approach to modeling the acoustic parameters of normal mammalian tissues has broad ramifications for several areas of bioacoustic investigation, as discussed in Chapter 8.

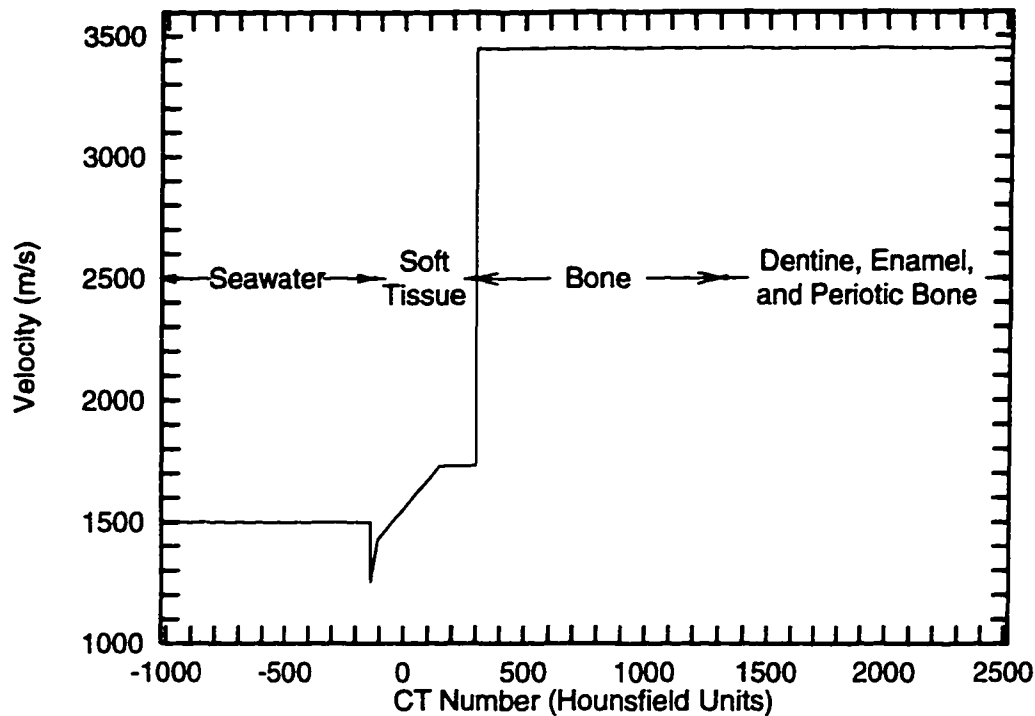


Figure 6.6. Plot of the linear mapping from CT values (in Hounsfield Units) to tissue velocity used in the simulations. This mapping (over the soft tissue range) is implied by the previous two figures. Tissue types corresponding to mapped CT ranges have been indicated.

generates good agreement between Cranford's (1992) plots of CT values through the *Tursiops melon* and Norris and Harvey's (1974) *Tursiops melon* velocity measurements. The low velocity melon core and surrounding tissues for the posterior third of the melon are mapped to the correct measured velocity magnitudes provided one shifts the *Tursiops* CT-to-velocity map approximately 130 HU down from the *Delphinus* map. While tissue velocities for *Delphinus* have not been measured, there seems little reason to doubt that a mapping which is based on the measured acoustic properties of normal mammalian tissues and which works for *Tursiops* will work for other delphinids¹⁴ as well, provided the CT data ranges for each specimen have been properly

¹⁴ Similar triglyceride and isovalerate wax ester lipid mixtures (roughly 60 and 40 percent composition by weight respectively) are found in the melon and lower jaw fats across the family Delphinidae (Litchfield *et al.* 1975). These ratios differ substantially from blubber compositions. Slight variations of the delphinid lipid density and velocity mappings presented in this thesis should be sufficient for modeling the odontocete families Phocoenidae and Monodontidae. The families Ziphiidae, Physeteridae, and Platanistidae, however, may require somewhat different treatments.

determined.

Several aspects of Figure 6.6 deserve discussion. First, the CT range below -138 HU (below all soft-tissue structures except air sacs) is again set equal to the velocity of seawater (1500 m/s). Next, note that soft tissue velocities above tendon (at 150 HU) and up to the bone threshold (at 300 HU) are modeled as a constant 1730 m/s. This was done for several reasons: 1) measured soft tissue velocities do not appear to exceed this value; 2) very little soft tissue can be found in the CT range 150-300 HU; and 3) the lower CT values of the partial-volume blurring of the soft tissue-bone interface appear in this range. Third, note that a large discontinuity in velocity at the bone threshold has been introduced to correct for the CT artifact of partial-volume blurring of the soft tissue-bone interface. The magnitude of this discontinuity correctly differentiates between the velocities of bone and the densest soft tissue.

Finally, note that the velocity above the bone threshold of 300 HU has been modeled as a constant 3450 m/s. A mapping from density to velocity could be constructed for dolphin skull bone,¹⁵ but does not appear to be necessary. Bone velocities do not increase substantially until densities well beyond those of tooth dentine are reached, approaching the high density of enamel.¹⁶ It should be noted that the delphinid skull is predominantly composed of cortical bone, and that most acoustic energy incident from soft tissue is reflected at the bone interface (even in the absence of covering air sacs). As we shall demonstrate in the next chapter, the value of the bone velocity constant can be varied by ± 15 percent without significantly affecting either the position of the source determined by inverse simulation or the emitted far field patterns computed

¹⁵ For example, Lees and Davidson (1979) discussed the correlation of bone velocity with the percentage composition of mineral hydroxyapatite (HAP) crystallites within a more compressible collagen matrix. Because of the difference in the densities of HAP and collagen, this correlation in turn implies a mapping between bone density and velocity.

¹⁶ See, for example, Goss *et al.* (1980b), or Lees and Davidson (1979).

by forward simulation.¹⁷

It should be mentioned that partial-volume blurring of the skin-seawater (skin-air in the CT scan) interface was corrected using a simple technique. CT values for skin normally rise slightly above the inner tissue values (note the slight ridge at the skin surface of the melon in the figures of Appendix 2). However, the partial-volume effect often shifts these values down below seawater values, creating an artificially lowered velocity and density 'skin' around the dolphin tissue model. This problem was corrected by searching for all points at the outer tissue surface that had CT values lower than seawater (-59 HU), and resetting their values to the next neighboring value *inside* the tissue. If the direction of the inner neighboring point is properly chosen, it is improbable that the partial-volume effect also occurred at the inner point.

Finally, note that no attempt was made in the current simulations to correct for tissue velocity dependence on temperature at the skin of the animal. For the following reasons, the author does not believe that this dependence is crucial to the current modeling. For integumental skin tissue itself, the velocity decreases only by about 1 percent (assuming seawater temperature near 20°C), which is a small effect. Although incomplete data exists on bodily temperature distribution, there probably exists a sharp gradient over the first few centimeters of tissue, especially over the blubber layer. Hence, we would expect a blubber velocity increase grading toward the outer skin of maximum magnitude 3 percent over these tissues, still not a large effect. The combined effect possibly makes the seawater-skin-blubber interface series slightly more transparent to sound. However, the net effect of a smooth, localized, and small amplitude distortion of the velo-

¹⁷ There are also technical reasons for modeling the bone velocity as a constant. For stability reasons, the numerical velocity in the finite difference programs is set equal to the highest velocity occurring in the tissue model, and all other velocities are scaled with respect to this maximum. The run times of the FD programs required to achieve a steady state over the grid therefore scale inversely with the value of the highest modeled velocity. Modeling the bone velocity as a constant simplifies these stability and efficiency issues.

city profile moving into the tissue is likely to be small since the total angular refraction of the sound paths remains the same.

Model of the Peribullary and Pterygoid Sinuses and the Nasal Air Sacs

Provided that numerical threshold values are properly chosen, x-ray CT data provides exceptionally accurate information on the 3-D geometry of skull-soft tissue and external soft tissue-air interfaces. The peribullary air sinuses surrounding the dolphin's middle and inner ear complexes, and the pterygoid sinuses, extending within the posterior bones of the palate,¹⁸ are very clearly defined in the CT data. Both were incorporated into the lower jaw hearing simulations and were considered distinct from the upper nasal air sac model.

Air spaces inside soft tissues, however, often suffer distortion in these scans due to postmortem changes. The difficulty of extracting accurate upper nasal sac outlines from postmortem CT data adversely impacts the quality of any nasal sac model proposed here (note also that the uppermost nasal sacs in live animals are reported to be quite mobile during phonation). I therefore have utilized the simplest model of the upper nasal sacs that is supported by the data and previous anatomical studies.

The outlines of the narial air spaces are very clear in the *Delphinus* CT data. The vestibular sacs, however, are only marginally discernable. By extracting all CT data coordinates with values below soft tissue thresholds, the narial sacs and portions of the vestibular sacs may be located in the data. Unfortunately, the inferior vestibules and the premaxillary, nasofrontal, and accessory sacs are not even marginally discernable in this data. Nevertheless, the location of the premaxillary sacs is so well documented in the literature¹⁹ that it was deemed permissible to

¹⁸ See, for example, Fraser and Purves (1960).

¹⁹ See, for example, Green *et al.* (1980), or Dormer (1979).

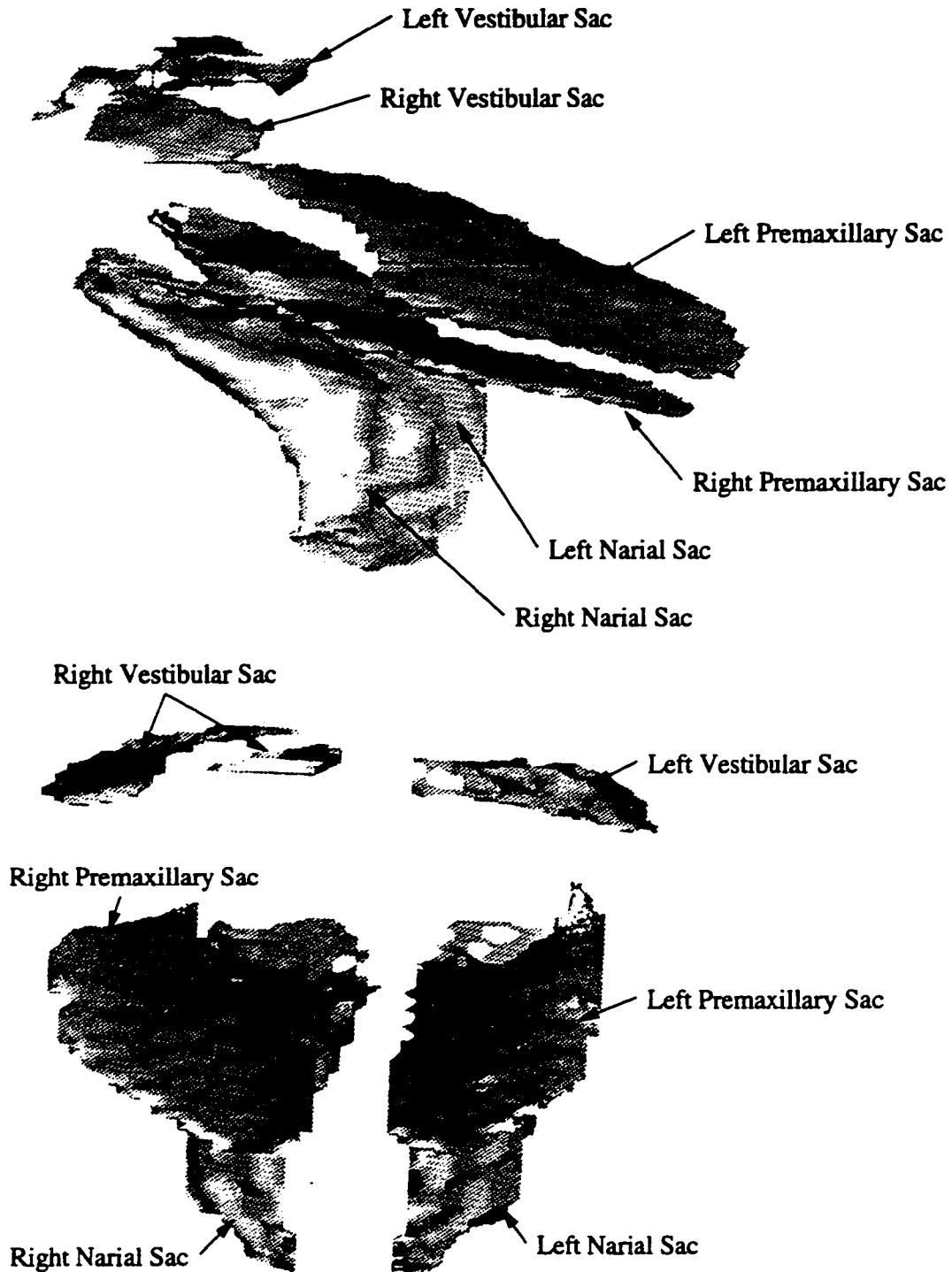


Figure 6.7. Visualizations of the model of the narial, vestibular, and premaxillary air sacs used in the simulations. Upper figure is an elevated right side view of the sac surfaces; lower figure is an elevated front view. Labels identify the individual sacs. Note that the vestibular sacs are incompletely represented in this model (see discussion in text).

include their positions above the premaxillary shelves of the skull in this conservative air sac model. With assistance from cetacean biologists it should be possible to reconstruct a more complete model of the upper nasal sacs. The author decided, however, only to include the narial, vestibular, and premaxillary sacs in the current model. Perspective views of this simplified air sac model are shown in Figure 6.7. Note that several portions of both left and right vestibular sacs are clearly missing from this model. Nevertheless, it was decided not to guess about filling them in. One consequence of this incomplete model is that some of the acoustic energy that would have been reflected forward by more complete sac structures will appear as spurious 'leaks' in upward and backward emission directions.

As in previously reported simulations (Aroyan 1990, Aroyan *et al.* 1992), the air sacs were simulated as 'pressure release' surfaces by setting the pressure to zero at all sac grid coordinates. Note that any possible air-cavity resonance behavior is eliminated by this procedure.

Chapter 7. Results of the Simulations

We now present results of the 3-D simulations for various tissue and source models of the common dolphin, *Delphinus delphis*. Grid layouts, model illustration, and graphical and numerical output are presented after the introductory comments for several cases of interest bearing on both the biosonar emission and reception processes. We shall weave together the results of the inverse and the forward simulations since, although related, each contains different types of information. We will present forward and inverse results for tissue models of the skull-only, of the skull and air sacs, of the skull and soft tissues (including the melon), and then for the skull, air sacs, and soft tissues combined. Finally, we shall present the results of two different types of lower jaw hearing simulations.

7.1. Skull-Only Simulations

The skull-only model was constructed as follows: the density and velocity of points in a selected region of the interpolated CT dataset that were equal to or greater than the bone threshold were computed from the CT-to-density and CT-to-velocity mappings described in Chapter 6. All other points were mapped to background seawater density (1.03g/cc) and velocity (1500m/s) values. The region of the CT dataset that was selected for all of the forehead simulations (including the skull-only simulations) is illustrated by an isosurface at the CT data bone threshold (300 HU) in Figure 7.1 and by bone and skin isosurfaces in Figure 7.2.¹ This tissue region is a rectangular volume having x,y,z side-lengths of 27.0cm, 12.6cm, and 12.6cm. The last few points of the density and velocity grids along the back, bottom, and side edges of the

¹ The full CT dataset was not used here because of computer CPU time and memory restraints. Inclusion of the rostral tip and the remaining tissues is not as important to the forehead simulations as it may appear. Initial simulations with the full CT dataset at half resolution agree very closely with the results of the truncated tissue model shown here.

tissue region were graded back to seawater values in order to reduce spurious reflections at the model boundary.

The grid setup used in all of the forehead tissue inverse simulations (including the inverse skull-only simulations) is diagrammed in Figure 7.3. Note that the front face of the grid is used as a flat source (a simulated transducer) to ensonify the skull with a cosine-windowed² 'echo' at a fixed angle of return. Absorbing boundary conditions were applied to all outer grid edges to absorb reflections, as discussed in Chapter 4.

The primary information obtained from the inverse emission simulation programs is the acoustic energy density [equation (3.3)] within a volume enclosing the upper nasal passages (region labeled 'PSR' in Figure 7.3). The acoustic reciprocity theorem³ tells us that we can reverse the roles of emitter and receiver in any acoustic medium without altering the transmitted signal. Thus, if the dolphin emits an acoustic pulse from within a small region of its tissues and that pulse travels out to be picked up by a distant receiving hydrophone, then the process can be reversed. That is, by propagating a returning plane wave 'echo' backwards into the tissues, we should see 'hot spots' at all potential source locations that could produce far-field beams at that specific frequency and propagation angle. This approach is closely analogous to the use of inverse seismologic simulations to pinpoint the epicenters of earthquakes. In effect, we are seeking to locate the 'epicenter' of the dolphin's biosonar signals. In most cases, the inverse simulations also clearly demonstrate patterns of sound propagation within the tissues, such as channel-

² A cosine-enveloped (in both y and z directions) aperture function was used to reduce the near-field interference of the source transducer. The dual cosine envelope corresponds roughly to the first axial guide-function mode for the grid-grid boundary system, as noted in Chapter 4. Although a tradeoff with equal illumination occurs (which can in turn be corrected by suitably enlarging the grid), the use of this envelope greatly decreases near-field diffraction effects. The energy density at the 'epicenters' found in the inverse simulations is generally between 2 and 3 orders of magnitude above the background variation caused by near-field diffraction and uneven illumination.

³ See, for example, Cook (1996), or Pierce (1980).

ing behavior, etc.

In order to establish positional reference with respect to the soft tissue structures in the inverse simulation data volume (I have labeled this volume the 'potential source region', or PSR for short), Figure 7.4 illustrates a parasagittal slice through the center of the right MLDB complex within the PSR. Several tissue structures have been labeled, but it is worth mentioning that the center of the left MLDB complex lies about 3.3cm to the left and about 0.7cm downward from the center of the right MLDB. Note that the PSR is a rectangular volume having x,y,z side-lengths of 12.0cm, 9.0cm, and 9.0cm. The skull isosurface is included in all PSR diagrams for positional reference.

We now illustrate some of the skull-only inverse simulation results. Figures 7.5-7.8 illustrate the energy density in PSR sections containing the maxima or 'epicenters' for skull-only inverse simulations at frequencies of 25, 50, 75, and 100 kHz. The direction of return propagation in this case was 5° below the negative x-axis, which corresponds to a forward beam direction of $\theta, \phi=5^\circ, 0^\circ$. The patterns of spatial interference caused by reflections off of different portions of the skull surface are clearly evident. Note that the sharpness and complexity of the interference maxima increase (as expected) with frequency. Note also that the positions of the maxima appear below the (right) MLDB and also up against the sharply rising surface of the cranial bone. The maxima lying immediately against the cranium may be caused simply by the process of reflection at hard surfaces, where the pressure amplitude nearly doubles, and the energy density quadruples. This does not necessarily imply source locations at these positions, since any hard surface oriented roughly perpendicular to the incident beam can exhibit such maxima. Indeed, the reader is cautioned against jumping to the conclusion that any one of these single frequency focal maxima is optimal for the animal -- especially for the simpler tissue models. As we shall see, multi-

ple maxima appear in most of the models, although the ambiguity decreases significantly when the air sacs and the soft tissue velocity information are both included.⁴ The reader is urged to examine the overall patterns of maxima for various tissue models before drawing final conclusions.

The positions of these 'epicenters' for several inverse simulations at the four frequencies 25, 50, 75, and 100 kHz are shown in two PSR projections (viewed from the right and the front sides) in Figures 7.9-7.11 for return angles of 10°, 5°, and 0° below the negative x-axis. The maxima up against the skull is shown if it exists and the 'soft tissue' position (not against the skull) of highest energy density for each frequency. The general trends in the positioning of these skull focal positions are clear. First, in the front-back direction, the focal maxima always occur in the region of the upper nasal passages, within a distance of about 3cm (generally less) from the steeply sloped cranium. Second, in the left-right direction, they appear on the right side of the nasal soft tissue region above the bony nares, and not on the left side. Third, the skull-only foci appear either up against the cranium or off of the skull and below the location of the right MLDB. A few of the lower focal positions against the cranium appear to lie within the vertical range of the right nasal plug. All but one of the locations away from the skull appear too high to be considered within the right nasal plug.

Now consider the emission patterns that result from placing point sources at the focal positions of the skull. Figures 7.12-7.15 illustrate the far-field emission distributions computed (using the forward simulation and extrapolation techniques discussed in Chapters 4 and 5) for point sources of frequencies 25, 50, 75, and 100 kHz placed at the 5° inverse simulation focal maxima of highest energy density (the 5° inverse simulation maxima locations were illustrated in

⁴ This is entirely analogous to the situation in inverse seismologic simulations where ambiguity decreases with the accuracy and completeness of the geologic models assumed.

Figures 7.5-7.8 and 7.10). The directions of peak emission (in degrees) and the directivity indexes (in dB) for these patterns are included in the figures. While a fair amount of energy is projected to the sides and upward (note the diffraction rings at the lower frequencies), the skull by itself is capable of forming significant forward beams. The directions of the forward maxima agree nicely with the reversed propagation direction of the inverse simulations, proving that the forward and inverse simulation techniques are symmetrically related.⁵

7.2. Skull and Air Sac Simulations

Figure 6.7 of Chapter 6 illustrated the model of the narial, vestibular, and premaxillary air sacs used in the current simulations. The air sacs are treated as 'pressure release' surfaces in these simulations. We emphasize that the vestibular sacs are incompletely represented in this model, and that several other sacs are entirely absent (see explanation in Chapter 6). However, the narial and premaxillary sacs are presumed to be well represented.

Figures 7.16-7.18 indicate the PSR focal positions (viewed from the right and the front sides) from several inverse skull and air sacs simulations at frequencies of 25, 50, 75, and 100 kHz for return angles of 10°, 5°, and 0° below the negative x-axis. The maxima up against the skull is shown if it exists and the 'soft tissue' position of highest energy density for each frequency. Note again that the focal positions lie in the nasal passage region within a few centimeters of the cranial slope, and on the right side. In addition, the 'soft tissue' foci again seem to lie below the right MLDB, but not so far down as to be considered within the right nasal plug.

⁵ Most of the inverse focal positions are actually somewhat distributed maxima (especially at the lower frequencies). Hence it is expected that placement of a point source at the single grid position of highest energy density will not reproduce the exact forward beam maxima. Use of more of the inverse maxima amplitude and phase information to simulate extended sources in the forward simulations would result in closer agreement.

The far-field emission patterns that result from placing point sources at the focal positions of the skull and air sacs model are shown in Figures 7.19-7.22. Again, these distributions were computed for point sources at frequencies of 25, 50, 75, and 100 kHz placed at the 5° inverse simulation foci of maximum energy density. The peak emission directions (in degrees) and directivity indexes (in dB) for these patterns are included in the figures. Note that a fair amount of energy is still projected in mid-azimuth directions and to the sides, but the air sac model (even though incomplete) is assisting the skull in forming forward beams. The air sacs have the effect of eliminating most of the downward and high upward angle emissions, of slightly narrowing the main lobes, of raising all of the directivity indexes, and of generally moving the pattern peaks closer to the forward direction.

7.3. Skull and Soft Tissue Simulations

For the skull and soft tissue model, the density and velocity of all points within the selected region of the interpolated CT dataset (see Figures 7.1-7.3, and also the figures of Appendix 2) were computed from the CT-to-density and CT-to-velocity mappings described in Chapter 6. Recall that these mappings assign all air CT scan voxels to the background seawater density (1.03g/cc) and velocity (1500m/s) values, so that air sac regions within the forehead soft tissue model are effectively simply 'filled' with seawater. (When the air sac model is added to the forehead soft tissue model, and for the peribullary air sinuses surrounding the middle and inner ear complexes in all of the hearing simulations, points within the air regions are treated separately as pressure release surfaces).

Examination of the inverse simulation results when the soft tissues of the dolphin's forehead are included indicates an astonishing shift in the patterns of acoustic energy flow through the PSR region from the skull-only and skull and air sacs models. Figures 7.23-7.25 illustrate a

series of isosurfaces at the 50%, 30%, and 10% levels of acoustic energy density viewed from both the right side and from above for the case of a 5° inverse 50 kHz simulation. Figures 7.26-7.28 illustrate 50%, 20%, and 10% isosurfaces for a 5° inverse 75 kHz simulation. The patterns no longer look simply like spatial interference caused by multiple reflections from a complex surface. A clear tendency towards collimation or channeling of energy is exhibited by the melon tissues. Energy is strongly channeled in both the vertical and horizontal directions back through a region passing approximately 1cm ventral to the right MLDB complex. Note that this channeling is most pronounced within the posterior throat of the melon (note the narrowing of the energy isosurfaces within the melon throat in the top diagrams of Figures 7.25 and 7.27). Note also that the anterior melon appears to be behaving as a broad lensing element (note the curvature of the wavefronts in Figures 7.25 and 7.28). Examination of the patterns at 25 and 100 kHz (not pictured here) reveals that the channeling efficiency and the complexity of the remaining interference patterns generally increase with frequency as expected. Note finally that interference lobes appear along the propagation channel. A significant amount of energy is reflecting off the steeply sloped surface of the cranium and propagating back out to interfere with the incoming energy. The incoming and outgoing paths do not always appear parallel (especially when viewed from above).

Figures 7.29-7.31 indicate collected PSR focal maxima positions (viewed from the right and the front sides) from inverse simulations at frequencies of 25, 50, 75, and 100 kHz for return angles of 10°, 5°, and 0° below the negative x-axis for the skull and soft tissue model. The maxima up against the skull is shown if it exists and the soft tissue position of highest energy density for each frequency. Again, note the focal positions occur in the nasal passage region within a few centimeters of the cranial slope. Most appear on the right side, but three are located within 3mm of the cranial slope on the left side (these are the only instances where this occurred). These left-sided maxima are positioned about 1.5cm posterior to, and about 1cm medial to, the center of the

left MLDB complex. Also, three maxima of the 10° pattern occur against the skull down within the right nasal plug. However, the foci not lying against the skull generally appear below the right MLDB.

Next we demonstrate the extraordinary effects that the soft tissues (including the melon) have on the emission patterns. The far-field patterns that result from placing point sources at the focal positions of the skull and soft tissue model are shown in Figures 7.32-7.35. Again, the distributions were computed for sources at frequencies of 25, 50, 75, and 100 kHz placed at the 5° inverse simulation foci of maximum energy density. The peak emission directions (in degrees) and directivity indexes (in dB) for these patterns are included in the figures. Note that addition of the soft tissues has dramatically narrowed the skull-only emission patterns. The melon (in combination with other soft tissue) is collimating much of the energy projected to the side and upward by the skull alone. The increased directivity indexes reflect a significant melon contribution to forward beam formation. As discussed in the concluding chapter, the magnitude of this effect largely explains the extraordinary evolutionary investment that the specialized melon tissues represent in delphinids.

7.4. Skull, Air Sacs, and Soft Tissue Simulations

The skull, air sacs, and soft tissue model utilized the same CT-to-density and CT-to-velocity mappings as the skull and soft tissue model (see above) but added in the air sac model. This combined model constitutes a fairly complete representation of the dolphin's forehead tissues (albeit a rather conservative air sac model). The results of this model are therefore of special interest.

We illustrate a series of isosurfaces at the 50%, 30%, and 10% levels of the PSR acoustic energy density in Figures 7.36-7.38 (viewed from both the right side and from above) for the case

of a 5° inverse 50 kHz skull, air sacs, and soft tissue simulation. Figures 7.39-7.41 illustrate 50%, 20%, and 10% isosurfaces for a 5° inverse 75 kHz simulation. Again, energy collimation is clearly exhibited within the posterior melon tissue, with strong channeling in both the vertical and horizontal directions back through a region passing approximately 1cm ventral to the right MLDB complex. Note that the channeling is most pronounced within the posterior throat of the melon, and that the anterior melon appears to be functioning as a broad but weak lensing element.

The focal maxima positions are plotted in Figures 7.42-7.44 (as viewed from the right and the front sides) from many inverse simulations at frequencies of 25, 50, 75, and 100 kHz and return angles of 10° , 5° , and 0° below the negative x-axis for the skull, air sacs, and soft tissue model. Again, the maxima up against the skull is shown when it exists and the soft tissue position of highest energy density for each frequency. Note that all of the foci occur on the right side of the nasal passages, not on the left, and that they have become fairly well grouped along the guide channel of the posterior melon which passes roughly 1cm below the right MLDB, but not so far down as to be considered within the right nasal plug. Note also that the focal positions appear to be most tightly grouped in the 0° inverse results, suggesting that the animal probably produces a beam centered close to 0° in vertical angle.

Figures 7.45-7.48 plot the far-field emission patterns that result from placing point sources at the focal positions of the skull, air sacs, and soft tissue model. The distributions were computed for sources at frequencies of 25, 50, 75, and 100 kHz placed at the 5° inverse simulation foci of highest energy density. The peak emission directions (in degrees) and directivity indexes (in dB) for these patterns are included in the figures. First note that these beam patterns are remarkably well focused in the forward direction. The relative importance of the (conservative) air sac model compared to the melon (and other soft tissues) varies with frequency. Generally

speaking, the air sacs tend to be more important in forward collimation of energy projected upward, sideways, and downward by the skull alone, while the melon is more important in narrowing the main forward lobe. However, to some extent, the air sac model and the melon both contribute to both effects. The net effect of the complete model is to produce fairly uniformly directed, well focused forward beams.

7.5. Inverse and Forward Hearing Simulations

Nearly the full dimensions of the CT dataset were used for the tissue model in the hearing simulations, but only at half resolution (a 3.0mm cubic grid was utilized).⁶ The grid setup for the inverse hearing simulations is diagrammed in Figure 7.49. The region of the grid holding the tissue model is a rectangular volume having x,y,z side-lengths of 45.0cm, 26.4cm, and 28.2cm. In these simulations, the acoustic energy density within a volume containing the pan bone of the lower jaw, the lower jaw fats, and the middle and inner ears was stored and visualized with graphics packages. The tissues within this volume, which I have labelled the 'PGR' region, are illustrated in various slice planes in Figure 7.50. In addition to the upper nasal sac model, the peribullary air sinuses, which surround the middle and inner ear complexes, and the pterygoid sinuses, which extend within the posterior bones of the palate and lateroposteriorly,⁷ were included as separate components in the hearing simulations. As with the nasal sacs, the lower sinuses were modeled as pressure release surfaces in the hearing simulations.

Let us begin with a 50 kHz, 0° inverse hearing simulation⁸ using a model *excluding* soft

⁶ On a 3mm grid, the errors at 50 kHz are equivalent to the errors at 100 kHz ($\lambda=10$ grid increments) on the 1.5mm grid. Although some precision is unavoidably lost at lower resolution, there is an enormous efficiency tradeoff with grid increment size. At half resolution, the FD propagation programs run 16 times faster, while the extrapolation programs run 4 times faster.

⁷ See, for example, Fraser and Purves (1960).

⁸ This terminology may be somewhat misleading, since an 'inverse' simulation which propagates echoes back into the lower jaw tissues is actually a 'forward' simulation of the hearing process. Nevertheless, we stick with the terminology as initially defined above.

tissues, but including the skull, the nasal air sacs, and the peribullary and pterygoid sinuses. Figures 7.51-7.52 illustrate 20% and 13% isosurfaces of energy density within the PGR volume (viewed from the right and from above) for this model. As with the forehead simulations using the skull and nasal air sacs model, strong reflections off of various portions of the lower jaw and skull are apparent, with energy distributed quite broadly over the entire region of the posterior and ventral skull and ear complexes. There are no especially distinct maxima near the inner ears.

Now consider what happens when the soft tissues (including the lower jaw fats) are added back into the tissue model. Figures 7.53-7.54 illustrate 20% and 13% isosurfaces of PGR energy density (viewed from above) for a 50 kHz, 0° inverse skull and soft tissue simulation. Note the dramatic shift in the energy distribution from the previous results without soft tissues. The acoustic energy now exhibits very clean maxima immediately adjacent both left and right ear complexes. Collimation or guiding appears within the jaw fats across and below⁹ the pan bone and back toward the region of the middle and inner ears. For this direction of return, the right 'funnel' of maximum energy density just touches the lateral and ventral section of the periotic bone of the right ear complex, while the left 'funnel' ends up against the outer middle section of the periotic bone of the left ear complex. Differences of this sort in the left-right ear reception patterns are expected to play a role in the dolphin's directional discrimination processes. Megaphone and waveguiding behaviors appear to be occurring within the posterior portions of the lower jaw fats, while a certain degree of lensing appears to be operating within the larger anterior portions. Another clear result (not illustrated here) is that sound is strongly channeled within the blubber layer over the inner tissues, confirming earlier studies (Fraser and Purves 1960, Norris and Harvey 1974). While much work remains to be done, these initial results, in conjunction

⁹ Besides filling the mandibular canals and extending anteriorly forward of the pan bone of the lower jaw, it is clear in the *Delphinus* CT data that the fat bodies also extend somewhat below the lower jaw pan bone.

with those presented above for the melon, resolve most of the conjecture that has surrounded the acoustic function of the lower jaw fats in dolphins -- they do indeed channel sound received from the forward direction through the lower jaw to the middle and inner ear complexes.

Finally, we illustrate how much can be learned from the far-field emission patterns generated by placing sources at the inner ear complexes. The first possibility here is to demonstrate the far-field emission patterns of each ear complex which are equivalent (by the reciprocity theorem) to the monaural receptivity patterns for each ear. Secondly, since both amplitude and phase are computed by the extrapolation programs, we can calculate the amplitude sum or difference patterns, and the phase difference (timing delay) pattern between the ears. The sum amplitude pattern has relevance to the binaural reception of the dolphin, while the difference amplitude and timing delay patterns are relevant to the directional localization mechanisms of the dolphin. Below, we include only a few examples from among many important results here.

We first illustrate the far-field patterns (intensity vs. emission angle) of the left and right ears using a model which includes only the skull and nasal air sacs (without soft tissues and without the peribullary and pterygoid sinuses). Figures 7.55 and 7.56 illustrate these emission patterns, which are equivalent to the left and right ear receptivity patterns, at a frequency of 50 kHz. In these simulations, the densest portion of the periotic bone of each ear was used as the cw source region. Note that the reception patterns appear to have very little directivity. Energy is spread over all downward directions in a fairly complicated interference pattern, and there is an unexpectedly broad backward and upward maximum which is opposite for each ear. The highest peaks for both ears, however, lie roughly 31° below the forward horizon, and occur on the same side as the ears themselves. These left-right differences will become clearer when we add the excluded components back into the model, but they are identifiable even at this stage.

Let us next add the peribullary and pterygoid sinuses back into the model. Figures 7.57 and 7.58 illustrate the left and right ear receptivity patterns at 50 kHz for a model including the skull, nasal air sacs, and the peribullary and pterygoid sinuses, but without soft tissues. Notice that the patterns are now directed almost exclusively downward and forward. This demonstrates that the peribullary and pterygoid sinuses of the lower skull and palate contribute quite significantly to the formation of downward and forward reception patterns, apparently insulating the ears from most other directions of incidence. The importance of these sinuses to the receptivity patterns was predicted by Norris (1968). The peaks for both ears again lie quite low (36° and 42°) below the forward horizon, and occur on the same side as the ears themselves. While most of the patterns are directed downward, note the shifts that occur in the receptivities as one moves through forward horizontal arcs. This differing receptivity of the two ears was also predicted by Norris (1968) as a consequence of propagation through the angled pan bones of the lower jaw.

Finally, adding the soft tissues (including the lower jaw fat bodies) back into the model causes another dramatic shift in the reception patterns. Figures 7.59 and 7.60 illustrate the left and right ear receptivity patterns at 50 kHz for the complete skull, soft tissue, nasal air sacs, peribullary and pterygoid sinuses model. Note that the patterns have become sharply enhanced in the forward direction. This enhancement is mostly due to the waveguide, megaphone, and lens effects of the lower jaw fat bodies, and explains the enormous evolutionary significance of these tissues. Again, note that clear differences exist in the left versus right ear receptivities as one moves through forward horizontal arcs. These differences undoubtedly contribute to the dolphin's directional discrimination capabilities. Figure 7.60 is in general agreement with the horizontal receptivity measured experimentally by Norris and Harvey (1974) at a point inside the fat channel near the right ear complex of a bottlenose dolphin. Figures 7.59 and 7.60 both agree roughly with the 60 kHz bottlenose dolphin receptivity pattern measurements of Au and Moore

(1984) reproduced in Chapter 2, although the vertical patterns are peaked nearly 20-25° lower. In summary, all results of the hearing simulations have confirmed the lower jaw hearing hypothesis of Norris (1968), and have also revealed the roles of several tissues in the reception process.

I have presented only a few of the results of an initial series of simulations in this chapter. The conclusions of this project regarding the mechanisms of delphinid biosonar signal production, emission, and reception will be summarized in the next chapter, as well as the enormous potential of this very powerful combination of modeling techniques.



Figure 7.1. Visualization of isosurfaces at the CT data bone threshold (300 HU) illustrating the skull surfaces within the region of the CT dataset selected for all forehead simulations.

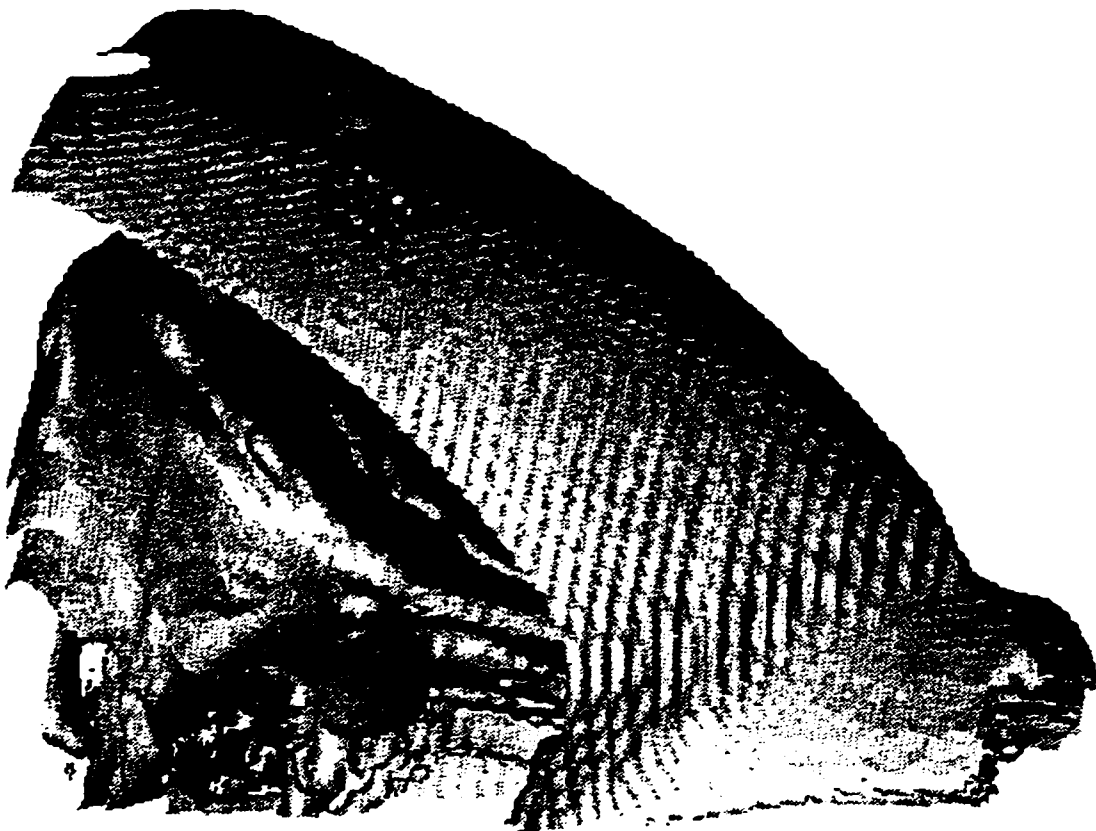


Figure 7.2. Visualization of skin and bone isosurfaces within the region of the CT dataset selected for all forehead simulations. The ribbed appearance of the skin surface is an artifact of the graphics package that produced the image.

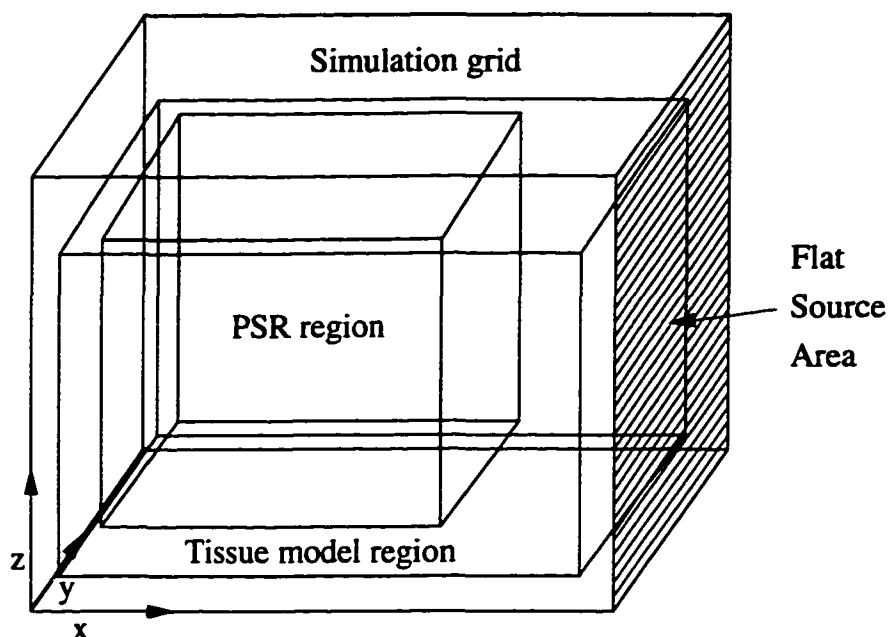


Figure 7.3. Grid setup for the inverse forehead tissue simulations. The region of the grid containing the tissue model is indicated. Note that the front face of the grid is used as a flat source to ensound the tissue model. The acoustic energy density within the volume labeled 'PSR' was calculated by the simulation programs and visualized with graphics packages.

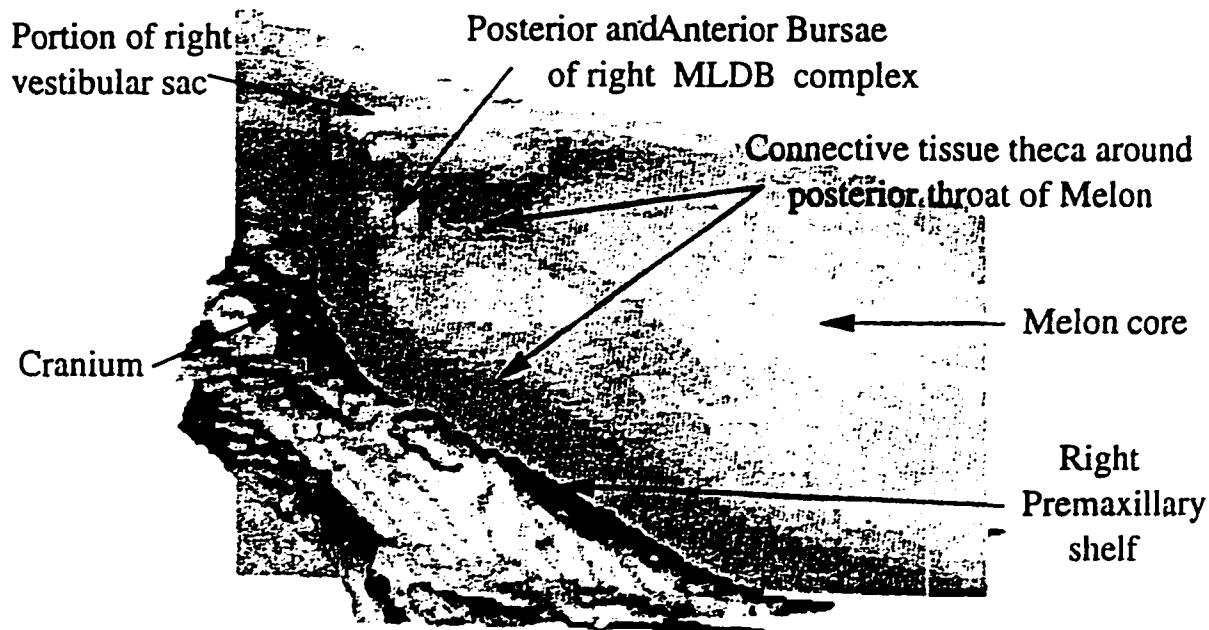


Figure 7.4. Perspective view of a parasagittal CT data slice through the center of the right MLDB complex within the PSR region. Several tissue structures are indicated and the skull isosurface added in order to provide positional reference in later diagrams of the results of the inverse simulations.



Figure 7.5. Illustration of the energy density in the PSR y-slice containing the maxima for a skull-only 5 degree inverse simulation at a frequency of 25 kHz. The skull isosurface and edge slices were added for positional orientation.



Figure 7.6. Illustration of the energy density in the PSR y-slice containing the maxima for a skull-only 5 degree inverse simulation at a frequency of 50 kHz. The skull isosurface and edge slices were added for positional orientation.

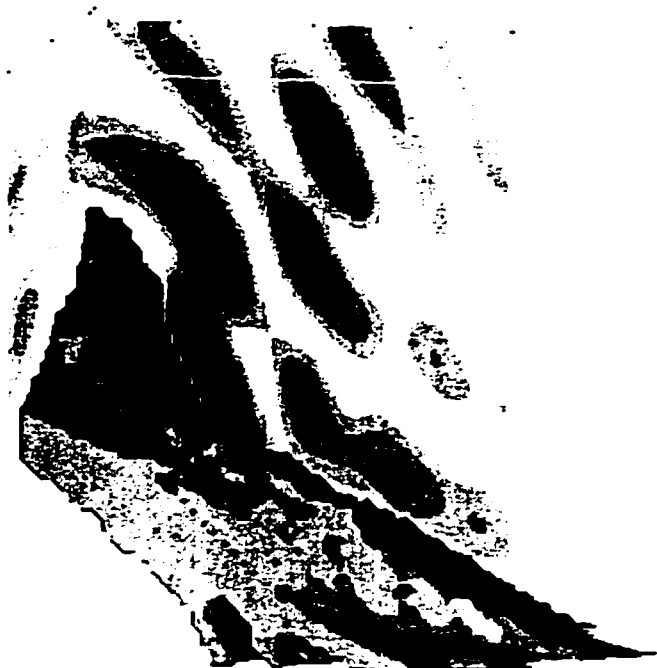


Figure 7.7. Illustration of the energy density in the PSR y-slice containing the maxima for a skull-only 5 degree inverse simulation at a frequency of 75 kHz. The skull isosurface and edge slices were added for positional orientation.



Figure 7.8. Illustration of the energy density in the PSR y-slice containing the maxima for a skull-only 5 degree inverse simulation at a frequency of 100 kHz. The skull isosurface and edge slices were added for positional orientation.

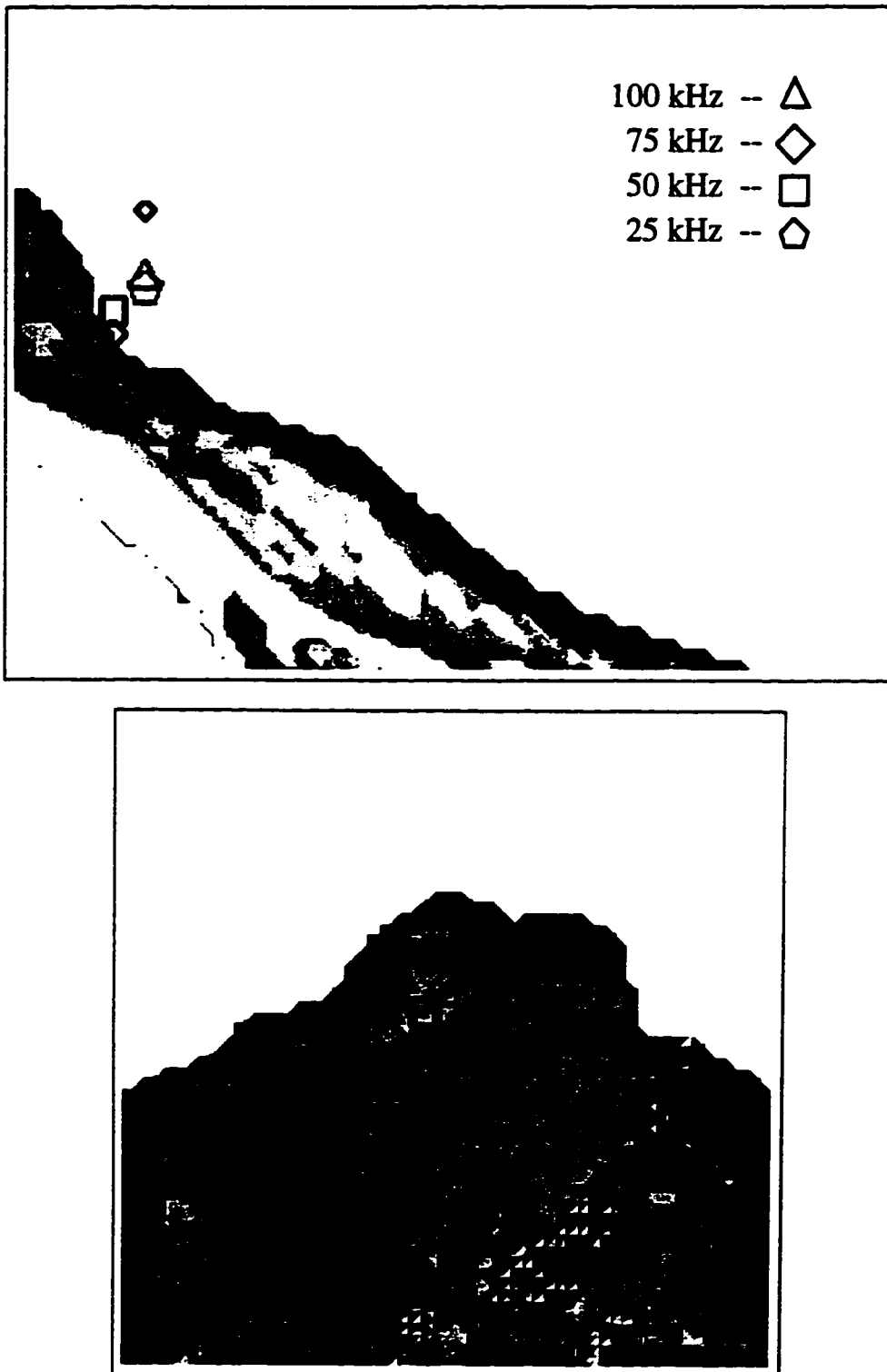


Figure 7.9. Positions of the 'epicenters' for the 0° inverse skull-only simulations at four frequencies. Top diagram is a PSR view of the maxima positions from the right side; bottom diagram is a PSR view from the front side. When multiple maxima exist, the size of the symbols have been scaled to the intensity of the maxima represented. The skull isosurface is included for positional orientation.

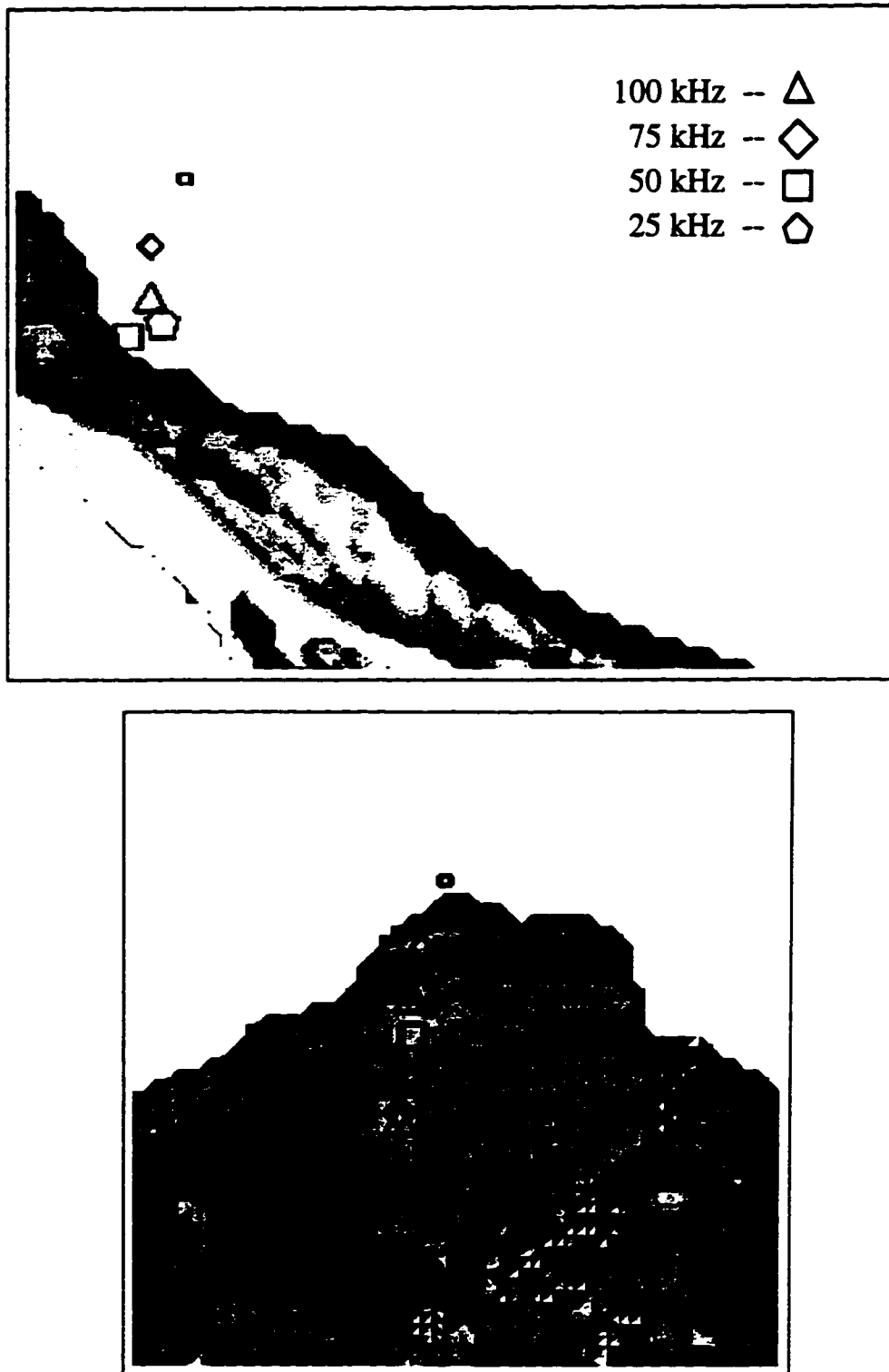


Figure 7.10. Positions of the 'epicenters' for the 5th inverse skull-only simulations at four frequencies. Top diagram is a PSR view of the maxima positions from the right side; bottom diagram is a PSR view from the front side. When multiple maxima exist, the size of the symbols have been scaled to the intensity of the maxima represented. The skull isosurface is included for positional orientation.

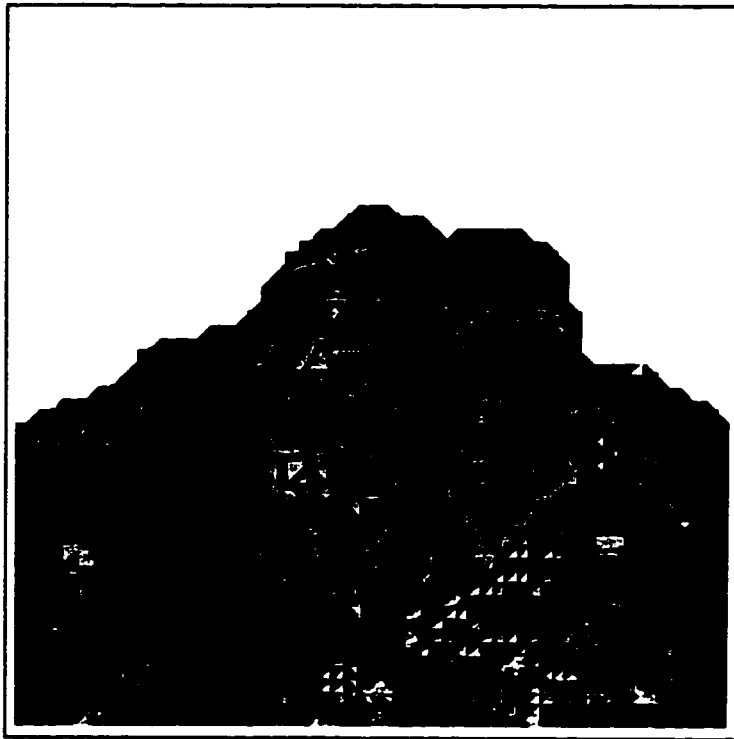
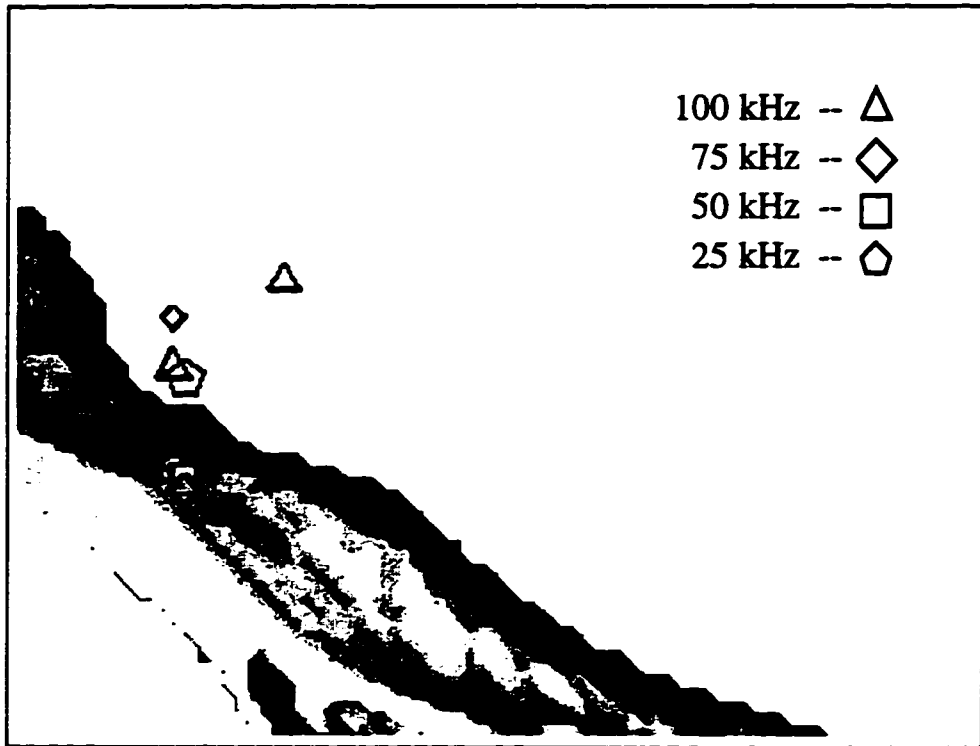


Figure 7.11. Positions of the 'epicenters' for the 10° inverse skull-only simulations at four frequencies. Top diagram is a PSR view of the maxima positions from the right side; bottom diagram is a PSR view from the front side. When multiple maxima exist, the size of the symbols have been scaled to the intensity of the maxima represented. The skull isosurface is included for positional orientation.

Thet,Phi=15.86,-1.78; DI=7.84; freq=25kHz

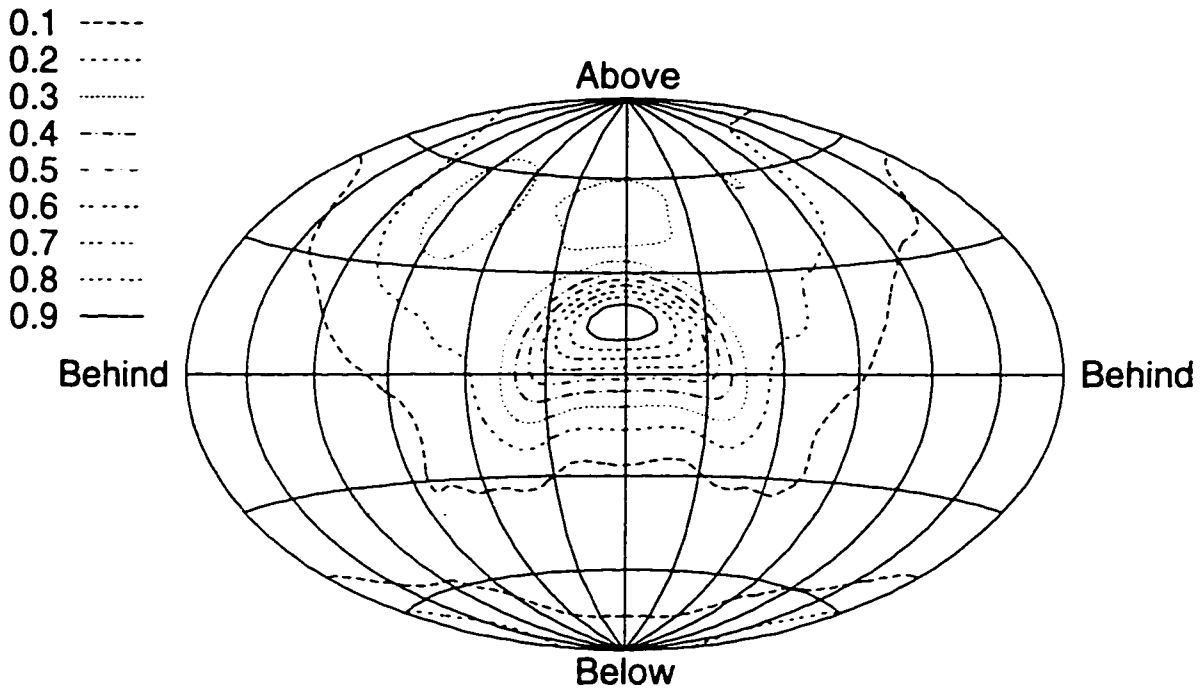
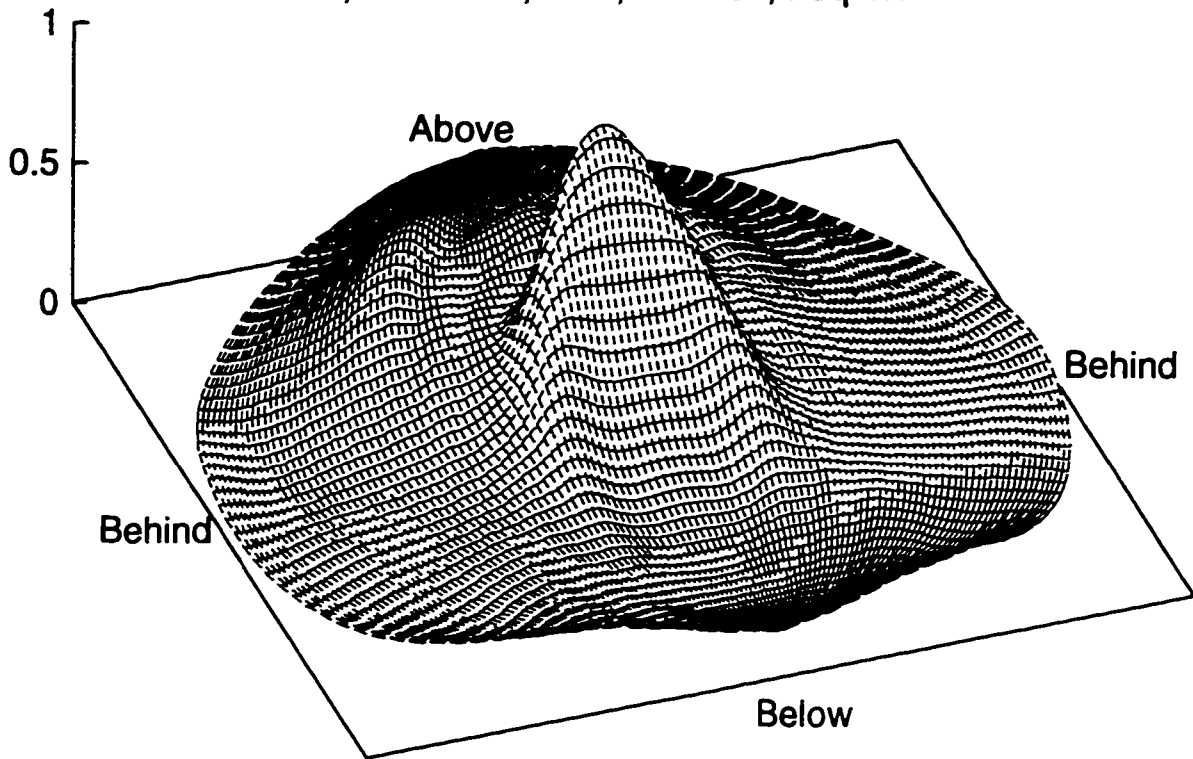


Figure 7.12. Extrapolated far-field emission pattern at 25 kHz for the skull-only model. The source point was the focal position of highest energy density obtained from a 25 kHz 5° inverse simulation (see Figure 7.10). Top diagram plots intensity as height in a perspective view of the far-field data. Bottom diagram is a contour plot of the same data, also plotted in the global equal-area projection. The direction angles of the emission peak and the directivity index for this pattern are indicated.

$\Theta, \Phi = 7.57, 4.17$; $DI = 10.87$; $\text{freq} = 50 \text{ kHz}$

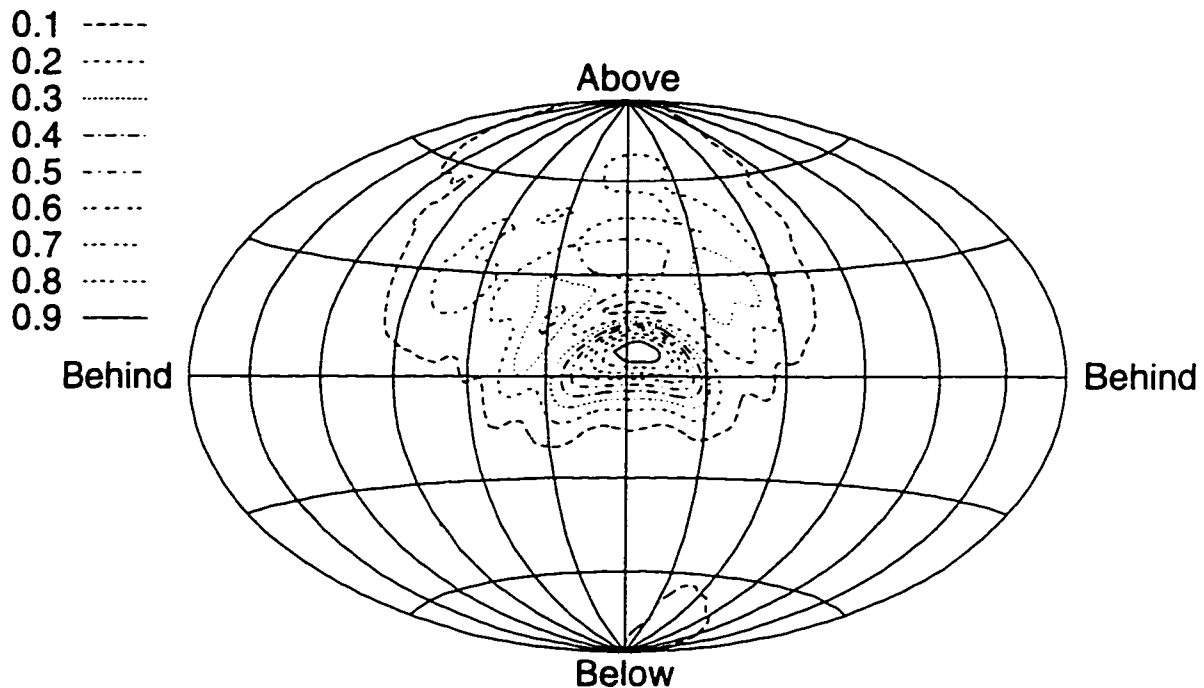
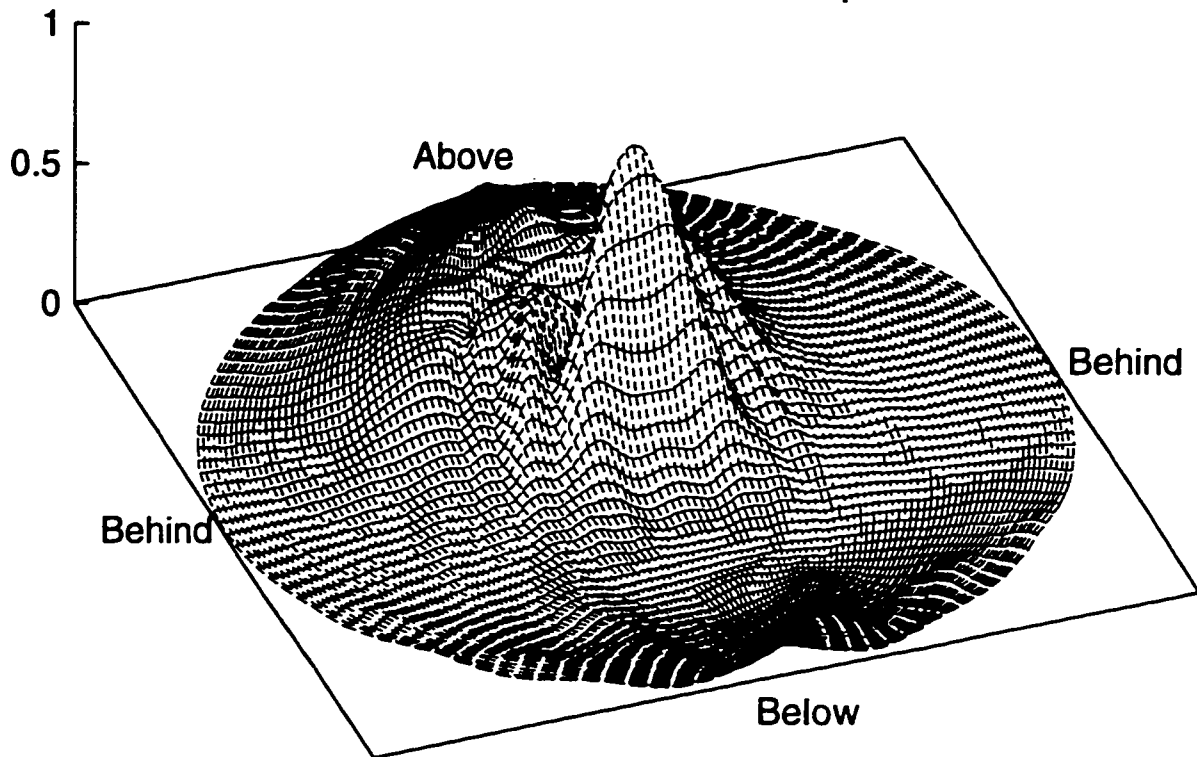


Figure 7.13. Extrapolated far-field emission pattern at 50 kHz for the skull-only model. The source point was the focal position of highest energy density obtained from a 50 kHz 5° inverse simulation (see Figure 7.10). Top diagram plots intensity as height in a perspective view of the far-field data. Bottom diagram is a contour plot of the same data, also plotted in the global equal-area projection. The direction angles of the emission peak and the directivity index for this pattern are indicated.

Thet,Phi=6.80,4.14; DI=12.39; freq=75kHz

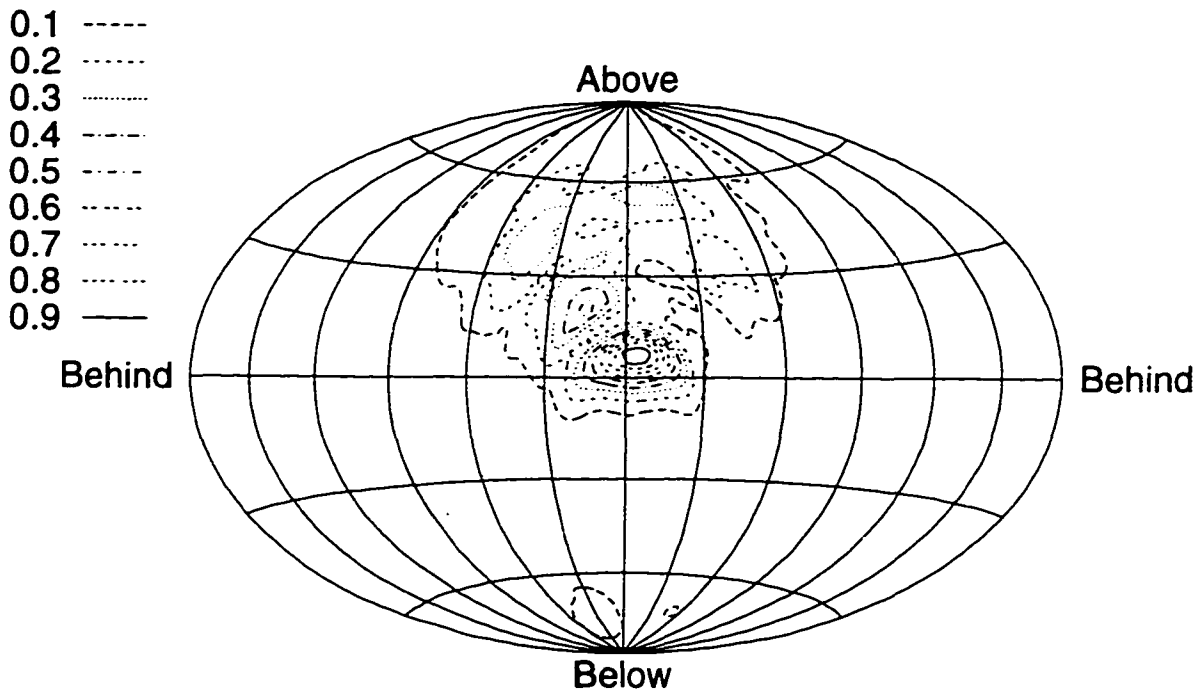
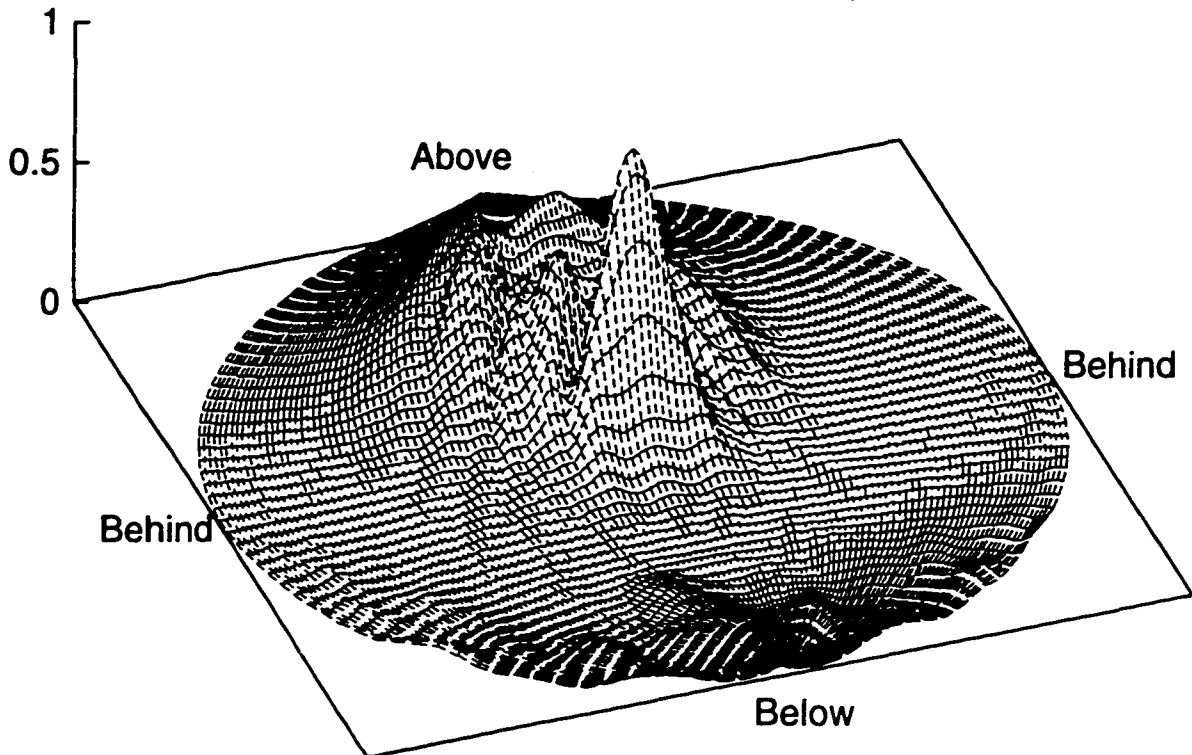


Figure 7.14. Extrapolated far-field emission pattern at 75 kHz for the skull-only model. The source point was the focal position of highest energy density obtained from a 75 kHz 5° inverse simulation (see Figure 7.10). Top diagram plots intensity as height in a perspective view of the far-field data. Bottom diagram is a contour plot of the same data, also plotted in the global equal-area projection. The direction angles of the emission peak and the directivity index for this pattern are indicated.

Thet,Phi=5.63,-0.59; DI=13.30; freq=100kHz

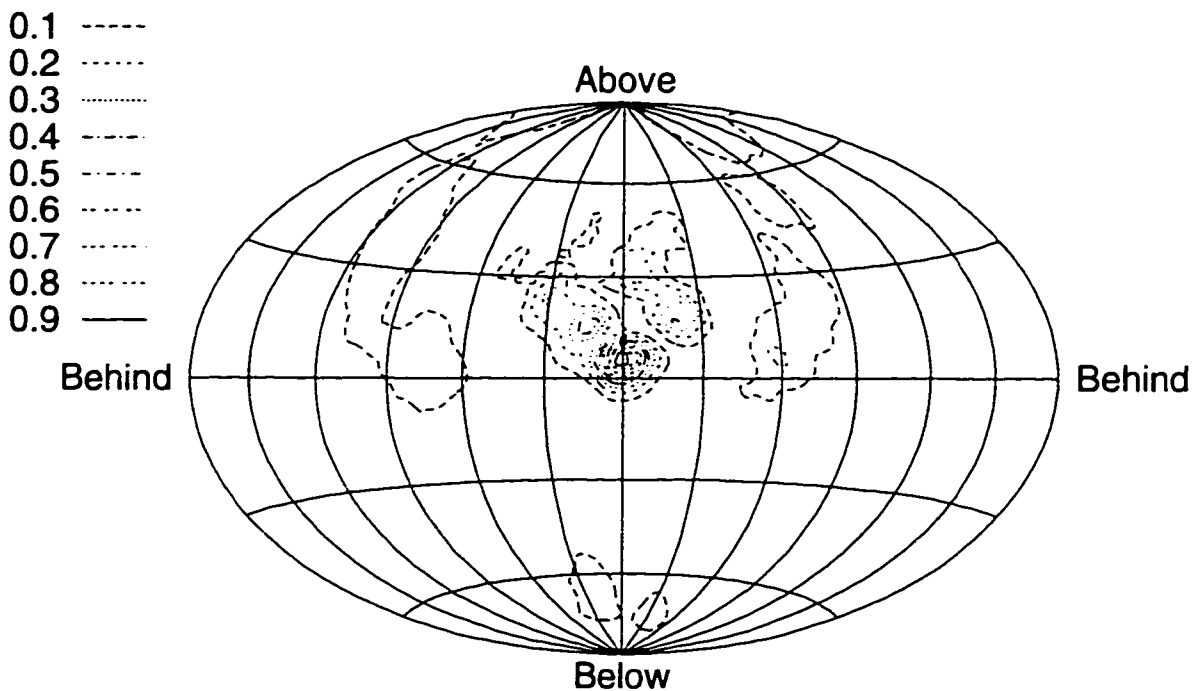
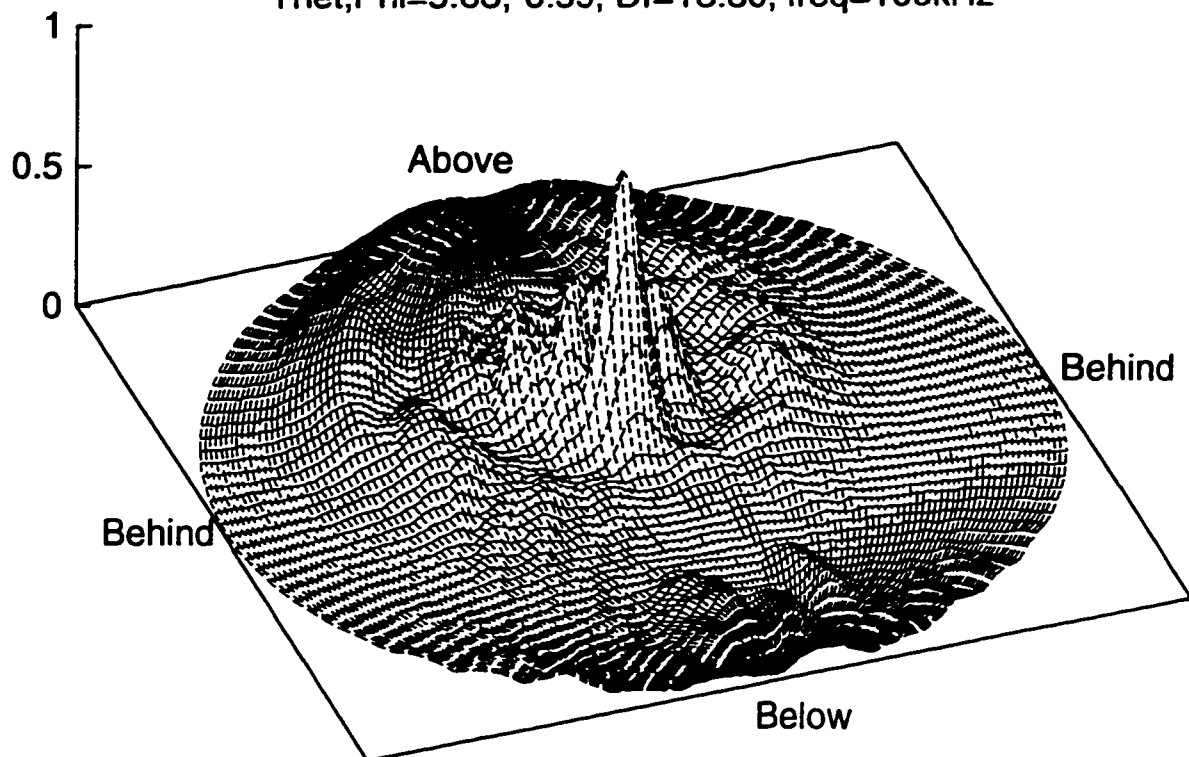


Figure 7.15. Extrapolated far-field emission pattern at 100 kHz for the skull-only model. The source point was the focal position of highest energy density obtained from a 100 kHz 5° inverse simulation (see Figure 7.10). Top diagram plots intensity as height in a perspective view of the far-field data. Bottom diagram is a contour plot of the same data, also plotted in the global equal-area projection. The direction angles of the emission peak and the directivity index for this pattern are indicated.

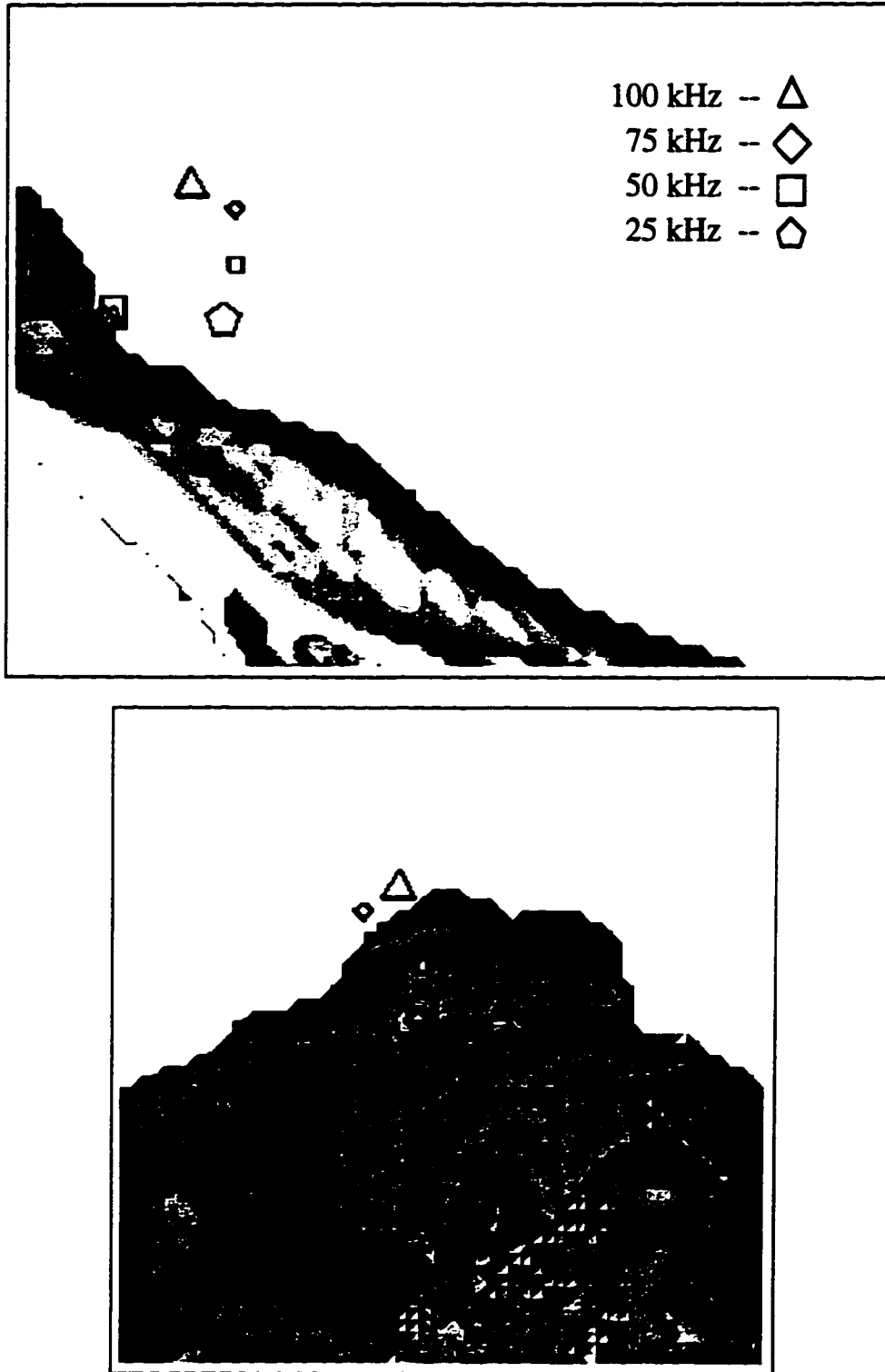


Figure 7.16. Positions of the 'epicenters' for the 0° inverse skull and air sacs simulations at four frequencies. Top diagram is a PSR view of the maxima positions from the right side; bottom diagram is a PSR view from the front side. When multiple maxima exist, the size of the symbols have been scaled to the intensity of the maxima represented. The skull isosurface is included for positional orientation.

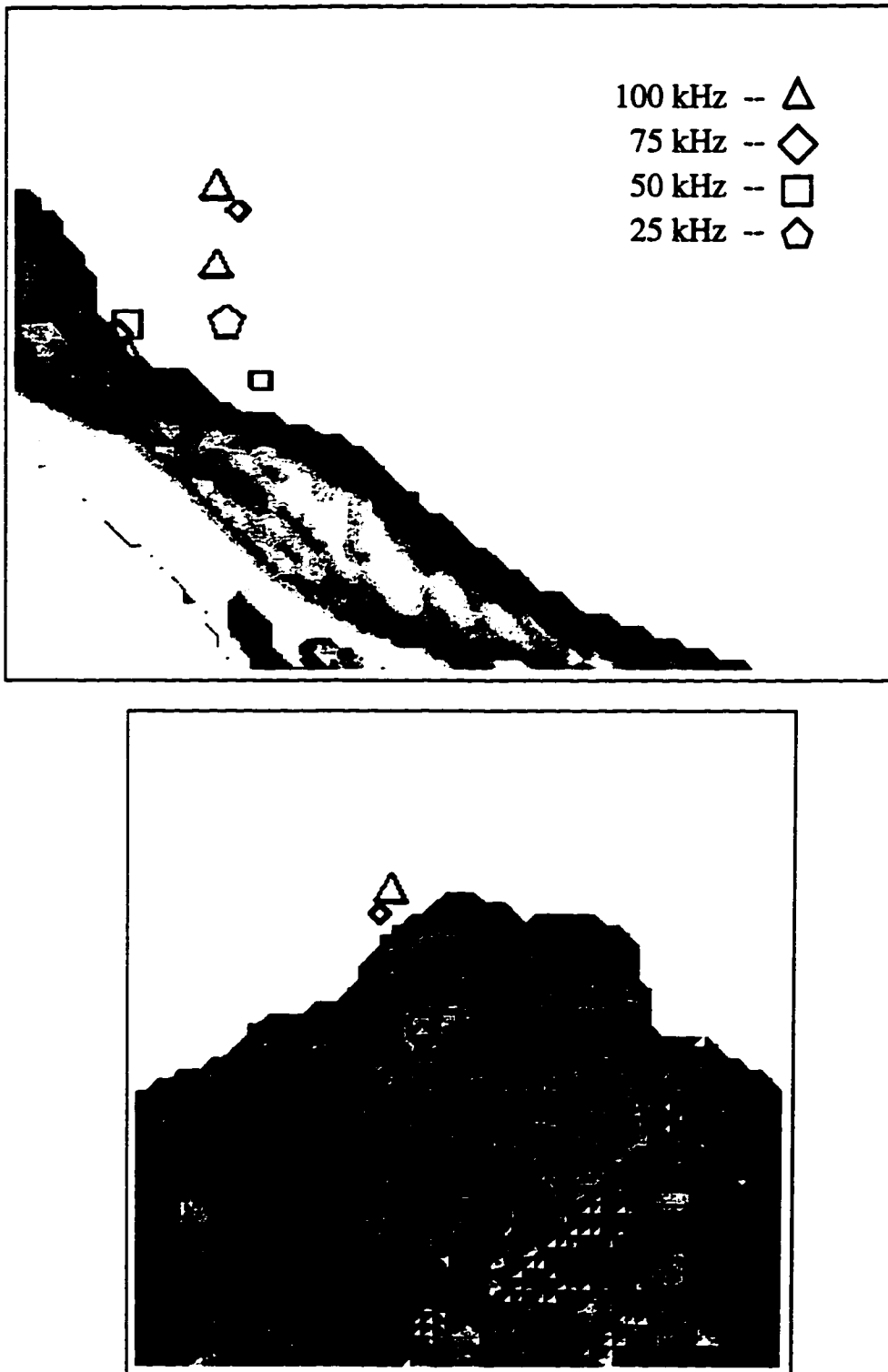


Figure 7.17. Positions of the 'epicenters' for the 5° inverse skull and air sacs simulations at four frequencies. Top diagram is a PSR view of the maxima positions from the right side; bottom diagram is a PSR view from the front side. When multiple maxima exist, the size of the symbols have been scaled to the intensity of the maxima represented. The skull isosurface is included for positional orientation.

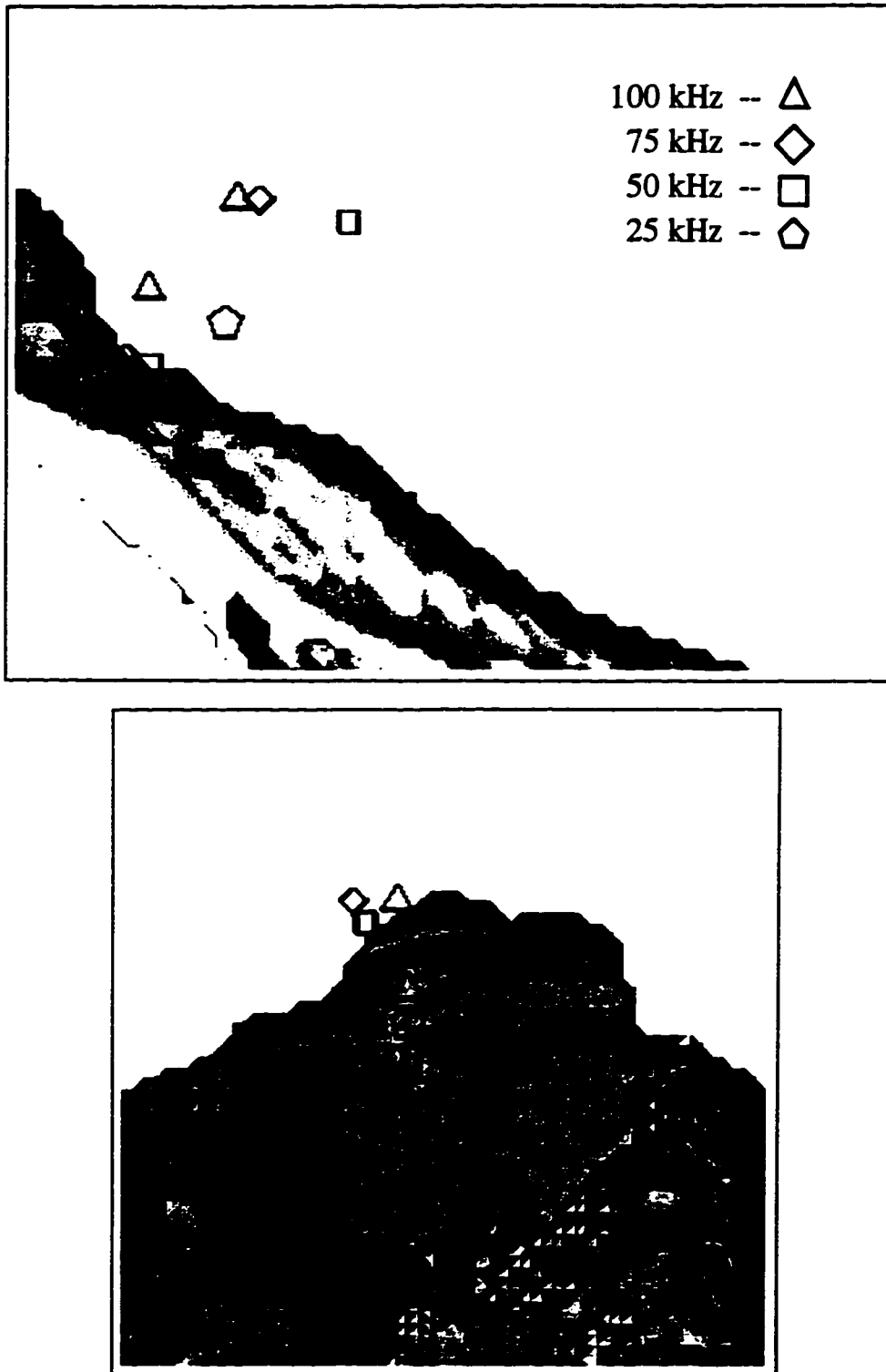


Figure 7.18. Positions of the 'epicenters' for the 10° inverse skull and air sacs simulations at four frequencies. Top diagram is a PSR view of the maxima positions from the right side; bottom diagram is a PSR view from the front side. When multiple maxima exist, the size of the symbols have been scaled to the intensity of the maxima represented. The skull isosurface is included for positional orientation.

Thet,Phi=13.17,-0.74; DI=8.99; freq=25kHz

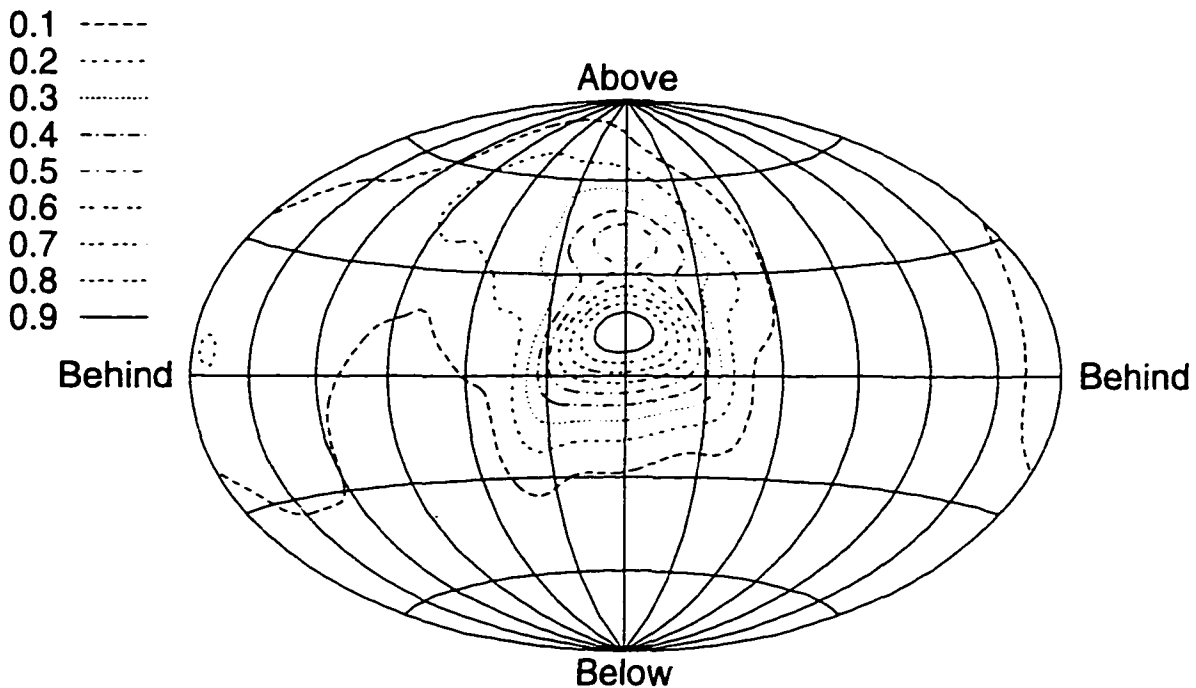
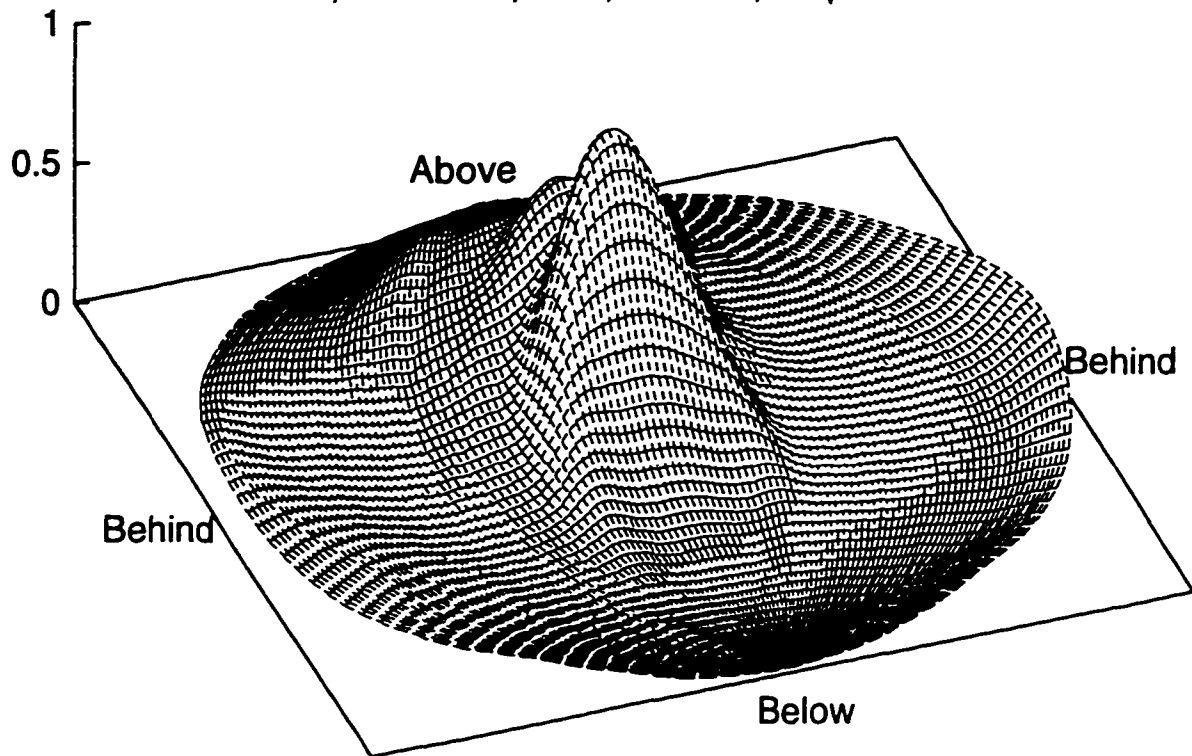


Figure 7.19. Extrapolated far-field emission pattern at 25 kHz for the skull and air sacs model. The source point was the focal position of highest energy density obtained from a 25 kHz 5° inverse simulation (see Figure 7.17). Top diagram plots intensity as height in a perspective view of the far-field data. Bottom diagram is a contour plot of the same data, also plotted in the global equal-area projection. The direction angles of the emission peak and the directivity index for this pattern are indicated.

Thet,Phi=4.08,-3.73; DI=11.46; freq=50kHz

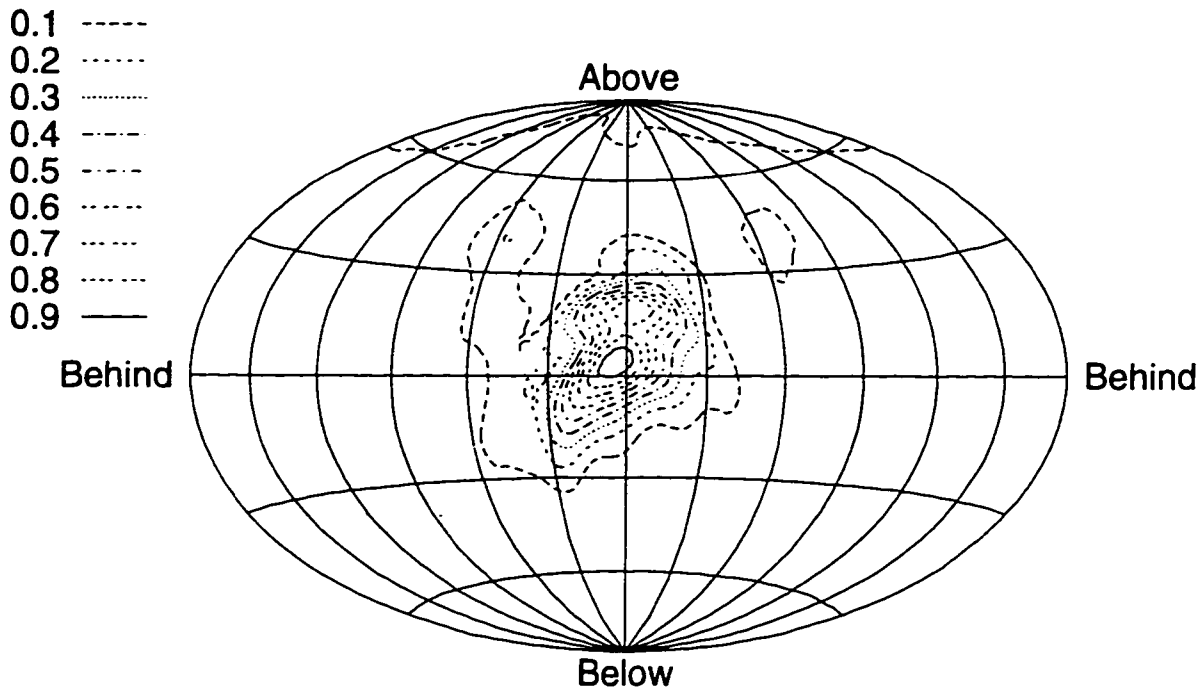
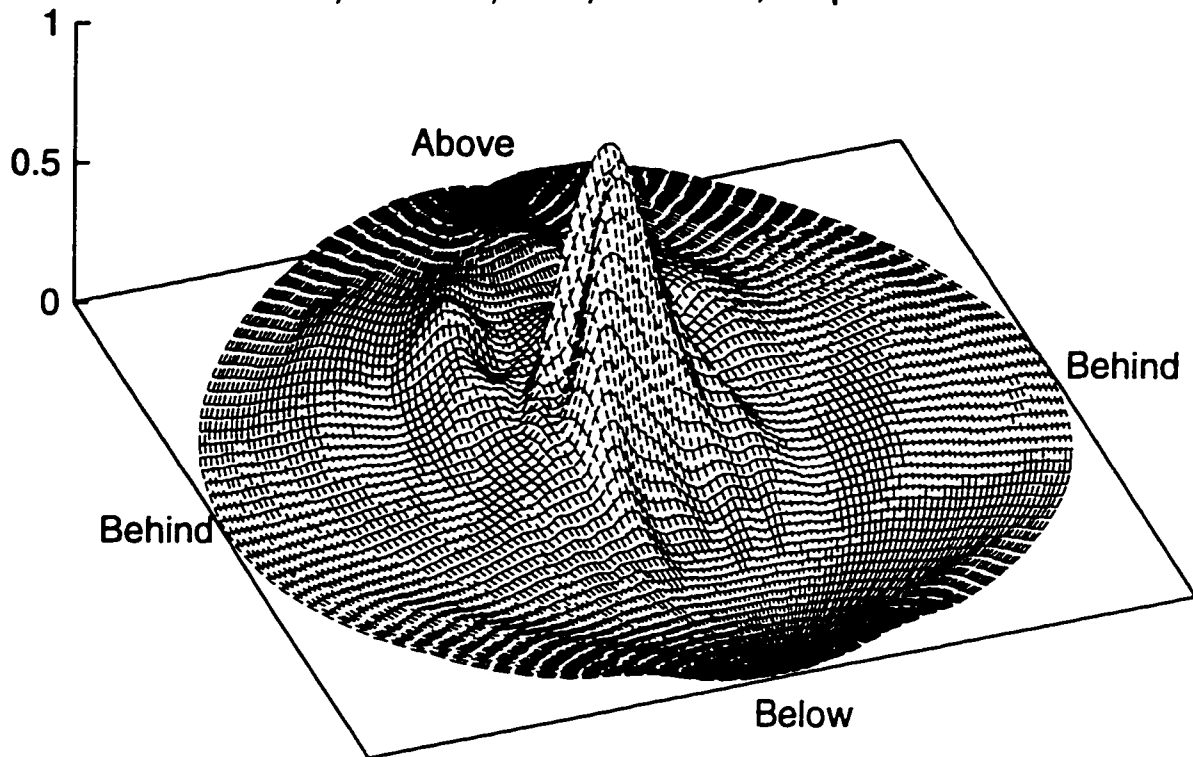


Figure 7.20. Extrapolated far-field emission pattern at 50 kHz for the skull and air sacs model. The source point was the focal position of highest energy density obtained from a 50 kHz 5° inverse simulation (see Figure 7.17). Top diagram plots intensity as height in a perspective view of the far-field data. Bottom diagram is a contour plot of the same data, also plotted in the global equal-area projection. The direction angles of the emission peak and the directivity index for this pattern are indicated.

Thet,Phi=4.35,1.94; DI=14.77; freq=75kHz

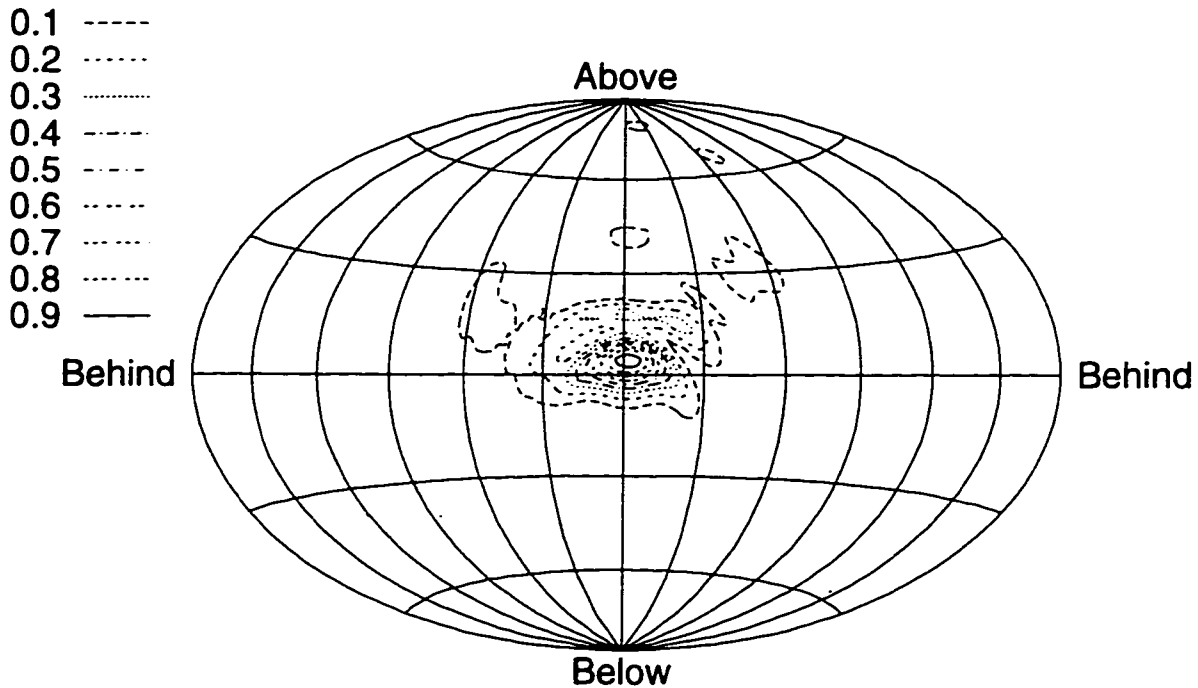
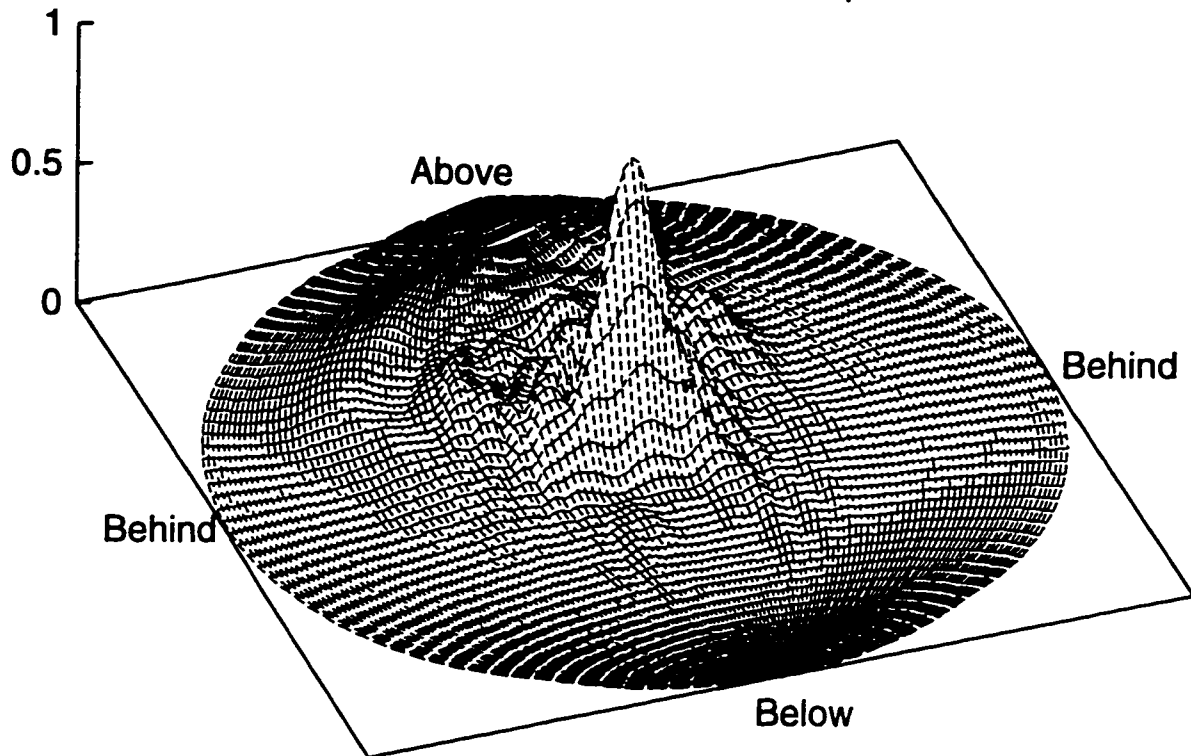


Figure 7.21. Extrapolated far-field emission pattern at 75 kHz for the skull and air sacs model. The source point was the focal position of highest energy density obtained from a 75 kHz 5° inverse simulation (see Figure 7.17). Top diagram plots intensity as height in a perspective view of the far-field data. Bottom diagram is a contour plot of the same data, also plotted in the global equal-area projection. The direction angles of the emission peak and the directivity index for this pattern are indicated.

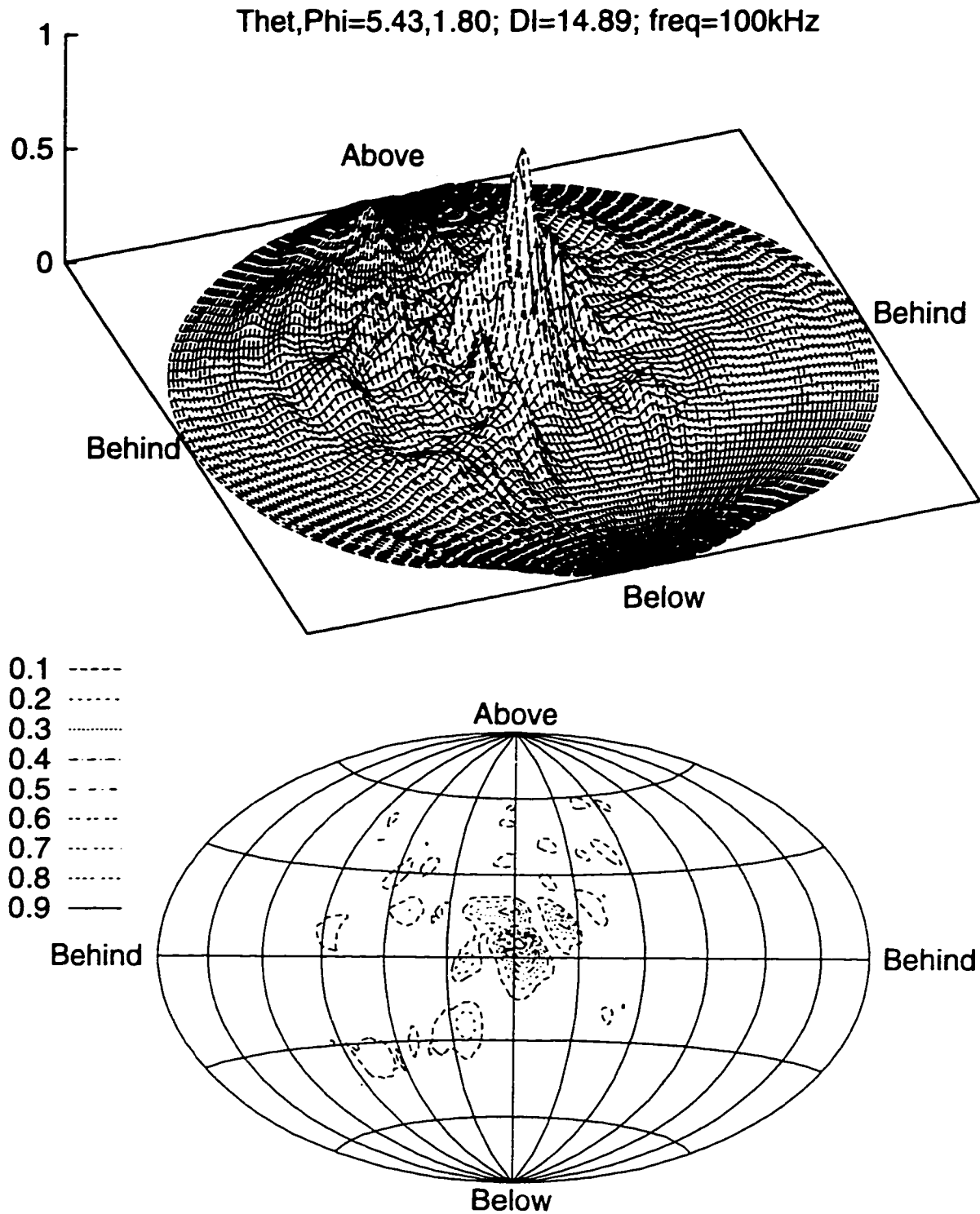


Figure 7.22. Extrapolated far-field emission pattern at 100 kHz for the skull and air sacs model. The source point was the focal position of highest energy density obtained from a 100 kHz 5° inverse simulation (see Figure 7.17). Top diagram plots intensity as height in a perspective view of the far-field data. Bottom diagram is a contour plot of the same data, also plotted in the global equal-area projection. The direction angles of the emission peak and the directivity index for this pattern are indicated.

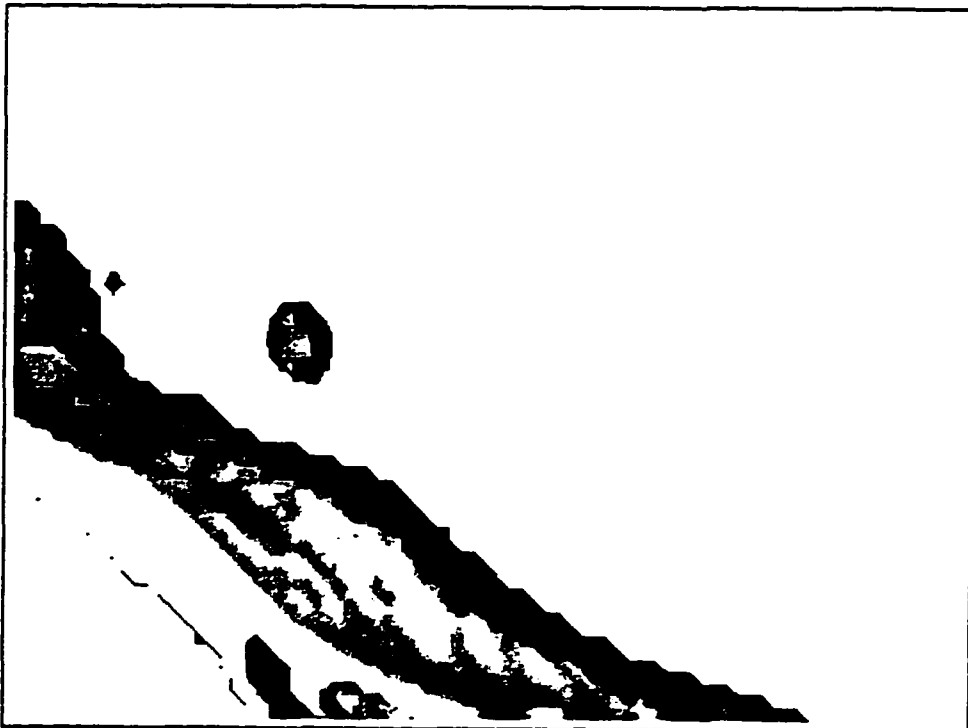


Figure 7.23. Visualizations of the isosurface at 50% of the PSR acoustic energy density for a 5th inverse 50 kHz skull and soft tissue simulation. Top diagram is a view of the PSR from above. Lower diagram is a view of the PSR from the right side. The skull isosurface is included for positional orientation.



Figure 7.24. Visualizations of the isosurface at 30% of the PSR acoustic energy density for a 5° inverse 50 kHz skull and soft tissue simulation. Top diagram is a view of the PSR from above. Lower diagram is a view of the PSR from the right side. The skull isosurface is included for positional orientation.

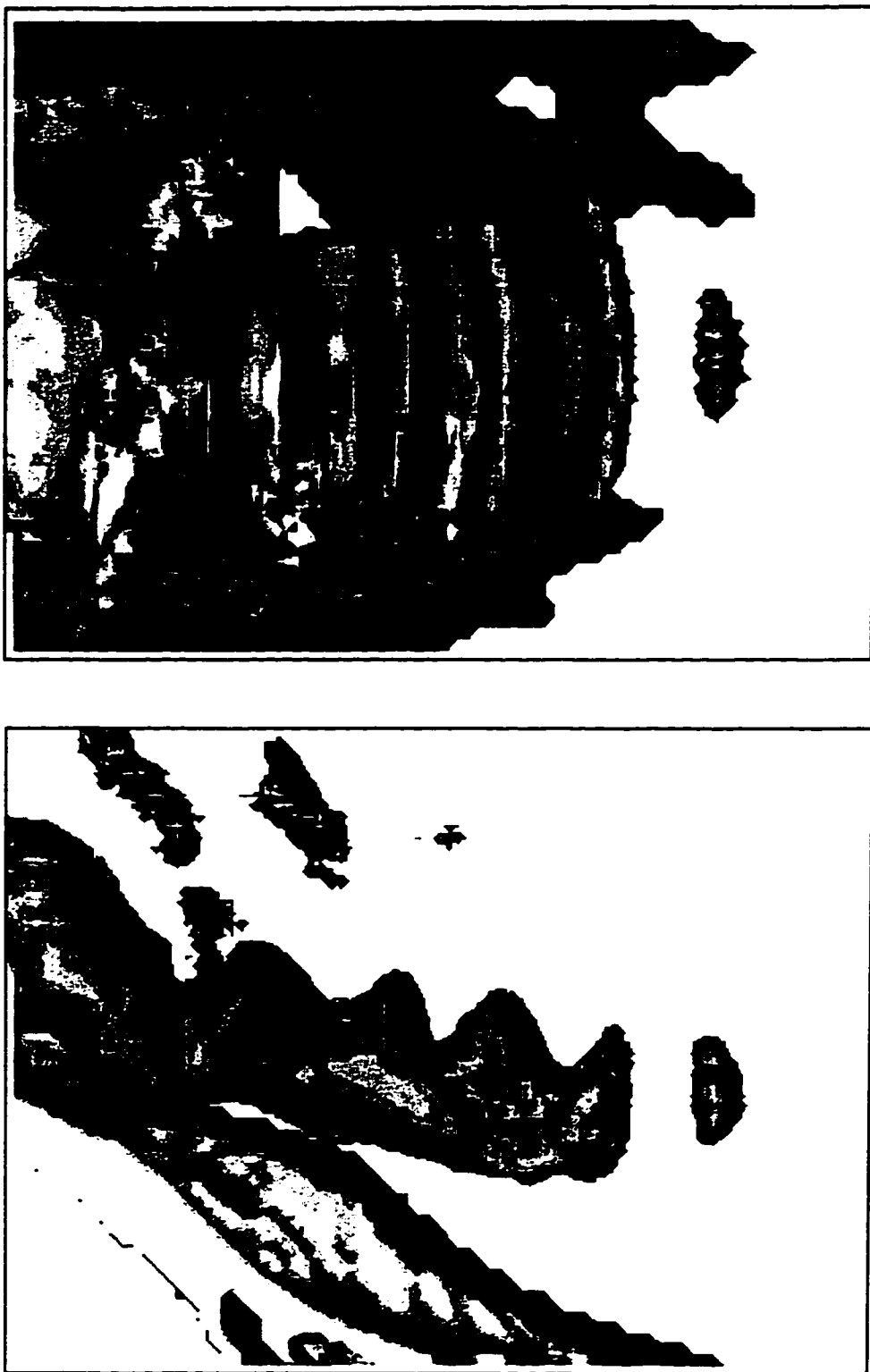


Figure 7.25. Visualizations of the isosurface at 10% of the PSR acoustic energy density for a 5° inverse 50 kHz skull and soft tissue simulation. Top diagram is a view of the PSR from above. Lower diagram is a view of the PSR from the right side. The skull isosurface is included for positional orientation.

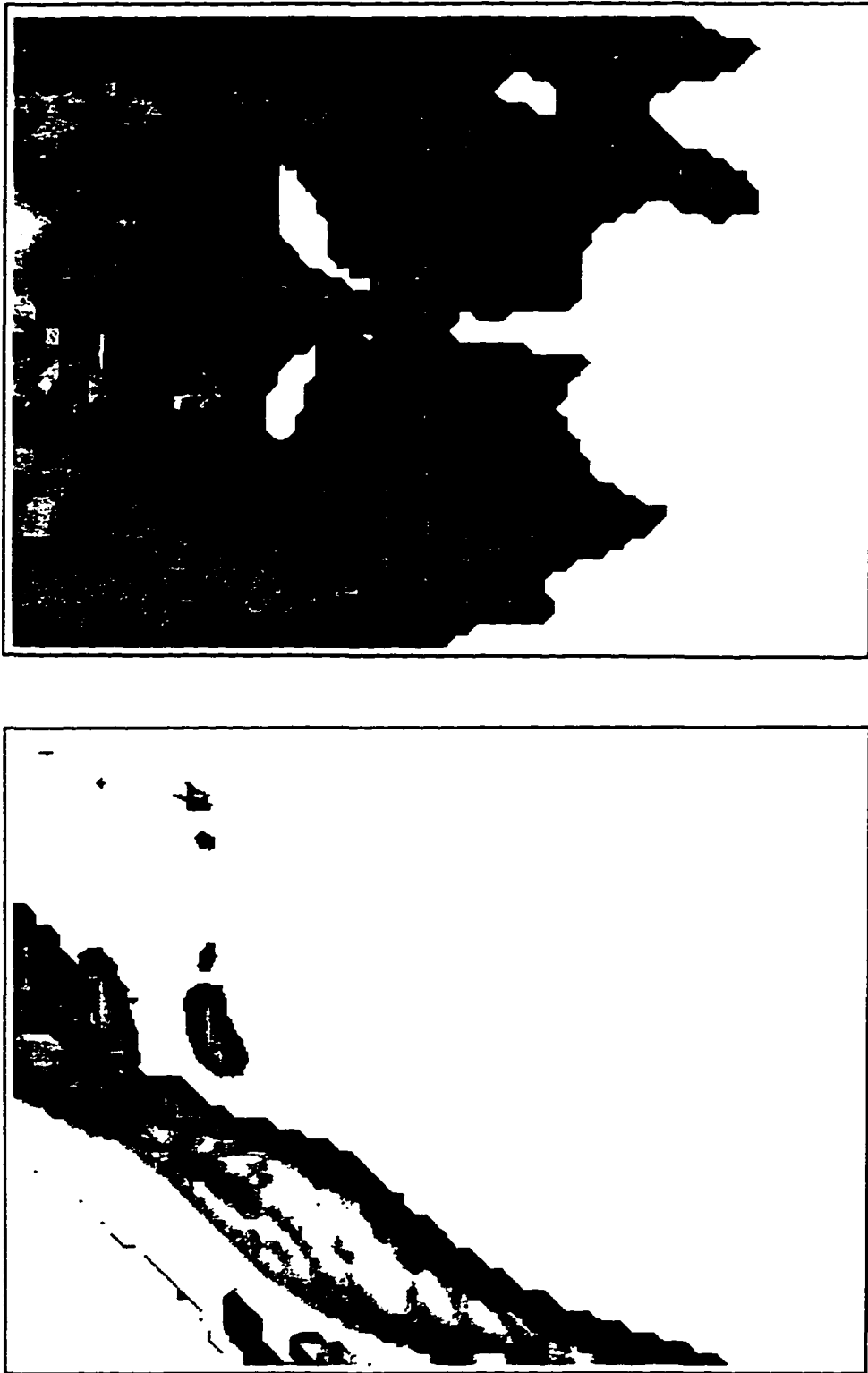


Figure 7.26. Visualizations of the isosurface at 50% of the PSR acoustic energy density for a 5° inverse 75 kHz skull and soft tissue simulation. Top diagram is a view of the PSR from above. Lower diagram is a view of the PSR from the right side. The skull isosurface is included for positional orientation.

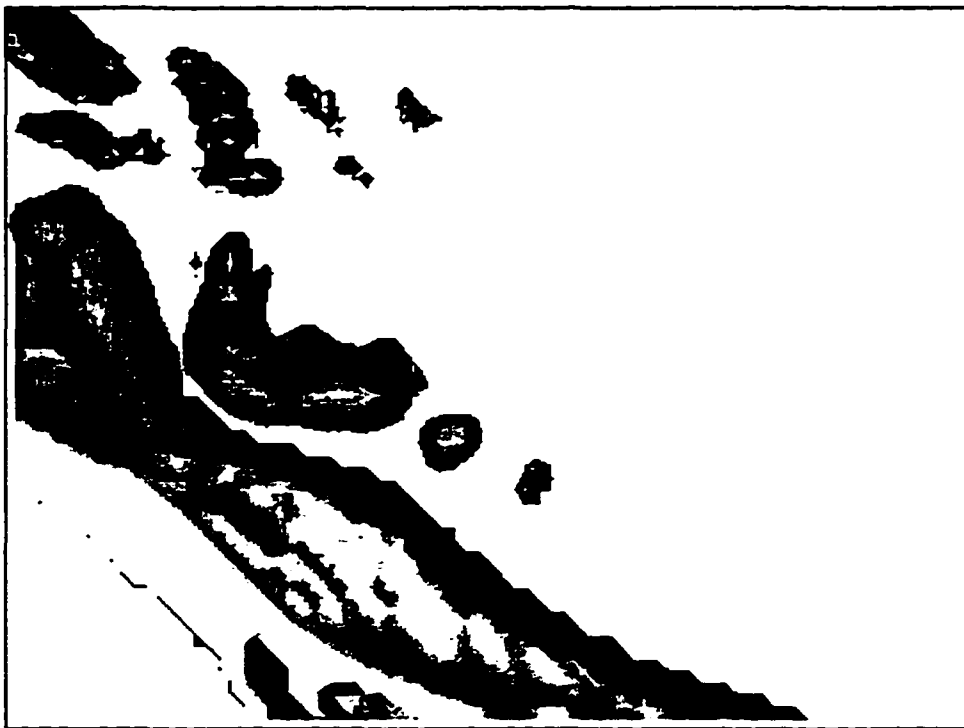
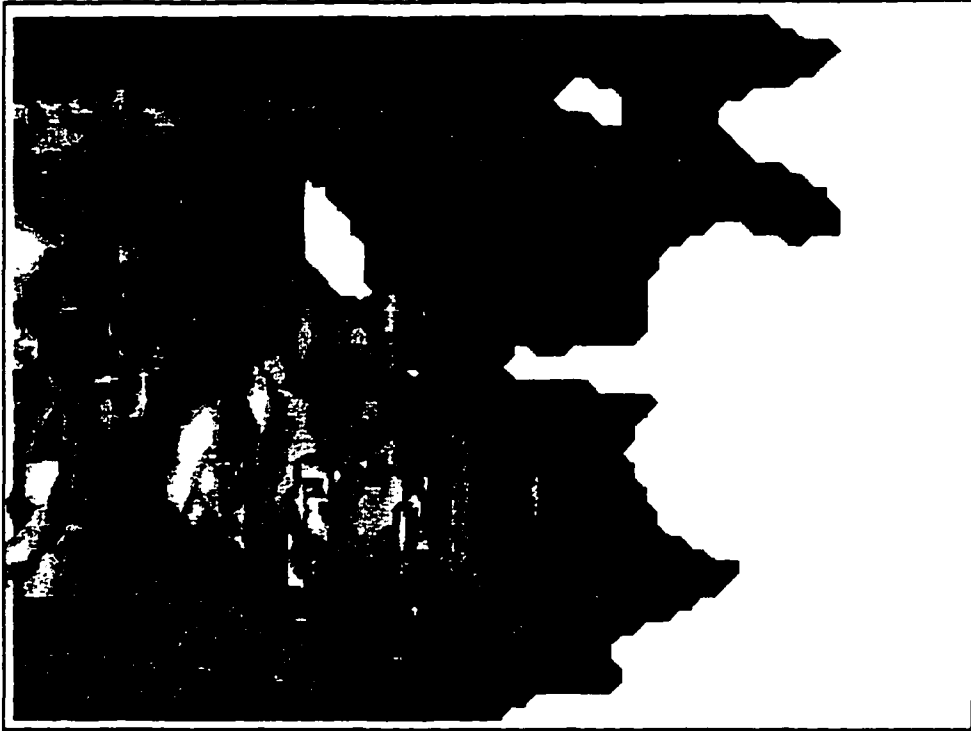


Figure 7.27. Visualizations of the isosurface at 20% of the PSR acoustic energy density for a 5° inverse 75 kHz skull and soft tissue simulation. Top diagram is a view of the PSR from above. Lower diagram is a view of the PSR from the right side. The skull isosurface is included for positional orientation.

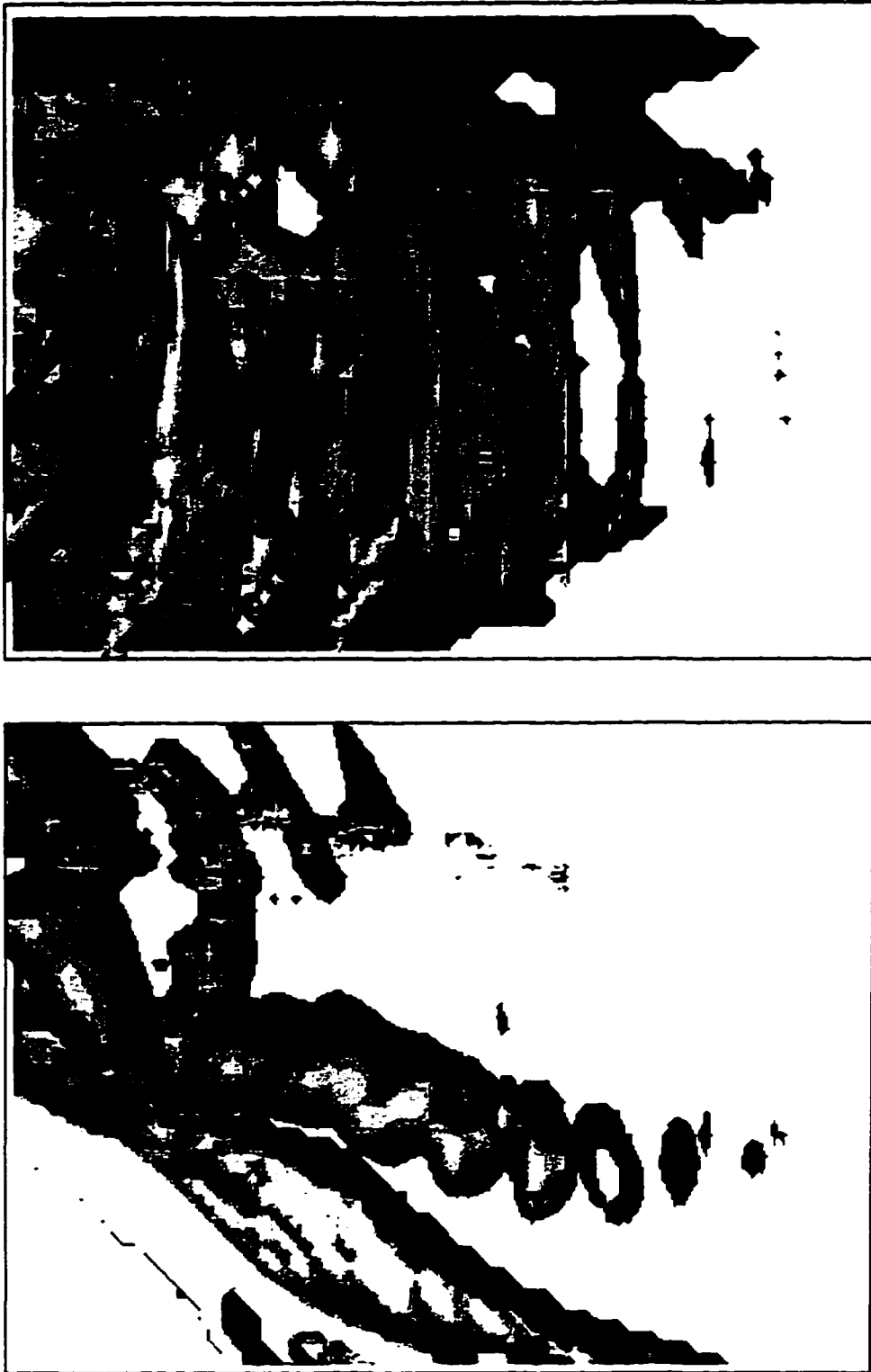


Figure 7.28. Visualizations of the isosurface at 10% of the PSR acoustic energy density for a 5° inverse 75 kHz skull and soft tissue simulation. Top diagram is a view of the PSR from above. Lower diagram is a view of the PSR from the right side. The skull isosurface is included for positional orientation.

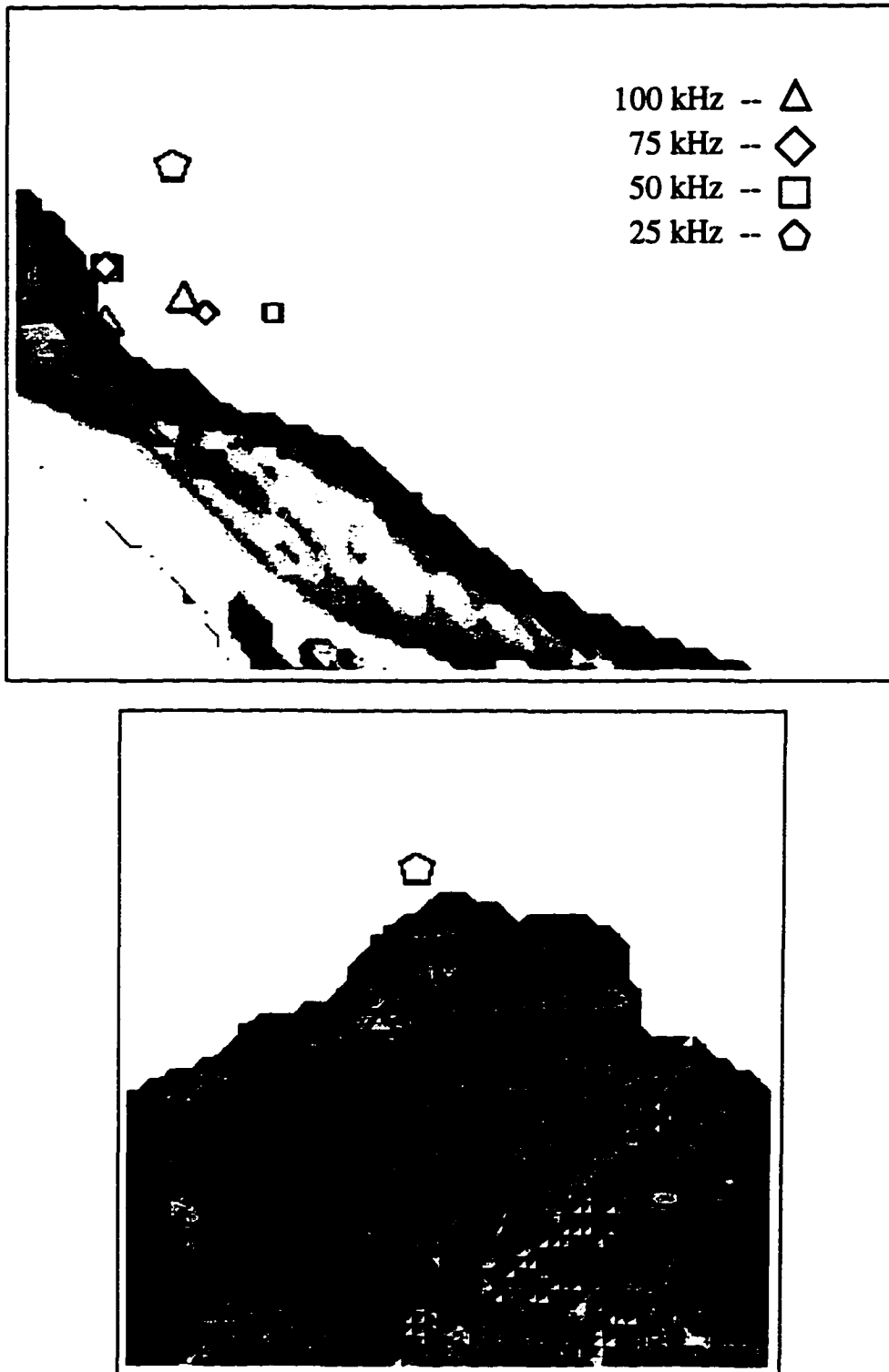


Figure 7.29. Positions of the 'epicenters' from the 0° inverse skull and soft tissue simulations at four frequencies. Top diagram is a PSR view of the maxima positions from the right side; bottom diagram is a PSR view from the front side. When multiple maxima exist, the size of the symbols have been scaled to the intensity of the maxima represented. The skull isosurface is included for positional orientation.

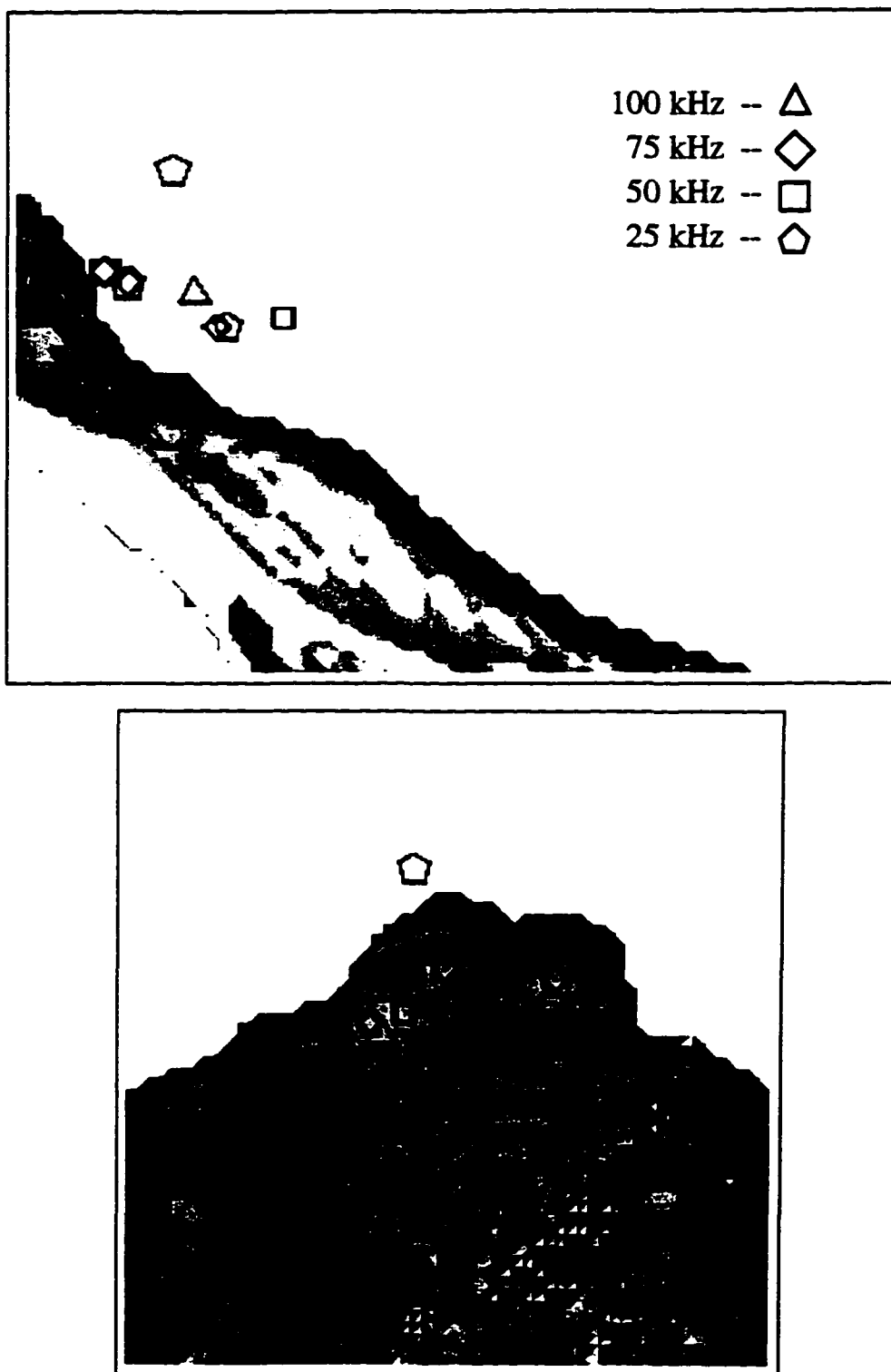


Figure 7.30. Positions of the 'epicenters' from the 5° inverse skull and soft tissue simulations at four frequencies. Top diagram is a PSR view of the maxima positions from the right side; bottom diagram is a PSR view from the front side. When multiple maxima exist, the size of the symbols have been scaled to the intensity of the maxima represented. The skull isosurface is included for positional orientation.

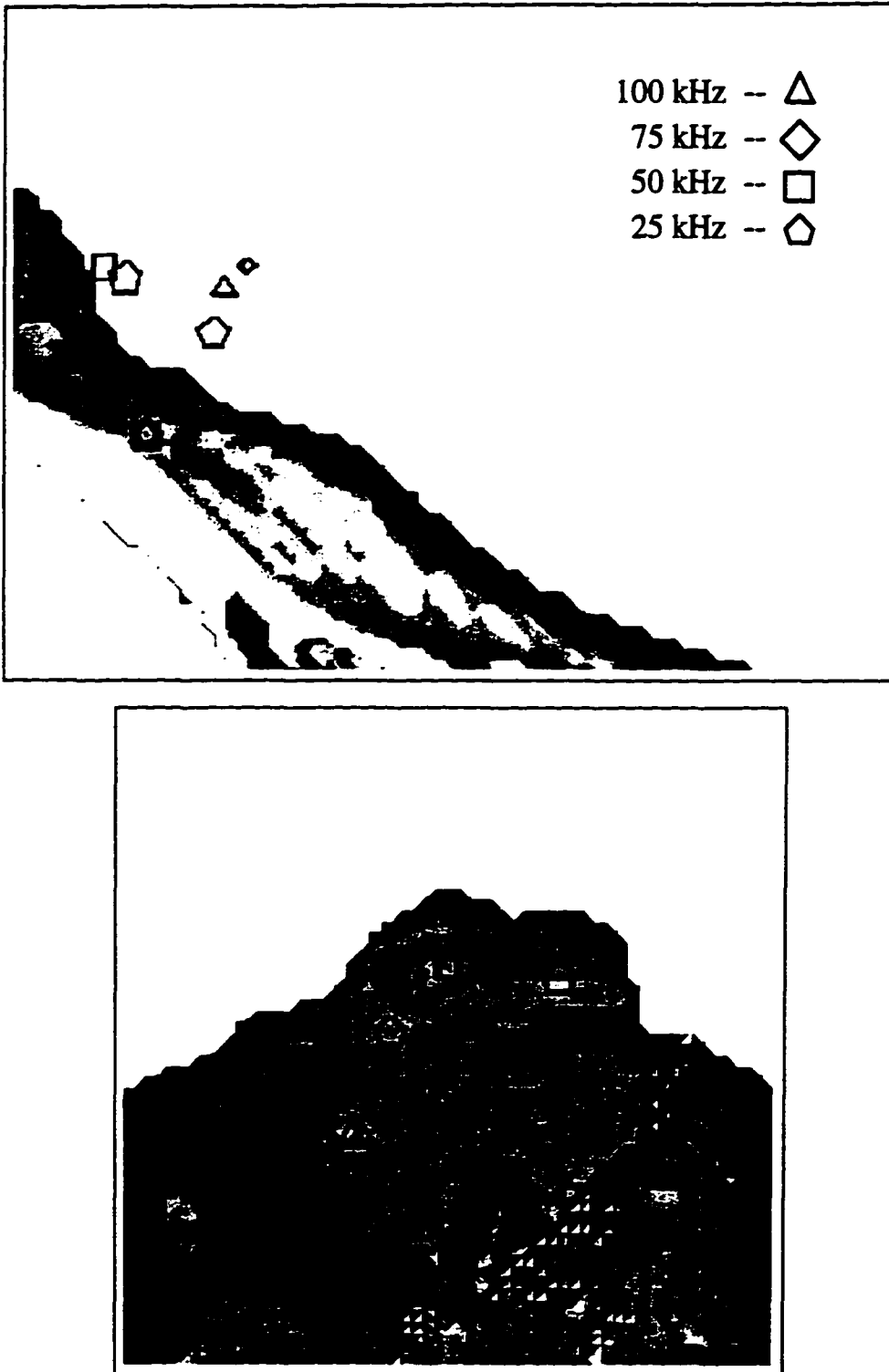


Figure 7.31. Positions of the 'epicenters' from the 10° inverse skull and soft tissue simulations at four frequencies. Top diagram is a PSR view of the maxima positions from the right side; bottom diagram is a PSR view from the front side. When multiple maxima exist, the size of the symbols have been scaled to the intensity of the maxima represented. The skull isosurface is included for positional orientation.

Thet,Phi=15.47,-14.55; DI=8.10; freq=25kHz

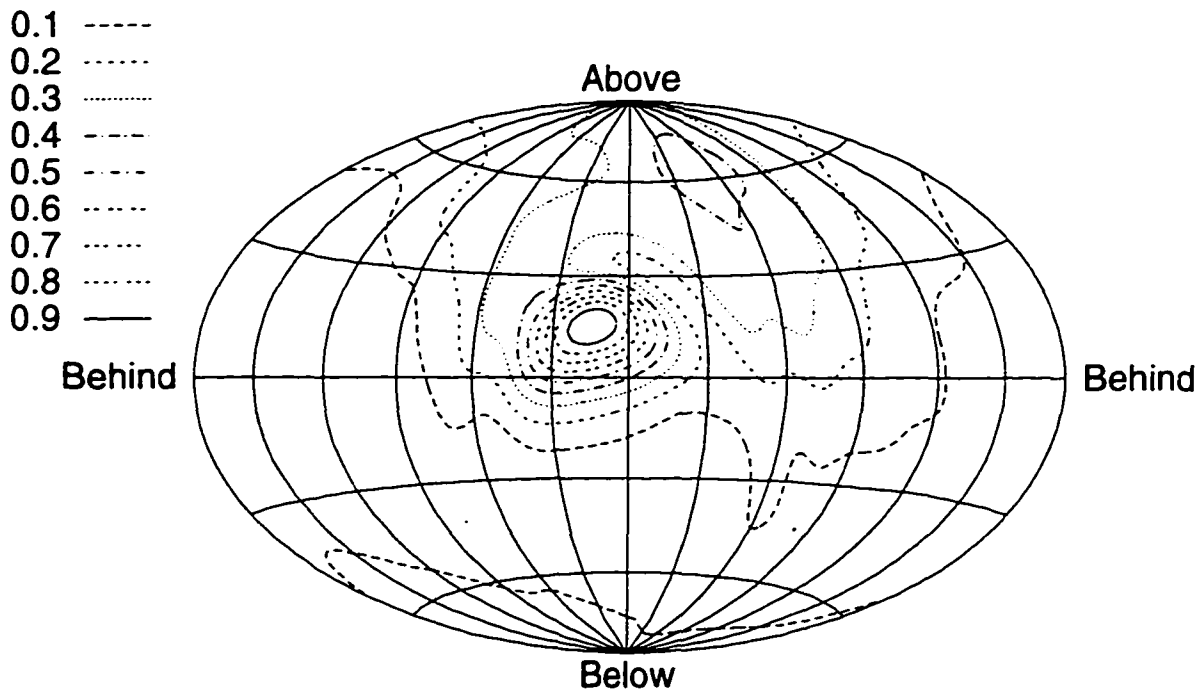
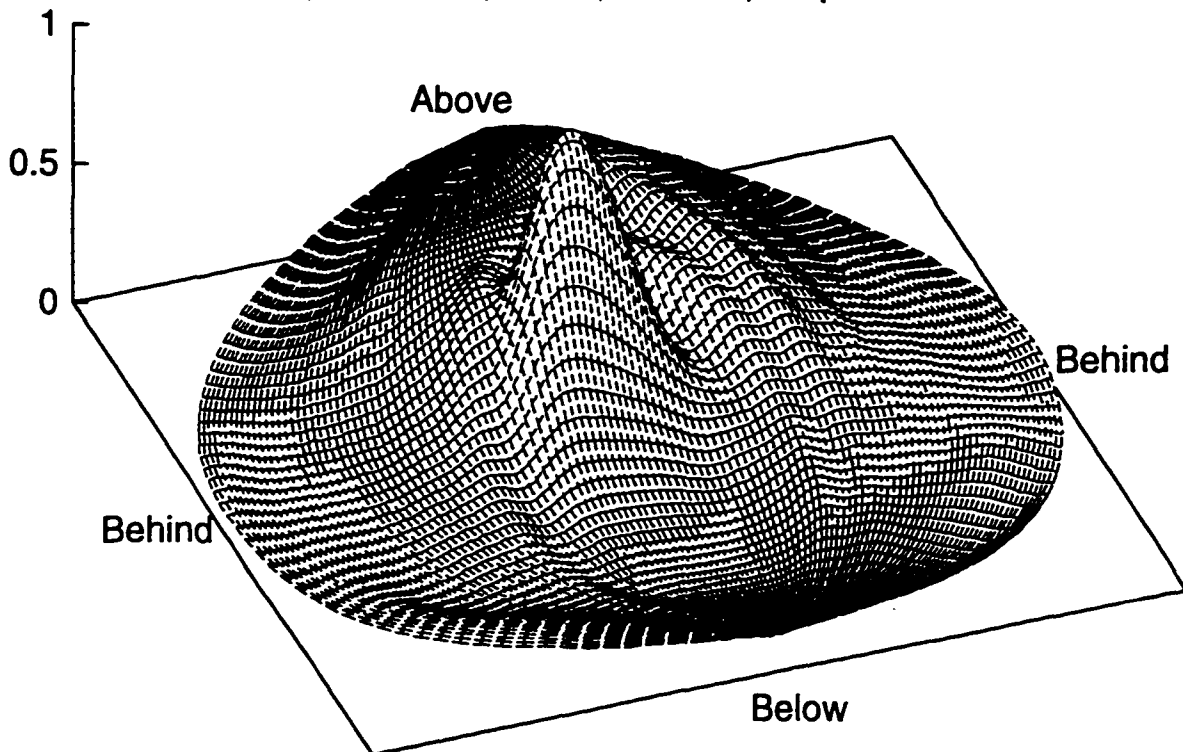


Figure 7.32. Extrapolated far-field emission pattern at 25 kHz for the skull and soft tissue model. The source point was the focal position of highest energy density obtained from a 25 kHz 5° inverse simulation (see Figure 7.30). Top diagram plots intensity as height in a perspective view of the far-field data. Bottom diagram is a contour plot of the same data, also plotted in the global equal-area projection. The direction angles of the emission peak and the directivity index for this pattern are indicated.

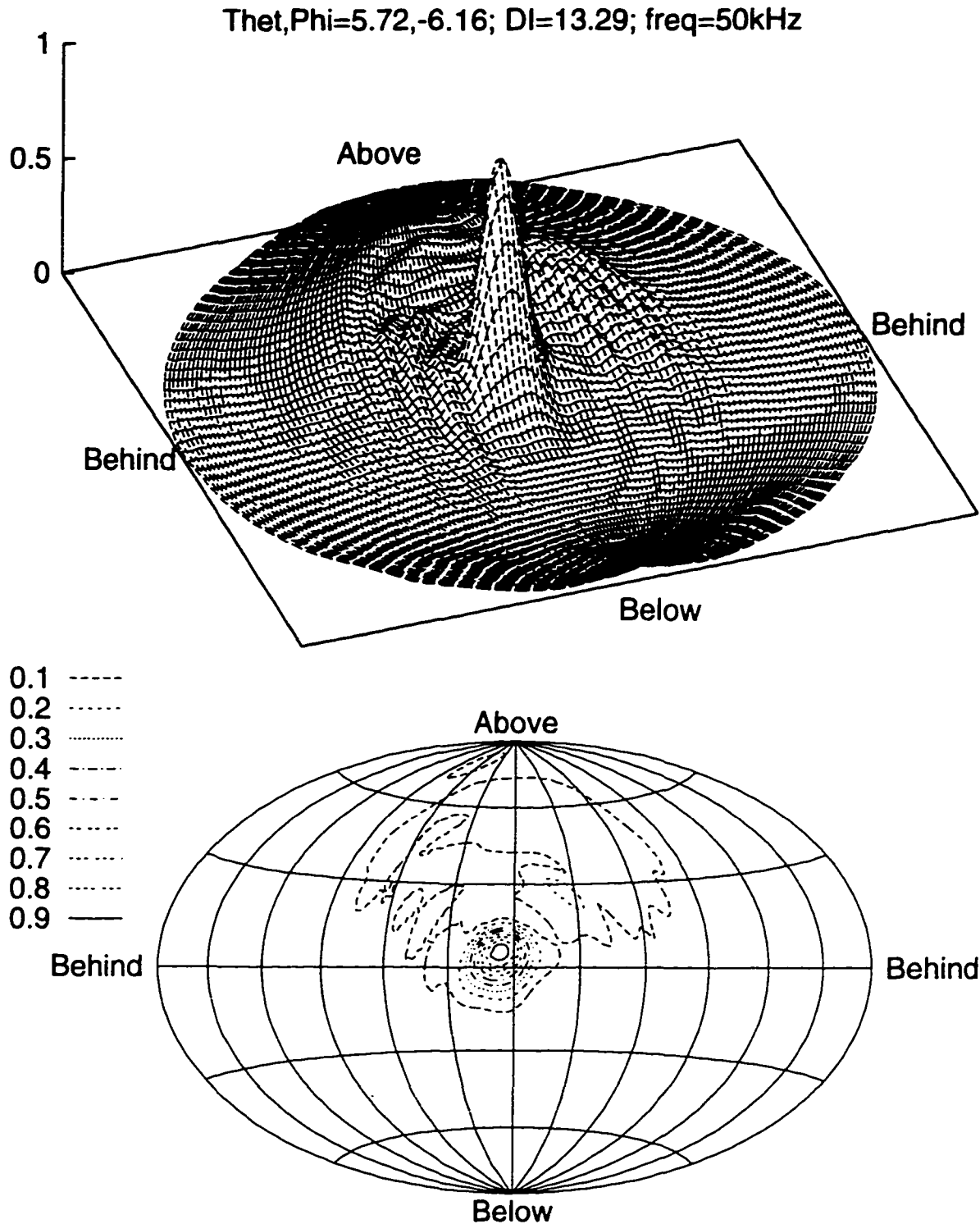


Figure 7.33. Extrapolated far-field emission pattern at 50 kHz for the skull and soft tissue model. The source point was the focal position of highest energy density obtained from a 50 kHz 5° inverse simulation (see Figure 7.30). Top diagram plots intensity as height in a perspective view of the far-field data. Bottom diagram is a contour plot of the same data, also plotted in the global equal-area projection. The direction angles of the emission peak and the directivity index for this pattern are indicated.

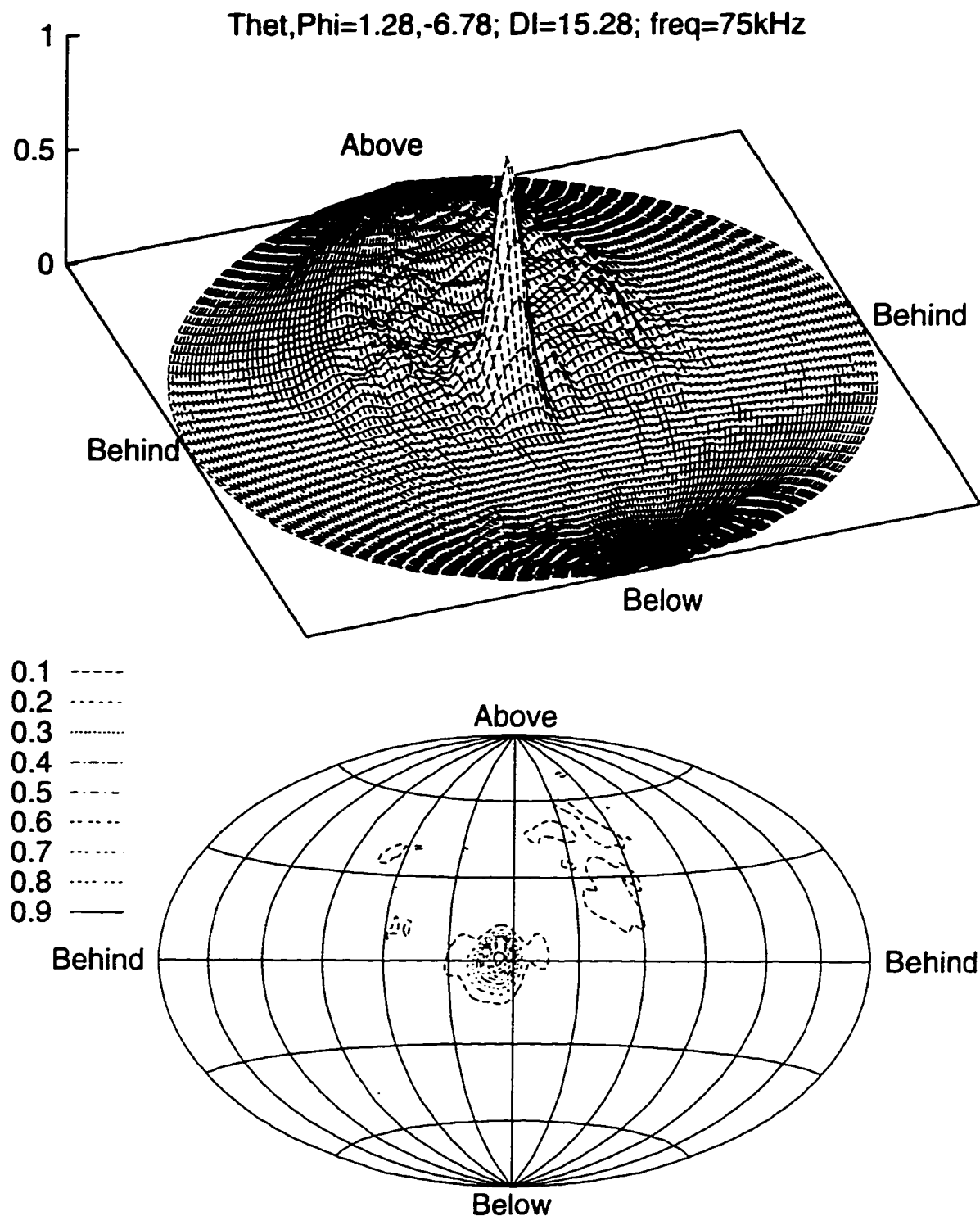


Figure 7.34. Extrapolated far-field emission pattern at 75 kHz for the skull and soft tissue model. The source point was the focal position of highest energy density obtained from a 75 kHz 5° inverse simulation (see Figure 7.30). Top diagram plots intensity as height in a perspective view of the far-field data. Bottom diagram is a contour plot of the same data, also plotted in the global equal-area projection. The direction angles of the emission peak and the directivity index for this pattern are indicated.

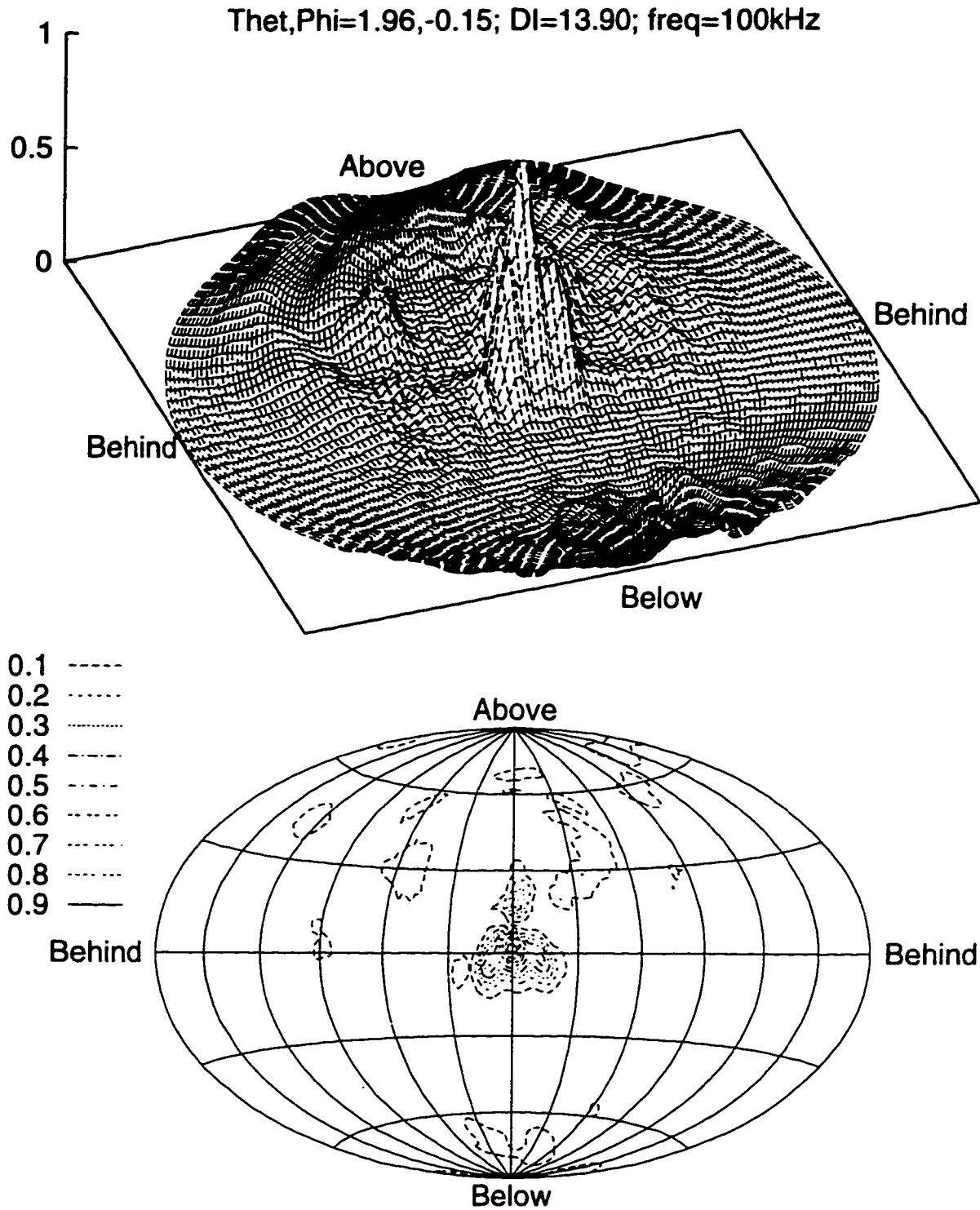


Figure 7.35. Extrapolated far-field emission pattern at 100 kHz for the skull and soft tissue model. The source point was the focal position of highest energy density obtained from a 100 kHz 5° inverse simulation (see Figure 7.30). Top diagram plots intensity as height in a perspective view of the far-field data. Bottom diagram is a contour plot of the same data, also plotted in the global equal-area projection. The direction angles of the emission peak and the directivity index for this pattern are indicated.

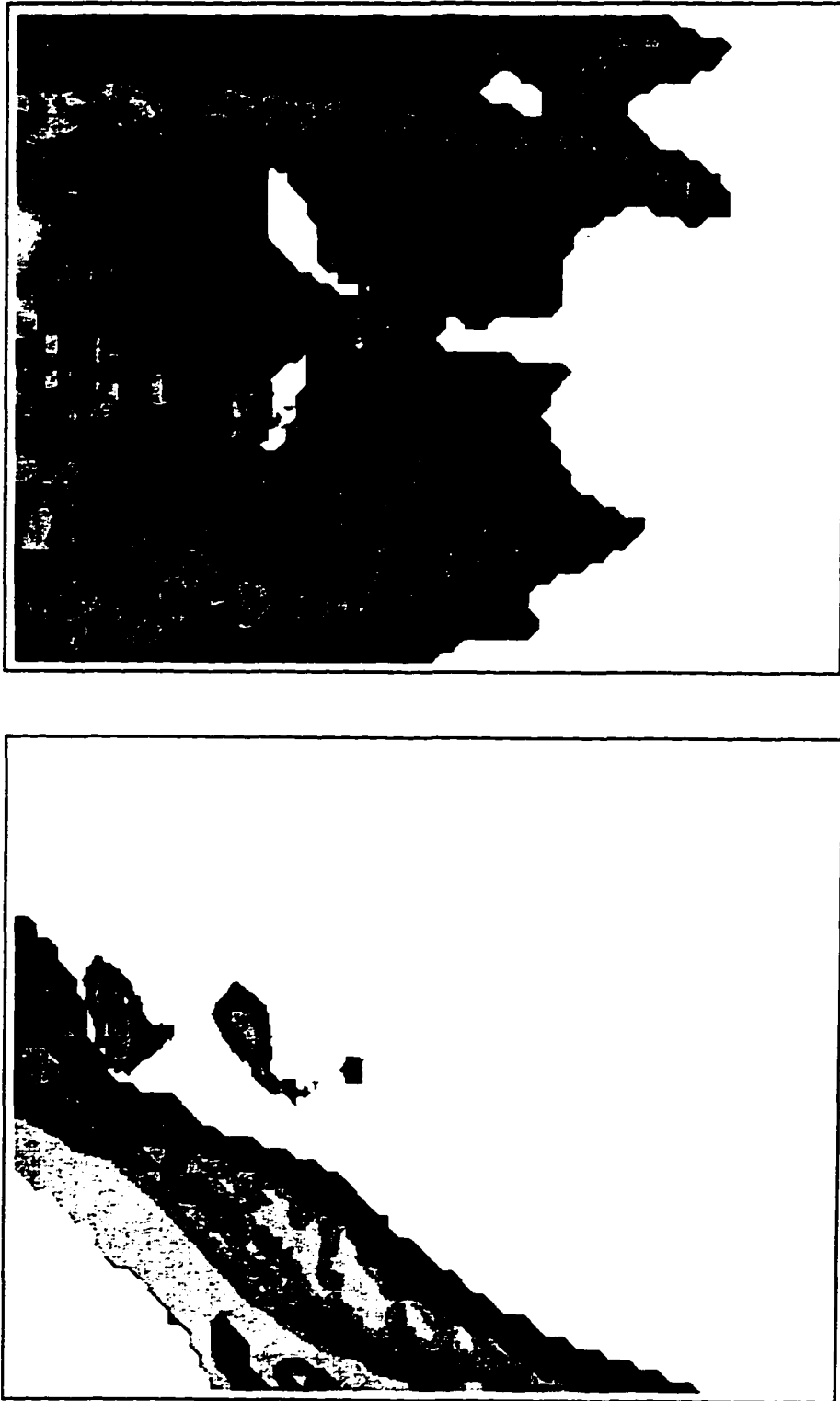


Figure 7.36. Visualizations of the isosurface at 50% of the PSR acoustic energy density for a 5th inverse 50 kHz skull, air sacs, and soft tissue simulation. Top diagram is a view of the PSR from above. Lower diagram is a view of the PSR from the right side. The skull isosurface is included for positional orientation.

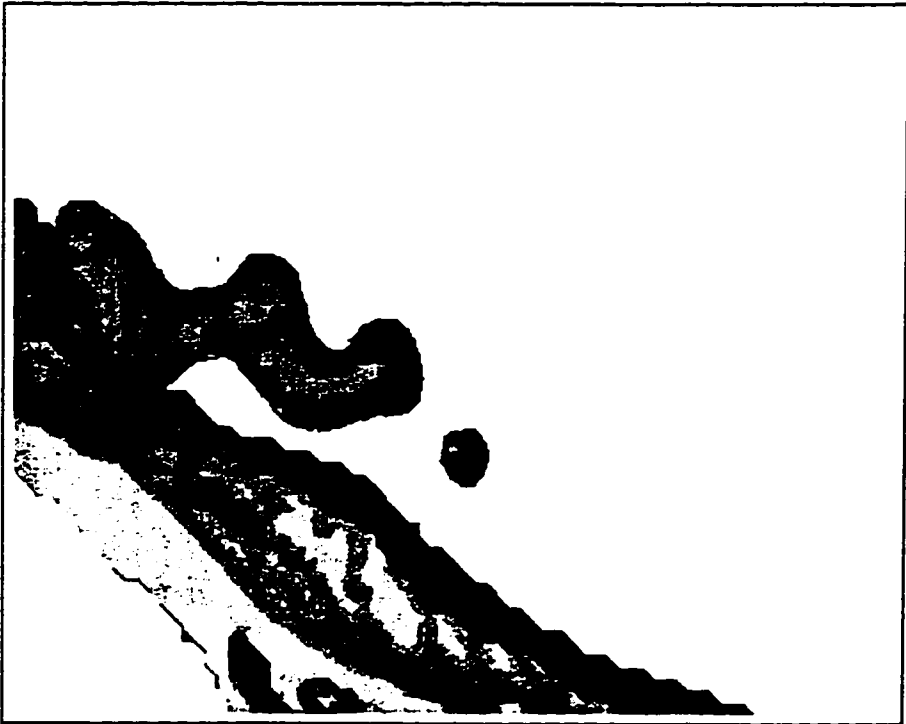


Figure 7.37. Visualizations of the isosurface at 30% of the PSR acoustic energy density for a 5° inverse 50 kHz skull, air sacs, and soft tissue simulation. Top diagram is a view of the PSR from above. Lower diagram is a view of the PSR from the right side. The skull isosurface is included for positional orientation.



Figure 7.38. Visualizations of the isosurface at 10% of the PSR acoustic energy density for a 5° inverse 50 kHz skull, air sacs, and soft tissue simulation. Top diagram is a view of the PSR from above. Lower diagram is a view of the PSR from the right side. The skull isosurface is included for positional orientation.



Figure 7.39. Visualizations of the isosurface at 50% of the PSR acoustic energy density for a 5° inverse 75 kHz skull, air sacs, and soft tissue simulation. Top diagram is a view of the PSR from above. Lower diagram is a view of the PSR from the right side. The skull isosurface is included for positional orientation.

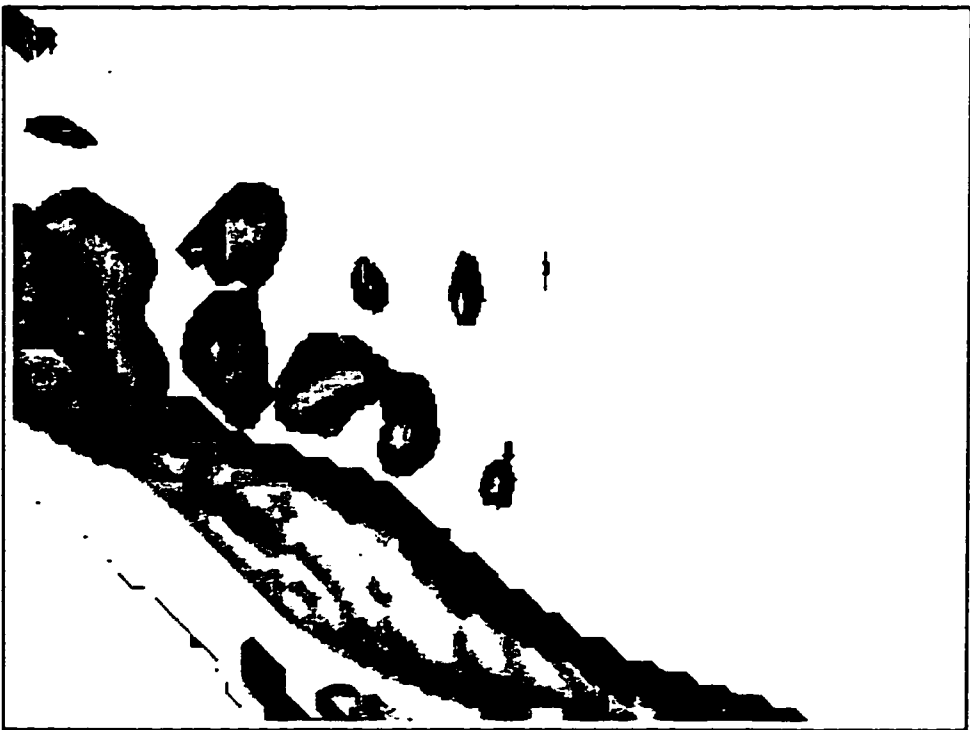
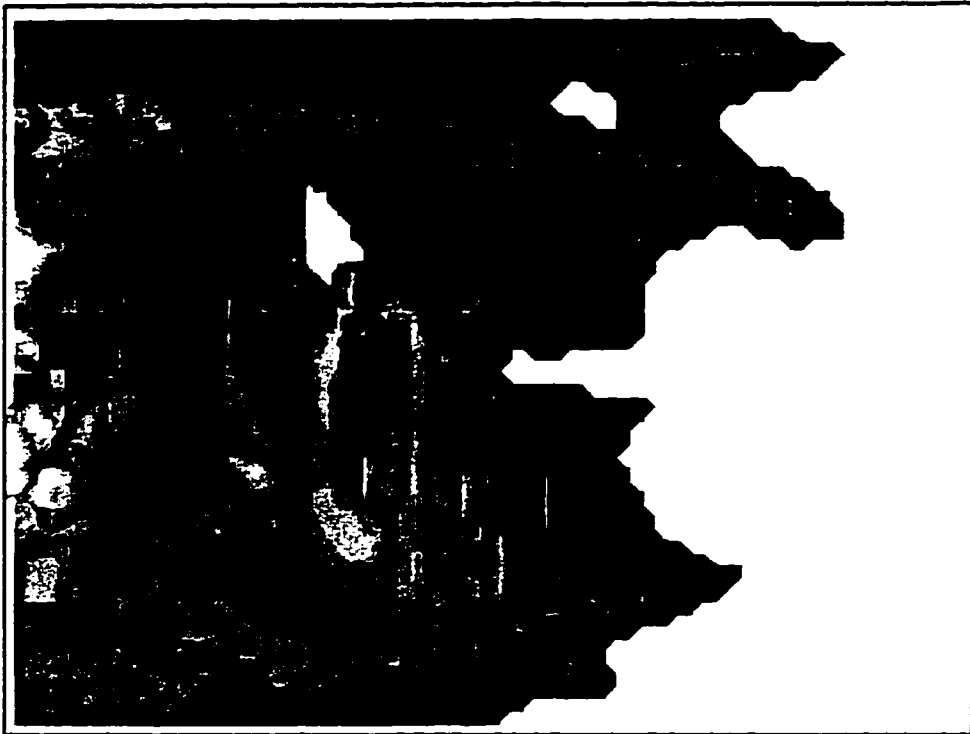


Figure 7.40. Visualizations of the isosurface at 20% of the PSR acoustic energy density for a 5° inverse 75 kHz skull, air sacs, and soft tissue simulation. Top diagram is a view of the PSR from above. Lower diagram is a view of the PSR from the right side. The skull isosurface is included for positional orientation.



Figure 7.41. Visualizations of the isosurface at 10% of the PSR acoustic energy density for a 5° inverse 75 kHz skull, air sacs, and soft tissue simulation. Top diagram is a view of the PSR from above. Lower diagram is a view of the PSR from the right side. The skull isosurface is included for positional orientation.

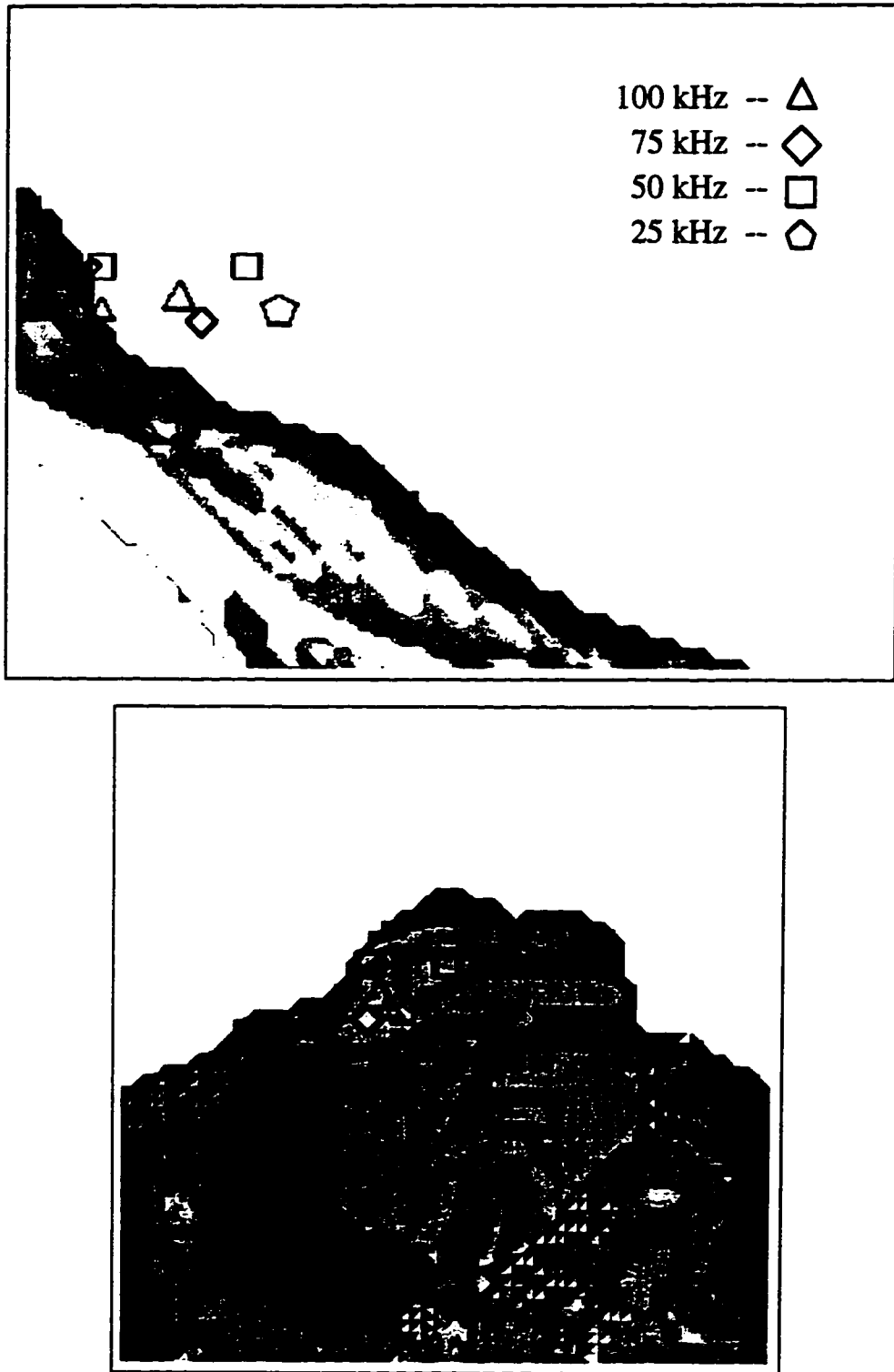


Figure 7.42. Positions of the 'epicenters' from the 0° inverse skull, air sacs, and soft tissue simulations at four frequencies. Top diagram is a PSR view of the maxima positions from the right side; bottom diagram is a PSR view from the front side. When multiple maxima exist, the size of the symbols have been scaled to the intensity of the maxima represented. The skull isosurface is included for positional orientation.

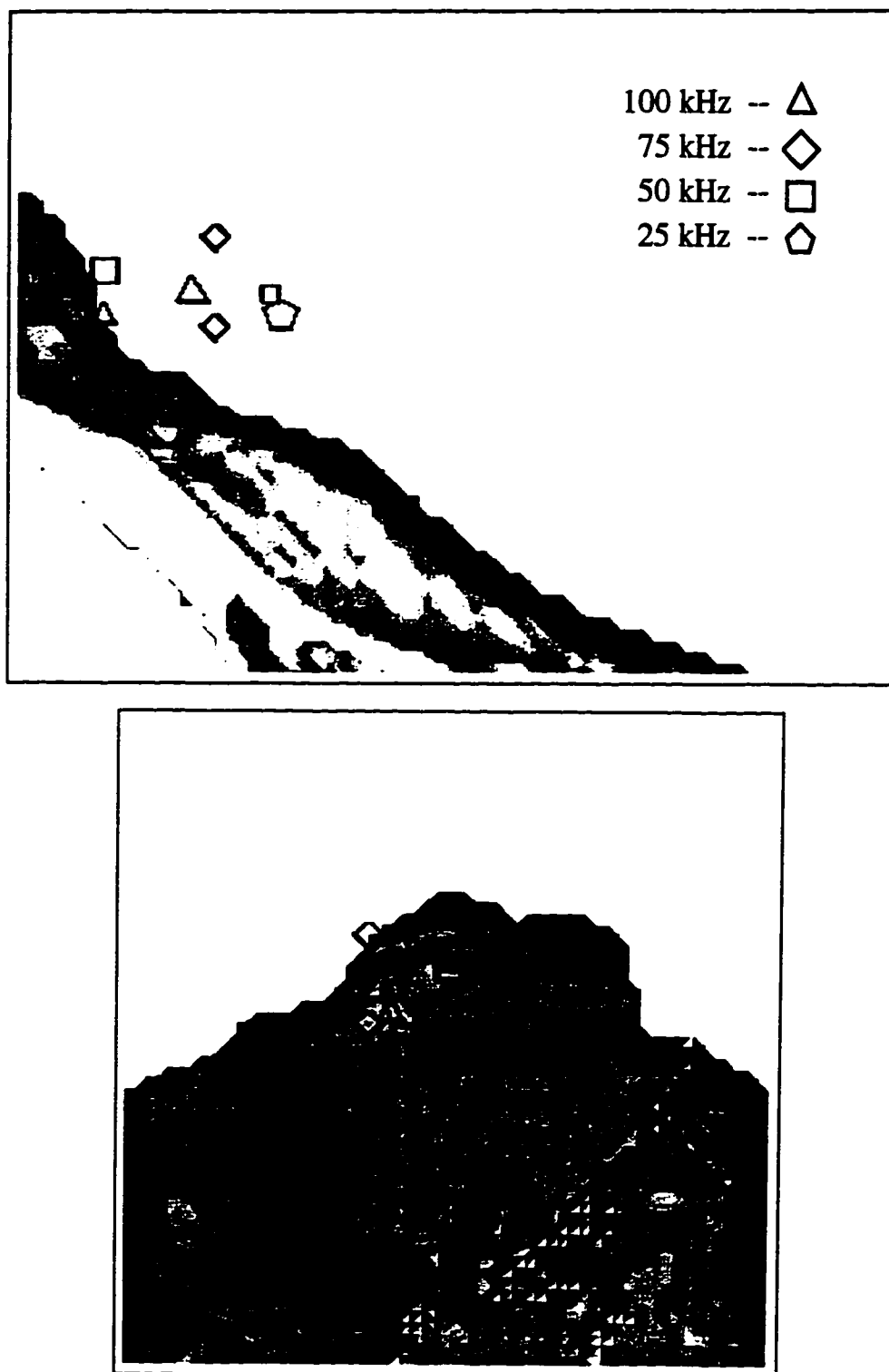


Figure 7.43. Positions of the 'epicenters' from the 5° inverse skull, air sacs, and soft tissue simulations at four frequencies. Top diagram is a PSR view of the maxima positions from the right side; bottom diagram is a PSR view from the front side. When multiple maxima exist, the size of the symbols have been scaled to the intensity of the maxima represented. The skull isosurface is included for positional orientation.

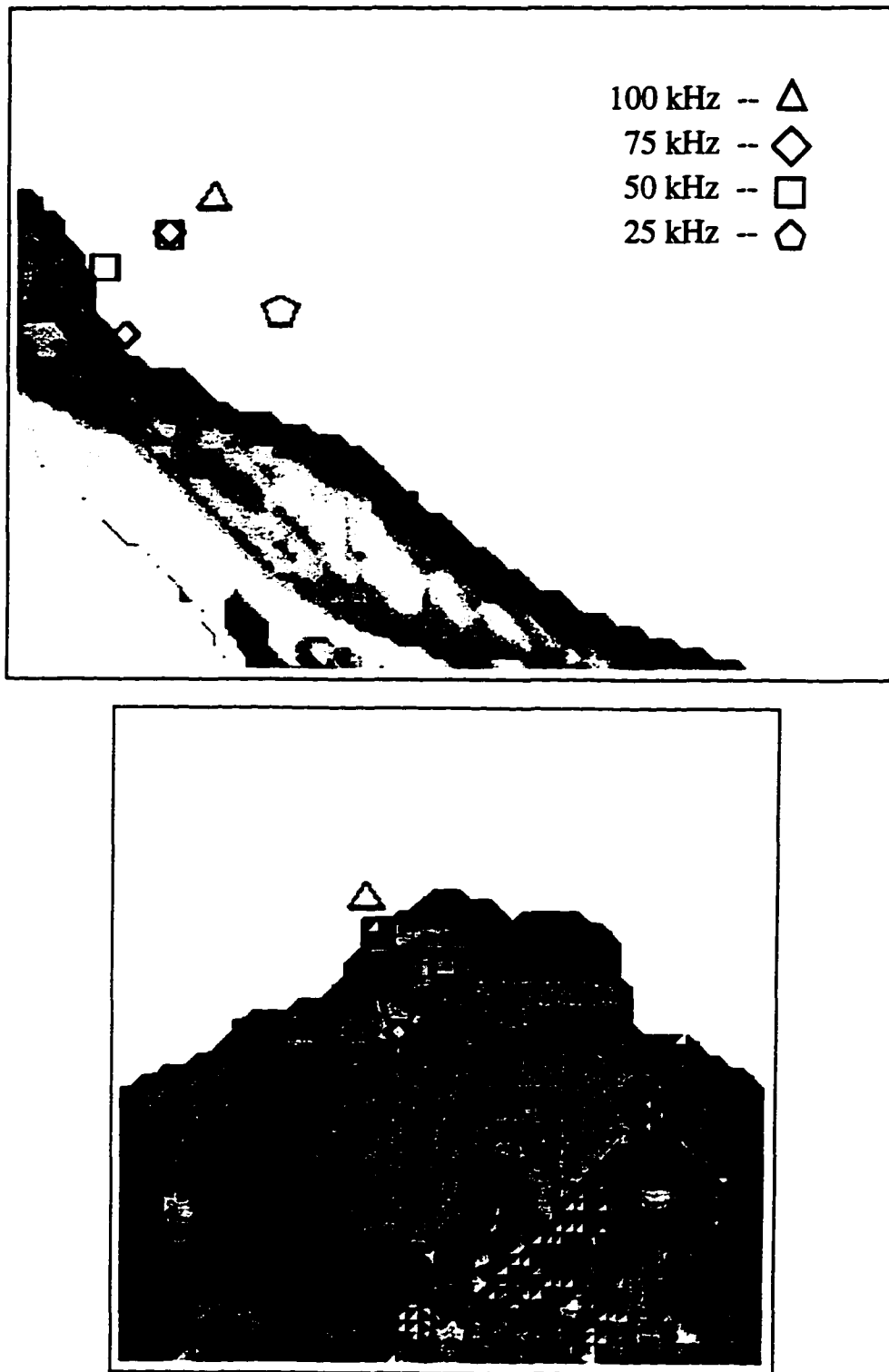


Figure 7.44. Positions of the 'epicenters' from the 10° inverse skull, air sacs, and soft tissue simulations at four frequencies. Top diagram is a PSR view of the maxima positions from the right side; bottom diagram is a PSR view from the front side. When multiple maxima exist, the size of the symbols have been scaled to the intensity of the maxima represented. The skull isosurface is included for positional orientation.

Thet,Phi=13.86,-1.37; DI=11.57; freq=25kHz

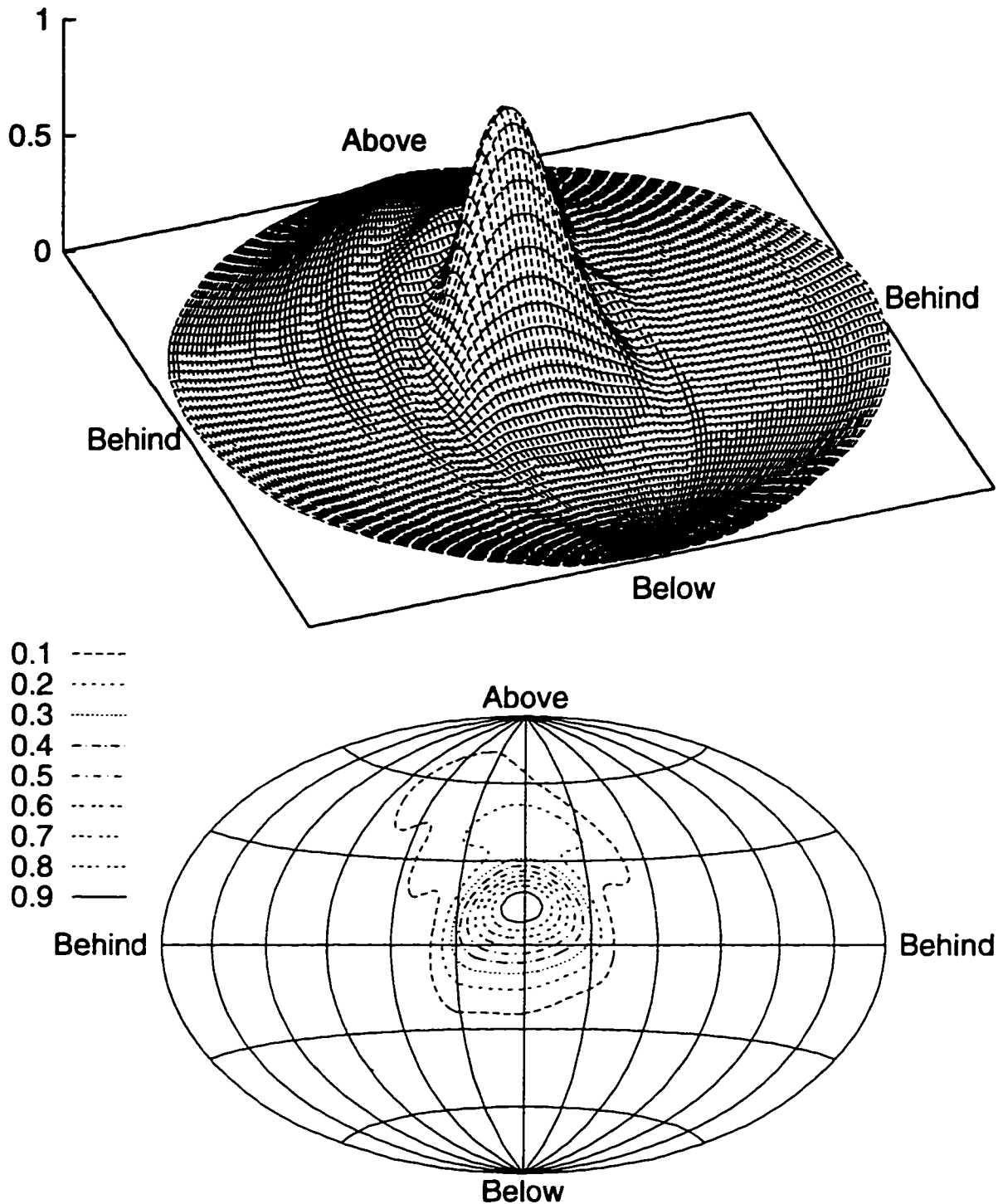


Figure 7.45. Extrapolated far-field emission pattern at 25 kHz for the skull, air sacs, and soft tissue model. The source point was the focal position of highest energy density obtained from a 25 kHz 5° inverse simulation (see Figure 7.43). Top diagram plots intensity as height in a perspective view of the far-field data. Bottom diagram is a contour plot of the same data, also plotted in the global equal-area projection. The direction angles of the emission peak and the directivity index for this pattern are indicated.

Thet,Phi=4.20,-7.91; DI=13.77; freq=50kHz

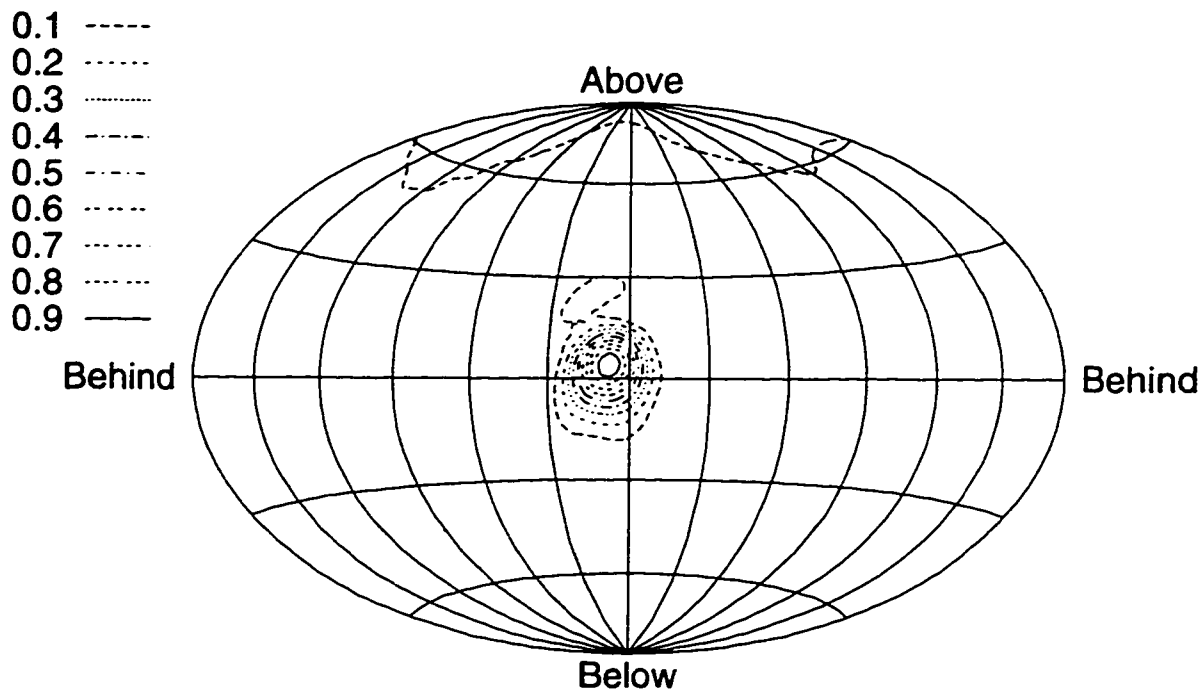
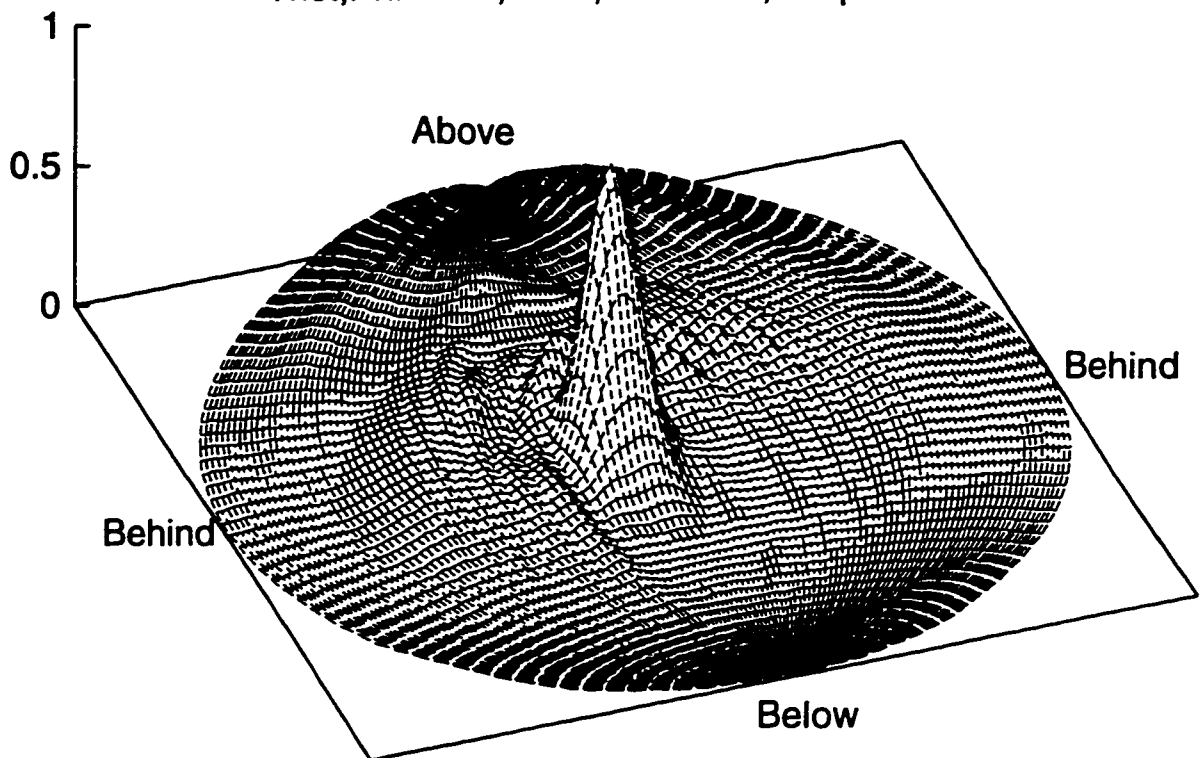


Figure 7.46. Extrapolated far-field emission pattern at 50 kHz for the skull, air sacs, and soft tissue model. The source point was the focal position of highest energy density obtained from a 50 kHz 5° inverse simulation (see Figure 7.43). Top diagram plots intensity as height in a perspective view of the far-field data. Bottom diagram is a contour plot of the same data, also plotted in the global equal-area projection. The direction angles of the emission peak and the directivity index for this pattern are indicated.

Thet,Phi=6.27,-0.19; DI=15.54; freq=75kHz

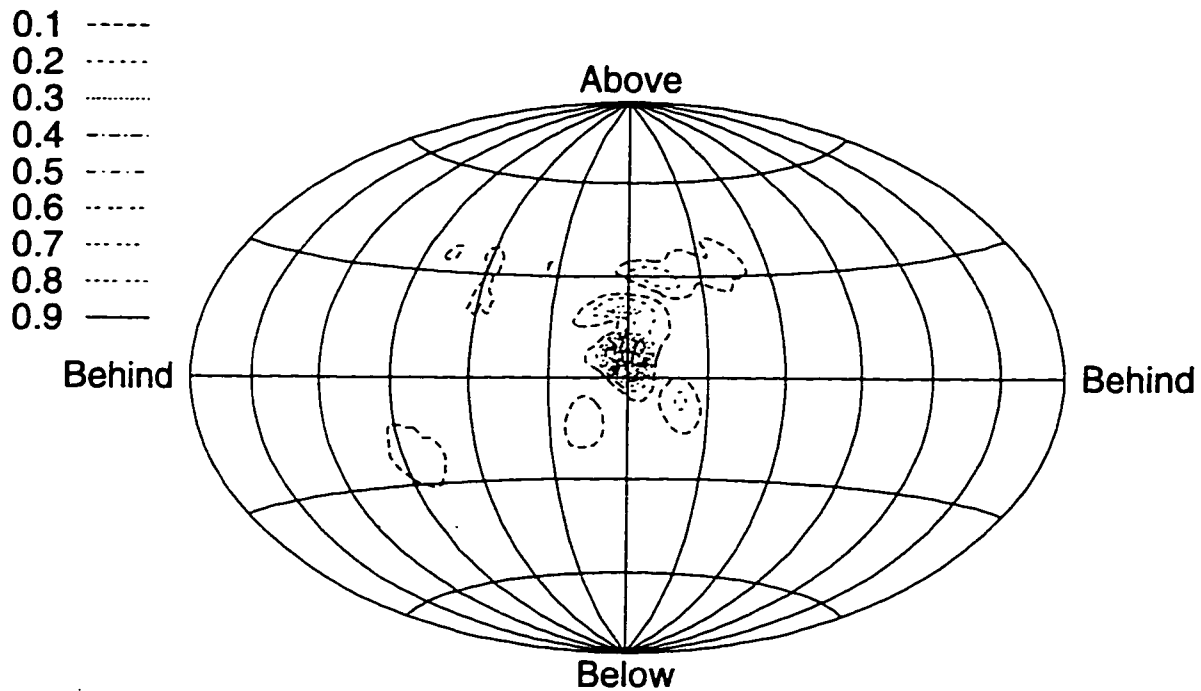
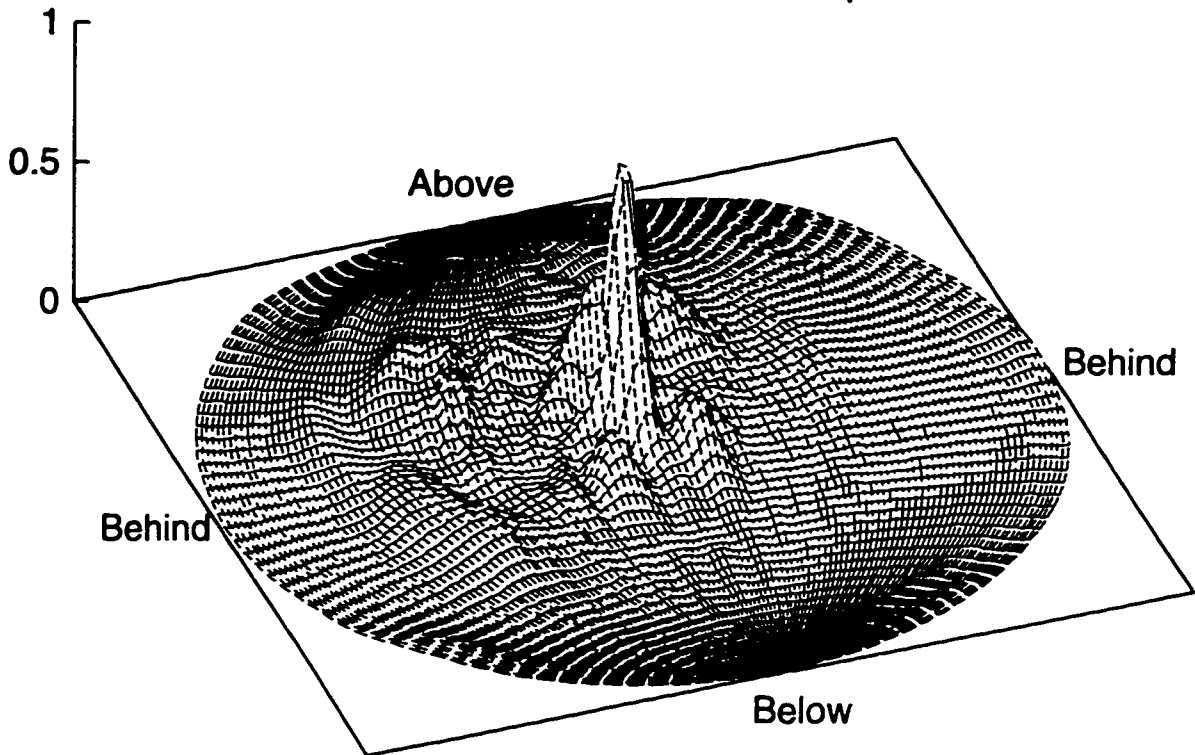


Figure 7.47. Extrapolated far-field emission pattern at 75 kHz for the skull, air sacs, and soft tissue model. The source point was the focal position of highest energy density obtained from a 75 kHz 5^o inverse simulation (see Figure 7.43). Top diagram plots intensity as height in a perspective view of the far-field data. Bottom diagram is a contour plot of the same data, also plotted in the global equal-area projection. The direction angles of the emission peak and the directivity index for this pattern are indicated.

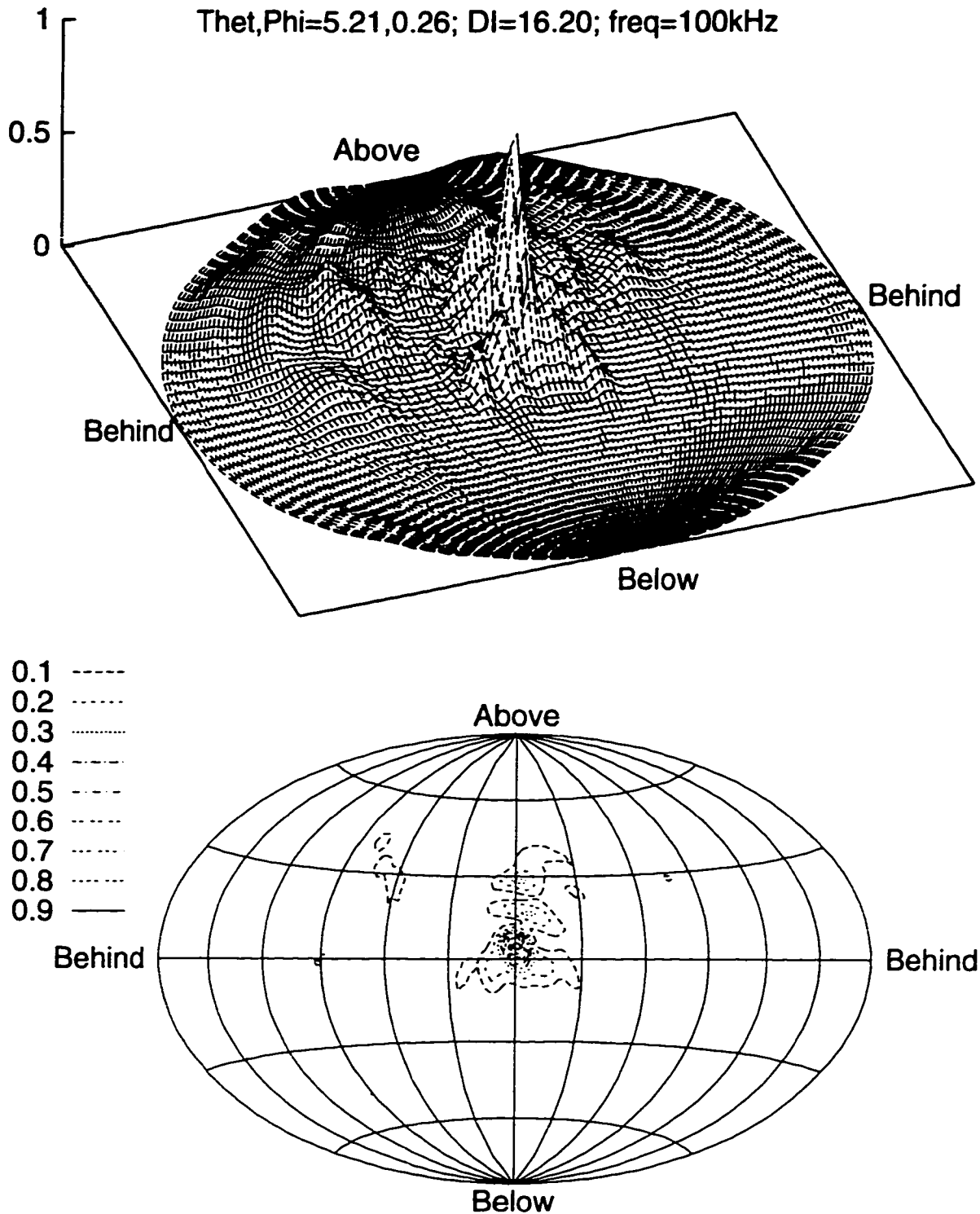


Figure 7.48. Extrapolated far-field emission pattern at 100 kHz for the skull, air sacs, and soft tissue model. The source point was the focal position of highest energy density obtained from a 100 kHz 5° inverse simulation (see Figure 7.43). Top diagram plots intensity as height in a perspective view of the far-field data. Bottom diagram is a contour plot of the same data, also plotted in the global equal-area projection. The direction angles of the emission peak and the directivity index for this pattern are indicated.

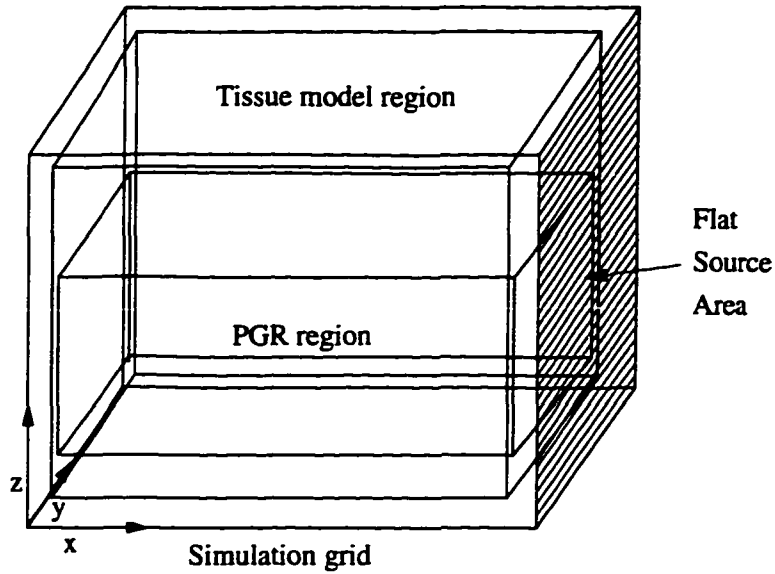


Figure 7.49. Grid setup for the inverse hearing simulations. The region of the grid containing the tissue model is indicated. Note that the front face of the grid is again used as a flat source to ensound the tissue model. The acoustic energy density within the volume labeled 'PGR' was calculated by the simulation programs and visualized with graphics packages.

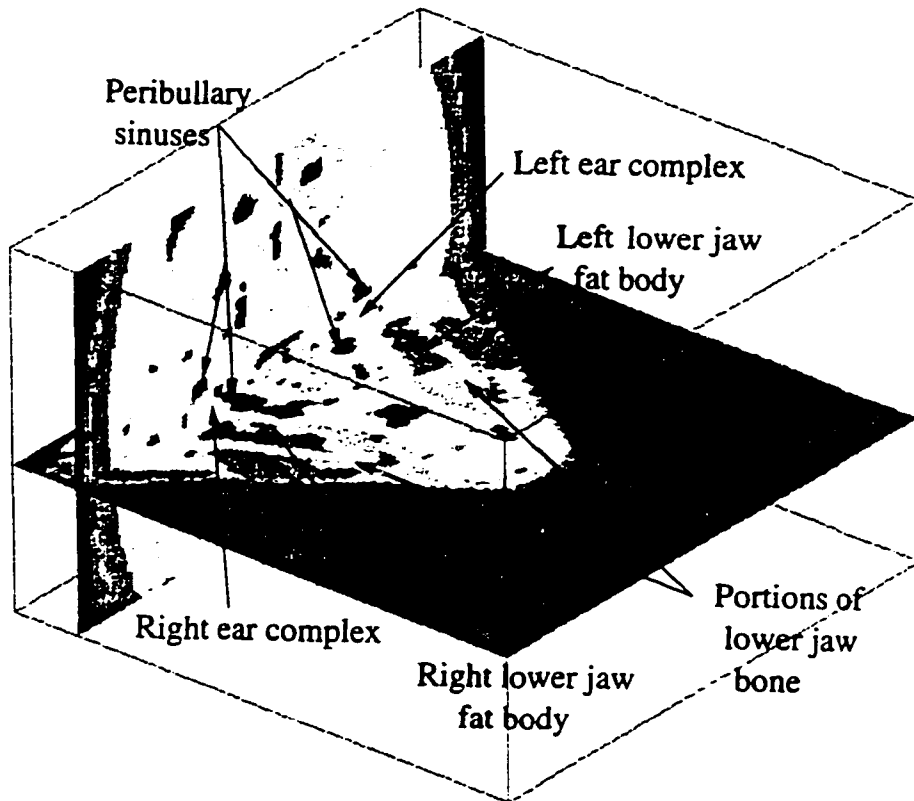


Figure 7.50. Tissues within the PGR region illustrated by several slice planes. Several structures are indicated to enable the reader to establish positional reference in later diagrams of the results of the inverse hearing simulations.

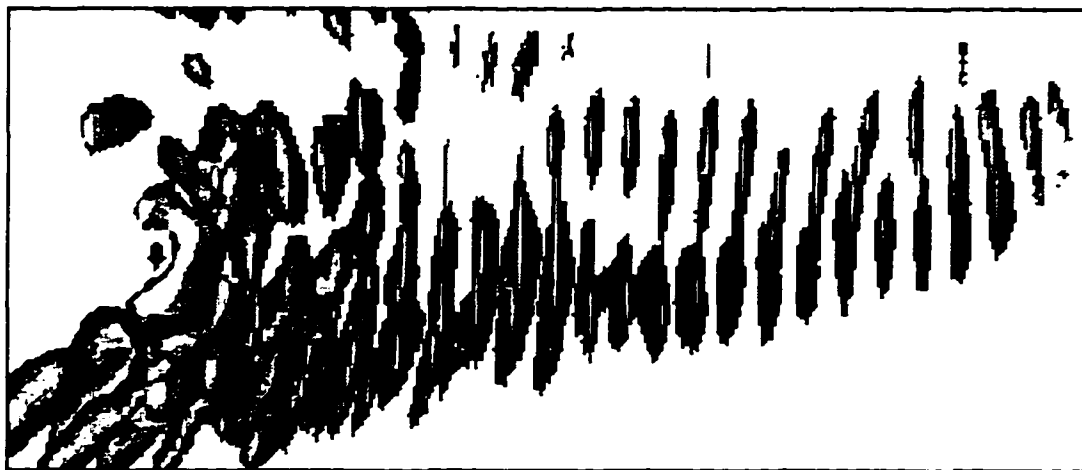
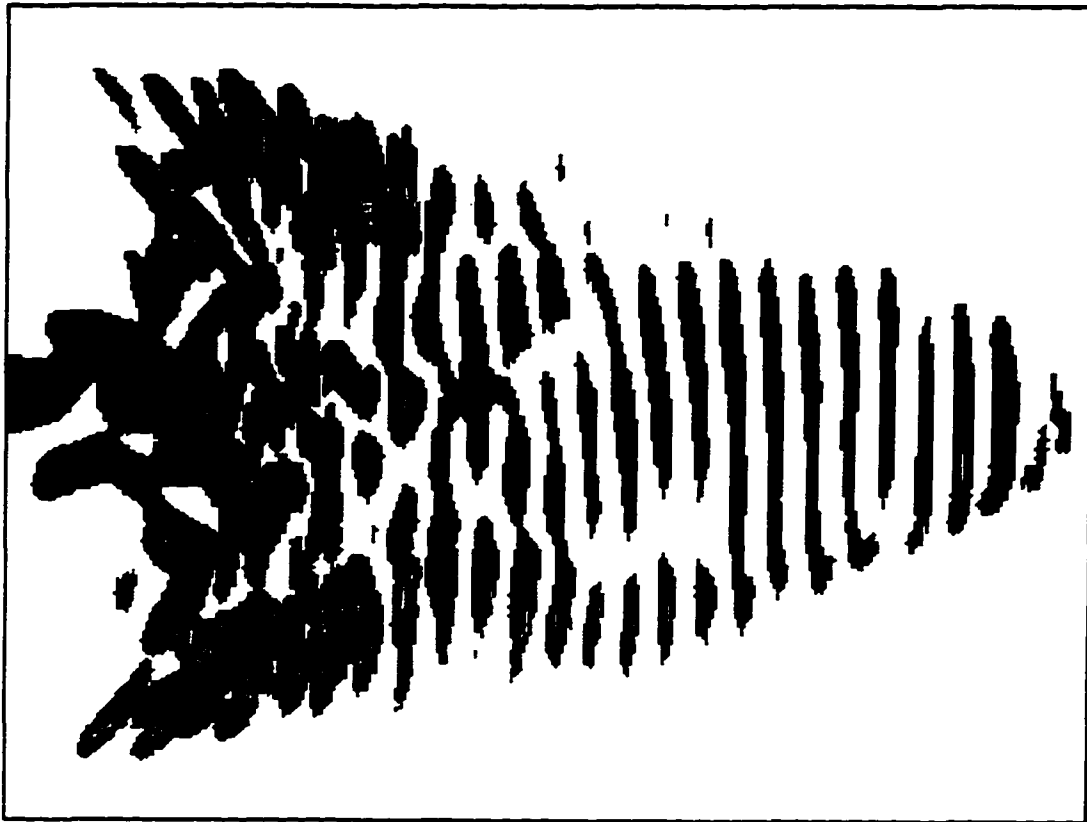


Figure 7.51. Visualizations of the isosurface at 20% of the PGR acoustic energy density for a 50 kHz 0° inverse hearing simulation using a model including the skull, the nasal air sacs, and the peribullary and pterygoid sinuses (but without soft tissue). Top diagram is a view of the PGR from above. Lower diagram is a view of the PGR from the right side.

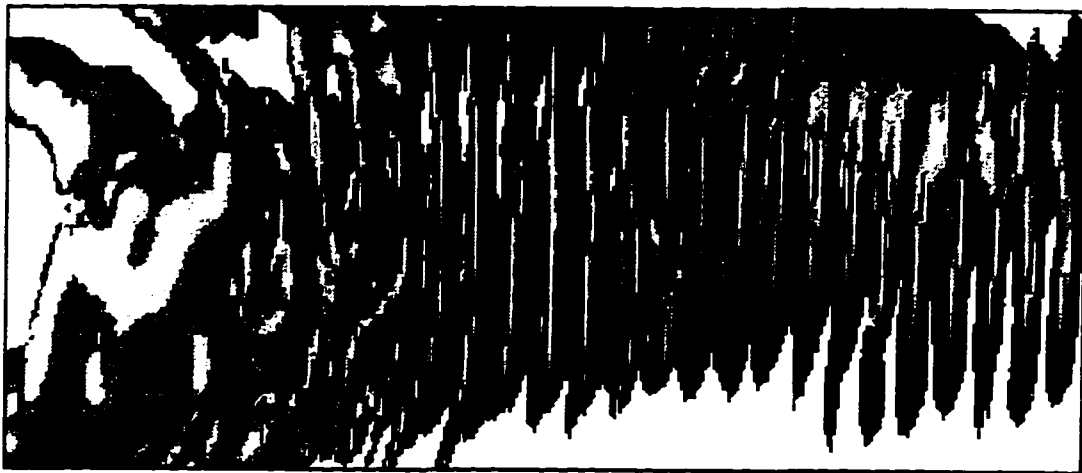
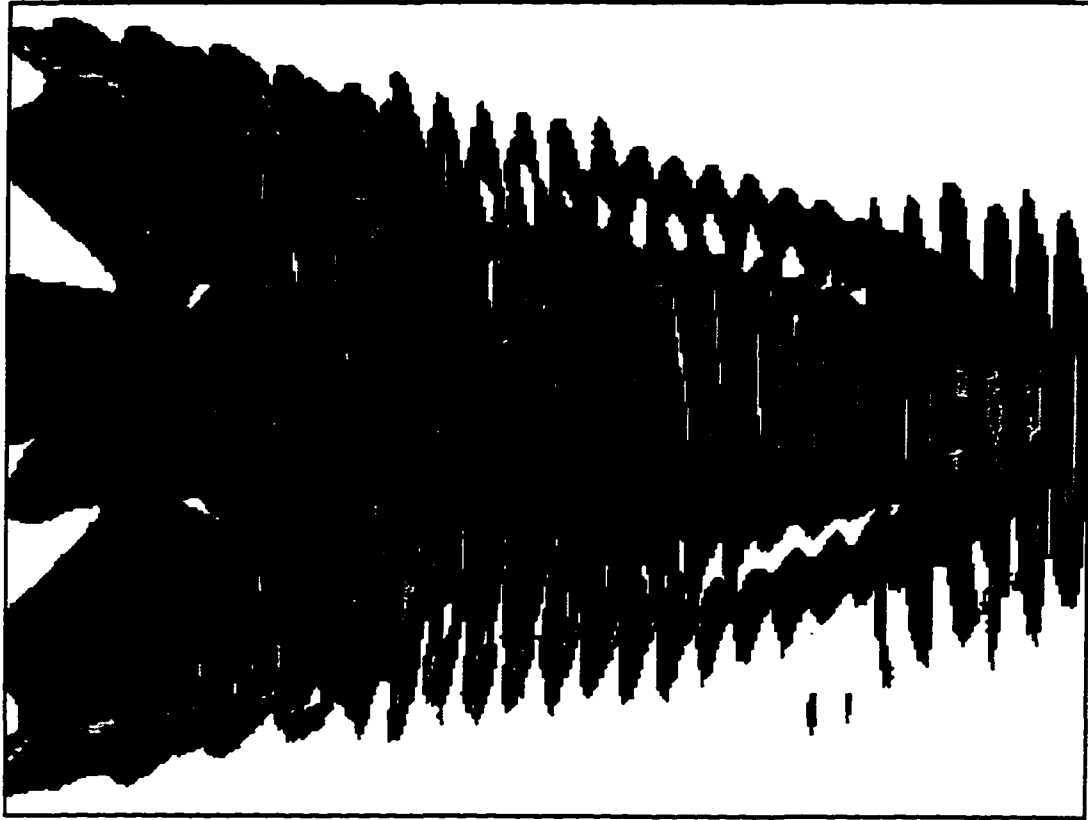


Figure 7.52. Visualizations of the isosurface at 13% of the PGR acoustic energy density for a 50 kHz 0° inverse hearing simulation using a model including the skull, the nasal air sacs, and the peribullary and pterygoid sinuses (but without soft tissue). Top diagram is a view of the PGR from above. Lower diagram is a view of the PGR from the right side.

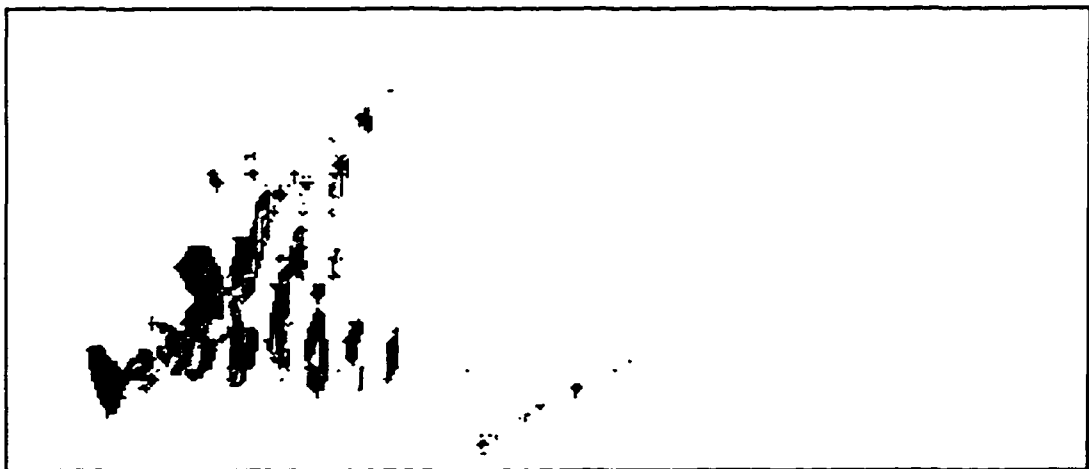
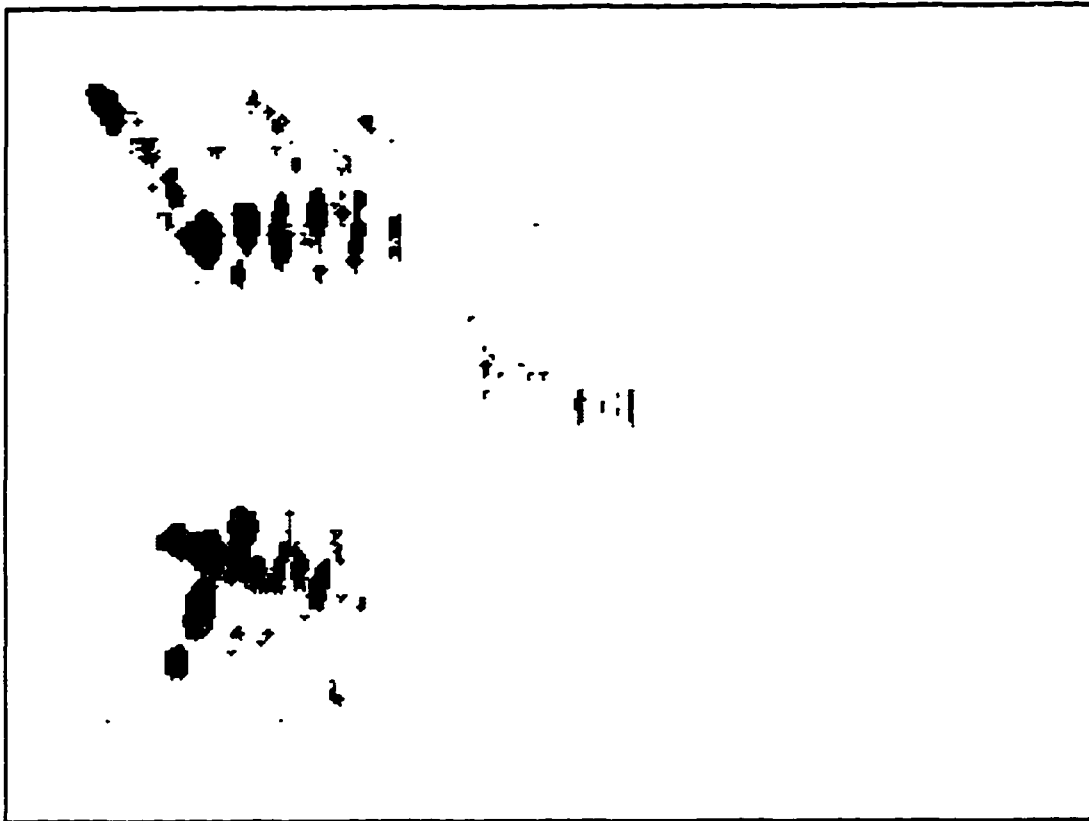


Figure 7.53. Visualizations of the isosurface at 20% of the PGR acoustic energy density for a 50 kHz 0° inverse hearing simulation using the complete model including the skull, soft tissues, nasal air sacs, and the peribullary and pterygoid sinuses. Top diagram is a view of the PGR from above. Lower diagram is a view of the PGR from the right side.

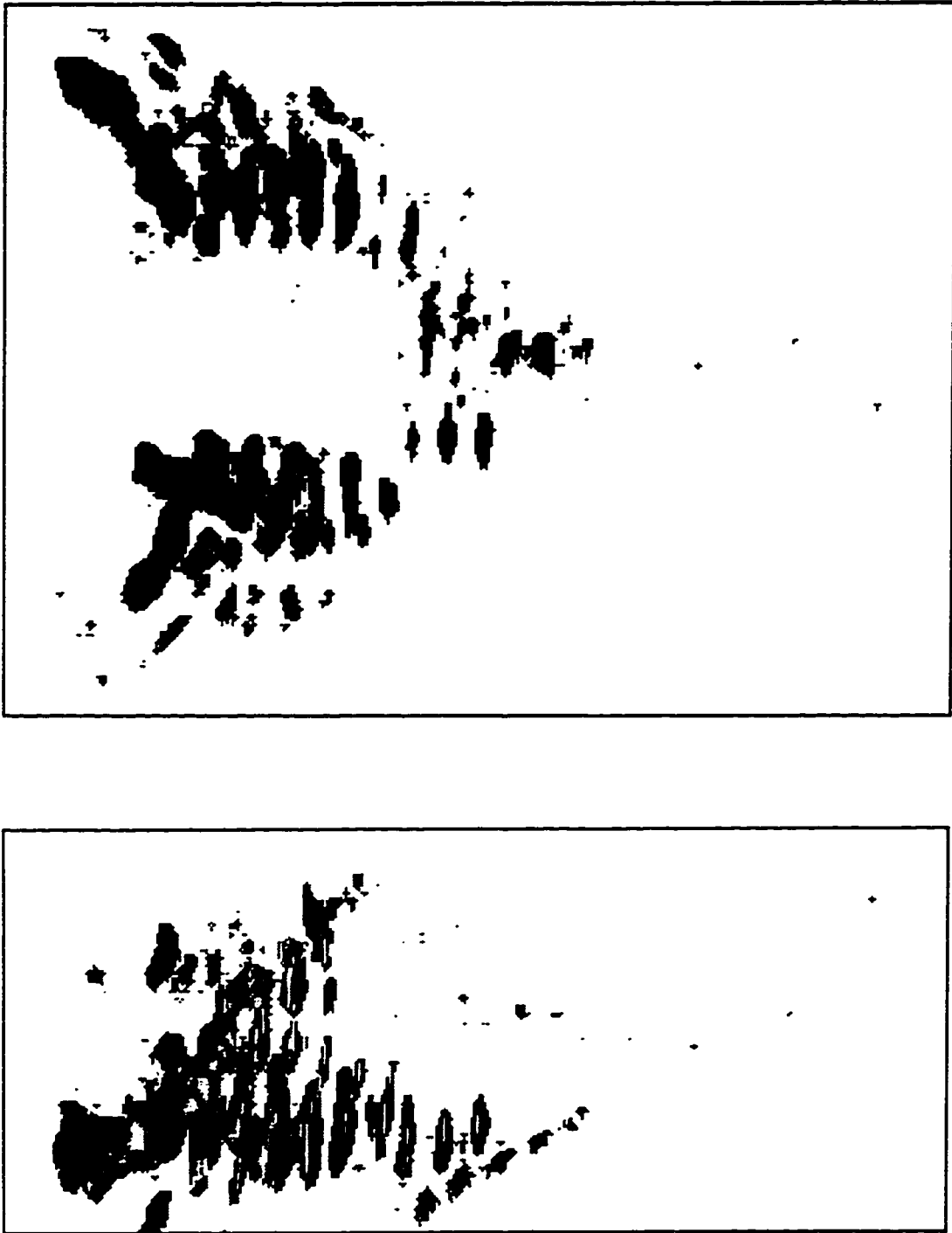


Figure 7.54. Visualizations of the isosurface at 13% of the PGR acoustic energy density for a 50 kHz 0° inverse hearing simulation using the complete model including the skull, soft tissues, nasal air sacs, and the peribullary and pterygoid sinuses. Top diagram is a view of the PGR from above. Lower diagram is a view of the PGR from the right side.

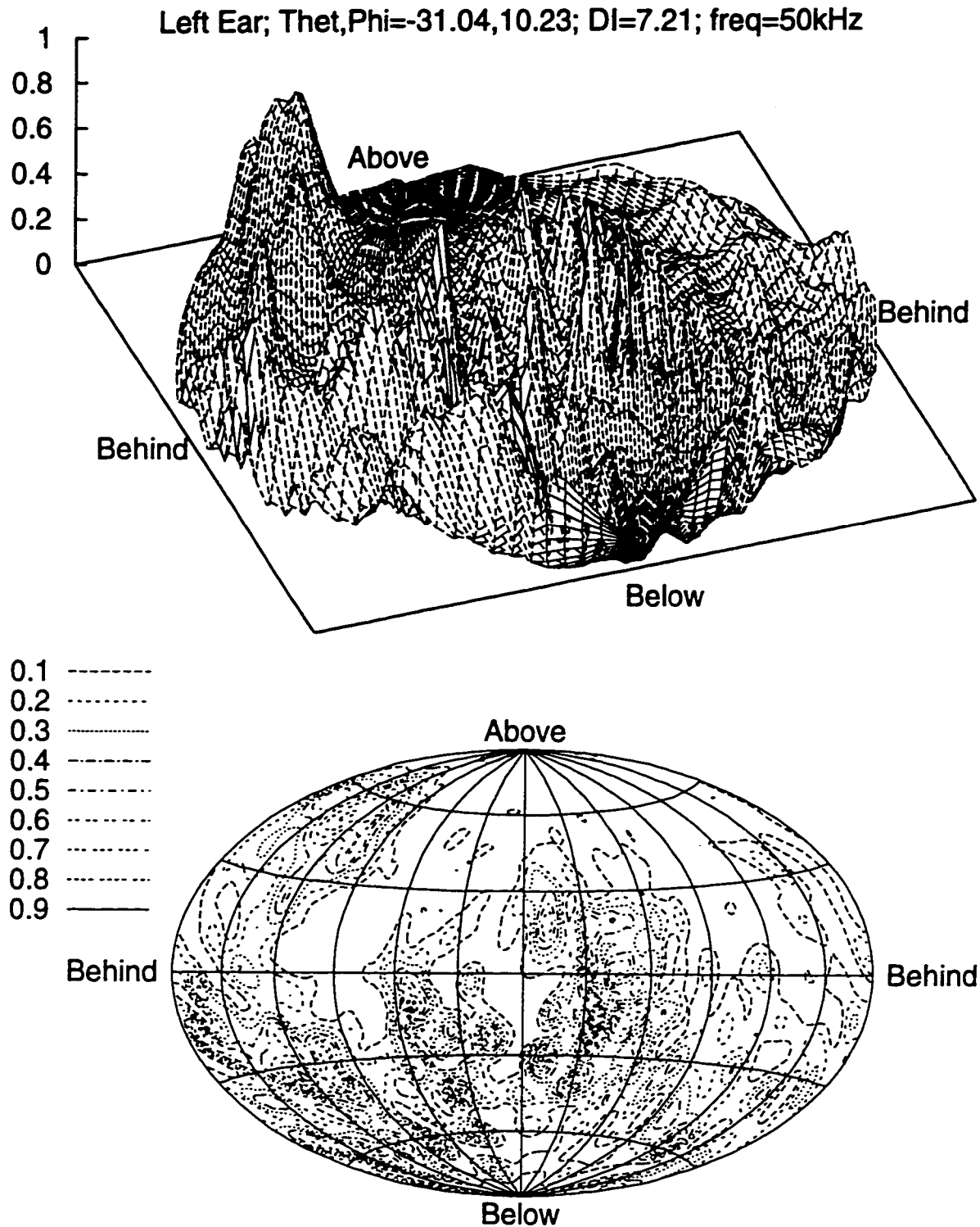


Figure 7.55. Extrapolated far-field emission (receptivity) pattern at 50 kHz for a source placed within the LEFT inner ear for a model including only the skull and the nasal air sacs (without soft tissue and without the peribullary and pterygoid sinuses). Top diagram plots intensity as height in a perspective view of the far-field data. Bottom diagram is a contour plot of the same data, also plotted in the global equal-area projection. The direction angles of the peak and the directivity index for the pattern are indicated.

Right Ear; $\Theta_{et}, \Phi_{et} = -32.18, -8.71$; $DI = 7.60$; $\text{freq} = 50\text{kHz}$

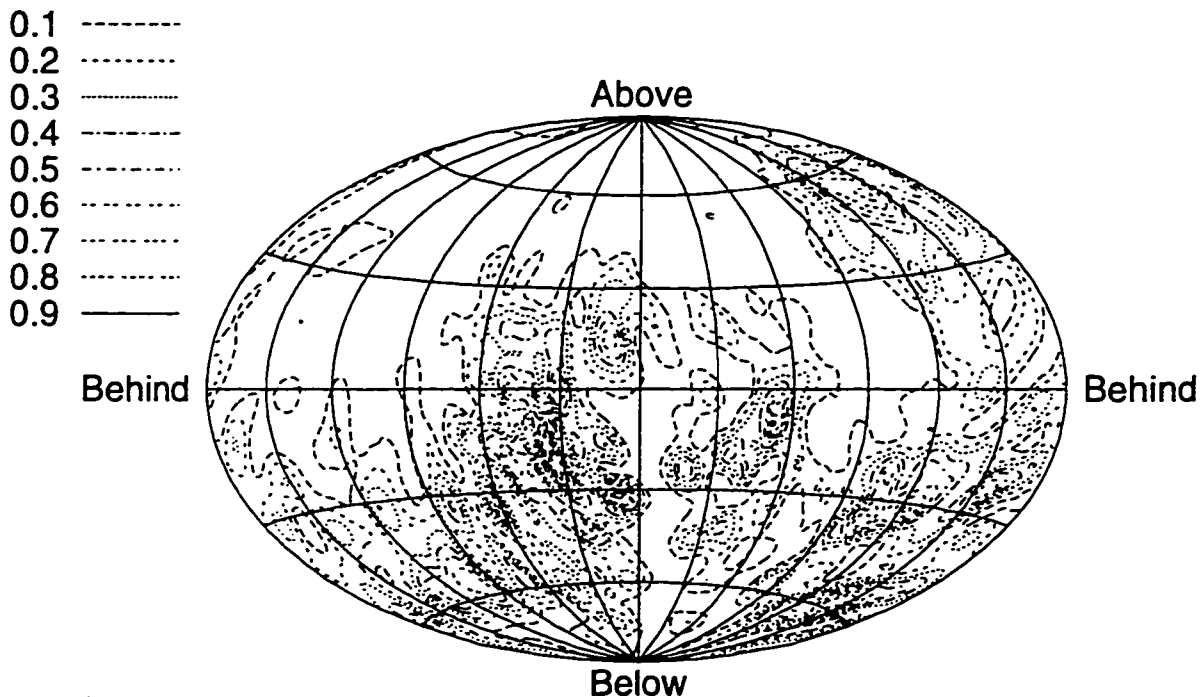
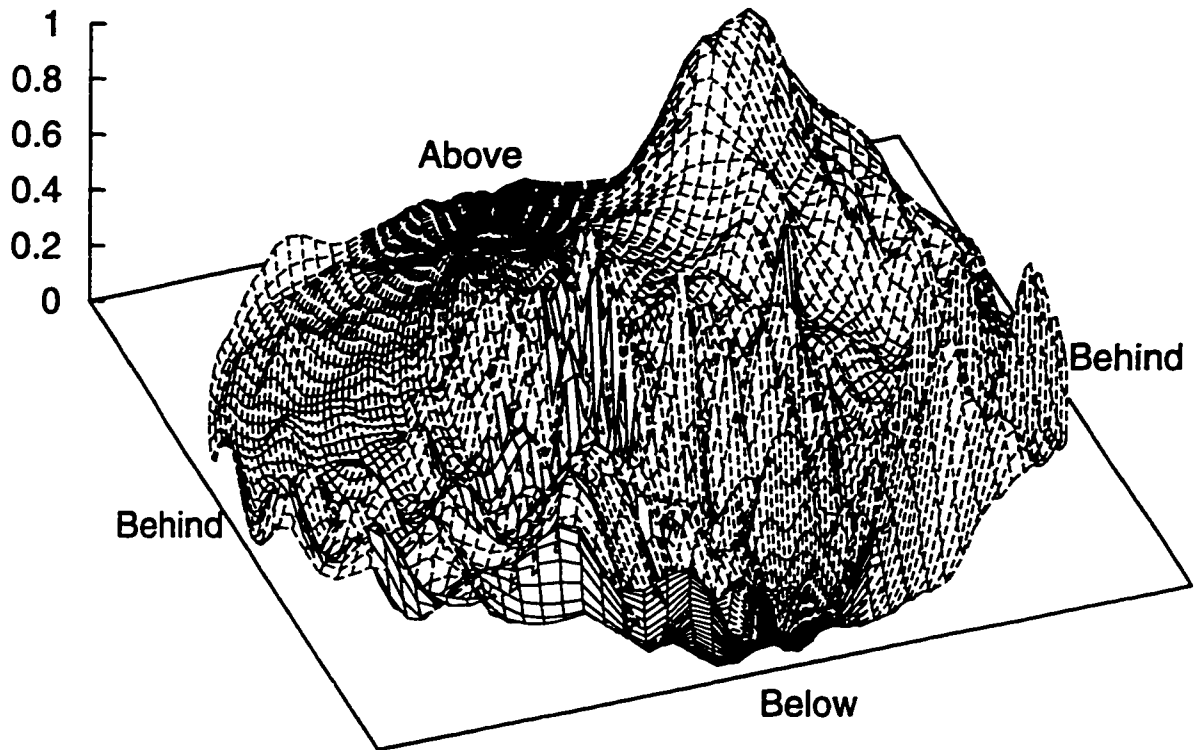


Figure 7.56. Extrapolated far-field emission (receptivity) pattern at 50 kHz for a source placed within the RIGHT inner ear for a model including only the skull and the nasal air sacs (without soft tissue and without the peribullary and pterygoid sinuses). Top diagram plots intensity as height in a perspective view of the far-field data. Bottom diagram is a contour plot of the same data, also plotted in the global equal-area projection. The direction angles of the peak and the directivity index for the pattern are indicated.

Left Ear; $\Theta_{et}, \Phi_{et} = -42.01, 10.06$; $DI = 12.00$; $\text{freq} = 50\text{kHz}$

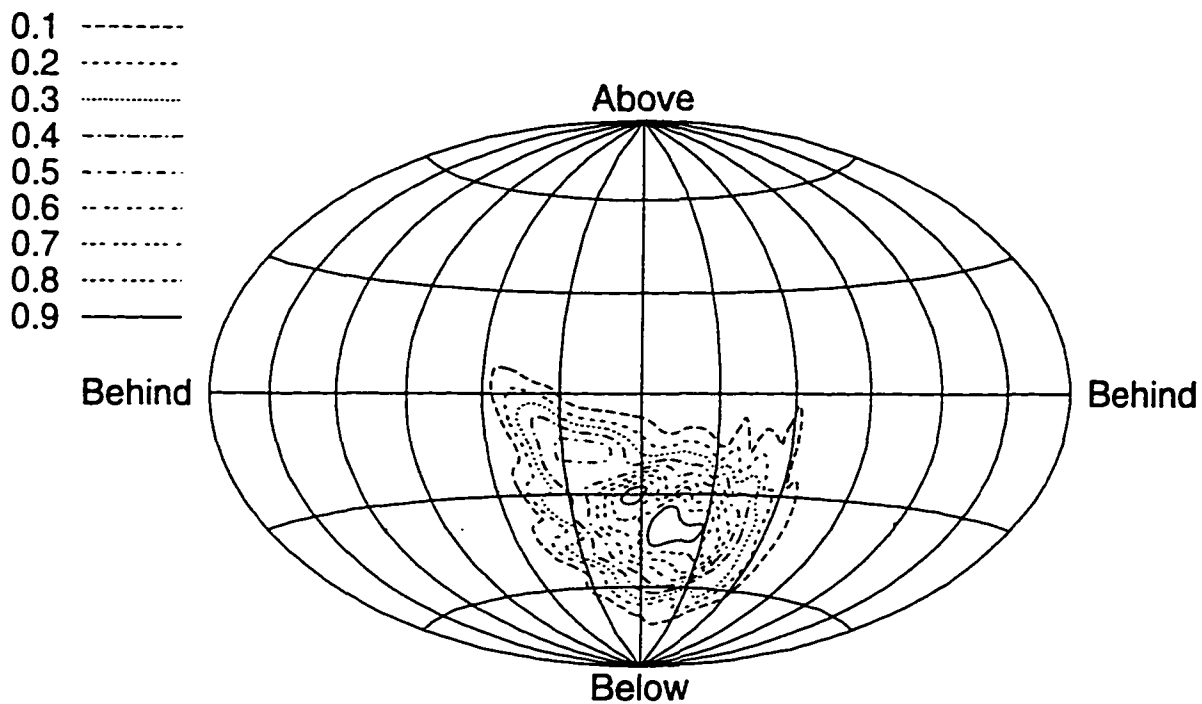
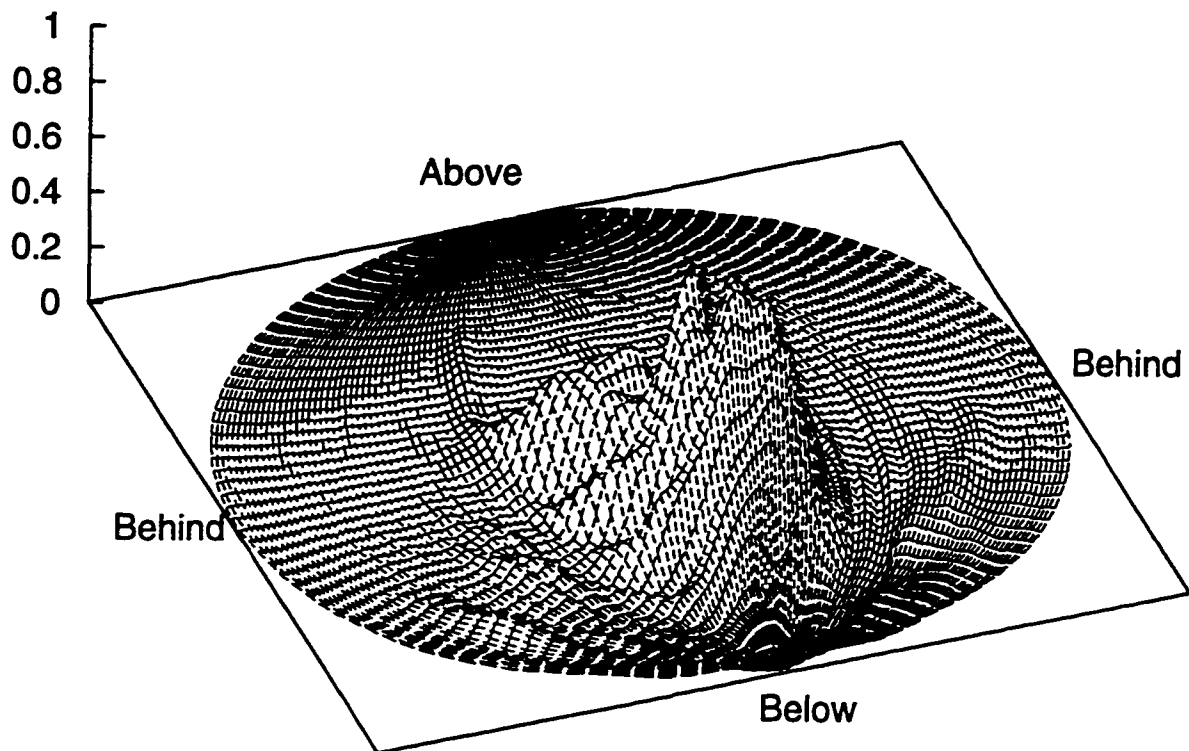


Figure 7.57. Extrapolated far-field emission (receptivity) pattern at 50 kHz for a source placed within the LEFT inner ear for a model including the skull, the nasal air sacs, and the peribullary and pterygoid sinuses (but without soft tissue). Top diagram plots intensity as height in a perspective view of the far-field data. Bottom diagram is a contour plot of the same data, also plotted in the global equal-area projection. The direction angles of the emission peak and the directivity index for the pattern are indicated.

Right Ear; $\Theta_{et}, \Phi_{et} = -35.80, -13.21$; $DI = 9.57$; $\text{freq} = 50\text{kHz}$

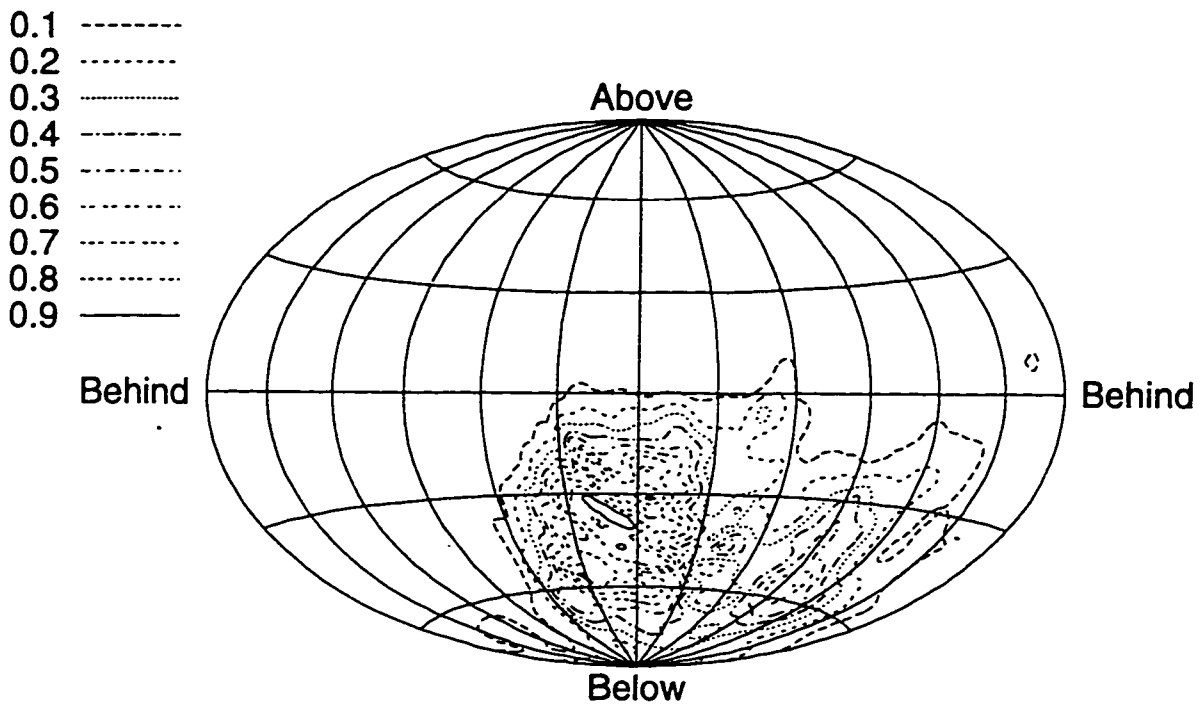
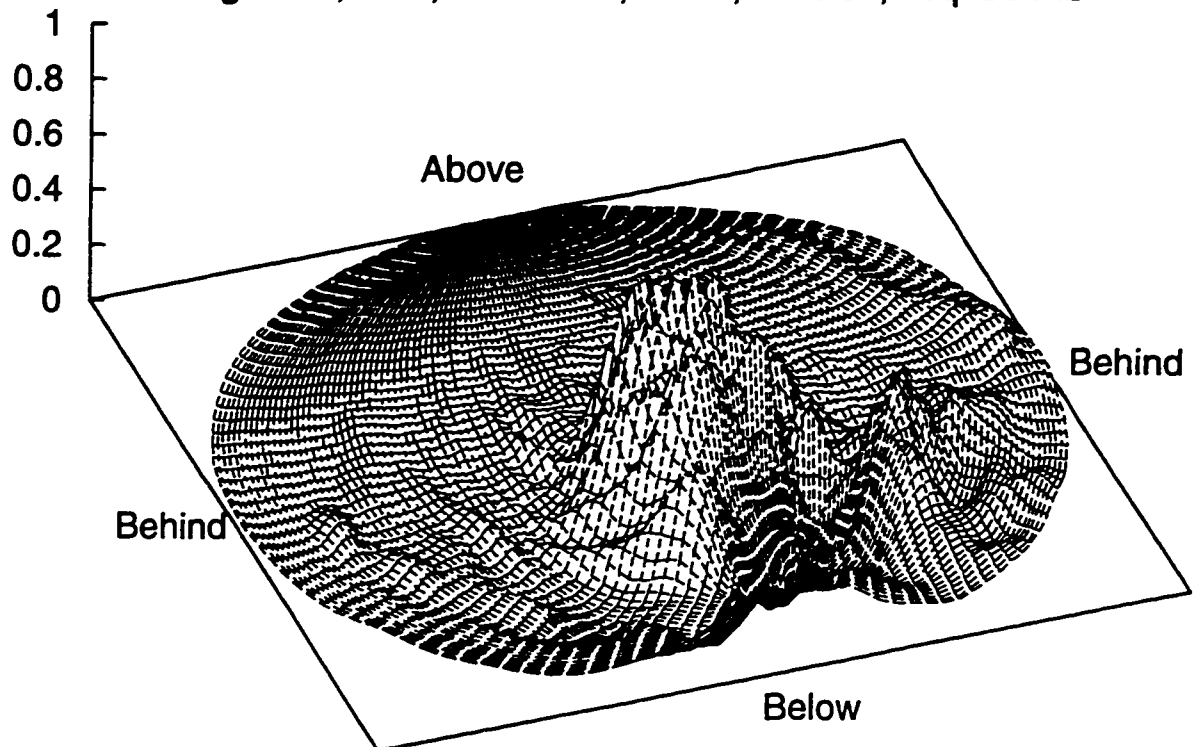


Figure 7.58. Extrapolated far-field emission (receptivity) pattern at 50 kHz for a source placed within the RIGHT inner ear for a model including the skull, the nasal air sacs, and the peribullary and pterygoid sinuses (but without soft tissue). Top diagram plots intensity as height in a perspective view of the far-field data. Bottom diagram is a contour plot of the same data, also plotted in the global equal-area projection. The direction angles of the emission peak and the directivity index for the pattern are indicated.

Left Ear; Thet,Phi=-22.04,7.12; DI=14.31; freq=50kHz

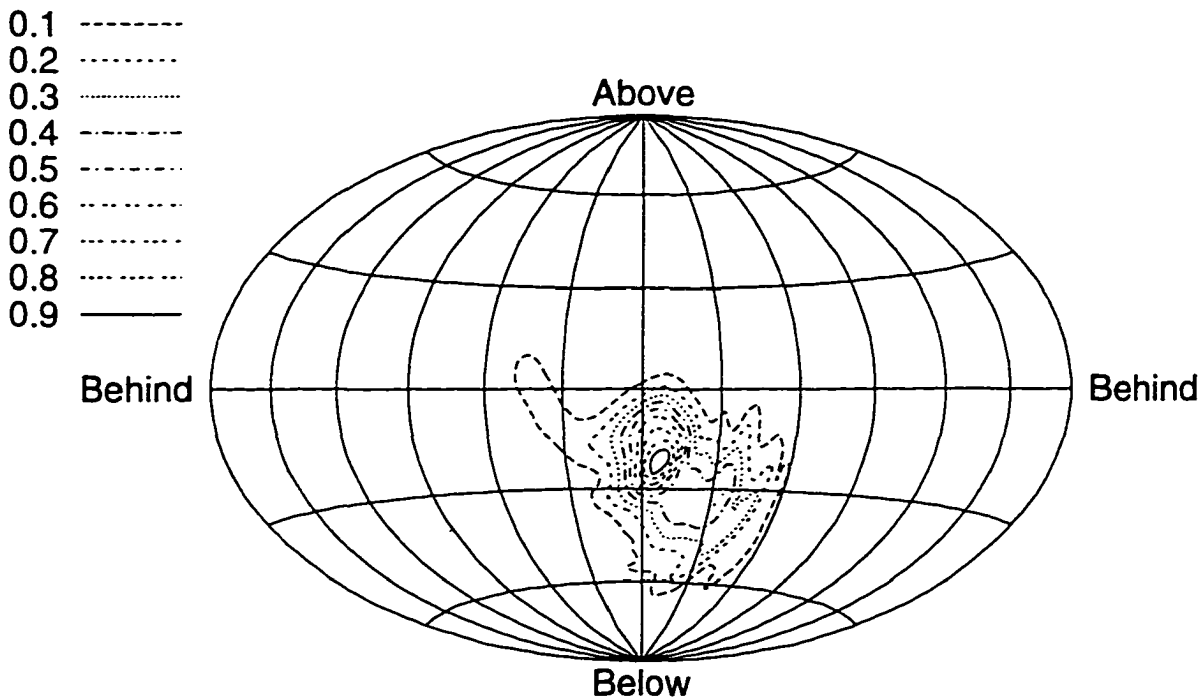
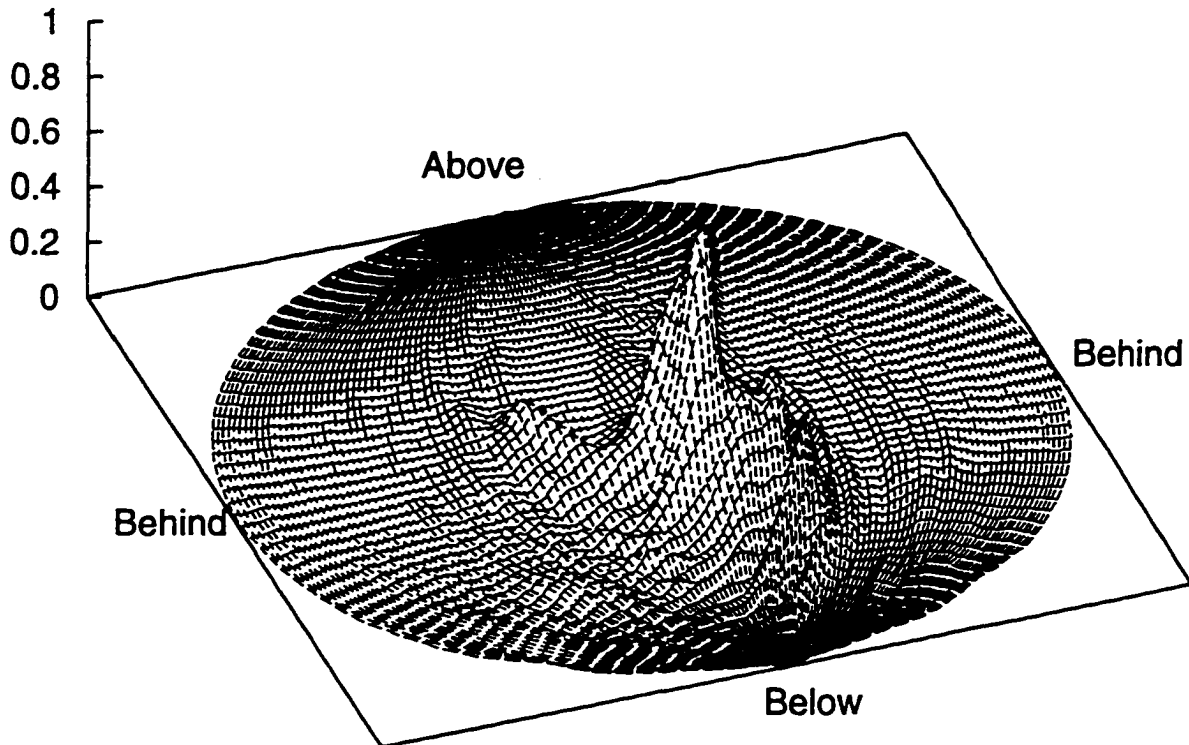


Figure 7.59. Extrapolated far-field emission (receptivity) pattern at 50 kHz for a source placed within the LEFT inner ear for the full model including the skull, soft tissue, nasal air sacs, and the peribullary and pterygoid sinuses. Top diagram plots intensity as height in a perspective view of the far-field data. Bottom diagram is a contour plot of the same data, also plotted in the global equal-area projection. The direction angles of the emission peak and the directivity index for the pattern are indicated.

Right Ear; $\Theta, \Phi = -14.78, -9.27$; $DI = 11.27$; $\text{freq} = 50\text{kHz}$

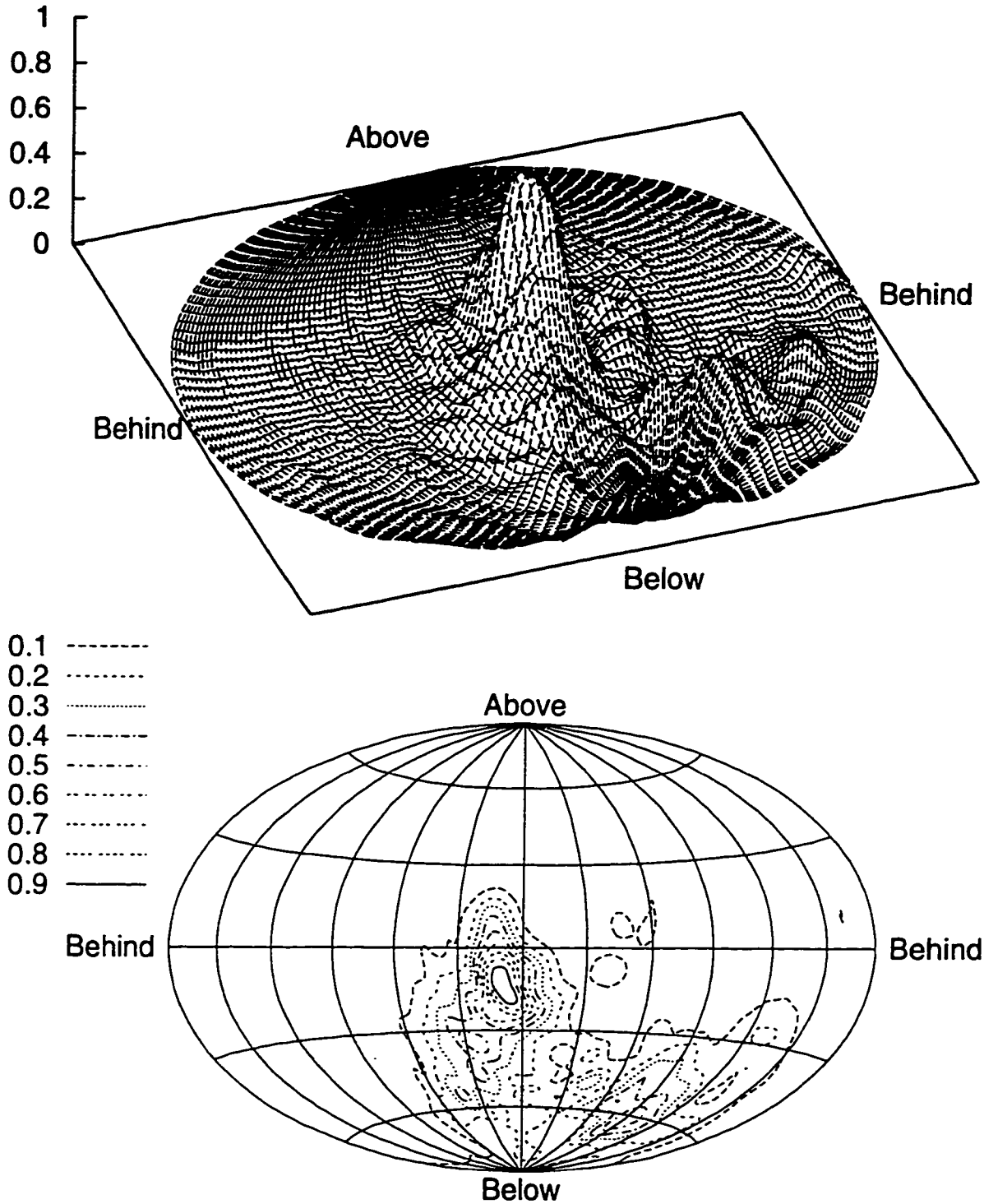


Figure 7.60. Extrapolated far-field emission (receptivity) pattern at 50 kHz for a source placed within the RIGHT inner ear for the full model including the skull, soft tissue, nasal air sacs, and the peribullary and pterygoid sinuses. Top diagram plots intensity as height in a perspective view of the far-field data. Bottom diagram is a contour plot of the same data, also plotted in the global equal-area projection. The direction angles of the emission peak and the directivity index for the pattern are indicated.

Chapter 8. Summary of Conclusions

In this chapter we summarize the conclusions of the project concerning the mechanisms of biosonar signal production, emission, and reception. We also discuss the potential of the methodology developed here for future applications.

The most far-reaching result of this project is that the acoustical parameters of soft biological tissues can be accurately modeled from x-ray CT data. This modeling technique applied in conjunction with highly accurate methods of 3-D numerical wave propagation constitutes an extraordinarily fruitful approach to the investigation of odontocete biosonar mechanisms.

Strong evidence for the tissue location of the source of biosonar signals in the common dolphin has been presented. Simulations with the full model have implicated a region slightly (~1cm) below the center of the right MLDB complex as the most plausible 'epicenter' of the dolphin's biosonar clicks. Note that this location may explain the observation of Romanenko (1973) that hydrophones placed on the skin surface above the right vestibular sac picked up almost no biosonar signals, while hydrophones placed just across the blowhole above the left vestibular sac picked up significant signals. Propagation paths between the right MLDB and the skin surface above the left vestibular sac appear to exist in the *Delphinus* data, while no direct paths exist between the right MLDB and the skin surface above the right vestibular sac. Several previously proposed source locations are contraindicated by the absence of inverse simulation foci at the proposed sites. In addition, while time and space limitations prevented their inclusion here, forward extrapolations of the far-field produced by sources at the proposed locations have demonstrated their nonviability. The contraindicated sites include the right and left nasal plugs, the larynx, and the left MLDB complex. In addition, we have noted that the focal positions cluster together for vertical return angles between 0 and +5 degrees. This suggests that the animal may

emit a pattern peaked in this vertical range.

The contributions of various tissues to the focal characteristics of the emitted patterns have been demonstrated. We have demonstrated the profound reflective focal behavior of the skull geometry by itself, corroborating many earlier studies (Evans *et al.* 1964, Dubrovskiy and Zaslavskiy 1975, and Romanenko 1973). The skull certainly plays the predominant role in 3-D beam formation.

A conservative model of the air sacs has been shown to be important in the forward reflection of energy projected upward, sideways, and downward by the skull alone, although it also contributes slightly to narrowing of the main forward lobe. Addition of the air sacs into the tissue model always improves the patterns and raises the directivity indexes, though the importance of the contribution varies with frequency.

Remarkably, we have also demonstrated that the melon and other soft tissues of the forehead play a far more significant role in beam formation than was indicated by previous simulations. While this role has been hypothesized by several investigators, demonstration of the magnitude of the contribution and the underlying mechanisms remain a significant achievement of this thesis. The melon's most important effect appears to be narrowing of the main forward lobe, although the exact contribution varies with frequency. The melon also contributes to collection of emitted energy into the main forward lobe, as do the air sacs. The experimental result of Romanenko (1973) that beams measured with the whole head are roughly half as wide as the beams measured with the skull alone has been corroborated for frequencies of 75 kHz and higher. The melon's effect on vertical beam widths is smaller. In addition, we have illustrated the detailed density, velocity, and impedance structure of the melon and the spatial patterns of sound propagation through it to reveal the mechanisms which produce its effects. The posterior throat

of the melon has been shown to operate as a waveguide and a megaphone, while the larger forward lobe of the melon has been shown to operate as a lens and an impedance matching device in the biosonar signal emission process.

From the structure of the nasal passage region in delphinids, a physical model has been proposed (see Chapter 3) which, in conjunction with the demonstrated behavior of the melon, may largely explain the observed temporal and spatial characteristics of delphinid (and perhaps all odontocete) biosonar emission fields. The analogy of a damped resonator driven by an impulsive mechanism has been proposed for the source region in dolphins, with projection of the ensuing signal aided by the waveguide and megaphone effects of the throat of the melon, with focusing and transmission into seawater aided by the lensing and impedance matching effects of the remaining melon. While several avenues of rigorous investigation with this model can be pursued, Chapter 3 has provided simplified equations for the expected behavior of such a source region. In addition, the author has offered a conjectured mechanism for the dolphin's production of the explosive sounds referred to as 'jaw pops' (see Appendix 1).

We have also demonstrated that the fats of the lower jaw act as efficient waveguides channeling the received acoustic energy back to the middle/inner ear complexes in the hearing process, confirming and explaining several aspects of the lower jaw hearing hypothesis. The same mechanisms operating in the melon have been shown to operate (in reverse order) in signal reception through the lower jaw fat bodies.

We have also computed and illustrated the individual reception patterns for the left and right ear complexes in the common dolphin. In the full model, we have seen that the reception patterns of the left and right ears are peaked at about -22° and -15° in vertical angle, respectively. Both are well below the main lobe of the illustrated emission patterns of the forehead models. In

the horizontal direction, the left and right ear patterns are peaked at about $+7^\circ$ and -9° , respectively. We have been able to confirm that differences in the left-right patterns exist which undoubtedly contribute to the directional hearing capabilities of the dolphin. By comparing these reception patterns with those produced by the model without soft tissues, we have also shown that the jaw fats significantly improve the reception patterns in the forward direction. In addition, we have demonstrated that the peribullary and pterygoid sinuses of the lower skull and palate contribute quite significantly to the formation of downward and forward reception patterns, apparently insulating the ears from most other directions of incidence. The importance of these sinuses to the receptivity patterns was predicted by Norris (1968).

Clearly, these initial simulations have only scratched the surface of the potential applications to investigation of the dolphin's hearing processes. For example, while not illustrated in this thesis, it is quite easy to obtain the time delay between the left and right inner ear complexes as a function of the direction of reception at any fixed frequency from the complex receptivity. Timing delay diagrams will be included, along with many other important results, in later publications.

Available funding and time imposed severe limitations on how far the author could carry his applications of these techniques - a preliminary investigation of a single delphinid species has been achieved. The generality of the above conclusions about the biosonar system of *Delphinus delphis* are limited somewhat by the large variation in odontocete forehead morphology. However, the common dolphin is a good representative of the typical forehead anatomy of members of the family Delphinidae having an intermediate-to-moderate value of soft tissue asymmetry (Cranford 1992). It is therefore expected that similar if not identical mechanisms operate in all delphinids exhibiting intermediate-to-moderate soft tissue asymmetry (including *Tursiops trun-*

catus). It is also reasonable to expect that similar mechanisms operate in all odontocetes possessing forehead and lower jaw structures of 'acoustic fat' resembling the common dolphin.

Obviously, the techniques utilized in this thesis are directly applicable to investigation of all x-ray CT scanned odontocete species. This project has proved the capability of its methodology for accurate modeling of biosonar emission and reception. Application of the same techniques to odontocete species with better documented biosonar fields (i.e., *Tursiops truncatus*, *Delphinapterus leucus*, *Pseudorca crasidens*) would allow closer comparisons with experimental data and tests of the generality of the mechanisms discussed in this thesis.

In addition, possibilities exist for investigation of many more questions than have been addressed here. For example, the author suggested several years ago that simulation of sound propagation into the inner ears and cochlea of dolphins is feasible. Such a project might utilize the sound field of larger scale simulations of the type conducted in this thesis as input to more detailed elastic simulations. Similar techniques are also applicable in studies of audition in other marine mammals including baleen whales, pinnipeds, and the phocid seals.

Another research direction holding extraordinary potential stemming from this thesis is extension of the methods for acoustical modeling of biological tissue from x-ray CT data presented in Chapter 6. Higher order mappings are certainly possible, and may provide levels of precision adequate for medical applications. For example, measurement of only a few tissue samples throughout the soft tissue range could provide calibration points for higher order density and velocity mappings. Or, consider the following. This thesis has shown how to obtain an acoustical model of biological tissues accurate to within a few percent for both density and velocity. Comparing the results of simulations using such a model with ultrasound measurements through the scanned tissues can yield refinement of the model (as is routinely done in seismologic

modeling). Because one is starting with a remarkably good 'geologic' model here, the convergence process should be quite rapid. Study of the converged model should yield information on how to improve the original mappings. Other possibilities here include the computer design of ultrasound equipment, or computer-aided ultrasound image enhancement.

Furthermore, applications of these methods are not limited to biological systems. The author has demonstrated the extraordinary usefulness of similar techniques in the design and performance analyses of electro-acoustic systems through consulting work with acoustic component manufacturers.

Finally, the author is awed by the opportunities for both research and education that have resulted from the application of 3-D visualization software to medical scanning data. The opportunity to examine the internal anatomy of a complex organism repeatedly in an unlimited variety of representations continues to be a deeply enriching experience. Biology departments may want to consider the potential benefits of providing student access to workstations with high quality graphics packages along with several varieties of medical scan data.

Appendix 1: A Conjecture for the 'Jaw-pop' Source Mechanism

Although this thesis is mostly concerned with the mechanisms underlying the emission and reception of echolocation pulses, dolphins also produce a wide variety of other sounds. One striking example is a loud explosive sound commonly referred to as a 'bang' or 'jaw-pop' that is often associated with aggressive behavior in captive animals. It has been hypothesized that these loud sounds may be used by a dolphin to momentarily stun or disorient their prey (Norris and Mohl 1983), thus permitting easier capture.

In 1991, Ted Cranford succeeded in training the Pacific White-sided dolphins (*Lagenorhynchus obliquidens*) at the Long Marine Laboratory of the University of California, Santa Cruz, to direct jaw-pops at a hydrophone suspended in their tank. Ted video taped the animals producing their bangs along with an oscilloscope display of the hydrophone output. In February 1991, after viewing some of these tapes, I personally communicated to Ted a conjectured mechanism for how the Lags could be producing their jaw-pops. This conjecture, as communicated at the time, went as follows:

Ken Norris mentioned that underwater explosions used to be made by breaking glass spheres deep in the ocean, right? What if the Lags were rapidly sucking air OUT of an inflated spiracular cavity instead of forcing air up through the cavity (as they normally do when producing echolocation clicks)? The tissue around the cavity would build up inward momentum as the air exited and the cavity closed, and should be enough to produce a huge slam.

Can the Lags be yanking air out of the nares rapidly enough to collapse the spiracular cavity? Is that why a ripple of muscle/fat moves down the underside of their throats just before the bangs occur? [Does this ripple initiate a rapid withdrawal of their larynx from the nares? See next paragraph.]. This process would not have to be very rapid on the time scale of the bangs -- the energy of the slapping tissue would be many times more than necessary to produce the bang. Exactly like quickly sucking the air out of a balloon underwater. Or analogous to slapping your hands together underwater on either side of an air-filled balloon -- the air allows your hands to clap together rapidly, while the 'clap' propagates directly through the palms and out into the water. This mechanism of sound production would be similar to the hypothesized MLDB source mechanism except: 1) the larger mass of tissue that is in motion; 2) the time

scale of the clap; and 3) the motion is not driven by pressurized air passing through 'lip' structures.

[We (humans) are able to produce glottal clucks by dropping the larynx and opening up our throats. Try speaking the word "gall" while touching your Adam's apple. Then over-emphasize the motion involved in pronouncing this word in order to produce a glottal cluck. Notice that your tongue also moves backward when the larynx is dropped. The Lags might be using a similar motion to suck air rapidly out of a widely opened spiracular cavity. This may also explain why a muscular ripple moves down the underside of their throats just before the bangs occur.]

Appendix 2: Density, Velocity, and Impedance Structure of the Melon of the Common Dolphin

In this appendix, we examine the acoustic characteristics of the forehead tissues of a dolphin with an accuracy that has never been possible before. The soft tissue CT-to-density and CT-to-velocity mappings presented in Chapter 6 allow us to illustrate the detailed density, velocity, and impedance structure of the melon of the common dolphin, *Delphinus delphis*. With this new information, we can develop an understanding of the mechanisms underlying the acoustic behavior of the unique fats of the delphinid forehead and lower jaw.

It has long been known that the melon constitutes an inhomogeneous impedance structure (see Chapter 2). In 1957, Forrest Wood (1964) hypothesized that the melon tissue in dolphins may serve as an acoustic impedance matching device coupling internally generated sound to the surrounding water. Such a coupling would minimize reflective losses and protect the ears from spurious echoes within the dolphin's own tissues of internally produced sound. Wood also speculated that the melon may act as an acoustic lens to focus the sound into a narrow beam. Let us keep Wood's hypotheses in mind, as well as the waveguide and megaphone principles discussed in Chapter 3, as we examine the following diagrams.

Figures A2.1, A2.2, and A2.3 illustrate the density, velocity, and impedance structures, respectively, in a 2-D parasagittal slice through the right MLDB complex of the common dolphin. The perspective in these diagrams is looking down from in front of the dolphin at the melon skin-seawater interface. This sectional plane also passes roughly through the axis of the melon. Height in each of these plots indicates the specified quantity relative to the value for seawater (density 1.03g/cc, velocity 1500m/s, acoustic impedance $1.55 \times 10^6 \text{ kg m}^{-2} \text{ s}^{-1}$). The quantities for bone have been truncated at the value 2.0 in all diagrams in order to better illustrate the

soft tissue range of values. Each of these diagrams is worthy of careful study.

Note that both the density and the velocity (hence also the impedance) of the melon-seawater interface region is quite well matched to seawater values, corroborating Wood's matched impedance hypothesis for the melon. In addition, the velocity structure exhibits a broad depression in the forward melon, grading back to form a relatively sharp channel through the posterior throat of the melon. In the author's opinion, the broad forward depression appears most closely analogous to a lens structure, while the posterior velocity channel appears more closely analogous to a waveguide which has been flared so as to behave additionally as a megaphone. The velocity distribution pictured in Figure A2.2 certainly corroborates Wood's melon lensing hypothesis, and suggests additional physical mechanisms for the posterior melon throat.

One way of visualizing the 3-D configuration of the melon tissue inside of the dolphin's forehead is illustrated in Figure A2.4. Isosurfaces have been plotted at the CT data bone threshold and at a CT value for an outer layer of the melon. Figure A2.4 thus represents the melon tissue in relation to the skull. Sections of the skin surface are also visible (mainly on the far side of the forehead) as well as portions of the vestibular sacs below the blowhole. Note the narrowing of the posterior melon as it approaches the region of the right MLDB. The data volume pictured here is the same region of the CT data that was used in all of the forehead tissue simulations (compare Figures 7.1 and 7.2).

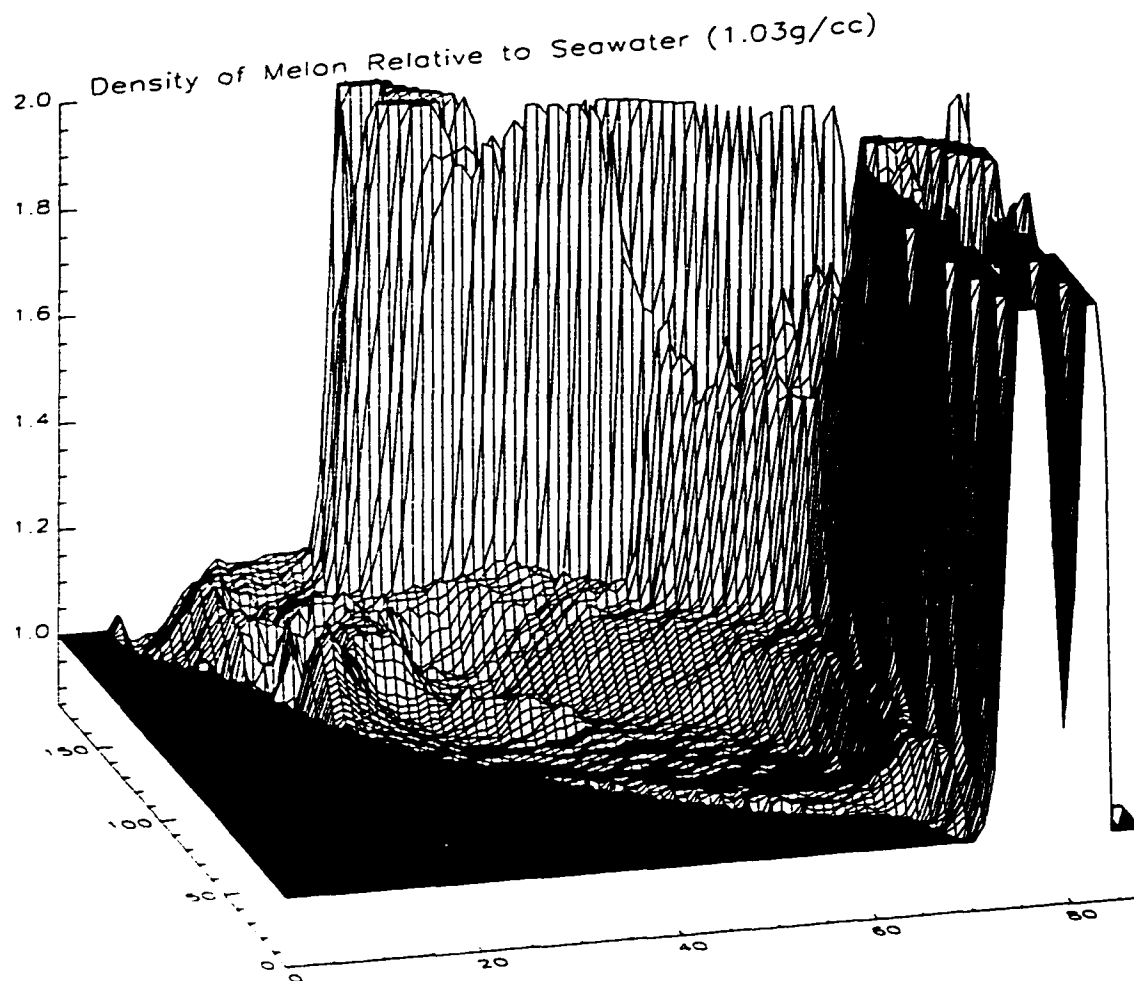


Figure A2.1. Density of melon tissues in a 2-D parasagittal slice through the right MLDB complex of the common dolphin. Height indicates density relative to seawater (1.03g/cc). Bone densities have been truncated at the value 2.0 to better illustrate the soft tissue density range.

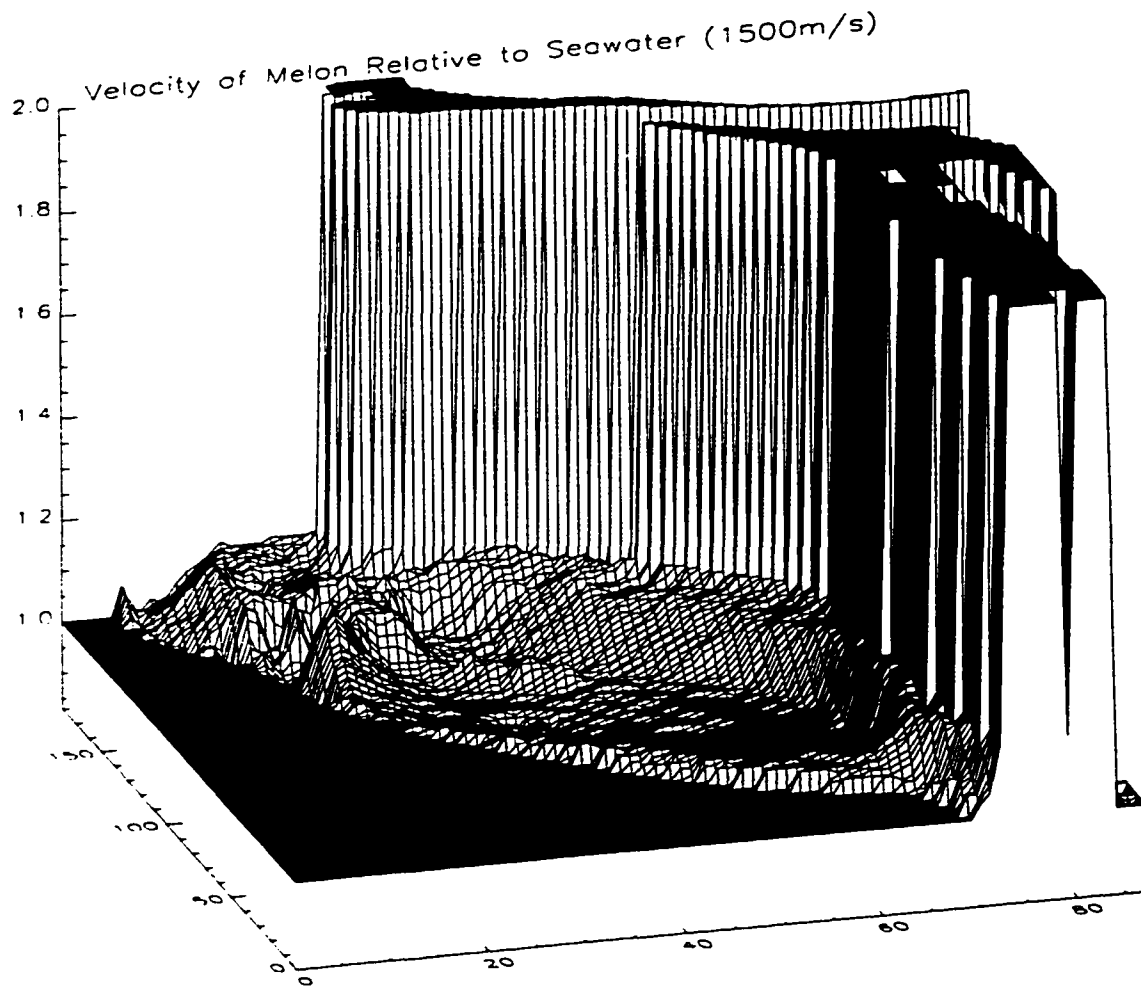


Figure A2.2. Acoustic velocity of melon tissues in a 2-D parasagittal slice through the right MLDB complex of the common dolphin. Height indicates velocity relative to seawater (1500m/s). Bone velocity has been truncated at the value 2.0 to better illustrate the soft tissue velocity range.

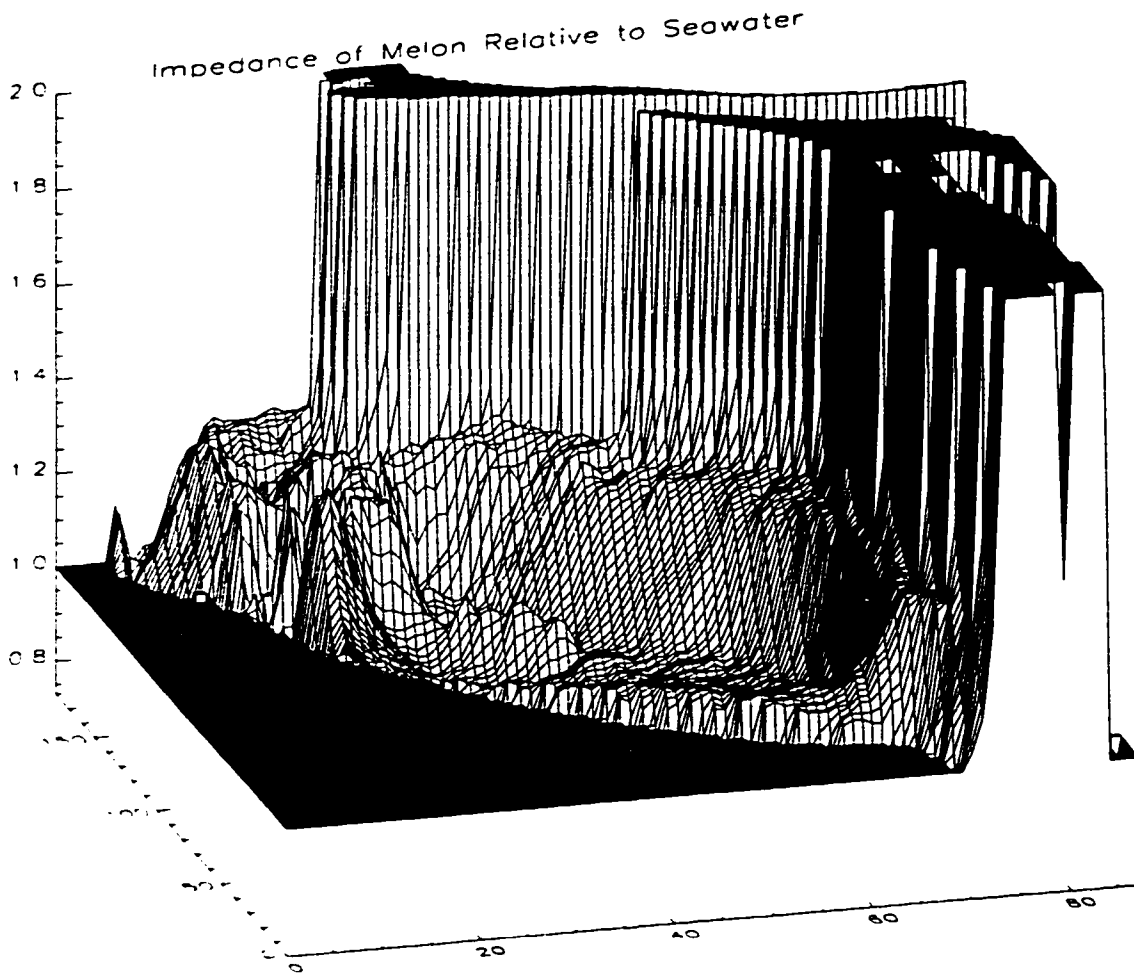


Figure A2.3. Acoustic impedance of melon tissues in a 2-D parasagittal slice through the right MLDB complex of the common dolphin. Height indicates impedance relative to seawater ($1.55 \times 10^6 \text{ kg m}^{-2} \text{ s}^{-1}$). Bone impedance has been truncated at the value 2.0 to better illustrate the soft tissue impedance range.



Figure A2.4. Visualization of the 3-D configuration of the melon inside of the dolphin's forehead. Isosurfaces are plotted at the CT data bone threshold and at a CT value for an outer layer of the melon. Sections of the skin surface are also visible (mainly on the far side of the forehead) as well as portions of the vestibular sacs below the blowhole. The data volume pictured here is the same region of the full CT dataset that was used in all of the forehead tissue simulations (compare Figures 7.1-7.2).

References:

- Alford, R.M., Kelly, K.R., and Boore, D.M. (1974), "Accuracy of finite-difference modeling of the acoustic wave equation", *Geophysics*, 39(6):834-42.
- Aroyan, J.L. (1990), "Numerical Simulation of Dolphin Echolocation Beam Formation", M.S. thesis, U.C. Santa Cruz, 1990.
- Aroyan, J.L., Cranford, T.W., Kent, J., and Norris, K.S. (1992), "Computer modeling of acoustic beam formation in *Delphinus delphis*", *J. Acoust. Soc. Am.*, 92(5):2539-2545.
- Au, W.W.L., Floyd, R.W., and Haun, J.E. (1978), "Propagation of Atlantic bottlenose dolphin echolocation signals", *J. Acoust. Soc. Am.*, 64:411-422.
- Au, W.W.L. (1980), "Echolocation signals of the Atlantic Bottlenose dolphin (*Tursiops truncatus*) in open waters", in *Animal Sonar Systems*, edited by R.G. Busnel and J.R. Fish, Plenum Pub., New York, 1980, pp. 251-282.
- Au, W.W.L., and Moore, P.W.B. (1984), "Receiving beam patterns and directivity indices of the Atlantic bottlenose dolphin", *J. Acoust. Soc. Am.*, 75:255-262.
- Au, W.W.L., Carder, D.A., Penner, R.H., and Scronce, B.L. (1985), "Demonstration of adaptation in beluga whale echolocation signals", *J. Acoust. Soc. Am.*, 77:726-730.
- Au, W.W.L., Moore, P.W.B., and Pawloski, D. (1986), "Echolocation transmitting beam of the Atlantic bottlenose dolphin", *J. Acoust. Soc. Am.*, 80(2):688-691.
- Au, W.W.L., Penner, R.H., and Turl, C.W. (1987), "Propagation of beluga echolocation signals", *J. Acoust. Soc. Am.*, 82:807-813.
- Au, W.W.L. (1993), *The Sonar of Dolphins*, Springer-Verlag, New York, 1993.
- Au, W.W.L., Pawloski, J.L., Nachtigall, P.E., Blonz, M., and Gisiner, R.C. (1995), "Echolocation signals and transmission beam pattern of a false killer whale (*Pseudorca crassidens*)", *J. Acoust. Soc. Am.*, 98(1):51-59.
- Auld, B.A., (1973), *Acoustic Fields and Waves in Solids*, John Wiley & Sons, Inc., 1973.
- Baker, B.B., and Copson, E.T. (1953), *The Mathematical Theory of Huygen's Principle*, 2nd ed., Oxford University Press, 1953.
- Backus, J. (1977), *The Acoustical Foundations of Music*, 2nd ed., W.W. Norton & Co., New York, 1977.
- Bel'kovitch and Reznikov (1971), in Bel'kovich, V.M., and Dubrovskiy, N.A. (1976), *Sensory Bases of Cetacean Orientation*, Izdatel'stvo Nauka, Leningrad, JPRS 7157, 1977.
- Bel'kovich, V.M., and Dubrovskiy, N.A. (1976), *Sensory Bases of Cetacean Orientation*, Izdatel'stvo Nauka, Leningrad, JPRS 7157, 1977.
- Benade, A.H. (1960), "The physics of wood winds", *Scientific American*, October 1960.
- Benade, A.H. (1973), "The physics of brasses", *Scientific American*, July 1973.
- Benade, A.H. (1976), *Fundamentals of Musical Acoustics*, Oxford University Press, New York, 1976.
- Beyer, R.T. (1960) "Parameter of nonlinearity in fluids", *J. Acoust. Soc. Am.*, 32(6):719-721.

- Bowen, T., Connor, W.G., Nasoni, R.L., Pifer, A.E., and Sholes, R.R. (1979), "Measurement of the temperature dependence of the velocity of ultrasound in soft tissues", in NBS Special Publication 525: *Ultrasonic Tissue Characterization II*, edited by M. Linzer, U.S. GPO, Washington, DC, 1979, pp. 57-61.
- Brill, R.L., Sevenich, M.L., Sullivan, T.J., Sustman, J.D., and Witt, R.E. (1988), "Behavioral evidence for hearing through the lower jaw by an echolocating dolphin (*Tursiops truncatus*)", *Marine Mammal Science*, 4:223-230.
- Bullock, T.H., Grinnell, A.D., Ikezono, E., Kameda, K., Katsuki, Y., Nomoto, M., Sato, O., Suga, N., and Yanagisawa, K. (1968), "Electrophysiological studies of central auditory mechanisms in cetaceans", in *Zeitschrift fur Vergleichende Phys.*, 59:117-156.
- Cann, C.E. (1988), "Quantitative CT for determination of bone mineral density: a review", *Radiology*, 166(2):509-522.
- Carstensen, E.L. (1979), "Absorption of sound in tissues", in NBS Special Publication 525: *Ultrasonic Tissue Characterization II*, edited by M. Linzer, U.S. GPO, Washington, DC, 1979, pp. 29-36.
- Cook, R.K. (1996), "Lord Rayleigh and reciprocity in physics", *J. Acoust. Soc. Am.*, 99(1):24-29.
- Copley, L.G. (1967), "Integral equation method for radiation from vibrating bodies", *J. Acoust. Soc. Am.*, 41:807-816.
- Copley, L.G. (1968), "Fundamental results concerning integral representations in acoustic radiation", *J. Acoust. Soc. Am.*, 44(1):22-32.
- Coppens, A.B., Beyer, R.T., Seiden, M.B., Donohue, J., Guepin, F., Hodson, R.H., and Townsend, C. (1965) "Parameter of nonlinearity in fluids. II", *J. Acoust. Soc. Am.*, 38:797-804.
- Cranford, T.W. (1986), "The anatomy of acoustic structures in the spinner dolphin forehead as shown by x-ray computed tomography and computer graphics", M.S. thesis, U.C. Santa Cruz, 1986.
- Cranford, T.W., Amundin, M., and Bain, D.E. (1987), "A unified hypothesis for click production in odontocetes", abstract, 7th Biannual Conf. on Biology of Marine Mammals, 1987.
- Cranford, T.W. (1988). "The Anatomy of Acoustic Structures in the Spinner Dolphin Forehead as shown by X-ray Computed Tomography and Computer Graphics", in *Animal Sonar: Processes and Performance*, edited by P.E. Nachtigall and P.W.B. Moore, Plenum Pub., New York, 1988, p67-77.
- Cranford, T.W. (1992). "Functional Morphology of the Odontocete Forehead: Implications for Sound Generation", Ph.D. dissertation, U.C. Santa Cruz, 1992.
- Cunefare, K.A., Koopmann, G., and Brod, K. (1989), "A boundary element method for acoustic radiation valid for all wavenumbers", *J. Acoust. Soc. Am.*, 85(1):39-48.
- Dormer, K.J. (1974), "The mechanism of sound production and measurement of sound processes in Delphinid cetaceans", Ph.D. dissertation, U.C. Los Angeles, 1974.
- Dormer, K.J. (1979), "Mechanism of sound production and air recycling in Delphinids: cineradiographic evidence", *J. Acoust. Soc. Am.*, 65:229-239.
- Dubrovskiy, N.A., and Zaslavskiy, G.L. (1975), "Role of the skull bones in the space-time development of the dolphin echolocation signal", *Zool. Zh.*, 21(3):255-258, (JPRS 65777, 1975, pp. 1-10).

- Dunn, F., Law, W.K., and Frizzell, L.A. (1981) "Nonlinear ultrasonic wave propagation in biological materials", IEEE Ultrasonic Symposium (IEEE, New York, 1981), pp. 527-532.
- Dziedzic, A. (1978), "Experimental study of the sonar emissions of certain delphinids, especially *D. delphis* and *T. truncatus*", D.Sc. dissertation, University of Paris, 1978.
- Eggleton, R.C., and Whitcomb, J.A. (1979), "Tissue simulators for diagnostic ultrasound", in NBS Special Publication 525: *Ultrasonic Tissue Characterization II*, edited by M. Linzer, U.S. GPO, Washington, DC, 1979, pp. 327-336.
- Endo, H. (1984) "Calculation of nonlinearity parameter for seawater", J. Acoust. Soc. Am., 76(1):274-279.
- Engquist, B., and Majda, A. (1977), "Absorbing boundary conditions for the numerical simulation of waves", Math. Comput., 31:629-651.
- Erlichman, M. (1986) "Single photon absorptiometry for measuring bone mineral density", National Center for Health Services Research and Health Care Technology Assessment, U.S. Dept. of Health and Human Services, Public Health Service; National Technical Information Service, 1986, no. 7.
- Evans, W.E., and Prescott, J.H. (1962), "Observations of the sound capabilities of the Bottlenose porpoise: a study of whistles and clicks", Zoologica, 47(3):121.
- Evans, W.E., Sutherland, W.W., and Beil, R.G. (1964), "The directional characteristics of delphinid sounds", in *Marine Bio-acoustics*, edited by W.N. Tavolga, Vol. 2, Pergamon Press, New York, pp. 353-372.
- Evans, W.E. (1973) "Echolocation by marine delphinids and one species of fresh-water dolphin", J. Acoust. Soc. Am., 54(1):191-99.
- Fraser, F.C., and Purves, P.E. (1960), "Hearing in cetaceans: evolution of the accessory air sacs and the structure and function of the outer and middle ear in recent cetaceans", Bull. British Mus. (Nat. Hist.), 7:1-140.
- Frizzell, L.A., Carstensen, E.L., and Dyro, J.F. (1976), "Shear properties of mammalian tissues at low megahertz frequencies", J. Acoust. Soc. Am., 60:1409-1411.
- Giro, L.R., and Dubrovskiy, N.A. (1973) "On the origin of low-frequency component of the echoranging pulsed signal of dolphins", in *Ref. Dokl. 8-ya Vses. Akust. Konf.* (Proceedings of the 8th All-Union Acoustics Conference), Moscow, 1973, [also in Bel'kovich and Dubrovskiy (1976)].
- Giro, L.R., and Dubrovskiy, N.A. (1974) "The possible role of supracranial air sacs in the formation of echo ranging signals in dolphins", Akust. Zh., 20(5):706-710.
- Goss, S.A., Frizzell, L.A., Dunn, F., and Dines, K.A. (1980a), "Dependence of the ultrasonic properties of biological tissue on constituent proteins", J. Acoust. Soc. Am., 67(3):1041-1044.
- Goss, S.A., Johnston, R.L., and Dunn, F. (1980b), "Compilation of empirical ultrasonic properties of mammalian tissues. II", J. Acoust. Soc. Am., 68(1):93-108.
- Green, R.F., Ridgway, S.H., and Evans, W.E. (1980), "Anatomy of the Bottlenosed dolphin", in *Animal Sonar Systems*, edited by R.G. Busnel and J.R. Fish, Plenum Pub., New York, 1980, pp. 199-238.
- Halpern, L., and Trefethen, L.N. (1988), "Wide-angle one-way wave equations", J. Acoust. Soc. Am., 84:1397-1404.

- Henson, P.W., Ackland, T., and Fox, R.A. (1987), "Tissue density measurement using CT scanning", *Australasian Phys. & Eng. Sci. in Med.*, July-Sept. 1987, v10(3):162-166.
- Hunter, J.A. (1988), "Dual-energy radiography, dual-photon absorptiometry, and quantitative computed tomography: comparative precision and accuracy in vitro", Ph.D. dissertation, U.C. San Diego.
- Hwang, J.Y., and Chang, S.C. (1991), "A retracted boundary integral equation for exterior acoustic problem with unique solution for all wave numbers", *J. Acoust. Soc. Am.*, 90(2):1167-1180.
- Jia, Z.H., Wu, T.W., and Seybert, A.F. (1993), "Simplified Hypersingular Boundary Integral Equations for Acoustic Scattering and Radiation", in *Computational Acoustics: Scattering, Supercomputing, and Propagation*, IMACS Symposium on Computational Acoustics (3rd: 1991: Cambridge, Mass.); North-Holland, 1993, v1:329-340.
- Johnston, R.L., Goss, S.A., Maynard, V., Brady, J.K., Frizzell, L.A., O'Brien, Jr., W.D., and Dunn, F. (1979), "Elements of tissue characterization: Part I - Ultrasonic propagation properties", in NBS Special Publication 525: *Ultrasonic Tissue Characterization II*, edited by M. Linzer, U.S. GPO, Washington, DC, 1979, pp. 19-27.
- Junger, M.C., and Feit, D. (1986), *Sound, Structures, and their Interactions*, 2nd ed., MIT Press, Cambridge, MA, 1986.
- Ketten, D.R., and Wartzok, D. (1990). "Three-dimensional Reconstructions of the Dolphin Ear", in *Sensory Abilities of Cetaceans*, edited by J. Thomas and R. Kastelein, Plenum Pub., New York, 1990, pp. 81-91.
- Kinsler, L.E., Frey, A.R., Coppens, A.B., and Sanders J.V. (1982), *Fundamentals of Acoustics*, 3rd ed., John Wiley & Sons, 1982.
- Korolev, L.D., Lipatov, N.V., Rezvov, R.N., Savel'yev, M.A., and Flenov, A.B. (1973), "Investigation of Delphinid Locating System Capabilities Passive Ranging", in *Ref. Dokl. 8-y Vses. Akust. Konf.*, Moscow, 1973, Vol. 1, pp. 125-126 [also in Bel'kovich and Dubrovskiy (1976)].
- Lachat, J.C., and Watson, J.O. (1976), "Effective numerical treatment of boundary integral equations: a formulation for three-dimensional elastostatics", *Int. J. Num. Meth. Eng.*, 10:991-1005.
- Law, W.K., Frizzell, L.A., and Dunn, F. (1981) "Ultrasonic determination of the nonlinearity parameter B/A for biological media", *J. Acoust. Soc. Am.*, 69(4):1210-1212.
- Law, W.K., Frizzell, L.A., and Dunn, F. (1983), "Comparison of thermodynamic and finite amplitude methods of B/A measurement in biological materials", *J. Acoust. Soc. Am.*, 74(4):1295-1297.
- Lees, S., and Davidson, C.L. (1979), "A theory relating sonic velocity to mineral content in bone", in NBS Special Publication 525: *Ultrasonic Tissue Characterization II*, edited by M. Linzer, U.S. GPO, Washington, DC, 1979, pp. 179-187.
- Lele, P.P., and Sleaf, G.E. (1985), "Ultrasonic tissue characterization", in *Ultrasound - Medical Applications, Biological Effects, and Hazard Potential*, edited by M.H. Repacholi, M. Grandolfo, and A. Rindi, Plenum Pub., New York, 1987, pp. 343-356.
- Lindman, E.L. (1975), "Free space boundaries for the scalar wave equation", *J. Comp. Phys.*, 18:66-78.

- Litchfield, C., Karol, R., and Greenberg, A.J. (1973), "Compositional topography of melon lipids in the Atlantic Bottlenose dolphin *Tursiops truncatus*: implications for echolocation", *Marine Biology*, 23:165-169.
- Litchfield, C., Greenberg, A.J., Caldwell, D.K., Caldwell, M.C., Sipos, J.C., and Ackman, R.G. (1975), "Comparative lipid patterns in acoustical and nonacoustical fatty tissues of dolphins, porpoises, and toothed whales", *Comp. Biochem. Physiol.*, 50B:591-597.
- Litchfield, C., Karol, R., Mullen, M.E., Dilger, J.P., and Luthi, B. (1979) "Physical factors influencing refraction of the echolocative sound beam in Delphinid Cetaceans", *Marine Biology*, 52:285-290.
- Mackay, R.S. (1980), "Dolphin air sac motion measurements during vocalization by two noninvasive ultrasonic methods", in *Animal Sonar Systems*, edited by R.G. Busnel and J.R. Fish, Plenum Pub., New York, 1980, pp. 933-938.
- Mackay, R.S. and Liaw, H.M. (1981), "Dolphin vocalization mechanisms", *Science*, 212(8):676-677.
- Mackay, R.S. (1988), "Whale heads, magnetic resonance images, ray diagrams and tiny bubbles", in *Animal Sonar: Processes and Performance*, edited by P.E. Nachtigall and P.W.B. Moore, Plenum Pub., New York, 1988, pp. 79-86.
- Malins, D.C., and Varanasi, U. (1975), "Cetacean Biosonar: Part 2 - The biochemistry of lipids in acoustic tissues", in *Biochemical and Biophysical Perspectives in Marine Biology*, edited by D.C. Malins and J.R. Sargent, Academic Press, New York, pp. 237-287.
- McCormick, J.G., Wever, E.G., Palin, J., and Ridgway, S.H. (1970), "Sound conduction in the dolphin ear", *J. Acoust. Soc. Am.*, 48(6):1418-1428.
- McCormick, J.G., Wever, E.G., Ridgway, S.H., and Palin, J. (1980), "Sound reception in the porpoise as it relates to echolocation", in *Animal Sonar Systems*, edited by R.G. Busnel and J.R. Fish, Plenum Pub., New York, 1980, pp. 449-467.
- Moore, P.W.B., and Pawloski, D.A. (1990), "Investigations on the control of echolocation pulses in the dolphin (*Tursiops truncatus*)", in *Sensory Abilities of Cetaceans: Laboratory and Field Evidence*, edited by J. Thomas and R. Kastelein, Plenum Pub., New York, 1990, pp. 305-316.
- Moore, T.G., Blaschak, J.G., Taflove, A., and Kriegsmann, G.A. (1988), "Theory and application of radiation boundary operators", *IEEE Trans. Antennas Propagat.*, 36:1797-1812.
- Morris, R. (1986), "The acoustic faculty of dolphins", in *Research on Dolphins*, edited by M.M. Bryden and R. Harrison, Clarendon Press, New York, 1986, pp. 369-399.
- Morse, P.M., and Ingard, K.U. (1968), *Theoretical Acoustics*, Princeton University Press, Princeton, 1968.
- Norris, K.S. (1964), "Some problems of echolocation in cetaceans", in *Marine Bio-acoustics*, Vol. 2, edited by W.N. Tavolga, Pergamon Press, New York, pp. 317-336.
- Norris, K.S., Evans, W.E., and Turner, R.N. (1966), "Echolocation in an Atlantic Bottlenose porpoise during discrimination", in *Animal Sonar Systems: Biology and Bionics*, edited by R.G. Busnel, Frascati, Italy, 1966, pp. 409-437.
- Norris, K.S. (1968), in *Evolution and Environment*, edited by E.T. Drake, Yale University Press, New Haven, 1968, pp. 297-324.

- Norris, K.S., Dormer, K.J., Pegg, J., and Liese, G.T. (1971), "The mechanism of sound production and air recycling in porpoises: a preliminary report", in *Proc. VIII Conf. Biol. Sonar Diving Mammals*, Menlo Park, CA.
- Norris, K.S. and Harvey, G.W. (1972), "A theory for the function of the spermaceti organ of the sperm whale (*Physeter catodon* L.)", in *Animal Orientation and Navigation*, Sci. and Tech. Office NASA, Washington D.C., SP-262, pp. 397-423.
- Norris, K.S. and Harvey, G.W. (1974), "Sound transmission in the porpoise head", *J. Acoust. Soc. Am.*, 56(2):659.
- Norris, K.S. and Mohl, B. (1983), "Can odontocetes debilitate prey with sound?", *American Naturalist*, 122:85-104.
- Novikov, B.K., Rudenko, O.V., and Timoshenko, V.I. (1987), *Nonlinear Underwater Acoustics*, American Institute of Physics (Acoustical Society of America Translation Book), 1987.
- Parry, R.J., and Chivers, R.C. (1979), "Data of the velocity and attenuation of ultrasound in mammalian tissues - A survey", in *NBS Special Publication 525: Ultrasonic Tissue Characterization II*, edited by M. Linzer, U.S. GPO, Washington, DC, 1979, pp. 343-360.
- Pierce, A.D. (1981), *Acoustics*, McGraw-Hill, 1981.
- Purves, P.E. and Pilleri, G. (1983), *Echolocation in Whales and Dolphins*, Academic Press, London, 1983.
- Randall, C.J., (1988). "Absorbing boundary condition for the elastic wave equation", *Geophysics*, 53(5):611-24.
- Renaut, R.A. (1992), "Absorbing boundary conditions, difference operators and stability", *J. Computat. Phys.*, 102(2):236-251.
- Reynolds, A.C. (1978), "Boundary conditions for the numerical solution of wave propagation problems", *Geophysics*, 43(6):1099-1110.
- Ridgway, S.H., Carder, D.A., Green, R.F., Gaunt, A.S., Gaunt, S.L.L., and Evans, W.E. (1980), "Electromyographic and pressure events in the nasolaryngeal system of dolphins during sound production", in *Animal Sonar Systems*, edited by R.G. Busnel and J.R. Fish, Plenum Pub., New York, 1980, pp. 239-249.
- Rizzo, F.J., and Shippy, D.J. (1977), "An advanced boundary integral equation method for three-dimensional thermoelasticity", *Int. J. Num. Meth. Eng.*, 11:1753-1768.
- Romanenko, Y.V. (1973), "Investigating generation of echolocation pulses in dolphins", *Zool. Zh.*, 11:1698, (JPRS 61553, 1974, pp. 1-8).
- Romanenko, Y.V. (1974), "On the mechanism of dolphin emission of some pulse and whistle signals", in Bel'kovich, V.M., and Dubrovskiy, N.A. (1976), *Sensory Bases of Cetacean Orientation*, Izdatel'stvo Nauka, Leningrad, JPRS 7157, 1977, pp. 137-148.
- Schenck, H.A. (1968), "Improved Integral Formulation for Acoustic Radiation Problems", *J. Acoust. Soc. Am.*, 44(1):41-58.
- Schenkkan, E.J. (1973), "On the comparative anatomy and function of the nasal tract in odontocetes (Mammalia, Cetacea)", *Bijdr. Dierk.*, 43(2):127-159.
- Sehgal, C.M., Bahn, R.C., and Greenleaf, J.F. (1984), "Measurement of the acoustic nonlinearity parameter B/A in human tissues by a thermodynamic method", *J. Acoust. Soc. Am.*, 76(4):1023-1029.

- Seybert, A.F., and Rengarajan, T.K. (1987), "The use of CHIEF to obtain unique solutions for acoustic radiation using boundary integral equations", *J. Acoust. Soc. Am.*, 81(5):1299-1306.
- Seybert, A.F., Soenarko, B., Rizzo, F.J., and Shippy, D.J. (1985), "An advanced computational method for radiation and scattering of acoustic waves in three dimensions", *J. Acoust. Soc. Am.*, 77(2):362-368.
- Shaw, R.P. (1974), "The outer boundary integral equation method applied to wave scattering in an infinite, locally inhomogeneous medium", Hawaii Institute of Geophysics, University of Hawaii: Joint Tsunami Research Effort, Pacific Oceanographic Laboratories, National Oceanic and Atmospheric Administration, 1974.
- Smith, G.D. (1985), *Numerical Solution of Partial Differential Equations: Finite Difference Methods*, 3rd ed., Oxford University Press, 1985.
- Tirkas, P.A., Balanis, C.A., and Renaut, R.A. (1992), "Higher order absorbing boundary conditions for the finite-difference time-domain method", *IEEE Trans. Antennas Propagat.*, 40(10):1215-1222.
- Titov, A.A. (1972), in Bel'kovich, V.M., and Dubrovskiy, N.A. (1976), *Sensory Bases of Cetacean Orientation*, Izdatel'stvo Nauka, Leningrad, JPRS 7157, 1977.
- Tobocman, W. (1984), "Calculation of acoustic wave scattering by means of the Helmholtz integral equation. I", *J. Acoust. Soc. Am.*, 76(2):599-607.
- Tritton, D.J. (1977), *Physical Fluid Dynamics*, Van Nostrand Reinhold (UK), 1977.
- Twizell, E.H. (1984), *Computational Methods for Partial Differential Equations*, Halsted Press (John Wiley & Sons), 1984.
- Varanasi, U., Feldman, H.R., and Malins, D.C. (1975), "Molecular basis for formation of lipid sound lens in echolocating cetaceans", *Nature*, 255:340-343.
- Varanasi, U., Markey, D., and Malins, D.C. (1982), "Role of isovaleroyl lipids in channeling of sound in the porpoise melon", *Chem. Phys. Lipids*, 31:237-244.
- Wood, F.G. (1964), in *Marine Bio-acoustics*, Vol. 2, edited by W.N. Tavolga, Pergamon Press, New York, pp. 395-396.
- Wood, F.G., and Evans, W.E. (1980), "Adaptiveness and ecology of echolocation in toothed whales", in *Animal Sonar Systems*, edited by R.G. Busnel and J.R. Fish, Plenum Pub., New York, 1980, pp. 381-426.
- Ziomek, L.J. (1995), *Fundamentals of acoustic field theory and space-time signal processing*, CRC Press, Boca Raton, 1995.